



HAL
open science

Assemblage systématique de capteurs électrochimiques d'antigène spécifique de la prostate à base de phtalocyanines Co(II) asymétriques, de points quantiques graphitiques et d'un aptamère

Siphesihle Nxele

► To cite this version:

Siphesihle Nxele. Assemblage systématique de capteurs électrochimiques d'antigène spécifique de la prostate à base de phtalocyanines Co(II) asymétriques, de points quantiques graphitiques et d'un aptamère. Chimie organique. Université Paris sciences et lettres; Rhodes university (Grahamstown, Afrique du Sud), 2021. Français. NNT : 2021UPSLC028 . tel-03727523

HAL Id: tel-03727523

<https://pastel.hal.science/tel-03727523>

Submitted on 19 Jul 2022

HAL is a multi-disciplinary open access archive for the deposit and dissemination of scientific research documents, whether they are published or not. The documents may come from teaching and research institutions in France or abroad, or from public or private research centers.

L'archive ouverte pluridisciplinaire **HAL**, est destinée au dépôt et à la diffusion de documents scientifiques de niveau recherche, publiés ou non, émanant des établissements d'enseignement et de recherche français ou étrangers, des laboratoires publics ou privés.



THÈSE DE DOCTORAT
DE L'UNIVERSITÉ PSL

Préparée à Chimie Paristech PSL

Dans le cadre d'une cotutelle avec l'Université de Rhodes (Afrique du Sud)

Assemblage systématique de capteurs électrochimiques d'antigène spécifique de la prostate à base de phtalocyanines Co(II) asymétriques, de points quantiques graphitiques et d'un aptamère

The systematic assembly of prostate specific antigen electrochemical sensors based on asymmetric Co(II) phthalocyanines, graphitic quantum dots and an aptamer

Soutenue par

Siphesihle Robin NXELE

Le 01-12-2021

Ecole doctorale n° 406

**Chimie moléculaire de
Paris centre**

Spécialité

Chimie moléculaire



ParisTech

PSL

Composition du jury :

Ilaria, CIOFINI Directrice de recherche, Chimie Paristech PSL	<i>Présidente</i>
Sophie, CASSAIGNON Professeur, Sorbonne Université	<i>Rapportrice</i>
Claire, MANGENEY Professeur, Université de Paris	<i>Rapportrice</i>
Nolwazi, NOMBONA Professeur, Université de Pretoria	<i>Examinatrice</i>
Philani, MASHAZI Professeur, Université de Rhodes	<i>Examineur</i>
Kenneth, OZOEMENA Professeur, Université de Witwatersrand	<i>Examineur</i>
Anne, VARENNE Professeur, Chimie Paristech PSL	<i>Co-Directrice de thèse</i>
Tebello, NYOKONG Professeur, Université de Rhodes	<i>Directrice de thèse</i>

Dedications

To the village that raised me and got me this far, to my parents Israel and Sharon Nxele, and to the researchers that will come after me and be inspired by this work.

"Here's to the end of this chapter. To all the late nights, early mornings, learnings gained, and experiences shared. Here's to the hardships that became our teachers, to the heaviness that taught us how to rise again and to the people who would stop their world to sit and celebrate our presence. Here's to the times we chose feeling over disconnection, freedom over perfection, courage over what's known and certain, and doing the work. Here's to releasing what wasn't ours to keep. Here's to holding our palms wide open to our blessings. And here's to taking one step forward into the hope and possibility of tomorrow."

- Danielle Doby

Acknowledgements

To my supervisor and the powerhouse who made this PhD dream a reality for me, distinguished Professor Tebello Nyokong, I cannot thank you enough Prof. I am forever grateful.

Thank you to Dr Fethi Bedioui as well as my supervisors at Chimie Paristech, Prof. Anne Varenne, Dr Fanny d'Orlye, Dr Laura Trapiella-Alfonso and my research group in France for hosting me and being a part of this PhD journey.

Thank you to Professor Philani Mashazi and Professor Janice Limson for helping me at the very beginning of this journey with bringing this project to life.

I also express my sincere gratitude to Miss Gail Cobus, Dr Jonathan Britton, Professor John Mack and Mr Francis Chindeka for their support and help during the course of this research. Thank you to Dr David Oluwole, who mentored me at that start of this PhD journey. Thank you to my lab S22 colleagues who have always been so helpful.

A special thank you goes to Mr Tendai Chonzi, Dr Allan Sanyanga, Miss Reitumetse Nkhahle, Miss Sivu Mapukata and Mr Nnamdi Nwahara for being my support structure in and out of this academic space.

Thank you to my friends and family for your love, kindness and patience throughout this journey.

Thank you to Rhodes University (South Africa) and Chimie Paristech (France).

Financial support from the French government (campus France) and the National Research Foundation (NRF) of South Africa through DST/NRF South African Research Chairs Initiative for Professor of Medicinal Chemistry and Nanotechnology (UID 62620) is gratefully acknowledged.

Preface

The need for low-cost, efficient and simple diagnostic tools has led to more research going into this subject, with the aim of making such medical devices more accessible where they are needed. This has led to more researchers developing point-of-care devices for this purpose worldwide, by sensor fabrication. This thesis focuses on electrochemical sensor development for the early diagnosis of prostate cancer. It is common knowledge that prostate cancer is one of the most prevalent carcinomas that have claimed lives due to late diagnosis where even the most invasive treatments have failed. For this reason, development of early detection devices that can even be used in the comfort of home is necessary and quite crucial. Electrochemical sensors have gained much attention due to their ease of fabrication, cost effectiveness, simplicity, ease of use and high efficiency. Using nanocomposites as modifiers has also become popular as they provide greater stability and improve detection limits when used together with biomolecules. With that said, the work reported herein has combined nanocomposites of graphene-based quantum dots, gold nanoparticles, phthalocyanines and an aptamer in order to fabricate aptasensors for the electrochemical detection of prostate cancer biomarker. The aptamer is specifically designed to bind to the biomarker, and the nanocomposites are expected to enhance current output thus lowering detection limits and increasing stability and efficiency. Reproducible results are also expected. Prior to the detection of the prostate cancer biomarker, the quantum dots-phthalocyanine nanohybrids were used to detect L-cysteine, which is an amino acid, in order to verify the synergistic effects as electrode modifiers that lead to the enhancement of current output. This increase in current output is then exploited for the

improvement of aptasensor functionality upon incorporation of the aptamer, for the detection of prostate specific antigen. The research in this thesis has been carried out with the intention of contributing to the world of medical research, more so because of the ever-increasing need for medical care to become accessible to all and not only to those who can afford expensive technologies and treatments.

Contents

Dedication	(ii)
Acknowledgements	(iii)
Preface	(v)
Table of contents	(viii)
List of abbreviations	(xv)
List of symbols	(xvii)
Résumé de la thèse	(xx)

Table of contents

Chapter 1

1.	Introduction	1
1.1	Overview of metallophthalocyanines (MPcs)	2
1.1.1	Synthesis of asymmetric MPcs	2
1.1.2	Phthalocyanine complexes used in this work	4
1.2	Overview of graphene-based quantum dots	5
1.2.1	The synthesis of GQDs, NGQDs and gCNQDs	9
1.2.2	GQDs characterization and structural determination	10
1.2.3	General applications of GQDs, NGQDs and gCNQDs	13
1.3	Gold nanoparticles (AuNPs)	15
1.3.1	Synthesis properties and applications	15
1.3.2	AuNPs and their conjugates with MPc in electrochemical sensing	16
1.4	Overview of aptamers	18
1.4.1	Discovery and development	18
1.4.2	Aptamers as biorecognition elements in biosensing	18
1.4.3	Aptamers as bioconjugates for sensing	19
1.5	Target analyte used in this work	21

1.5.1 L-cysteine	21
1.5.2 PSA	21
1.6 Methods of electrode surface modifications	28
1.6.1 Adsorption by 'drop and dry' modification technique	28
1.6.2 Electrodeposition & self-assembly	28
1.6.3 Electrochemical grafting by reduction and 'click' reaction	29
1.7 Summary of aims of this thesis	35

Chapter 2

2. Materials, equipment and experimental	38
2.1 Materials	39
2.1.1 Solvents and general materials	39
2.1.2 Synthesis of MPcs and conjugates	39
2.1.3 Quantum dots	39
2.1.4 Biological samples	39
2.1.5 Capillary electrophoresis-mass spectrometry (CE-MS)	40
2.1.6 Electrode modification	40
2.2 Solution preparation	40
2.2.1 Capillary electrophoresis-mass spectrometry (CE-MS)	40
2.2.2 Aptamer	41
2.2.3 Electrochemical detection	41
2.3 General equipment	41

2.4 Capillary electrophoresis-mass spectrometry experiments	44
2.4.1 CE-UV experiments	45
2.4.2 MS detection	46
2.5 Synthesis	47
2.5.1 Complex (1)	47
2.5.2 Complex (2)	48
2.5.3 Quantum dots	49
2.5.4 Conjugation of nanocomposites	51
2.5.4.1 $\pi\pi$ conjugation: QDs-CoPc (1), Scheme 3.5	51
2.5.4.2 Covalent conjugation: GODs@Aptamer, gCNQDs@Aptamer and CoPc(1)@Aptamer (Scheme 3.4)	52
2.5.4.3 Non-covalent combination of gCNQDs@Aptamer with complex (1) and (2)	53
2.6 Electrode modification	53
2.6.1 Drop and dry electrode modification	54
2.6.2 Electrodeposition and self-assembly, Scheme 4.2 (a)	55
2.6.3 Electrografting and click chemistry, Scheme 4.2 (b)	55
2.7 Electrode and solution preparation for detection of PSA	56

Chapter 3

3. Characterization	59
3.1 Characterization of GODs, NGQDs and gCNQDs	60
3.1.1 Dispersity and size distribution	62
3.1.1.1 TEM	62

3.1.1.2 DLS	66
3.1.2 Elemental composition and structure	68
3.1.2.1 Energy dispersive X-ray (EDX) analysis	68
3.1.2.2 Raman spectra	70
3.1.2.3 FTIR spectra	72
3.1.2.4 XPS spectra	74
3.1.3 Dispersity, charge density and colloidal stability	80
3.1.3.1 Zeta potential (ζ)	80
3.1.3.2 CE-ESI-MS	84
3.2 Characterization of MPcs, Complex (1) and complex (2)	104
3.3 Characterization of conjugates	105
3.3.1 Verification of covalently linked conjugates GQDs@Aptamer, gCNQDs@Aptamer and CoPc(1)@Aptamer	106
3.3.1.1 XPS spectra	106
3.3.1.2 DLS and zetametry	110
3.3.1.3 FTIR spectra	113
3.3.1.4 Raman spectra	115
3.3.2 $\pi\pi$ conjugation	116
3.3.2.1 UV/vis spectroscopy	117
3.3.2.2 DLS and zetametry	120
3.3.2.3 Raman spectra	122
3.4 Conclusion	125

Chapter 4

4. Electrode modification and characterization	128
4.1 Electrode modification by adsorption: Table 4.1, group A-C	130
4.1.1 Cyclic voltammetry	131
4.1.2 SECM	137
4.2 Preparation and characterization of AuNPs, CoPc (2) and aptamer-based electrodes	141
4.2.1 Electrodeposition of AuNPs	143
4.2.1.1 Cyclic voltammetry	143
4.2.1.2 Scanning electron microscopy (SEM)	146
4.2.2 Self-assembly, electrochemical grafting and click chemistry and	148
4.2.3 Cyclic voltammetry characterization	151
4.2.4 SECM characterization	155
4.2.5 XPS spectra	157
4.3 Conclusions	165

Chapter 5

5. Electrochemical detection	167
5.1 Electrochemical detection of L-cysteine	168
5.1.1 Cyclic voltammetry	168
5.1.2 Chronoamperometry	170
5.1.3. Kinetics: Scan rate studies	177
5.1.4 Stability	179
5.2 The electrochemical detection of PSA	180

5.2.1	GQDs-CoPc(1)($\pi\pi$)-Aptamer conjugates	180
5.2.1.1	EIS	180
5.2.1.2	Concentration studies: DPV and EIS	186
5.2.1.3	Stability, selectivity, and reproducibility studies	190
5.2.2	The effects of QDs composition and structure: Comparing GQDs, NGQDs and gCNQDs	196
5.2.2.1	EIS	196
5.2.2.2	Concentration studies using EIS and DPV	199
5.2.2.3	Selectivity, stability, and reproducibility studies	201
5.2.3	Influence of MPc substituents	206
5.2.3.1	EIS	206
5.2.3.2	Concentration studies using EIS	208
5.2.3.3	Stability, reproducibility, and repeatability	212
5.2.4	AuNPs-MPc conjugates	214
5.2.4.1	EIS	214
5.2.4.2	Concentration studies using EIS and DPV	216
5.2.4.3	Effects of scan rate	218
5.2.4.4	Selectivity, stability, repeatability, and reproducibility studies	220
5.3	Conclusions	224
Chapter 6		
6.	Real sample analyses	227
6.1	$\pi\pi$ -conjugates	229
6.2	Covalently linked conjugates	235

6.3 Self-assembly, electrografting and click chemistry	239
6.4 Conclusions	243
Chapter 7	
7. Summary, conclusions, and prospects	245
7.1 Overview of the thesis	246
7.2 Future prospects and final remarks	247
References	249

List of abbreviations

AuNPs = gold nanoparticles

BE = binding energy

BGE = background electrolyte

CE-MS = capillary electrophoresis mass spectrometry

CoPc = cobalt phthalocyanine

CV = cyclic voltammetry

DBU = 1,8-Diazabicyclo [5.4.0]undec-7-ene

DMF = dimethylformamide

DMSO = dimethylsulphoxide

DPV = differential pulse voltammetry

EIS = electrochemical impedance spectroscopy

ESI = electrospray ionization

FTIR = fourier transform infra-red

GCE = glassy carbon electrodes

gCNQDs = graphitic carbon nitride quantum dots

GPES = general purpose electrochemical system

GQDs = graphene quantum dots

MPcs = metallophthalocyanines

NGQDs = nitrogen doped graphene quantum dots

NM = neutral marker

PCa = prostate cancer

PSA = prostate specific antigen

SECM = scanning electrochemical microscopy

SEM = scanning electron microscopy

TEM = transmission electron microscopy

tert-butyl = tertiary butyl

UME = ultra-micro electrode

UV/vis = ultraviolet/visible

XPS = X-ray photoelectron spectroscopy

XRD = X-ray diffraction

List of symbols

α = non-peripheral position

A = electrode surface area.

B = peripheral position

b = the Tafel slope

C = concentration

C_{dl} = double layer capacitance

D = diffusion coefficient

ΔE = Peak potential separation

E_{pa} = anodic peak potential

E_{pc} = cathodic peak potential

eV = electron volt

F = Faraday's constant

f = frequency

I_{ac} = anodic peak current.

I_{buf} = currents in the absence analyte

I_{cat} = currents in the presence of analyte

I_D = intensity of Raman D band

I_G = intensity of Raman G band

i_{Lim} = limiting current

I_p = peak current

I_{pc} = cathodic peak current.

k_{app} = apparent rate transfer constant

k_{cat} = the catalytic rate constant

K = constant

n_a = number of electrons involved in the rate determining step

R = the universal gas constant

R_{ct} = charge transfer resistance

R_s = solution resistance

δ = standard deviation

Γ = surface coverage

T = temperature (298 K)

v = scan rate

W = Warburg Impedance

Z' = real impedance.

Z'' = imaginary impedance

Résumé de la thèse

Cette thèse traite du développement d'aptacapteurs électrochimiques pour la détection précoce du cancer de la prostate. Une détection précoce est réalisée en déterminant les niveaux de concentration de l'antigène spécifique de la prostate (PSA), biomarqueur qui est directement lié au cancer de la prostate. Chez les hommes en bonne santé, le taux de PSA se situe entre 0 et 4 ng/mL [1] ; une concentration supérieure peut être un signe de développement d'un cancer. C'est pourquoi le développement de capteurs est crucial pour surveiller les niveaux de PSA en vue d'un diagnostic précoce. Parmi les outils de diagnostic utilisés pour la détection du PSA, nous pouvons citer les tests immuno-enzymatiques (ELISA), les tests immunologiques par fluorescence et électrochimiques, la chimioluminescence, la résonance plasmonique de surface (SPR), la diffusion Raman exaltée de surface (surface-enhanced Raman spectroscopy, SERS) et la réaction en chaîne par polymérase (PCR) [2-14]. Ces méthodes permettent la détection de plusieurs échantillons à la fois et sont considérées comme fiables, mais elles sont coûteuses et nécessitent des méthodes onéreuses qui ne peuvent être utilisées que par des personnes qualifiées. Dans le contexte du diagnostic, les capteurs électrochimiques sont devenus populaires car ils peuvent être facilement fabriqués et sont efficaces. La modification d'électrodes par des biomolécules greffées sur des nanocomposites modifiés génère une reconnaissance moléculaire augmentant la stabilité et la sélectivité du capteur et diminuant les limites de détection. Les capteurs électrochimiques à base d'aptamères (« aptasensors ») sont en plein essor : ils sont miniaturisables, peu coûteux en production de masse, efficaces et faciles à utiliser, ce qui offre un accès au chevet du patient à un coût faible.

Dans ce travail, des “quantum dots”, points quantiques à base de graphène, et des nanoparticules d'or ont été modifiés par des phthalocyanines de cobalt ainsi qu'un aptamère et immobilisés sur des électrodes de carbone vitreux pour la détection électrochimique du PSA. L'aptamère sélectionné est spécifique exclusivement du PSA [15]. Les nanostructures, incluant les phthalocyanines permettent d'améliorer le débit de courant et d'augmenter la surface d'immobilisation de l'aptamère, ce qui devrait favoriser la liaison du PSA à cet élément de reconnaissance. En vue du développement de cet aptacapteur, chaque élément du système a été caractérisé physico-chimiquement pour justifier de sa pureté de synthèse ainsi que de son intérêt dans l'intégration dans un aptacapteur. Après conception de l'aptacapteur, celui-ci est optimisé et validé sur des échantillons de sérum dopés et des mélanges complexes pour

s'assurer qu'ils sont sélectifs et utilisables dans des tests cliniques. Ce résumé explique brièvement le contenu de chaque chapitre.

1. Chapitre 1 : Introduction

Ce chapitre présente les différents composants synthétisés dans ce travail de thèse et intégrés dans la conception d'aptacapteurs électrochimiques stables, efficaces, sélectifs et spécifiques. Ces éléments comprennent les QDs (points quantiques) à base de graphène et les nanoparticules d'or combinés avec des métallophthalocyanines et un aptamère pour la détection électrochimique du PSA. Ces nanoconjugués sont, pour la première fois, liés à un aptamère et immobilisés sur des électrodes en carbone vitreux pour fabriquer des outils de diagnostic du cancer de la prostate.

1.1 Les Métallophthalocyanines (MPcs)

La synthèse de MPcs asymétriques a été réalisée à l'aide de diverses méthodes, y compris la condensation croisée [16] en utilisant le rapport 3:1. Dans ce travail, les nouveaux complexes de phthalocyanine substitués asymétriquement suivants ont été utilisés : l'acide 2-benzoïque-9(10),16(17),23(24)-tris(2,6-di-tert-butyl-4-méthylphénoxy) phthalocyaninato de cobalt (II) (Figure 1, Complexe 1) et le 2-N,N',N''-hex-5-yn-1-yloxy)-9(10),16(17), 23(24)-tris(benzène-4,1-diyl))triacétamidophthalocyaninato de cobalt(II) (Figure 1, Complexe 2). Le complexe 1 possède des groupes (tert-butyle) qui agissent comme des groupes donneurs d'électrons (« push ») et la fonction acide carboxylique unique comme un groupe attracteur d'électrons (« pull »). Le complexe 2 possède un groupe terminal alcyne qui sera utilisé pour immobiliser la molécule sur une électrode par électrogreffage et chimie click avant d'incorporer l'aptamère par adsorption. Le complexe 2 possède également des groupes alcoxy donneurs d'électrons qui abaissent les potentiels d'oxydation. Une différence de potentiel plus faible implique un meilleur transfert d'électrons, ce qui pourrait affecter les performances des capteurs fabriqués dans leur ensemble. En outre, les deux complexes sont liés aux QDs par des interactions π - π .

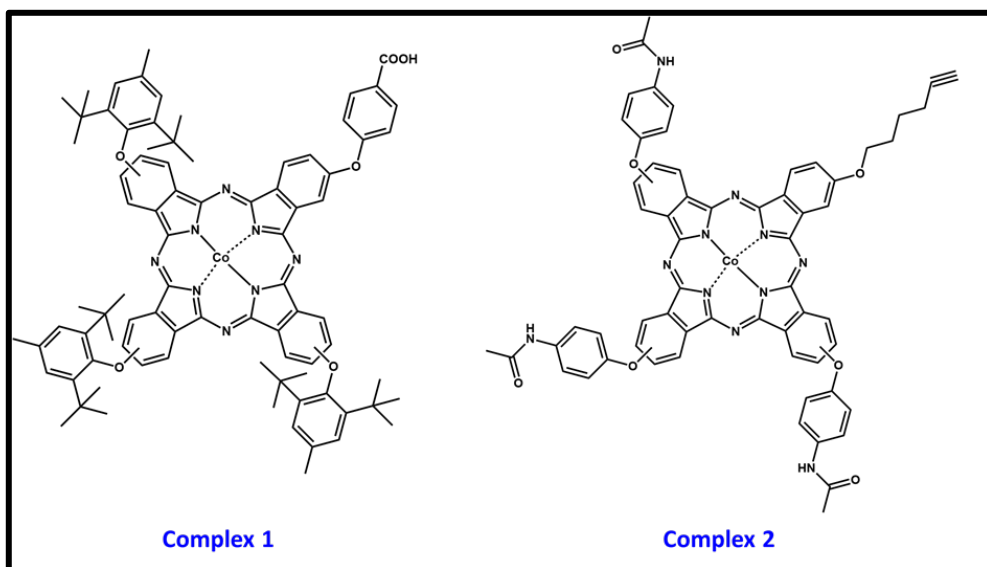


Figure 1 : Structures des molécules de phtalocyanine utilisées dans ce travail.

1.2 Points quantiques (GQDs) à base de graphène et nanoparticules d'or (AuNPs)

Le graphène et les points quantiques de graphène (GQDs) sont des composites bien dispersés dans l'eau, biocompatibles, facilement fonctionnalisables à leur surface, et possédant également une faible toxicité, avec une gamme de taille de 1 à 20 nm [17]. Les GQDs sont devenus populaires en électrocatalyse en raison de leur grande stabilité, de leur surface élevée et de leurs bonnes capacités de transfert de charge [18]. Ces caractéristiques ont permis d'améliorer la production de courant et, par conséquent, les performances des capteurs électrochimiques. Le dopage des GQDs avec des hétéroatomes a montré une amélioration de l'activité électrocatalytique. L'azote a une électronégativité plus élevée (3,04) que le C (2,55), ce qui favorise la modification des états électroniques du graphène et améliore donc la capacité électrocatalytique de ces nanostructures.

Dans ces travaux de doctorat, trois structures de GQDs ont été synthétisées et caractérisées: les GQDs, les points quantiques de graphène dopés à l'azote (NGQDs) et les points quantiques de nitrure de carbone graphitique (gCNQDs). Les structures théoriques sont présentées dans la Figure 2.

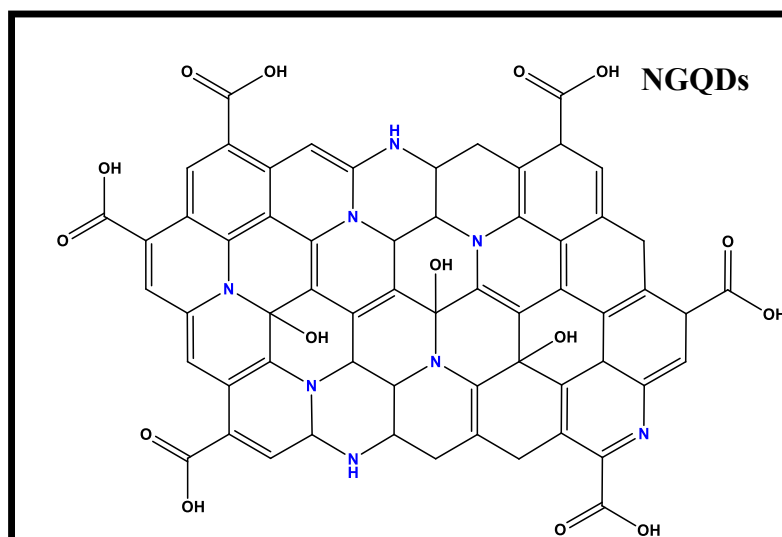
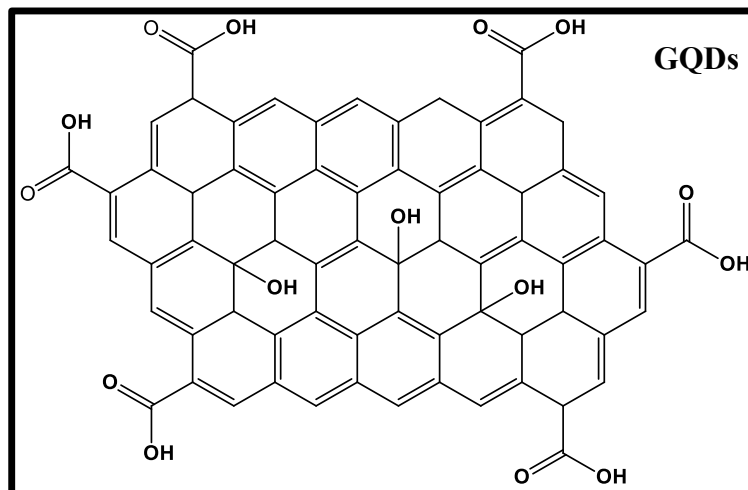
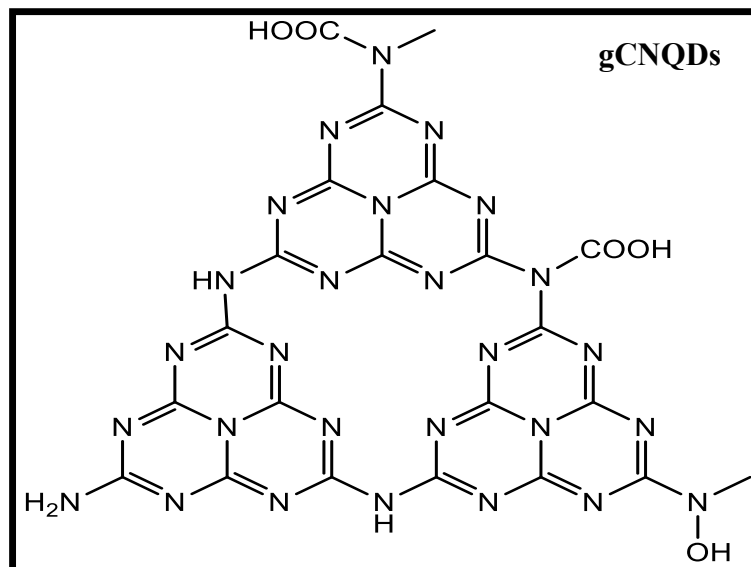


Figure 2: Structures theoretiques des gCNQDs, GQDs and NGQDs.

Ces composites ont été synthétisés par des méthodes hydrothermales. Leur caractérisation a été réalisée de façon approfondie à l'aide de diverses méthodes spectroscopiques telles que les spectroscopies Raman, d'absorption et infrarouge à transformée de Fourier (FTIR), spectroscopie électronique à transmission (TEM), diffusion dynamique de la lumière (DLS), analyse par rayons X à dispersion d'énergie (EDX), spectroscopie Raman, spectroscopie photoélectronique à rayons X (XPS) et zétamétrie. Récemment, l'électrophorèse capillaire est apparue comme une méthode de choix pour la caractérisation de nanoparticules [19-21]. La caractérisation par électrophorèse capillaire (couplée à la détection UV-visible et de fluorescence) des trois lots de GQDs a montré une grande polydispersité dans les lots et a donc conduit à un travail d'optimisation de la synthèse des GQDs en modifiant le paramètre temps de synthèse. L'électrophorèse capillaire (CE) couplée à la spectrométrie de masse par ionisation électrospray (ESI-MS) a été ensuite développée pour la première fois pour une caractérisation plus fine des structures des GQDs. Les GQDs étant des feuillets stratifiés et les approches synthétiques utilisées n'étant pas contrôlées, il est probable que l'on obtienne des échantillons polydispersés, ce qui signifie que des GQDs de structures et d'étendue de fonctionnalisation différentes existent dans un même lot. Certains rapports récents ont montré l'optimisation des points quantiques mais en se concentrant uniquement sur leurs propriétés de fluorescence [22, 23]. Dans ces travaux, les variations structurelles, la dispersité et l'étendue de la fonctionnalisation ont été étudiées et ont montré l'intérêt de la CE-ESI-MS pour ces objets nanoparticulaires particuliers, en termes d'information qualitative et quantitative [24].

La bonne compatibilité biologique, la capacité conductrice et le rapport surface/volume élevé ont montré l'intérêt des nanoparticules d'or (AuNPs) pour les études électrocatalytiques [25], ce qui nous a conduit à les utiliser dans la fabrication des aptacapteurs dans ce travail. Parmi les procédures de synthèse des AuNPs, l'électrodépôt via la réduction électrochimique de sels d'Or a été utilisée pour fabriquer directement des surfaces d'électrodes avec ces nanoparticules, conduisant à une plus grande fraction des atomes actifs sur la surface.

Les conjugués d'AuNPs-MPc ont été utilisés pour l'électrocatalyse de divers analytes tels que le nitrite, l'hydrazine et le bisphénol A [26-28], pour n'en citer que quelques-uns. Cependant, les MPcs et les AuNPs sont rarement utilisés en combinaison pour la détection électrochimique de biomarqueurs connus du cancer. Dans ce travail, les nanoconjugués AuNPs-MPc sont utilisés pour la première fois pour la détection électrocatalytique du PSA.

Il n'existait pas de littérature sur la synthèse et l'étude d'aptacapteurs à base de GQDS et MPCs. Pour la première fois, ces travaux présentent la modification des trois lots de GQDs par les

MPcs décrites précédemment en vue d'augmenter leurs performances électrocatalytiques . Les points quantiques de nitrure de carbone graphitique (gCNQDs) sont particulièrement intéressants car ils possèdent un cadre principalement π -conjugué de couches C-N qui sont liées de manière covalente [29].

1.3 Les Aptamères

Les aptamères sont de courtes séquences oligonucléotidiques d'acides desoxyribonucléiques (ADNs) ou d'acides ribonucléiques (ARN) monocaténares [30, 31]. Ils sont hautement sélectifs et spécifiques à un analyte cible auquel ils se lient. Les aptamères sont capables de discriminer entre des molécules très similaires, telles que des isomères conformationnels, des molécules ciblées possédant différents groupes fonctionnels ainsi que la mutation d'acides aminés, ce qui en fait des molécules encore plus intéressantes à explorer [31]. L'affinité des aptamères pour leur cible semble accrue lorsqu'ils sont conjugués à des nanoplateformes [32-37]. La sélection de la séquence de l'aptamère spécifique a été effectuée à partir d'une étude bibliographique. Nous avons ainsi sélectionné un aptamère fonctionnalisé par une amine en fin de chaîne qui a ensuite été synthétisé par Integrated DNA Technologies (IDT) et purifié par chromatographie liquide à haute performance. Sa séquence est la suivante : ADN simple brin (ssDNA) : 5'-NH₂-(CH₂)₆-TTT TTA ATT AAA GCT CGC CAT CAA ATA GCT TT-3' (235 nmol, pureté >90%). La fonction amine a été incluse afin de conjuguer de manière covalente l'aptamère aux groupements COOH de la molécule de phtalocyanine ainsi qu'aux GQDs via un couplage amide. Les effets du couplage amide comparés à ceux de la conjugaison par adsorption des composites ont été étudiés afin d'identifier la méthode qui permettra d'obtenir le meilleur fonctionnement des aptacapteurs. La figure 3 montre la conjugaison de gCNQDs avec l'aptamère par couplage amide, comme exemple pour illustrer la construction de ces conjugués.

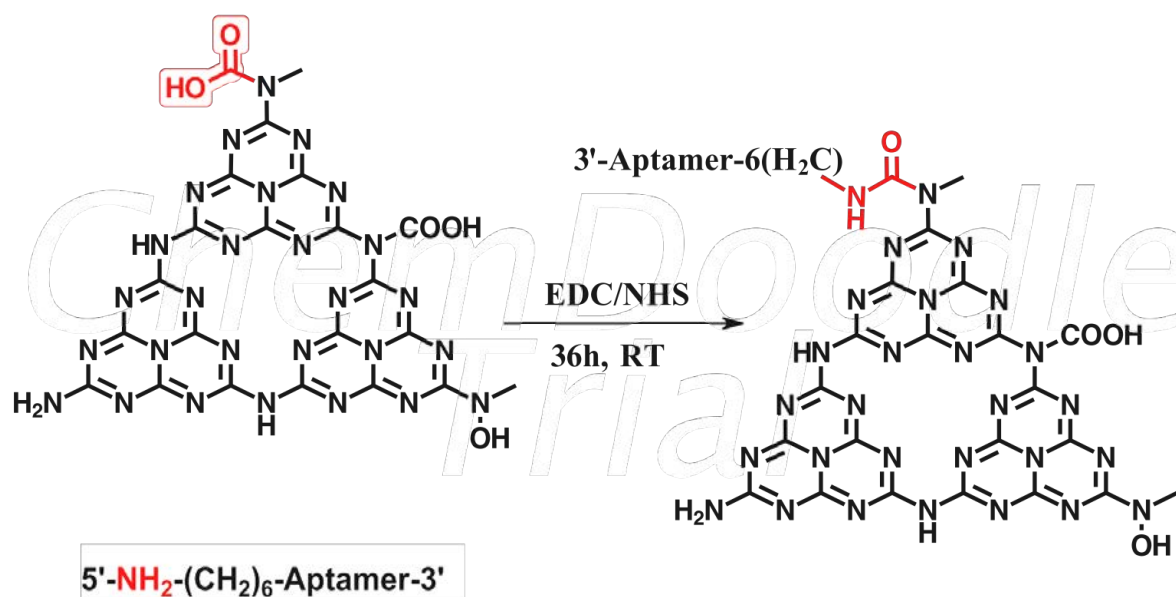


Figure 3: Procédure de couplage via une fonction amide des gCNQDs et de l'aptamère à terminaison amine (EDC = 1-éthyl-3-(3-diméthylaminopropyl)-carbodiimide, NHS = N-hydroxysuccinimide).

1.4 Analyte d'intérêt

Le principal analyte d'intérêt dans le travail rapporté ici est l'antigène spécifique de la prostate (PSA), qui est un biomarqueur directement lié au cancer de la prostate. Le PSA est également connu sous le nom de kallikréine III (KLK-3), une glycoprotéine de 34 kDa composée de 261 acides aminés, avec un pI théorique de 7,26, produite presque exclusivement par la prostate [38] (Figure 4).

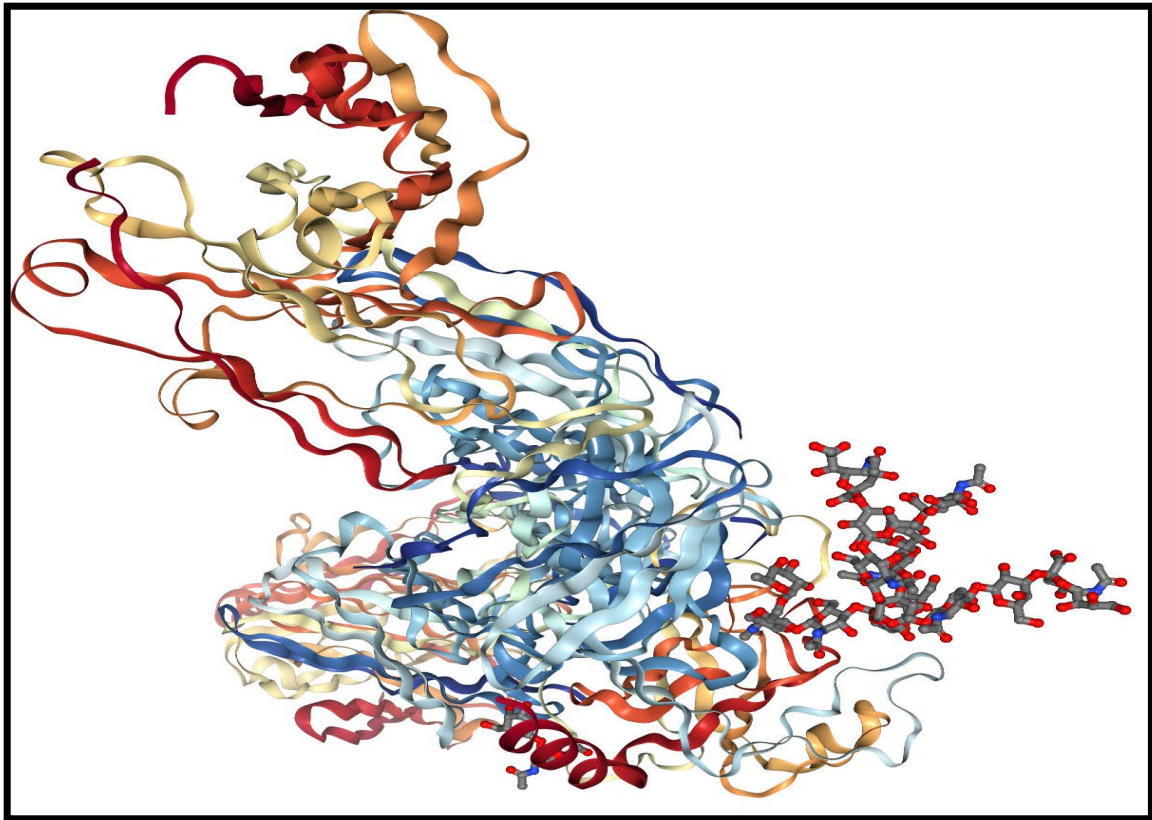


Figure 4: Structure du PSA lié à un élément de reconnaissance [38].

La concentration de PSA est élevée dans le sérum sanguin des patients atteints de cancer de la prostate, résultant de la perte des cellules basales, de la membrane basale et de l'architecture de la lumière, permettant ainsi au PSA d'avoir un accès direct à la circulation périphérique [39]. Cette valeur élevée permet le suivi du PSA dans le sérum sanguin. La figure 5 illustre comment le PSA se lie à l'aptamère. En bref, l'aptamère immobilisé subit un changement de conformation lors de la liaison du PSA, de sorte que l'ADN double brin se forme et se lie simultanément au PSA et le recouvre [32].

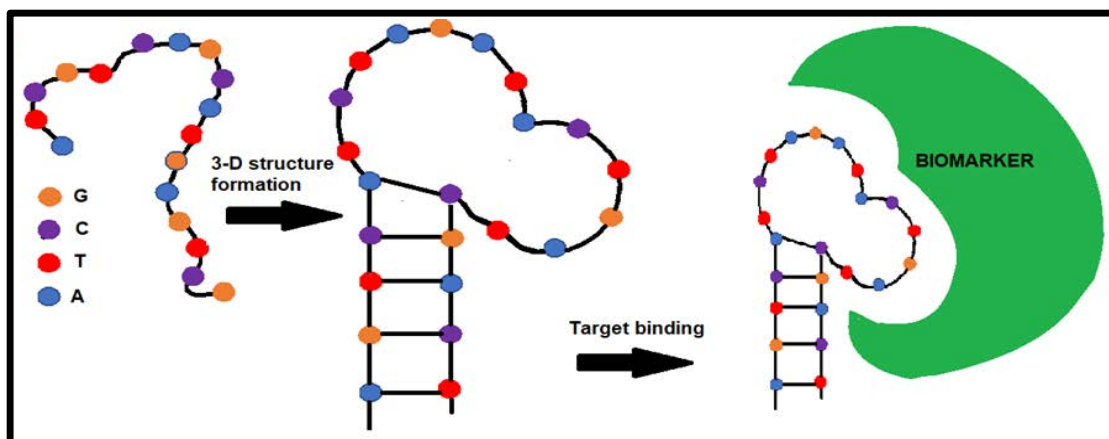


Figure 5: Représentation schématique de l'interaction entre un aptamère et sa cible.

[32].

En ce qui concerne le développement des nanocomposites électroactifs et pour prouver que leurs effets synergiques entraînent une augmentation du courant de sortie, la L-cystéine a été utilisée comme analyte test. De plus, cet analyte sera utilisé plus tard pour prouver la sélectivité de notre aptacapteur pour la détection électrocatalytique du PSA.

1.5 Méthodes de modification de la surface des électrodes

Les méthodes de modification des électrodes utilisées dans ces travaux sont l'adsorption, l'électrodépôt, l'auto-assemblage, le greffage électrochimique et la chimie click. L'adsorption physique implique l'interaction entre la surface et la molécule sans modification structurale. Dans ce travail, la méthode du goutte-à-goutte a été employée en dissolvant les différents modificateurs dans un solvant approprié et en appliquant une goutte d'un certain volume sur la surface de l'électrode. L'utilisation de l'électrodépôt et de l'auto-assemblage comme méthodes de modification des électrodes présentent des avantages tels qu'un faible coût, un taux de croissance élevé à température ambiante, une bonne reproductibilité, et un contrôle plus facile de la taille et de la forme. L'électrodépôt a été utilisé pour synthétiser et immobiliser les AuNPs à la surface de l'électrode de carbone vitreux (GCE). Ensuite, l'électrode a été immergée dans une solution d'aptamère pour induire l'auto-assemblage, car l'atome

d'azote de la fonction amine de l'aptamère est connu pour avoir une affinité avec Au comme montré Figure 6. [40].

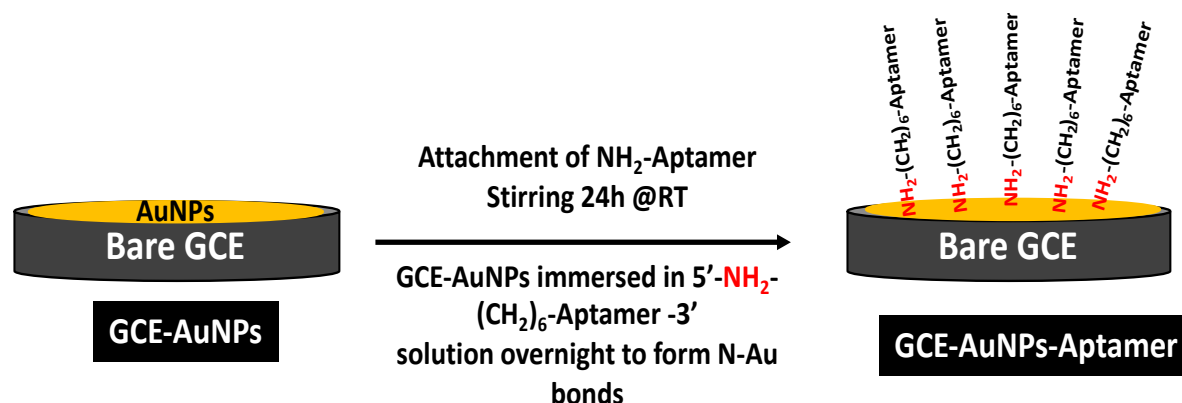


Figure 6 : Auto-assemblage d'un aptamère à fonction amine sur une surface d'or.

Le greffage électrochimique implique l'immobilisation de molécules à la surface de l'électrode via une liaison covalente. Dans le cas présent, l'électrogreffage d'un sel de 4-azidobenzène diazonium a été utilisé pour obtenir des groupes azides terminaux sur une électrode en carbone vitreux afin que ces groupes réagissent avec les groupes alcynes terminaux du complexe 2 (figure 7). La figure 8 illustre la réaction "click" qui se produit à la surface de l'électrode avec des groupes azides terminaux. Bien que le nombre de groupes phénylazide sur la surface de l'électrode soit inconnu, la fixation des molécules par liaison covalente augmente la stabilité du capteur, ce qui favorise la reproductibilité de l'électrocatalyseur. La réaction de chimie « click » catalysée par le Cu(I) et développée par Sharpless [41] est une méthode utile et pratique car elle peut être réalisée à température ambiante et ne nécessite pas de conditions inertes, tout en formant des liaisons covalentes fortes avec d'autres molécules.

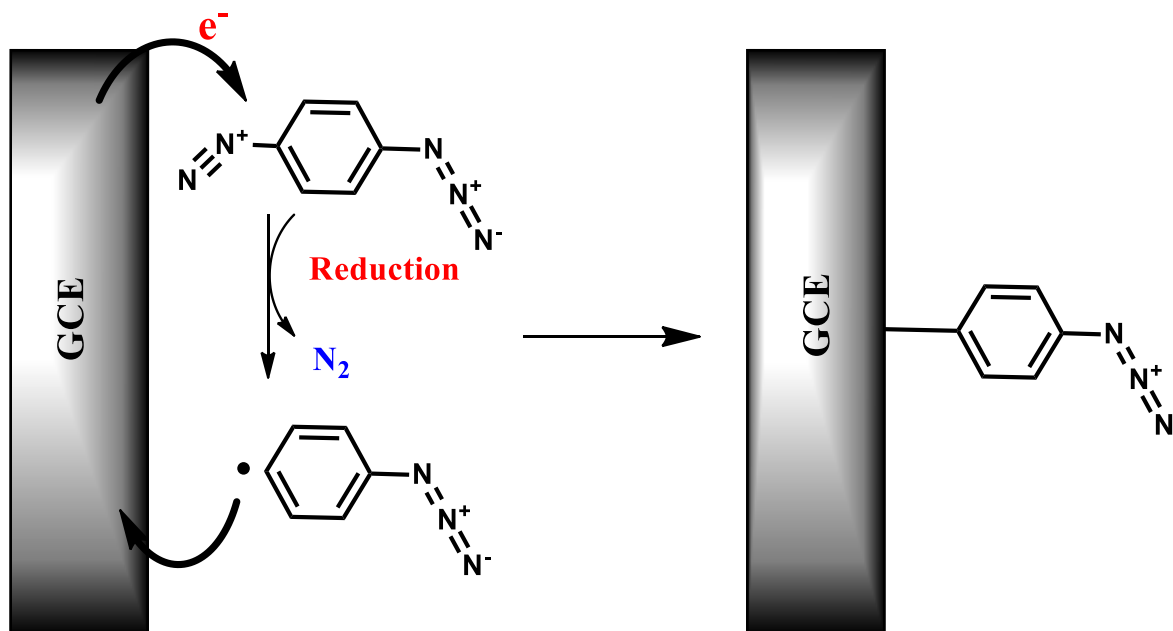


Figure 7: Approche de la fixation de groupes phényl azide sur une électrode de carbone vitreux par réduction électrochimique.

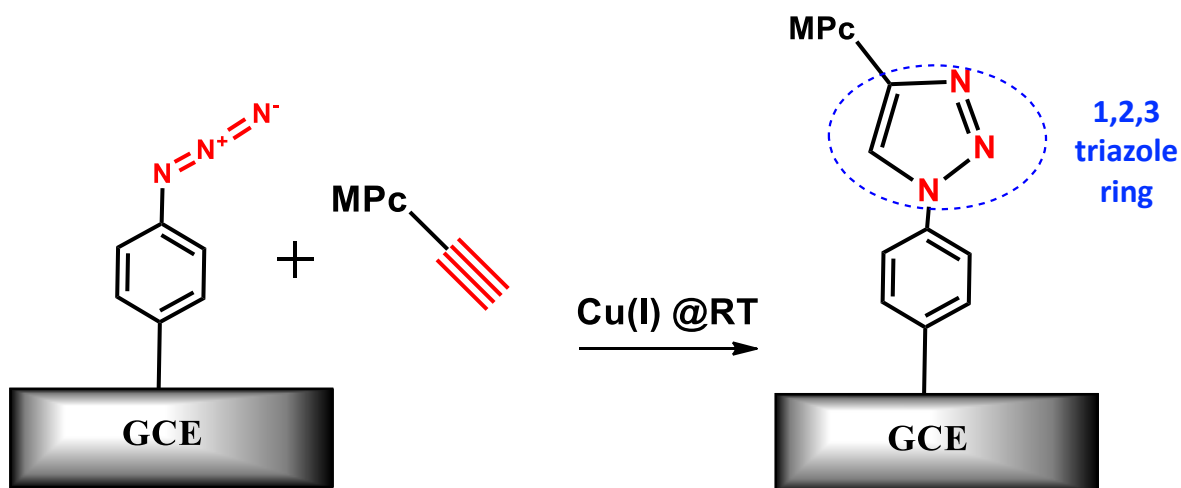


Figure 8: Réaction de chimie « click » entre les groupes alcynes terminaux d'un MPc et les groupes azoture de phényle immobilisés sur une électrode de carbone vitreux.

1.6 Résumé des objectifs de cette thèse

Les objectifs généraux de la recherche menée peuvent alors être résumés comme suit :

La L-cystéine est d'abord utilisée comme analyte test pour valider l'efficacité de l'utilisation des GQDs, NGQDs et gCNQDs en combinaison avec le complexe 1, comme amplificateurs de signaux et plateformes stables avant de les utiliser pour fabriquer des aptacapteurs. Lorsque l'aptamère est incorporé, différentes combinaisons de GQDs, MPc et aptamère sont immobilisées sur la surface de l'électrode par adsorption et testées en présence de PSA pour la détermination des limites de détection. L'électrode la plus performante a ensuite été utilisée pour réaliser une étude comparative des GQDs synthétisés, où les NGQDs et les gCNQDs remplacent les GQDs, puis leur réponse électrocatalytique a été étudiée et comparée. Une étude comparative de l'influence des GQDs sur les capacités d' « aptasensing » est menée en termes de structure et de composition, et l'influence des complexes (1) et (2) sur les performances d'un aptacapteur en termes de substituants est étudiée. Enfin, les effets synergiques sur les performances de l'aptacapteur du conjugué AuNPs-MPc via le greffage électrochimique et la chimie click sont étudiés et déterminés. Dans chaque cas où l'aptamère est inclus, le capteur le plus performant (sauf indication contraire) est testé dans des échantillons de sérum dopés afin de vérifier sa faisabilité.

2. Chapitre 2 : Matériaux, équipements et expérimentations

Tous les réactifs et équipements utilisés lors de ces travaux de thèse sont décrits dans ce chapitre. Les solutions préparées pour les études analytiques et les méthodes de synthèse opérées sont également présentées. Un bref aperçu des méthodes de synthèse employées est résumé ci-dessous ainsi que les modificateurs de surface des électrodes qui n'ont pas été préparés par des méthodes électrochimiques.

2.1 Synthèse

2.1.1 Complexe (1), Schéma 1

Les synthèses du 2,6-di-tert-butyl-4-méthylphénoxy phthalonitrile (i) [42] et du 4-(4-carboxyphénoxy) phthalonitrile (ii) [43] ont été effectuées selon les protocoles de la littérature. Le complexe 1 n'a pas été caractérisé par RMN car le cobalt est paramagnétique.

Rendement : 35 % (p/p) ; UV-vis (CHCl₃) : $\lambda_{\text{max}}/\text{nm}$ (log ϵ) : 600(3.27), 665(3.05). IR [(KBr) $v_{\text{max}}/\text{cm}^{-1}$] : 1600 (-C-C-), 1470 (-C-H-), 1360 (-C-N-), 1225 (-C-O-C-), 1170 (-C-O). (Calculé pour C₈₄H₈₆N₈O₆Co ; (C 74.04 H 6.36 N 8.22) %, Trouvé C 74.52 H 7.26 N 8.54) % ; MS (MALDI-TOF) (m/z) : calculé pour C₈₄H₈₆N₈O₆ ; 1361.60 ; trouvé : [M]. 1361.34.

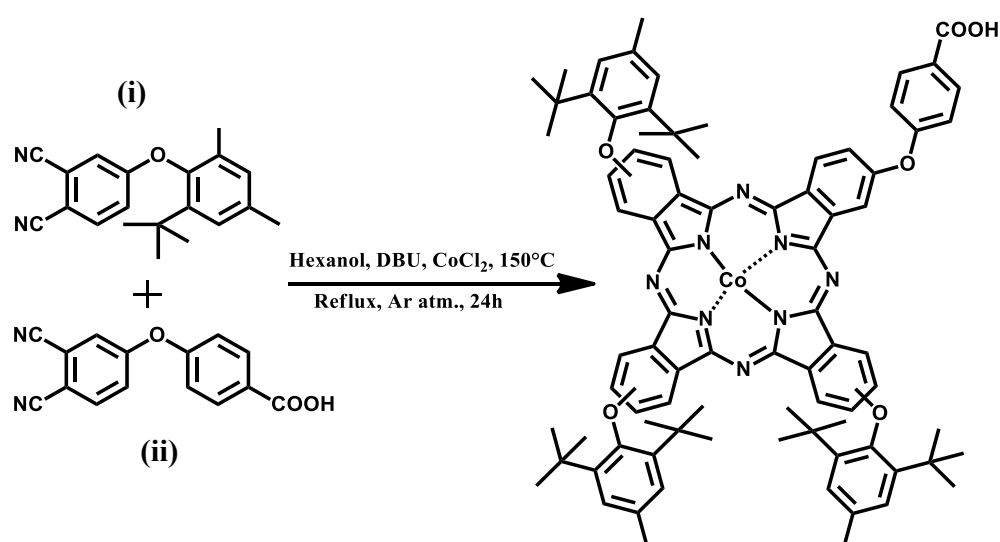


Schéma 1 : Synthèse du complexe 1.

2.1.2 Complexe (2), schéma 2

Les phthalonitriles 4-(hex-5-yn-oxy) phthalonitrile (iii) [44] et N-(4-(3,4-dicyanophenoxy)phenyl)acetamide (iv) [45] ont également été synthétisés comme indiqué dans la littérature (idem i and ii). Ce complexe n'a pas été caractérisé par NMR pour la même raison que le complexe 1. Rendement : 0,0394 g, 12,3 % (p/p) ; UV/vis (DMF) : $\lambda_{\text{max}}/\text{nm}$ (log ϵ) : 667 (4,86), 608 (4,31), 327 (4,71). IR [(KBr), $v_{\text{max}}/\text{cm}^{-1}$] : 746, 795 (C-Hstr aromatique), 1087 (C-O-C), 1258 (C-N), 1464 (C=C), 1501 (C-H), 1537 (N-H), 1662 (C=O), 2849, 2916 (C-H aliphatique), 3273 (C \equiv C-H). Calcul analytique pour C₆₂H₄₅CoN₁₁O_{7.5}H₂O : C, 61.80 ; H, 4.57 ; N, 11.46. Trouvé : C 61.70, H, 3.60 ; N, 10.90. MS (MALDI-TOF) (m/z) : calc. : 1114,28 amu ; trouvé : 1114,34 amu [M]⁺.

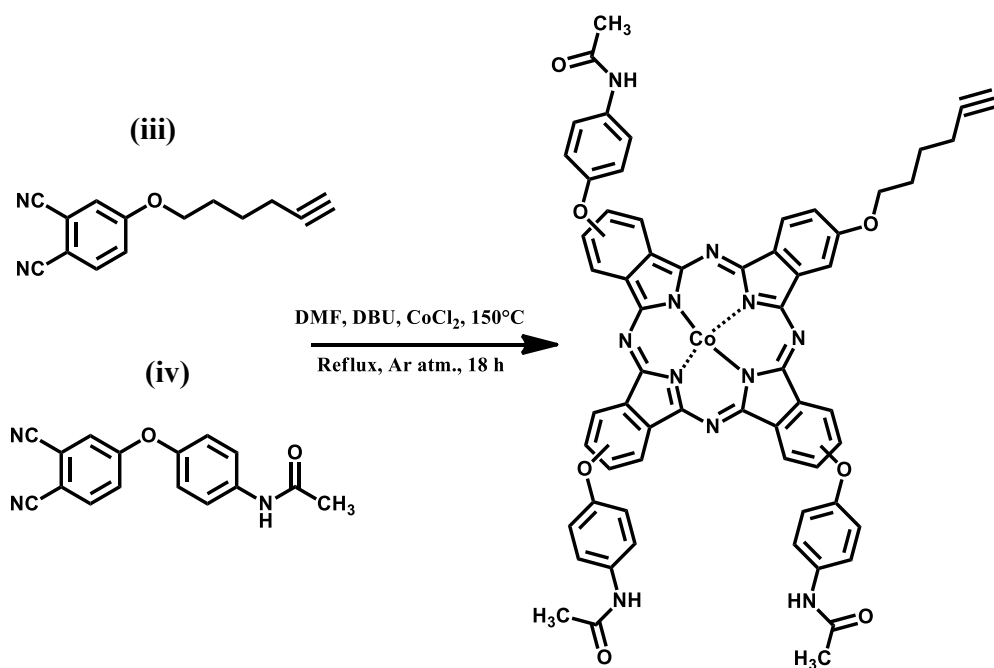


Schéma 2 : Synthèse du complexe 2.

2.1.3 Quantum dots de graphène

La synthèse des gCNQDs, GQDs et NGQDs a été effectuée selon le protocole de la littérature [46] [47].

2.2 Conjugaison des nanocomposites

Ce paragraphe présente la synthèse de différents nanocomposites à base de GQDS sur lesquels sont greffés les complexes 1 ou 2 des phthalocyanines et/ou l'aptamer anti-PSA. Les conjugués utilisés dans ce travail sont listés dans le tableau 1.

Tableau 1 : Conjugués utilisés dans ce travail (à l'exception de ceux directement conjugués à la surface de l'électrode).

Modification	Mode de conjugaison
GQDs-CoPc(1)($\pi\pi$)	Interactions $\pi\pi$
NGQDs-CoPc(1)($\pi\pi$)	Interactions $\pi\pi$
gCNQDs-CoPc(1)($\pi\pi$)	Interactions $\pi\pi$
CoPc(1)@Aptamer	Liaison covalente
GQDs@Aptamer	Liaison covalente
gCNQDs@Aptamer	Liaison covalente
gCNQDs@Aptamer-CoPc(1) ($\pi\pi$)	Liaison covalente et interactions $\pi\pi$ interactions
gCNQDs@Aptamer-CoPc(2) ($\pi\pi$)	Liaison covalente et interactions $\pi\pi$ interactions

2.3 Modification des électrodes

Un système à trois électrodes, comprenant une électrode de référence de Ag|AgCl (3M KCl), une contre-électrode en fil de platine (Pt) et une électrode en carbone vitreux (GCE) comme électrode de travail, a été utilisé. Avant modification, la surface de l'électrode de travail a été nettoyée au moyen d'un polissage sur un papier d'émeri dans une solution pâteuse de nanopoudre d'alumine et rincée plusieurs fois avec de l'eau Millipore. En outre, toutes les

solutions analytiques ont été purgées avec du gaz argon pendant 20 min pour éliminer l'oxygène dissous avant chaque analyse de voltampérométrie cyclique, et l'atmosphère d'argon a été maintenue pendant toute la période d'analyse afin de s'assurer qu'aucune perturbation due à l'oxygène ne se produise pendant les analyses.

3. Chapitre 3 : Caractérisation des différents éléments de l'aptacapteur

Ce chapitre décrit la caractérisation des nanomatériaux utilisés, des MPC synthétisés et des conjugués décrits dans le tableau 1. Tous les protocoles sont illustrés par des schémas dans le texte principal.

3.1 Caractérisation des GQDs synthétisés à l'aide de différentes méthodes analytiques

Les GQDs ont été synthétisés à différents temps de synthèse afin d'étudier les effets de la durée de synthèse sur leur structure, leur degré de fonctionnalisation et leur dispersité. Après avoir analysé les données obtenues à partir de la caractérisation de tous les lots, les échantillons utilisés pour les études ultérieures tout au long de cette thèse ont été ceux obtenus au bout de 8 h (GQDs), 6 h (NGQDs) et 6 h (gCNQDs) de synthèse.

Une caractérisation précise des GQDS obtenus à partir de différents temps de synthèse, a été effectuée afin de déterminer la qualité des différents lots de synthèse. Pour cela, différentes méthodes ont été employées : la zétamétrie pour la dispersité, la densité de charge et la stabilité colloïdale, le TEM, la diffusion dynamique de la lumière (DLS) et la composition élémentaire pour la dispersité et la distribution de taille, et la FTIR, l'analyse par rayons X à dispersion d'énergie (EDX), la spectroscopie Raman et la spectroscopie photoélectronique à rayons X (XPS) pour la structure.

Ces caractérisations ont alors permis de sélectionner l'échantillon le mieux adapté à la caractérisation par électrophorèse capillaire. Les échantillons mentionnés ci-dessous ont été choisis pour une caractérisation plus poussée pour la raison suivante :

* Le lot de GQDs obtenus au bout de 8h de synthèse présente la plus faible valeur d'indice de polydispersité (PDI) par mesure de la diffusion dynamique de la lumière (DLS), et les images TEM ont montré une meilleure dispersion par rapport aux autres lots. Une valeur de potentiel zêta élevée a été mesurée, indicateur d'une meilleure stabilité colloïdale, comparativement aux lots de GQDs avec des temps de synthèse différents.

* Le lot de NGQDs obtenus au bout de 6h de synthèse a également montré des valeurs de PDI et de taille hydrodynamique les plus faibles en DLS, par rapport aux lots obtenus à d'autres temps de réaction. Par mesure de spectroscopie photoélectronique à rayons X (XPS), ce lot présente la concentration la plus élevée en % d'oxygène à 6 h de synthèse, ce qui suggère la présence de plus de groupes COOH disponibles sur les GQDs, favorable à la création ultérieure d'une liaison amide lors de la modification ultérieure des QDs.

* Bien que les gCNQDs présentent une valeur de PDI et une faible taille mesurées en DLS pour un temps de synthèse de 2 h, le lot synthétisé pendant 6 h a été choisi pour des études ultérieures car il a montré la valeur la plus élevée dans les mesures de potentiel zêta, ce qui est un indicateur d'une meilleure stabilité en solution par rapport au lot synthétisé pendant seulement 2 h.

L'électrophorèse capillaire (EC) est une méthode électrocinétique utilisée pour séparer et caractériser les nanostructures, permettant leur discrimination en termes de taille, de densité de charge de surface et de fonctionnalisation ainsi que la compréhension de leur comportement dans différents environnements pour permettre de nouvelles applications [48-50]. La détection a été réalisée par UV-Vis à une longueur d'onde de 200 nm. Comme prévu, tous les GQDs ont montré des mobilités négatives ($-7.5 \times 10^{-4} \text{ cm}^2 \cdot \text{V}^{-1} \cdot \text{s}^{-1}$) qui étaient en accord avec les résultats obtenus par les mesures de potentiel zêta, et les fonctions acides carboxyliques accessibles sur les structures. A titre d'exemple, l'électrophérogramme des GQDs synthétisés à 8 h est présenté dans la Figure 9.

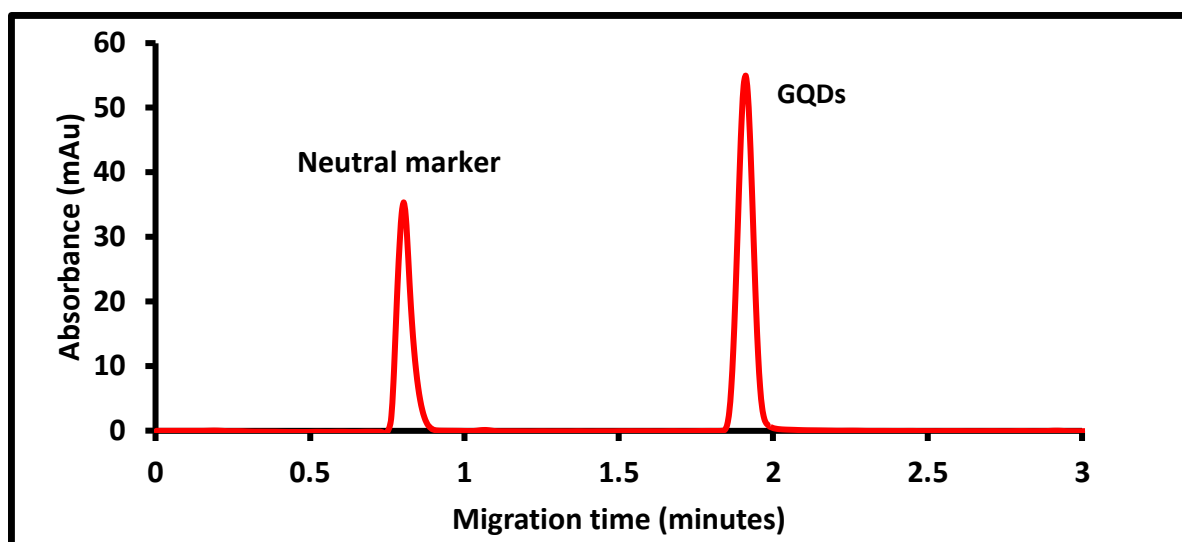


Figure 9: Séparation électrocinétique des GQDs après optimisation de synthèse. Conditions expérimentales : échantillon à $1 \text{ mg}\cdot\text{mL}^{-1}$ dans le tampon carbonate d'ammonium (10 mM, pH 7.4) ; injection hydrodynamique du marqueur neutre (paracétamol) par l'entrée (5s, 50 mbar) et des QDs par la sortie (5s, 50 mbar) ; séparation électrocinétique : 18 kV ; détection UV à 200 nm ; Longueur totale du capillaire = 35 cm ; longueur effective jusqu'au détecteur, depuis l'entrée du capillaire = 26.5 cm.

Après avoir analysé les échantillons en CE-UV, les échantillons ont été préparés pour être séparés et caractérisés par CE-ESI-MS. L'effet du pH était l'un des paramètres étudiés car il joue un rôle dans la charge de surface des nanostructures en solution et donc sur les valeurs de mobilités électrophorétique. La gamme de pH étudiée a été 7-10 afin d'étudier la déprotonation des groupes carboxyliques à la surface des QDs.

3.2. Caractérisation des MPcs, du complexe (1) et du complexe (2)

Les complexes MPcs synthétisés ont été caractérisés à l'aide de diverses méthodes analytiques telles que les spectroscopies UV/vis et FTIR, le MALDI-TOF ainsi que l'analyse élémentaire, ce qui a donné une indication du succès de la réaction de synthèse. Les masses mesurées pour les complexes 1 et 2 sont de 1361.34 pour [M] et 1114.34 pour [M]⁺ respectivement, vérifiant le succès des synthèses.

3.3 Caractérisation des conjugués

Les GQDs ont d'abord été modifiés par l'un des composants, aptamère ou phtalocyanine, par liaison covalente ou interactions $\pi\pi$, (GQDs-CoPc (**1**) ($\pi\pi$) and GQDs@Aptamer) puis la fonctionnalisation des GQDs par les MPcs et l'aptamère a permis de synthétiser des systèmes à trois composants (GQDs-CoPc (**1**) ($\pi\pi$)-aptamer). Les différentes combinaisons sont présentées dans le tableau 1.

Les conjugués formés ont été entièrement caractérisés à l'aide de méthodes telles que la spectroscopie UV/vis, la DLS et la zétamétrie. Ces résultats ont montré que la combinaison de ces composites entraînait une modification des diamètres hydrodynamiques (par DLS) et du potentiel zeta (mesures zétamétriques), par exemple, induisant des changements de stabilité des nano-objets fonctionnalisés. En ce qui concerne les conjugués covalents (CoPc(1)@Aptamer, GQDs@Aptamer and gCNQDs@Aptamer), la spectroscopie photoélectronique à rayons X (XPS) et la spectroscopie infrarouge à transformée de Fourier (FTIR) ont été utilisées pour prouver avec succès la formation des liaisons covalentes.

4. Chapitre 4 : Modification et caractérisation des électrodes

Les méthodes de modification des électrodes utilisées dans ce travail sont l'adsorption, l'électrodépôt, le greffage électrochimique et la chimie « click ». Elles sont décrites à nouveau dans ce chapitre ainsi que les méthodes de caractérisation des surfaces des électrodes. Il est important de caractériser toutes les surfaces modifiées afin de connaître les changements qui se produisent à la surface de l'électrode et de vérifier chaque étape de modification effectuée. Des techniques telles que la voltampérométrie cyclique, la microscopie électrochimique à balayage (SECM) et la XPS ont été utilisées pour caractériser avec succès les surfaces modifiées avant de les utiliser pour la détection du PSA.

4.1 Modification de l'électrode par adsorption

Le tableau 2 de ce résumé présente la liste des surfaces d'électrodes caractérisées ainsi que les différences de potentiel (ΔE) et les recouvrements de surface (Γ). L'équation 1 de Randles-Sevcik peut être appliquée au couple redox $[\text{Fe}(\text{CN})_6]^{3-/4}$ pour déterminer la surface effective de l'électrode.

$$I_p = 2.69 \times 10^5 n^{3/2} A C D^{1/2} v^{1/2} \quad (1)$$

où I_p , A , C , D , n et v sont respectivement le courant de pic, la surface effective, la concentration de $[\text{Fe}(\text{CN})_6]^{3-/4}$, le coefficient de diffusion de $[\text{Fe}(\text{CN})_6]^{3-/4}$, le nombre d'électrons impliqués et la vitesse de balayage. La valeur de la littérature a été utilisée pour le $[\text{Fe}(\text{CN})_6]^{3-/4}$ ($D = 7,6 \times 10^{-6} \text{ cm}^2\text{s}^{-1}$) [51]. En utilisant la surface effective des électrodes modifiées déterminée à l'aide de l'équation (1) et la charge totale déterminée en intégrant la surface du pic anodique dans une solution tampon, puis en employant l'équation (2), les recouvrements de surface ont été calculés.

$$\Gamma = \frac{Q}{nFA} \quad (2)$$

où n est le nombre d'électrons transférés (~ 1), F la constante de Faraday ($96,485 \text{ C mol}^{-1}$), A la surface effective obtenue à partir de l'équation (1) et Γ le recouvrement de surface (tableau 2). Leur valeur est généralement plus élevée que celle rapportée pour les phtalocyanines reposant à plat sur la surface de l'électrode ($1 \times 10^{-10} \text{ mol cm}^{-2}$) [52]. Les valeurs plus élevées indiquent une augmentation de la surface de l'électrode, qui offre plus de surface électrocatalytique. Ces résultats fournissent des informations sur les performances attendues de chaque surface d'électrode modifiée et sur la manière dont l'une pourrait être plus performante que l'autre lorsqu'elle est comparée.

Tableau 2: Liste des différentes structures synthétisées par la fabrication d'électrodes

Conjugates	ΔE (mV)	Γ ($\times 10^{-10}$ mol.cm ⁻²)
Bare GCE	77	-
GQDs-CoPc (1) ($\pi\pi$)	161	0.09
• GQDs	321	1.59
• CoPc(1)	158	0.33
• GQDs-CoPc(1) (sequential)	107	6.50
NGQDs-CoPc (1) ($\pi\pi$)	100.1	15.5
• NGQDs	466	3.1
• NGQDs-CoPc(1) (sequential)	615	8.2
gCNQDs-CoPc (1) ($\pi\pi$)	100	30.2
• gCNQDs	90.4	39.3
• gCNQDs-CoPc(1) (sequential)	174	12.0
GQDs-CoPc (1) ($\pi\pi$)-aptamer	361.5	2.99
NGQDs-CoPc (1) ($\pi\pi$)-aptamer	139.1	28.1
gCNQDs-CoPc (1) ($\pi\pi$)-aptamer	202.6	39.6
CoPc(1)@Aptamer	166	0.96
• CoPc(1)-Aptamer (sequential)	300	3.00
• CoPc(1)-Aptamer (premixed)	262	0.55
GQDs@Aptamer	617	1.99
• aptamer	178	0.11
• GQDs-Aptamer (sequential)	68	1.57
• GQDs-Aptamer (premixed)	262	0.009
gCNQDs@Aptamer	292	-
gCNQDs@Aptamer-CoPc(1) ($\pi\pi$)	288	0.151
gCNQDs@Aptamer-CoPc(2) ($\pi\pi$)	356	0.215
• CoPc(2)	169	0.066

4.2 Préparation et caractérisation d'électrodes à base de nanoparticules d'or fonctionnalisées par le complexe CoPc(2) et un aptamère

Le complexe **2** et les nanoparticules d'or (AuNPs) ont également été utilisés comme nanoplateformes pour l'immobilisation d'un aptamère afin de préparer de nouveaux aptacapteurs et d'étudier leurs effets synergiques sur les performances de l'aptacapteur fabriqué. La littérature a montré l'utilisation de nanoconjugés contenant des NPs d'or comme plateformes pour l'immobilisation de l'aptamère liant le PSA en vue de sa détection [53- 56] mais la combinaison des AuNPs électrodéposés et des phtalocyanines avec l'aptamère n'a pas été étudiée, introduisant ainsi un autre aspect nouveau dans cette thèse. De plus, le greffage électrochimique et la chimie « click » ont été utilisés, car ce sont des méthodes de conjugaison covalente, augmentant la stabilité des capteurs. Les surfaces ont été caractérisées par voltamétrie cyclique, spectroscopie à rayons X à dispersion d'énergie (EDX), microscopie électronique à balayage (MEB) et SECM. De plus, le XPS a été utilisé pour prouver le succès de la réaction de chimie « click ». Les surfaces des électrodes ont été recouvertes avec succès d'AuNP et de complexe **2** par greffages successifs sur GCE, suivi de l'adsorption de l'aptamère de liaison au PSA.

5. Chapitre 5 : Détection électrocatalytique

Ces aptacapteurs fabriqués ont été entièrement caractérisés et ensuite utilisés pour la détection électrochimique de la L-cystéine et du PSA. La détection électrochimique de la L-cystéine a été réalisée pour prouver les capacités d'amélioration du signal des conjugués QDs-MPc par rapport au nanocomposites seuls. La structure que nous avons synthétisée (QDs, MPc et aptamères) n'avait pas encore été étudiée dans la littérature pour cette détection. De plus, la combinaison d'AuNPs et de MPcs utilisant l'électrogreffage et la chimie click est utilisée ici pour la première fois en utilisant le complexe **2** pour la détection du PSA. Les techniques électrochimiques utilisées dans ce chapitre pour déterminer les performances des capteurs fabriqués sont la voltampérométrie différentielle (DPV) et la spectroscopie d'impédance électrochimique (EIS).

Les électrodes modifiées avec des GQDs et des MPcs ont d'abord été utilisées pour catalyser la L-cystéine afin de vérifier leurs effets synergiques pour une utilisation ultérieure en tant qu'amplificateurs de signal et immobilisation d'aptamères pour l'aptascapteur. La combinaison de ces nanocomposites a amélioré la réponse du signal et s'est avérée très prometteuse pour être appliquée en tant qu'amplificateurs de signal pour la fabrication d'aptacapteurs de PSA. Ensuite, le GQDs-CoPc (1) ($\pi\pi$) conjugué a été utilisé à titre d'exemple, conjointement avec l'aptamère pour la détection de PSA dans des solutions tampons. Cette combinaison a été choisie comme la meilleure après que les limites de détection aient été déterminées à l'aide d'aptacapteurs fabriqués avec différentes combinaisons de GQD, MPc et aptamère. Les résultats ont montré que l'électrode modifiée séquentiellement, GCE-GQDs-CoPc(1)-Aptamère, a présenté les meilleures performances. Cette séquence de modification a donc été utilisée pour une étude plus approfondie sur les effets de la structure et de la composition des QDs. L'étude comparative a montré que toutes les électrodes produisaient de faibles limites de détection avec une bonne stabilité, reproductibilité et répétabilité ainsi qu'une sélectivité pour le PSA dans des échantillons complexes. Cependant, l'aptcapteur basé sur les NGQDs a donné les meilleurs résultats en terme de limite de détection, en particulier. Les complexes CoPcs ont également été comparés et il a été constaté que la nature du substituant influençait les performances de l'aptacapteur pour la détection du PSA. Le complexe **2** a montré des performances supérieures à celles du complexe 1 dans cette étude particulière, en raison de l'effet de résonance des substituants dominants du paracétamol qu'il possède, ainsi que de la présence des atomes d'azote à la périphérie du complexe. En plus de la détermination des limites de détection, la reproductibilité, la stabilité et la sélectivité ont été déterminées et les résultats obtenus étaient acceptables et conformes aux résultats rapportés pour d'autres aptacapteurs fabriqués.

Lorsque les AuNPs ont été combinés avec CoPc(**2**) pour la détection de PSA, il a été montré que l'incorporation d'un complexe CoPc au capteur améliorerait ses performances par opposition à l'utilisation du CoPc ou des AuNPs seuls. De plus, l'utilisation d'une immobilisation covalente par électrogreffage et chimie click des nanocomposites a augmenté la stabilité de l'aptacapteur. Les aptacapteurs contenant des AuNPs ont également montré une bonne stabilité, reproductibilité et répétabilité. Des études de vitesse de balayage ont indiqué des processus contrôlés par adsorption se produisant entre l'électrode

et l'analyte. Les résultats obtenus ici seront présentés dans la section suivante à côté des résultats obtenus pour les mêmes capteurs fabriqués dans des échantillons réels.

6. Chapitre 6 : Analyse d'échantillons réels

Les aptacapteurs fabriqués ont été testés dans des échantillons de sérum humain dopés pour valider la fiabilité et la faisabilité. Les échantillons de sérum ont été dilués 100 fois dans le PBS (pH 7,4) pour réduire les effets de matrice de l'échantillon réel. Ensuite, différentes concentrations de PSA ont été ajoutées aux solutions de sérum diluées. Les méthodes analytiques ainsi que les concentrations utilisées dans cette étude étaient les mêmes que les méthodes utilisées pour la détection du PSA dans le PBS. Les tests d'échantillons réels ont été effectués à l'aide de la voltampérométrie différentielle à impulsions (DPV) et la spectroscopie d'impédance électrochimique (EIS) à des fins de comparaison des deux techniques, sauf indication contraire. **Le tableau 3** résume les limites de détection obtenues dans les échantillons de solution tampon et de sérum. Comme on peut le voir, les résultats obtenus dans les échantillons de sérum sont en accord avec ceux obtenus dans le tampon. Les limites de détection sont également inférieures au niveau de coupure de PSA qui est rapporté comme 4 ng/mL. Les taux de récupération des électrodes à base d'aptamères (tableaux dans la thèse principale) ont tous montré de bonnes récupérations à toutes les concentrations étudiées (1,2 à 2,0 pM).

Tableau 3 : Résumé des valeurs de LoD (**ng/mL**) déterminées dans les échantillons de tampon et de sérum enrichi d'aptacapteurs à l'aide de l'EIS, sauf indication contraire.

Électrode	TAMPON LoD	SÉRUM LoD
GCE -GQDs-CoPc (1)($\pi\pi$) - aptamère	0,051	0,099 (DPV) 0,098
GCE -NGQDs-CoPc (1)($\pi\pi$) - aptamère	0,044 (DPV) 0,046	0,043
GCE -gCNQDs-CoPc (1) ($\pi\pi$) - aptamère	0,053 (DPV) 0,055	0,047 (DPV) 0,046
GCE-gCNQDs@ aptamère	0,042	0,054 0
GCE-gCNQDs @ aptamère-CoPc (1) ($\pi\pi$)	0,031	0,032 0
GCE-gCNQDs @ aptamère-CoPc (2) ($\pi\pi$)	0,023	0,027
GCE-AuNPs- aptamère	0,035 0,031 (DPV)	0,037 0,040 (DPV)
GCE Ø CoPc(2)- aptamère	0. 052 0,031 (DPV)	0. 056 0,043 (DPV)
GCE-AuNPs Ø CoPc(2)- aptamère	0,026 0,025 (DPV)	0. 028 0,027 (DPV)

Le tableau 4 montre les taux de récupération déterminés pour les électrodes à base de gCNQDs à titre d'exemple.

Tableau 4: Résumé des mesures de récupération du PSA dans des échantillons de sérum humain dopés pour les aptacapteurs à base de gCNQDs. % RSD. (écart-type relatif) = écart-type/moyenne $\times 100$; n = 3.

[PSA] added/ pM in buffer	R_{ct} (kΩ) in buffer	[PSA] found/ pM In serum	R_{ct} (kΩ) In serum	% RSD	% Recovery
GCE-gCNQDs@Aptamer					
1.2	16.4	1.13	15.4	1.8	93.9
1.4	19.3	1.37	18.9	2.1	97.9
1.6	24.7	1.39	21.5	1.2	87.0
1.8	28.8	1.64	26.2	3.3	90.9
2.0	33.2	1.94	32.3	7.2	97.3
GCE-gCNQDs@AptamerCoPc(1)($\pi\pi$)					
1.2	26.7	1.16	25.8	1.4	96.6
1.4	30.5	1.35	29.5	2.6	96.7
1.6	37.9	1.38	32.8	1.8	86.5
1.8	44.9	1.54	38.4	3.8	85.5
2.0	51.6	1.96	50.5	6.2	97.9
GCE-gCNQDs@Aptamer-CoPc(2)($\pi\pi$)					
1.2	29.2	1.13	27.4	5.4	93.8
1.4	36.2	1.25	32.3	3.1	89.2
1.6	41.6	1.52	39.6	2.8	95.2
1.8	49.2	1.70	46.5	1.2	94.5
2.0	58.9	1.84	54.3	1.7	92.2

7. Chapitre 7 : Résumé, conclusions et perspectives

Ce chapitre résume les résultats obtenus dans les travaux présentés dans les chapitres précédents, les conclusions tirées de ces résultats ainsi que les perspectives. Ces travaux de thèse ont démontré pour la première fois la combinaison de points quantiques à base de graphène, d'or, de MPcs et d'aptamères pour la fabrication d'aptacapteurs électrochimiques, en vue de la détection de PSA. Une caractérisation complète des composites utilisés et des surfaces d'électrodes modifiées a été réalisée. De plus, les effets synergiques des points quantiques à base d'AuNPs et de CoPcs ont été prouvés à l'aide de méthodes électrochimiques. Les aptacapteurs ont été utilisés pour détecter la PSA dans une solution tampon et se sont avérés efficaces, sélectifs et spécifiques, avec des limites de détection faibles qui ont été comparées aux valeurs de la littérature. Les aptacapteurs les plus performants qui ont été fabriqués dans ces travaux ont ensuite été utilisés pour détecter la PSA dans des échantillons de sérum enrichis afin de vérifier leur faisabilité et leur utilisation potentielle dans les études cliniques. Les résultats concordaient avec ceux obtenus dans les analyses dans un tampon, avec parfois de meilleurs résultats dans les analyses de sérum. De plus, les capteurs étaient stables, reproductibles, et se sont avérés réutilisables pour plusieurs expériences avant de devoir les re-fabriquer.

8. Références

Les références utilisées dans cette thèse sont répertoriées dans la section des références, dans l'ordre où elles apparaissent dans la thèse. Les références énumérées ci-dessous sont celles utilisées dans le résumé du travail de thèse.

- [1] D. Ilic, M. Djulbegovic, J. H. Jung, E. C. Hwang, Q. Zhou, A. Cleves, T. Agoritsas, P. Dahm, Prostate cancer screening with prostate-specific antigen (PSA) test: a systematic review and meta-analysis, *British Med. J.* 362 (2018) k3519-k3531.
- [2] K. Matsumoto, N. Konishi, Y. Hiasa, E. Kimura, Y. Takahashi, K. Shinohara, T. Samori, A highly sensitive enzyme-linked immunoassay for serum free prostate specific antigen (f-PSA), *Clin. Chim. Acta* 281 (1999) 57–69.
- [3] H.H. Lee, M.A. Dineva, Y.L. Chua, A. Ritchie, I. Ushiro-Lumb, C.A. Wisniewski, Simple amplification-based assay: A nucleic acid-based point-of-care platform for HIV-1 testing, *J. Infect. Dis.* 201 (2010) S65–S71.
- [4] T. Yang, P. Hou, L.L. Zheng, L. Zhan, P.F. Gao, Y.F. Li, C.Z. Huang, Surface-engineered quantum dots/electrospun nanofibers as a networked fluorescence aptasensing platform toward biomarkers, *Nanoscale* 9 (2017) 17020–17028.
- [5] R.-M.Kong, X. Zhang, L. Ding, D. Yang, F. Qu, Label-free fluorescence turn-on aptasensor for prostate-specific antigen sensing based on aggregation-induced emission–silica nanospheres, *Anal. Bioanal. Chem.* 409 (2017) 5757–5765.
- [6] Y.-B.Choi, N.-H.Kim, S.-H.Kim, G.-S.Tae, H.-H. Kim, Heterogeneous Electrochemical Immunoassay of Hippuric Acid on the Electrodeposited Organic Films, *Sensors* 14 (2014) 18886–18897.
- [7] S.B. Nimse, M.D. Sonawane, K.-S.Song, T. Kim, Biomarker detection technologies and future directions, *Analyst* 141 (2016) 740–755.

- [8] S. Gutkin, O. Green, G. Raviv, D. Shabat, O. Portnoy, Powerful Chemiluminescence Probe for Rapid Detection of Prostate Specific Antigen Proteolytic Activity: Forensic Identification of Human Semen, *Bioconj. Chem.* 31 (2020) 2488–2493.
- [9] G. Ertürk, H. Özen, M.A. Tümer, B. Mattiasson, A. Denizli, Microcontact imprinting based surface plasmon resonance (SPR) biosensor for real-time and ultrasensitive detection of prostate specific antigen (PSA) from clinical samples, *Sens. Actuators B Chem.* 224 (2016) 823–832.
- [10] P. Singh, SPR Biosensors: Historical perspectives and current challenges, *Sens. Actuators B Chem.* 229 (2016) 110–130.
- [11] Y.Z. Grasso, M.K. Gupta, H.S. Levin, C.D. Zippe, E.A. Klein, Combined nested RT-PCR Assay for prostate-specific antigen and prostate-specific membrane antigen in prostate cancer patients: correlation with pathological stage, *Cancer Res.* 58 (1998) 1456–1459.
- [12] L. Xie, X. Yang, Y. He, R. Yuan, Y. Chai, Polyacrylamide gel-contained Zinc finger peptide as the “lock” and zinc ions as the “key” for construction of ultrasensitive prostate-specific antigen SERS immunosensor, *ACS Appl. Mater. Interf.* 10 (2018) 15200–15206.
- [13] Y.C. Cao, R. Jin, C.A. Mirkin, Nanoparticles with Raman spectroscopic fingerprints for DNA and RNA detection, *Science* 297 (2002) 1536–1540.
- [14] M. Souada, B. Piro, S. Reisberg, G. Anquetin, V. Noël, M.C. Pham, Label-free electrochemical detection of prostate-specific antigen based on nucleic acid aptamer, *Biosens. Bioelectron.* 68 (2015) 49–54.
- [15] A. Raouafi, A. Sánchez, N. Raouafi, R. Villalonga, Electrochemical aptamer-based bioplatfrom for ultrasensitive detection of prostate specific antigen, *Sensors Actuators B Chem.* 297 (2019) 126762.
- [16] J. Mack, N. Kobayashi, Low symmetry phthalocyanines and their analogues, *Chem. Rev.* 111 (2011) 281–321.
- [17] M. Bacon, S.J. Bradley, T. Nann, Graphene quantum dots, *Part. Part. Syst. Charact.* 31 (2014) 415–428.

- [18] S. Campuzano, P. Yáñez-Sedeño, J.M. Pingarrón, Carbon dots and graphene quantum dots in electrochemical biosensing, *Nanomat.* 9 (2019) 634-651.
- [19] L. Trapiella-Alfonso, F. d'Orlyé, A. Varenne, Recent advances in the development of capillary electrophoresis methodologies for optimizing, controlling, and characterizing the synthesis, functionalization, and physicochemical, properties of nanoparticles, *Anal. Bioanal. Chem.* 408 (2016) 2669–2675.
- [20] G. Ramirez-García, L. Trapiella-Alfonso, F. d'Orlyé, A. Varenne. Electrophoretic methods for characterizing nanoparticles and evaluating their bio-interactions for their further use as diagnostic, imaging and therapeutic tools. In : *Capillary Electromigration Separation Methods, Handbooks in Separation Science*, Elsevier (2018), 397-421.
- [21] L. Trapiella-Alfonso, G. Ramirez-Garcia, F. d'Orlyé, A. Varenne. Electrokinetic methodologies for the characterization of nanoparticles and the evaluation of their behaviour in biological systems. *Tracs, Trends in Analytical Chemistry* (2016) 84, 121-130. Invited review.
- [22] S. Wang, Z.-G. Chen, I. Cole, Q. Li, Structural evolution of graphene quantum dots during thermal decomposition of citric acid and the corresponding photoluminescence, *Carbon* 82 (2015) 304–313.
- [23] R. Adel, S. Ebrahim, A. Shokry, M. Soliman, M. Khalil, Nanocomposite of CuInS/ZnS and nitrogen-doped graphene quantum dots for cholesterol sensing, *ACS Omega* 6 (2021) 2167–2175.
- [24] M. Mokaddem, P. Gareil, J. Belgaied, A. Varenne, A new insight into suction and dilution effects in capillary electrophoresis coupled to mass spectrometry via an electrospray ionization interface. Part I-Suction effect, *Electrophoresis* 29 (2008) 1957–1964.
- [25] A. Ananthi, K.L. Phani, Self-assembly of gold nanoparticles on sulphide functionalized polydopamine in application to electrocatalytic oxidation of nitric oxide, *J. Electroanal. Chem.* 764 (2016) 7–14.

- [26] A.A. Saeed, B. Singh, M.N. Abbas, Y.M. Issa, E. Dempsey, Electrocatalytic nitrite determination using iron phthalocyanine modified gold nanoparticles. *Electroanalysis* 27 (2015) 1086–1096.
- [27] P. Chauke, E. Antunes, T. Nyokong, Comparative behavior of conjugates of tantalum phthalocyanines with gold nanoparticles or single walled carbon nanotubes towards bisphenol A electrocatalysis, *J. Electroanal. Chem.* 661 (2011) 1–7.
- [28] A.J. Jeevagan, S.A. John, Synthesis of non-peripheral amine substituted nickel(ii) phthalocyanine capped gold nanoparticles and their immobilization on electrode for the electrocatalytic oxidation of hydrazine, *RSC Adv.* 3 (2013) 2256–2264.
- [29] Y. Zhan, Z. Liu, Q. Liu, D. Huang, Y. Wei, Y. Hu, X. Lian, C. Hu, A facile and one-pot synthesis of fluorescent graphitic carbon nitride quantum dots for bio-imaging applications, *New J. Chem.* 41 (2017) 3930–3938.
- [30] M. Hu, K. Zhang. The application of aptamers in cancer research: an up-to-date review. *Future Oncol.* 9 (2013) 369–376.
- [31] J. Zhou, J. Rossi, Aptamers as targeted therapeutics: current potential and challenges. *Nat. Rev Drug Discov.* 16 (2017) 181–202.
- [32] J.K. Herr, J.E. Smith, C.D. Medley, D. Shangguan, W. Tan. Aptamer-conjugated nanoparticles for selective collection and detection of cancer cells. *Anal. Chem.* 78 (2006) 2918–2924.
- [33] Y-F. Huang, K. Sefah, S. Bamrungsap, H-T. Chang, W. Tan. Selective photothermal therapy for mixed cancer cells using aptamer-conjugated nanorods. *Langmuir* 24 (2008) 11860–11865.
- [34] X. Chen, M.-C. Estévez, Z. Zhu, Y-F. Huang, Y. Chen, L. Wang, W. Tan. Using aptamer-conjugated fluorescence resonance energy transfer nanoparticles for multiplexed cancer cell monitoring. *Anal. Chem.* 81 (2009) 7009–7014.

- [35] R. Savla, O. Taratula, O. Garbuzenko, T. Minko. Tumor targeted quantum dot-mucin 1 aptamer-doxorubicin conjugate for imaging and treatment of cancer. *J. Controlled Release* 153 (2011) 16-22.
- [36] J.A. Hanson, J. Wang, A-N. Kawde, Y. Xiang, K.V. Gothelf, G. Collins. Quantum-dot/aptamer-based ultrasensitive multi-analyte electrochemical biosensor. *J. Am. Chem. Soc.* 128 (2006) 2228–2229.
- [37] F-B.Wang, Y. Rong, M. Fang, J-P.Yuan, C-W.Peng, S-P. Liu, Y. Li. Recognition and capture of metastatic hepatocellular carcinoma cells using aptamer-conjugated quantum dots and magnetic particles. *Biomater.* 34 (2013) 3816-3827.
- [38] H. Koistinen, A. Närvänen, M. Pakkala, C. Hekim, J.M. Mattsson, L. Zhu, P. Laakkonen, U.-H. Stenman, Development of peptides specifically modulating the activity of KLK2 and KLK3, *Biol. Chem.* 38 (2008) 633-642.
- [39] E. Song, A. Mayampurath, C.-Y. Yu, H. Tang, Y. Mechref, Glycoproteomics: identifying the glycosylation of prostate specific antigen at normal and high isoelectric points by LC-MS/MS, *J. Proteome Res.* 13 (2014) 5570–5580.
- [40] G.J. Ashwell, A.T. Williams, S.A. Barnes, S.L. Chappell, L.J. Phillips, B.J. Robinson, B. Urasinska-Wojcik, P. Wierzchowiec, I.R. Gentle, B.J. Wood, Self-Assembly of amino– thiols via gold– nitrogen links and consequence for in situ elongation of molecular wires on surface-modified electrodes, *J. Phys. Chem. C.* 115 (2011) 4200–4208.
- [41] Y. Liu, D.D. Díaz, A.A. Accurso, K.B. Sharpless, V. V Fokin, M.G. Finn, Click chemistry in materials synthesis. III. Metal-adhesive polymers from Cu (I)-catalyzed azide–alkyne cycloaddition, *J. Polym. Sci. Part A Polym. Chem.* 45 (2007) 5182–5189.
- [42] G. C. Eastmond, P. C. B. Page, J. Paprotny, R. E. Richards and R. Shaunak, Poly (ether imide)s with hindering substituents in the anhydride moiety: synthesis, properties and gas permeabilities, *Polymer* 35 (1994) 4215–4227.

- [43] X. Zhang, L. Mao, D. Zhang, L. Zhang. Synthesis, characterization and electrochemistry of novel unsymmetrical zinc phthalocyanines sensitizer with extended conjugation. *J. Mol. Struc.* 1022 (2012) 153-158.
- [44] D. Quinton, E. Antunes, S. Griveau, T. Nyokong, F. Bedioui, Cyclic Voltammetry and Spectroelectrochemistry of a Novel Manganese Phthalocyanine Substituted with Hexynyl Groups. *Inorg. Chem. Comm.* 14 (2011) 330–332.
- [45] M.S. Ağirtas, M.S. Izgi, Synthesis and Characterization of New Metallophthalocyanines with Four Phenoxyacetamide Units. *J. Mol. Structure* 927 (2009) 126–128.
- [46] O.J. Achadu, T. Nyokong, In situ one-pot synthesis of graphitic carbon nitride quantum dots and its 2,2,6,6-tetramethyl(piperidin-1-yl)oxyl derivatives as fluorescent nanosensors for ascorbic acid, *Anal. Chim. Acta* 991 (2017) 113-126.
- [47] O.J. Achadu, T. Nyokong, Interaction of Graphene Quantum Dots with 4-Acetamido-2,2,6,6-Tetramethylpiperidine-Oxyl Free Radicals: A Spectroscopic and Fluorimetric Study. *J. Fluoresc.* 26 (2016) 283–295.
- [48] F. d’Orlye, A. Varenne, T. Georgelin, J-M. Siaugue, B. Teste, S. Descroix, P. Gareil, Charge-based characterization of nanometric cationic bifunctional maghemite/silica core/shell particles by capillary zone electrophoresis, *Electrophoresis* 30 (2009) 2572-2582.
- [49] G. Ramírez-García, D.O. Oluwole, S.R. Nxele, F. d’Orlyé, T. Nyokong, F. Bedioui, A. Varenne, Characterization of phthalocyanine functionalized quantum dots by dynamic light scattering, laser Doppler, and capillary electrophoresis, *Anal. Bioanal. Chem.* 409 (2017) 1707–1715.
- [50] N. Surugau, P.L. Urban, Electrophoretic methods for separation of nanoparticles, *J. Sep. Sci.* 32 (2009) 1889 – 1906.
- [51] J. Gooding, V. Praig, E. Hall. Platinum-Catalyzed Enzyme Electrodes Immobilized on Gold Using Self-Assembled Layers, *Anal. Chem.* 70 (1998) 2396-2402.

- [52] Z. Li, M. Lieberman, W. Hill. XPS and SERS Study of Silicon Phthalocyanine Monolayers: Umbrella vs Octopus Design Strategies for Formation of Oriented SAMs, *Langmuir* 17 (2001) 4887-4894.
- [53] P. Jolly, P. Zhuravski, J.L. Hammond, A. Miodek, S. Liébana, T. Bertok, Jan Tkáč, P. Estrela, Self-assembled gold nanoparticles for impedimetric and amperometric detection of a prostate cancer biomarker, *Sens. Actuators B Chem.* 251 (2017) 637-643.
- [54] A.R. Jalalvand, Fabrication of a novel and ultrasensitive label-free electrochemical aptasensor for detection of biomarker prostate specific antigen, *Int. J. Biol. Macromol.* 126 (2019) 1065-1073.
- [55] F. Duan, S. Zhang, L. Yang, Z. Zhang, L. He, M. Wang, Bifunctional aptasensor based on novel two-dimensional nanocomposite of MoS₂ quantum dots and g-C₃N₄ nanosheets decorated with chitosan-stabilized Au nanoparticles for selectively detecting prostate specific antigen, *Anal. Chim. Acta* 1036 (2018) 121-132.
- [56] A. Rahi, N. Sattarahmady, H. Heli, Label-free electrochemical aptasensing of the human prostate-specific antigen using gold nanospears, *Talanta* 156–157 (2016) 218-224.

1. Introduction

This chapter introduces graphene-based quantum dots, gold nanoparticles and their use in combination with metallophthalocyanines and aptamer for use in electrochemical sensing and more specifically, electrochemical biosensing of the prostate cancer biomarker, prostate specific antigen (PSA).

These nanoconjugates are, for the first time, linked to an aptamer and immobilized on glassy carbon electrodes to fabricate prostate cancer diagnostic tools. The importance of using these nanostructures in combination is also described in this chapter.

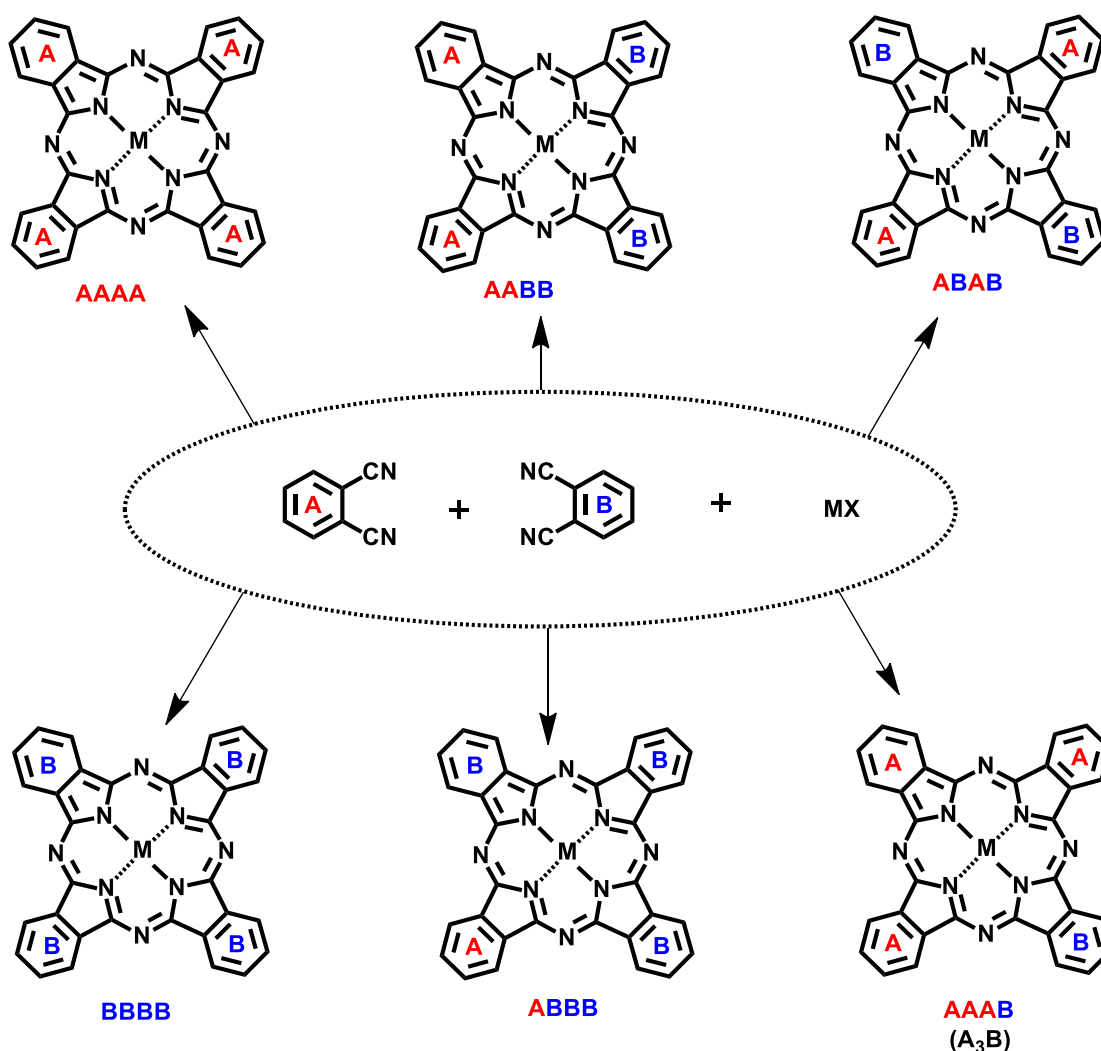
1.1 Overview of metallophthalocyanines (MPcs)

Phthalocyanines are chemically and thermally stable planar macrocycles with a conjugated 18π electron system [1]. Amongst their proven characteristics is their ability to coordinate with a number of central metals to form metallophthalocyanines [2,3]. These macrocycles can be substituted peripherally (β) and non-peripherally (α) [4, 5]. Substitution of the rings may also be carried out with the aim of conjugating these macrocycles with other molecules [6-8]. MPcs have been used in areas of study such as photodynamic therapy (PDT) of cancers [9-11], optical limiting and non-linear optics [12, 13], fluorescence imaging [14-16], photocatalysis [17-19] and electrochemical sensing [20-23]. In electrochemical sensing especially, electroactive central metals such as Mn, Co and Fe are used in order to catalyze specific reactions and promote charge transfer [24]. These metals have orbitals with energy levels lying between the highest occupied molecular orbital (HOMO) and the lowest unoccupied molecular orbital (LUMO) of the Pc, resulting in redox processes on both the central metal and the Pc ring [25]. The symmetry has shown to influence their performance in applications such as electrochemical sensing [26, 27], which is of interest in this work. Asymmetrical MPcs especially, have been shown to improve electrochemical sensing capabilities of sensors [28-30].

1.1.1 Synthesis of asymmetric MPcs

Different approaches have been used to synthesize asymmetrical MPcs such as cross condensation between two phthalonitrile components, cross condensation between one phthalonitrile and one non-nitrile component, the sub-phthalocyanine ring-

expansion method, modification of pre-formed symmetric or asymmetric systems [31] and solid-phase synthesis [32]. The most common approach, which is the one that has been used to synthesize the phthalocyanines used in this work, is the cross condensation between two phthalonitrile components, generally using the 3:1 ratio. In most cases, this results in other products forming which can be separated by chromatographic methods [32]. Scheme 1.1 illustrates the possible products that can form from using the aforementioned synthetic approach for mono-MPCs. The desired MPC, which is employed in this work, is the one with the A₃B symmetry.



Scheme 1.1: Asymmetric MPC synthesis and other possible formed products. MX refers to the metal salt.

1.1.2 Phthalocyanine complexes used in this work

In this work, the following novel asymmetrically substituted phthalocyanine complexes are employed: 2- benzoic acid-9(10),16(17),23(24)-tris(2,6-di-tert-butyl-4-methylphenoxy) phthalocyaninato cobalt (II) (1) and 2-N,N',N''-hex-5-yn-1-yloxy)-9(10),16(17), 23(24)- tris(benzene-4,1-diyl))triacetamidophthalocyaninato cobalt(II) (2), Fig. 1.1. These asymmetrically substituted Co phthalocyanine derivatives (complexes 1 and 2) are used in combination with quantum dots (QDs), gold nanoparticles (AuNPs) and an aptamer for the electrochemical detection of prostate specific antigen (PSA). They are employed as electrode modifiers towards the development of aptasensors. The combination of MPcs with AuNPs and QDs, as aptamer immobilizers and signal enhancers towards the Electrochemical detection of PSA, is reported for the first time. Complex 1 has a -COOH substituent which can be used for covalent linking with an NH₂ terminated molecule via an amide bond. Complex 2 on the other hand will be immobilized on an electrode via electrografting and click chemistry before incorporating the aptamer by adsorption. Both complexes are linked to QDs by π - π interactions. The complexes reported herein are novel and reported in this thesis for the first time. Complex 1 has substituents (*tert*-butyl) that act as electron donating groups (push) and the single COOH as an electron withdrawing group (pull). Such push-pull substituents have been reported to enhance electron transfer properties of complexes [30]. Complex 2 has electron donating alkoxy groups which lower oxidation potentials. A lower potential difference implies better electron transfer which could affect the performance of the fabricated sensors overall.

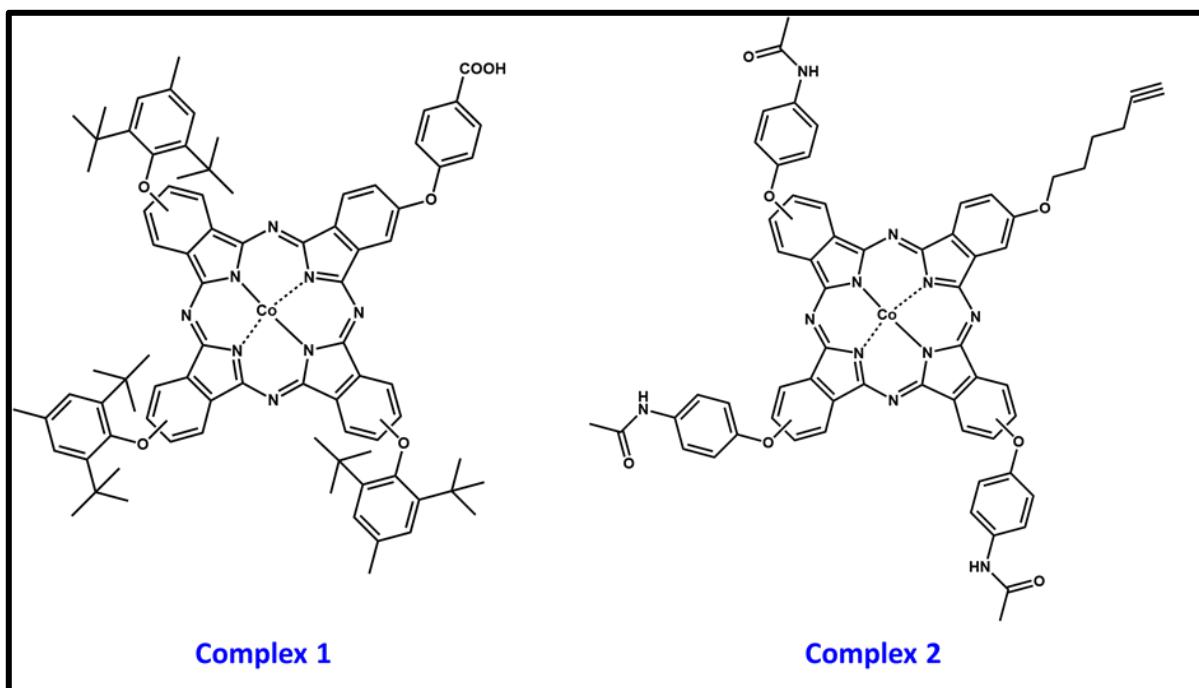


Figure 1.1: Structures of phthalocyanine molecules used in this work.

1.2 Overview of graphene-based quantum dots

Graphene is a 2-dimensional, sp^2 hybridized derivative of graphite made up of covalently linked carbon atoms [33]. Graphite and graphene representations are illustrated in Fig.1.2 [34]. Graphene is characterized by its robustness, good electronic properties and low toxicity in biological applications [35-37]. Graphene quantum dots (GQDs) can be defined as layered fragments of graphene which are well dispersed in water, biocompatible, easy to functionalize at the surface, and also possess low toxicity, with a size range of 1-20 nm [38]. Different synthetic routes have been followed to obtain these nanostructures. Moreover, their surface functionalization also depends on their intended application.

Doping of GQDs with heteroatoms such as boron, nitrogen, oxygen, phosphorous, and sulphur, has led to improved electrochemical sensing capabilities. Nitrogen lies adjacent to carbon in the periodic table thus possess similarity in atomic radius (0.70

Å) with carbon (0.77 Å) which makes it easier to incorporate nitrogen into the pristine carbon network. Nitrogen also has a higher electronegativity (3.04) than C (2.55) which promotes altered electron states of graphene and therefore improving electrochemical sensing capabilities of these nanostructures. QDs, nitrogen doped graphene quantum dots (NGQDs) and graphitic carbon nitride quantum dots (gCNQDs) have all been employed in this work for electrochemical sensing in combination with MPcs. The conjugates are expected to perform better than using the nanostructures as individual components. Graphitic carbon nitride quantum dots (gCNQDs) are of particular interest because they possess the layered structure like QDs, but the difference lies in their exhibition of predominantly π -conjugated framework of C-N layers which are linked covalently [39], Fig.1.3. This nitrogen rich structure will likely play a role in enhancing the electrochemical sensing capabilities of the fabricated sensors. The work reported here shows, for the first time, the use of gCNQDs in the presence of Pcs for electrochemical sensing. The covalent linking of these QDs with an aptamer is also shown herein for the first time although well-known amide coupling is used for conjugation.

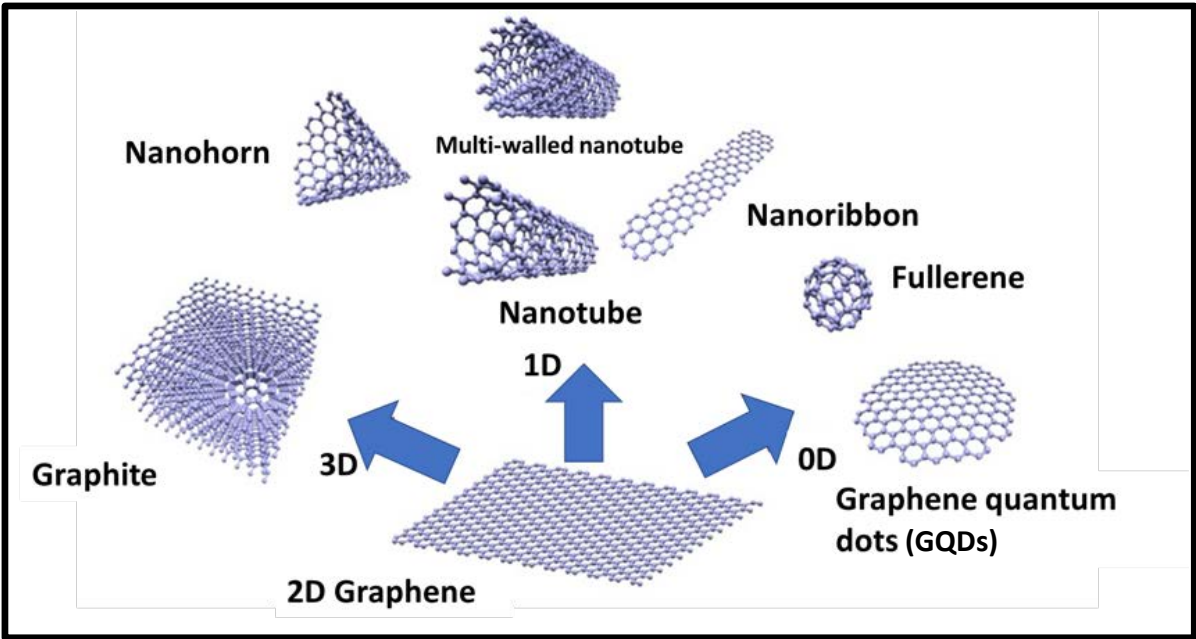


Fig.1.2: Graphite, graphene and their derivatives [34].

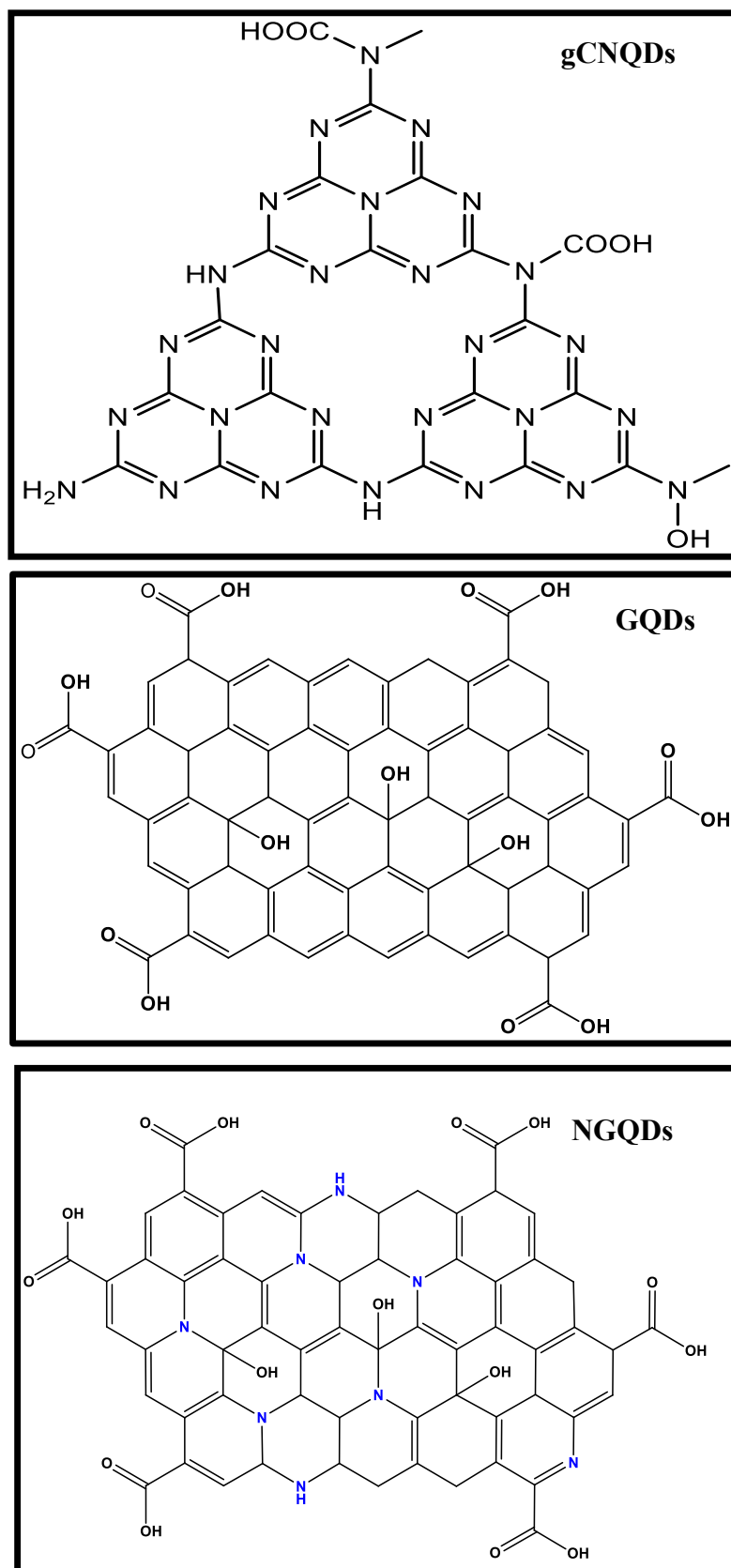


Figure 1.3: Theoretical structural representation of gCNQDs, GQDs and NGQDs.

1.2.1 The synthesis of QDs, NGQDs and gCNQDs

There are two main approaches to obtaining QDs. These are the top-down approach and the bottom-up approaches. The top-down approach involves the cutting or breaking down of large materials with graphene-like structures into nanosized (<100 nm) structures and the bottom-up synthetic routes employ carbon-rich precursors to synthesize QDs [40]. These approaches have been illustrated in Fig. 1.4. Examples of top-down approaches include chemical exfoliation [41], microwave-assisted [42] and solvothermal processes [43]. The bottom-up approach includes hydrothermal [44], microwave-assisted pyrolysis [45] and precursor pyrolysis [46, 47]. The QDs synthesized in this work were obtained by employing the bottom-up hydrothermal approach. Hydrothermal synthesis is achieved in solution under high pressure and high temperatures [48]. The maximum temperatures are generally 300 °C and maximum pressure 200 bar.

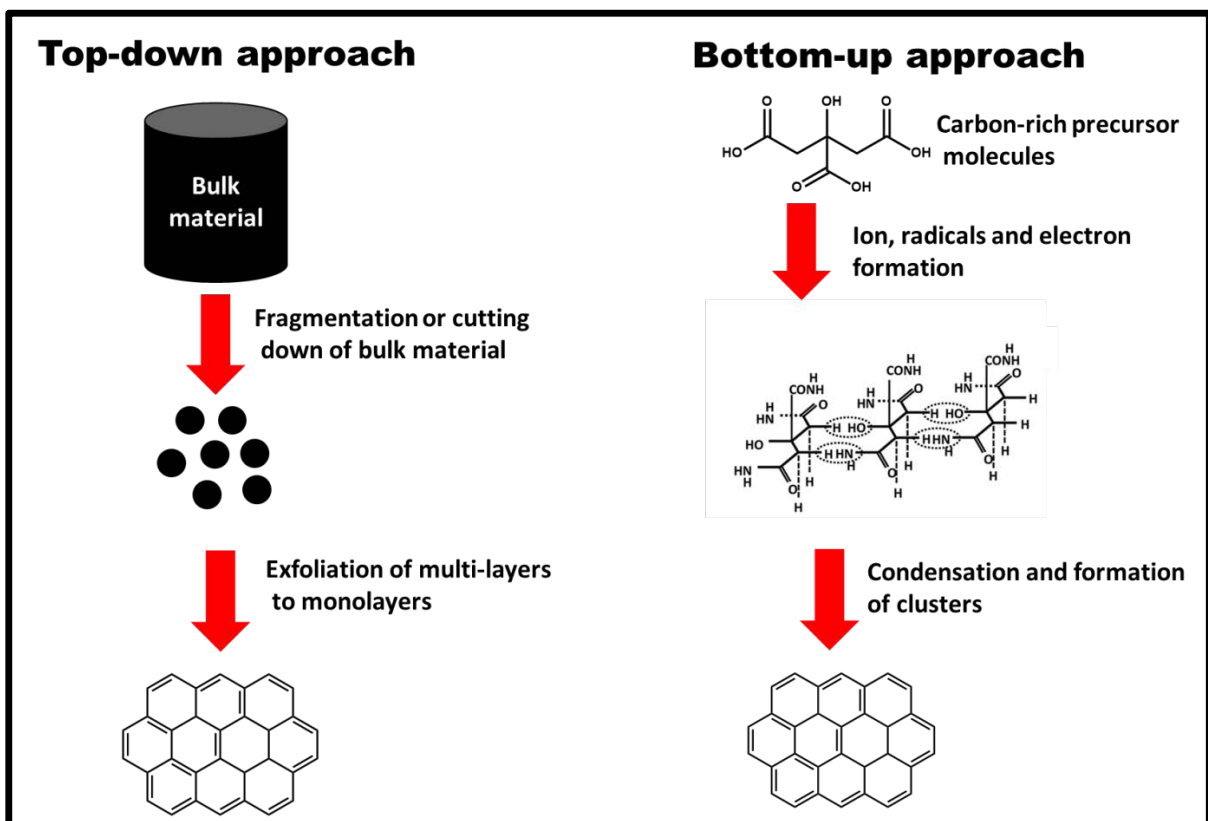


Fig.1.4: GQDs synthetic approaches [47].

1.2.2 GQDs characterization and structural determination

The list of reports on the optimization of graphene-based quantum dots is a very short one. Some spectroscopic techniques are classical employed to characterize graphene-based QDs such as dynamic light scattering (DLS), energy dispersive X-ray (EDX) microanalysis, Raman, absorption and Fourier transform infrared (FTIR) spectroscopies, just to name a few. Some recent reports have shown optimization of quantum dots but only focusing on their fluorescent properties [50, 51]. These techniques have provided information regarding the physical and optical properties of these QDs. However, with QDs being layered sheets and the synthetic approaches used not being controlled, polydisperse samples are likely to be obtained, meaning that QDs of different structures and extent of functionalization exist in one batch. Although methods such as molecular modelling have been used in understanding the structure and chemical composition of graphene-based quantum dots [49], literature rarely reports structural information in detail of the synthesized nanostructures. Herein, the synthetic routes of the GQDs, NGQDs and gCNQDs were optimized by varying the synthesis time and each batch was characterized using different methods, such as TEM and DLS. These characterizations allowed then to select the synthesis times leading to the most stable and monodisperse DQs, that were further deeply characterized by electrophoretic modes. Therefore, electrophoretic separations (CE) coupled to UV-visible or electrospray ionization mass spectrometry (ESI-MS) were employed in order to obtain a deeper physico-chemical characterization of the nano-objects. Indeed, electrophoresis allows to add a separation step, so as to discriminate between different components of the GQDs synthesis batches, thanks to a separation according to their size and surface

charge, allowing for determining their polydispersity, colloidal stability in various media. Electrophoresis coupled to mass spectrometry has become an attractive analytical technique as it combines the advantage of qualitative and quantitative information that would not be obtained if instruments were used separately [52]. Therefore, the coupling of CE with MS, which has not yet been described in the literature for such nano-objects, was implemented so as to help for elucidating the exact structures and overall surface functionalization of the QDs reported in this thesis.

In electrophoretic methods, the sample is injected at the inlet of a capillary and is separated in a background electrolyte (BGE), thanks to the generation of an electric field, according to surface charge density and particle size [53]. Fig. 1.5 illustrates the electrophoretic mobility of particles within a buffer-filled fused silica capillary under application of a voltage, inducing the electrophoretic separation of the different components of the sample. The capillary is made up of an internal silanol layer, which becomes negatively charged upon activation, with a magnitude which is dependent of the BGE pH and ionic strength. Since size of particles influence their migration, particles that have the same charge will be differentiated according to their size meaning the larger the particle, the slower it will move through the capillary. The advantage of using CE is that it has low sample consumption, short analysis time, high separation efficiency, ease of operation and ability to run automatically once the optimized parameters have been entered into the operating system [54, 55].

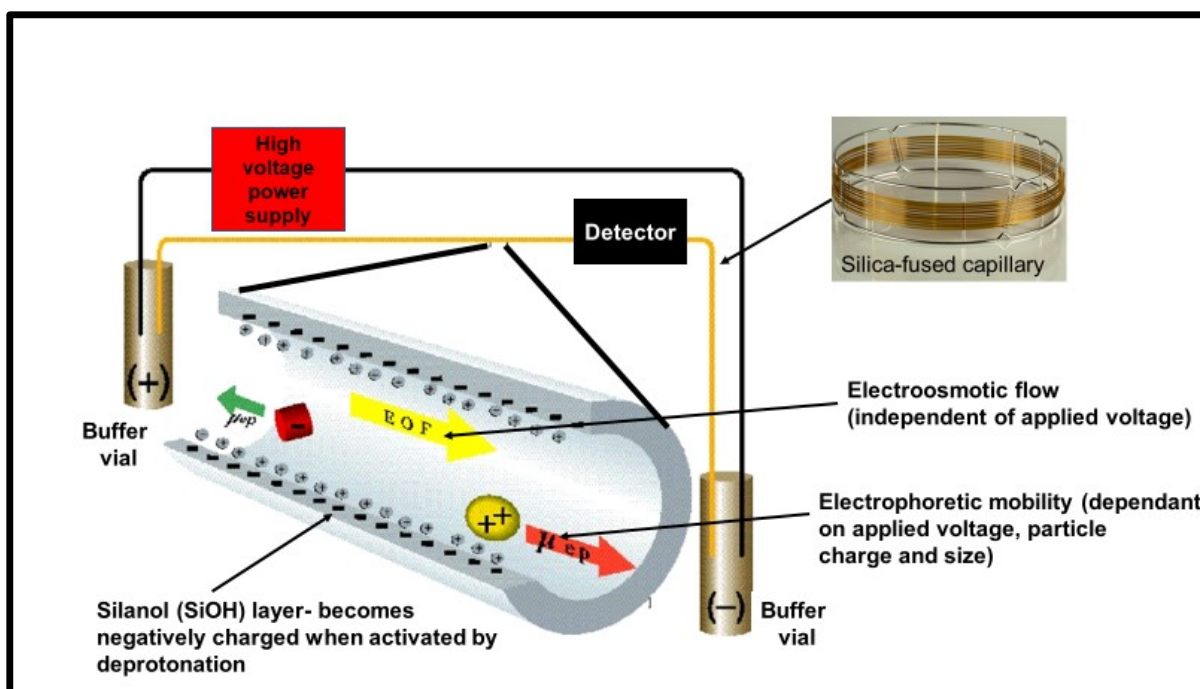


Figure 1.5: Illustration of particle separation in CE [53].

The detection modes employed were either UV-visible spectroscopy or mass spectrometry (MS). MS is a powerful detection mode to characterize the separated nanostructures. The interface between CE and MS developed in this work is an electrospray ionization (ESI) interface (Fig. 1.6), which should induce very few modifications of the sample, and therefore should allow for the preservation of the entire GQDs and the elucidation of their composition in terms of layers.

ESI allows for the detection of large molecular species by generating ions with multiple charges [56]. To briefly explain how it operates, the electrospray promotes the formation of a stream of charged particles carried through a buffer solution by an applied voltage [57]. For this to be achieved successfully, a number of parameters need to be optimized. Among these parameters is the sheath liquid which needs to be suitable for ionization and evaporation as well as the nebulizing gas (whose flow rate and temperature needs to be optimized) to evaporate the

solvent for ions to be detected and quantified [57]. The sheath gas needs to also be optimized in order to maintain the spray and flow of the sheath liquid through a continuous channel, ensuring the ionized particles reach the detector. Samples may be analyzed in single ion mode (SIM) or scan mode depending on whether or not expected ions are known. SIM will only show the specified ions in the spectrum whereas scan mode will show all ions detected. Moreover, the analysis setup has to specify positive or negative ion mode depending on the expected charges of the ions.

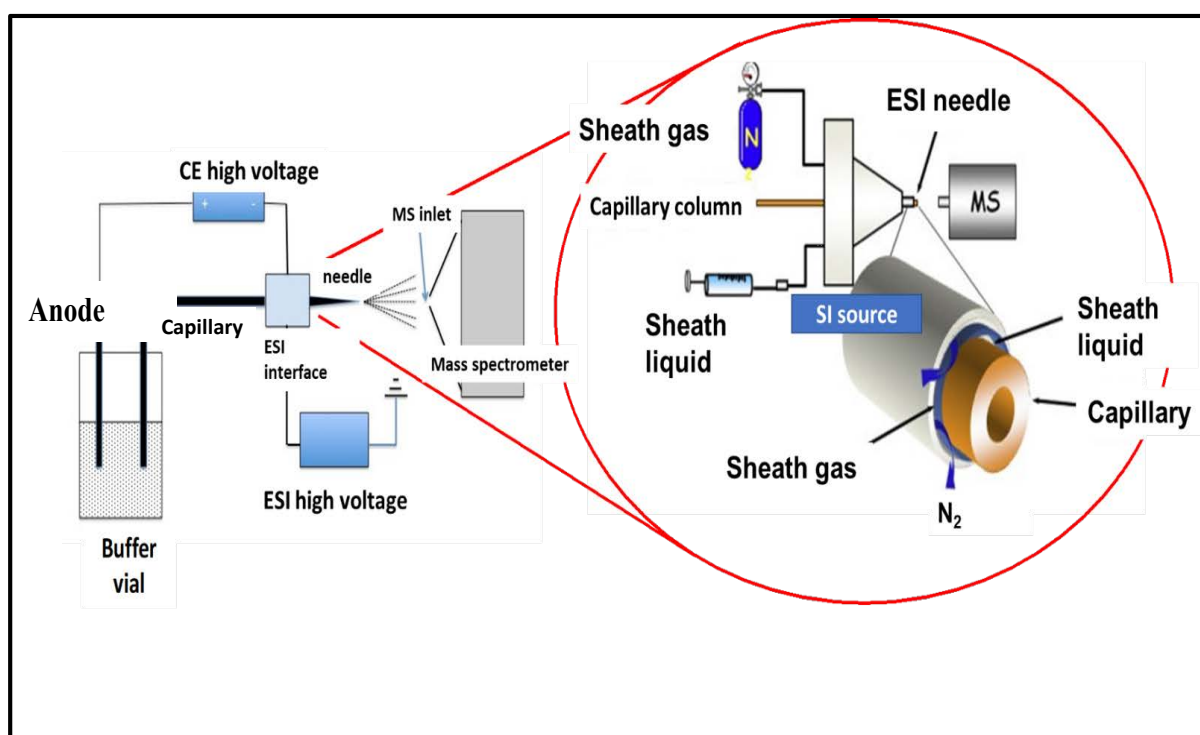


Figure 1.6: Schematic of CE-ESI-MS interface.

1.2.3 General applications of QDs, NGQDs and gCNQDs

QDs have been used alone and in combination with, for example, other small organic molecules by mixing or covalent linking in various fields of study such as bio-imaging [58], photo catalysis [59], photo detection [60], electrochemiluminescence [61], optical sensors [62] and photovoltaic devices [63]. This is owing to their good fluorescence properties. However, QDs have also become popular in electrochemical sensing due to their high stability, high surface area and good charge transfer capabilities [64]. These characteristics have been found to enhance current output which in turn, enhances the performance of electrochemical sensors, hence their use in this work.

The planar structure of graphene layers of QDs consisting of delocalized π -electrons of graphene, enables strong π - π interactions with other π -conjugated aromatic molecules [65]. The presence of carboxyl and hydroxyl groups on the surface (Figure 1.3) allows for the covalent attachment, electrostatic interactions and hydrogen bonding with other suitable molecules. The combination of graphene based QDs with biomolecules and macrocycles such as MPcs has resulted in changes in their chemical properties, leading to their use in various applications. In this thesis QDs are combined with the MPc complexes for electrochemical sensing. Table 1.1 shows examples of graphene based QDs linked to MPcs for sensing [30, 66-70]. As can be seen, a few examples exist where MPcs have been conjugated to graphene-based quantum dots for sensing in general. However, no work has been shown where these nanoconjugates have been used in the fabrication of biomarker detection and is therefore shown herein, for the first time.

Table 1.1: Graphene based quantum dots linked to MPcs for sensing.

Nanoconjugate	QDs-MPc interaction	Application	Reference
NGQDs-CoPc	π - π stacking and covalent linking	Electrochemical sensing of hydrazine	[30]
GQDs-ionic liquid-CoPc	π - π stacking	Electrochemical sensing of glucose	[66]
GQDs-CoPc	π - π stacking	NO ₂ gas sensing	[67]
GQDs/SNGQDs-ZnPc	π - π stacking	Optical sensing of ascorbic acid	[68]
GQDs-CoPc	π - π stacking	Fluorescence sensing of CN ⁻ ion	[69]
GQDs-ZnPc	π - π stacking	Fluorescence sensing of biothiols	[70]

1.3 Gold nanoparticles (AuNPs)

1.3.1 Synthesis properties and applications

AuNPs are generally obtained by the chemical reduction of gold salt [71]. Among the reported synthetic procedures of AuNPs, electrochemical methods have been used [72-75]. This involves the electrodeposition of the AuNPs onto substrates via the electrochemical reduction of Au salts. This efficient method has been employed in this thesis. AuNPs, like other precious metals, are known to exhibit completely different properties from bulk gold [76]. This means, a larger fraction of the active

atoms is on the surface. The optical and electronic properties of AuNPs can be adjusted by changing their size, shape and surface chemistry. These properties have been exploited for biological and pharmaceutical applications such as sensing, therapeutics, catalysis and drug delivery [77-80].

1.3.2 AuNPs and their conjugates with MPc in electrochemical sensing

The good biological compatibility, conducting capability and high surface-to-volume ratio has resulted in the attraction of AuNPs for electrochemical sensing [81]. AuNPs have been used in electrochemical sensing for the improvement of sensitivity and selectivity of fabricated sensors. Peptides, proteins, polymers, small molecules, drugs, carbohydrates and nucleic acids are often used for the functionalization of AuNPs [82-84]. AuNPs-MPc conjugates have been used for the electrochemical sensing of various analytes such as nitrite, hydrazine and bisphenol A [85-87], just to name a few. However, MPcs and AuNPs are rarely used in combination for electrochemical sensing of known cancer biomarkers. The AuNPs-MPc nanoconjugates are used in this work for the first time for the Electrochemical detection of PSA. Moreover, symmetrical MPcs are commonly used in these rare cases, so the role of symmetry of MPcs is not considered or studied. This work will also highlight the effects the structural makeup of the nanocomposites reported herein have on the efficient functioning of the fabricated aptasensors. Table 1.2 shows a non-exhaustive list of reports on MPcs, QDs or AuNPs and their conjugates with affinity molecules used for the Electrochemical detection of various biomarkers [88-97]. As the development of aptasensors has demonstrated their performance for selective and sensitive diagnostics, the combination of aptamers with both MPcs and QDs or AuNPs was investigated in this work

Table 1.2: Examples of MPcs, QDs or AuNPs and their conjugates with affinity molecules used for the Electrochemical detection of various biomarkers

Nanostructure/conjugate	Electrode	Target biomarker	Reference
AuPd-ANPs/GQDs/ACF	Microchip	H ₂ O ₂ (Breast cancer)	[88]
Au/fGQDs	Au electrode	Cardiac troponin I	[89]
GQDs-AuNPs	SPGE	Cardiac troponin I	[90]
GQD/AuNP/NG	GCE	CEA	[91]
CuPc	SPGE	ACP	[92]
Ti ₃ C ₂ T _x MXenes@FePcQDs-cDNA	Au electrode	MicroRNA-155	[93]
Zn-PcTCa-antibody	ITO	KLK4	[94]
N-G/FePc/Nafion/PLL	ITO	NO	[95]
Cr-MOF@CoPc-Aptamer	Au electrode	CT26	[96]
Ab1/AuNPs/PEDOT:PSS	GCE	p53 protein	[97]

Abbreviations: AuPd-ANPs/GQDs/ACF (gold-palladium alloy nanoparticles/ graphene quantum dots/ activated carbon fibres), Au/fGQDs (functionalized graphene quantum dots), SPGE (screen printed gold electrodes), GQD/AuNP/NG (graphene quantum dots/ gold nanoparticles/ nitrogen doped graphene), CEA (carcinoembryonic antigen), ACP (Acid phosphatase), CuPc (copper phthalocyanine), Ti₃C₂T_xMXenes@FePcQDs-cDNA (iron phthalocyanine quantum dots-complementary DNA), Zn-PcTCa (zinc(II) phthalocyanine tetracarboxylic acid), ITO (Indium tin oxide), KLK4 (kallikrein-related peptidase 4), N-G/FePc/Nafion/PLL (nitrogen doped graphene/iron phthalocyanine/nafion/poly-L-lysine), NO (nitric oxide), Cr-MOF@CoPc-Aptamer (Chromium metal organic framework@cobalt phthalocyanine-aptamer), CT26 (colorectal cancer cells), Ab1/AuNPs/PEDOT:PSS (Antibody/gold nanoparticles/polymers poly (3, 4-ethylenedioxythiophene): polystyrene sulfonate).

1.4 Overview of aptamers

1.4.1 Discovery and development

Aptamers are oligonucleotide sequences which are identified as short, single-stranded deoxyribonucleic acid (ssDNA) or ribonucleic acid (RNA) [98, 99]. They are highly selective and specific to a “target” to which they bind. Aptamers are generated and selected through a molecular evolution process or more formally, through the systematic evolution of ligands by exponential enrichment (SELEX) [99-103]. SELEX works by enriching high affinity ligands from randomly selected nucleotides in a library of many oligonucleotidic sequences. The sequences are subjected to rounds of grammatical rules that are applied repeatedly, increasing the high affinity sequences in the system until the most affine aptamer dominates within the randomly selected species [99-103].

1.4.2 Aptamers as biorecognition elements in biosensing

Aptamers are able to distinguish between closely related molecules such as conformational isomers, targeted molecules possessing different functional groups as well as the mutation of amino acids, which makes them even more interesting molecules to look into [99]. Moreover, using aptamers is more advantageous than using antibodies. Antibodies are proteins that circulate in the blood, which can recognize foreign substances called antigens, and they neutralize them by binding to them, Fig. 1.7. Aptamers work in a similar way and are synthesized to strongly and specifically bind to a specific target. They are more stable than antibodies, in a large pH and ionic strength window, at different temperatures, which makes them adequate candidates for biomolecular recognition in sensors. They have already been used for these diagnostics (named “aptasensors”) [98]. In the case of PSA, the

aptamer undergoes a conformational change upon PSA binding such that the double stranded DNA is formed with simultaneous binding to (and covering with) PSA [104].

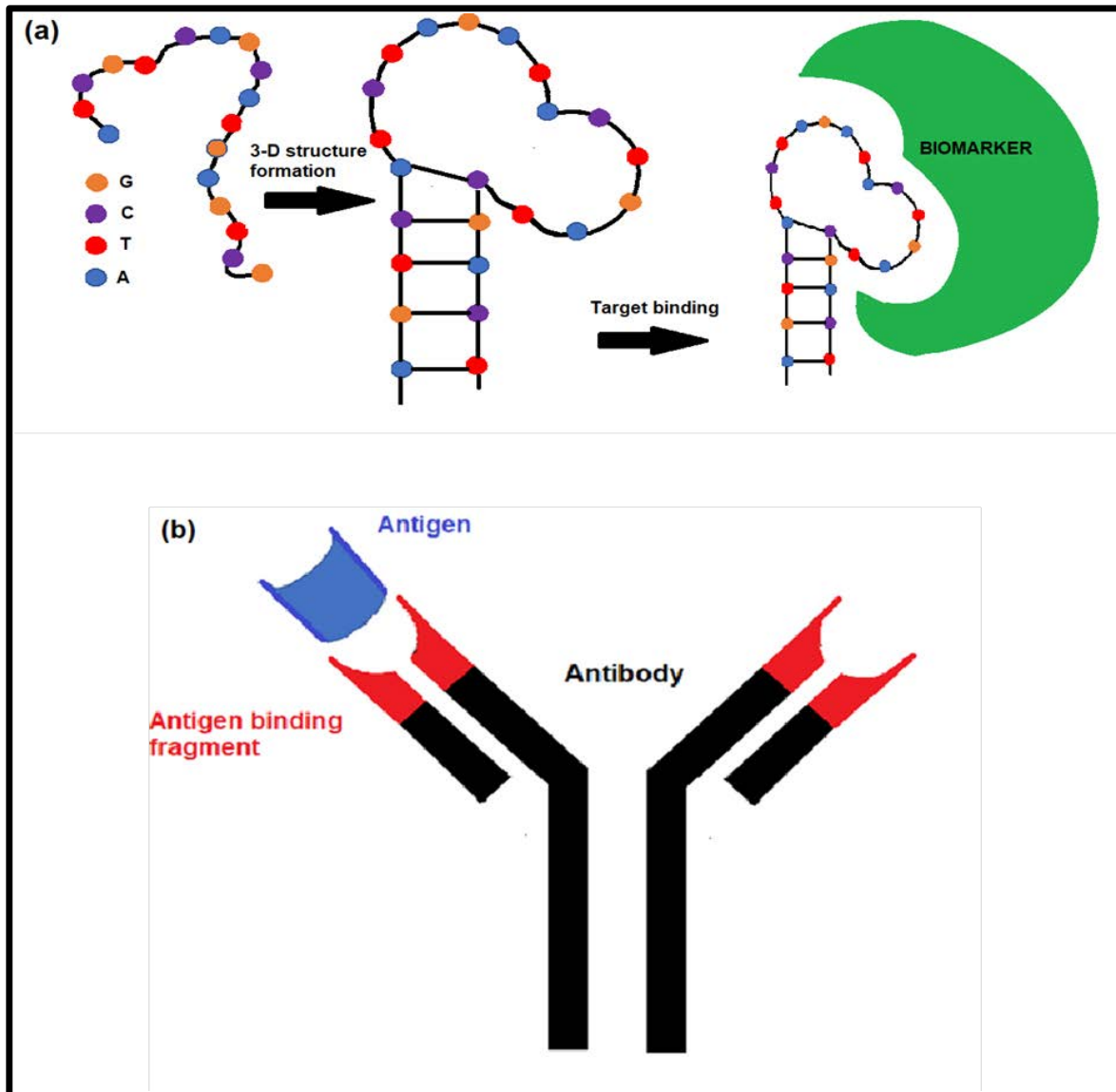


Figure 1.7: Schematic representation of binding of (a) aptamer and (b) antibody to biomarker or target.

1.4.3 Aptamers as bioconjugates for sensing

Aptamers have been conjugated with nanocarriers [104-109] for biosensor applications. Table 1.3 [110-114] summarizes various aptamer-nanostructure conjugates, as well as the advantages of these conjugates for sensing. Some of the improvements that have been observed regarding the use of aptamers and nanocarriers in combination are increased sensitivity and selectivity. Reproducibility is also crucial so that accurate results are reported, which some of these conjugates clearly show. It can be seen though, that the list of aptamer conjugates with graphene based QDs is not exhaustive, especially when it comes to the electrochemical detection of biomarkers such as PSA. No conjugate of QDs with MPcs has been used for aptasensing and therefore it is reported in this thesis for the first time, introducing another novel aspect.

Table 1.3: Aptamer-QDs conjugates for sensing.

Conjugate	Analyte	Advantages	Reference
Aptamer-GQD-Peg-Porphyrin	cancer-related miRNA detection	<ul style="list-style-type: none"> • good capability of identifying specifically cancer cells rather than somatic cells • good cancer-related miRNA detection 	[110]
Aptamer-rGQDs/GO	Lead detection	<ul style="list-style-type: none"> • good biocompatibility • resistance to photo bleaching • controllable fluorescence turn-on process • high sensitivity and good reproducibility • low detection limit 	[111]
gCNQDs-CdSe-Aptamer	tetracycline (TET)	<ul style="list-style-type: none"> • high selectivity • good reproducibility • high stability 	[112]
GQD-Aptamer	Cocaine	<ul style="list-style-type: none"> • highly selective quenching of the photoluminescence when QD-aptamer conjugate binds to target 	[113]
GQD-Aptamer	Doxorubicin (Dox)	<ul style="list-style-type: none"> • sensitivity, • selectivity, • specificity for cancer imaging, therapy and sensing in vitro 	[114]

Abbreviations: Polyethylene glycol (Peg), graphene oxide (GO), microRNA (mRNA), cadmium selenide (CdSe)

1.5 Target analyte used in this work

The main analyte of interest in the work reported herein is Prostate Specific Antigen (PSA). However, in the development of the electroactive nanocomposites and proving that their synergistic effects results in the enhancement of current output, L-cysteine was used as a test analyte. Moreover, this test analyte would later be used to prove selectivity of our aptasensor towards the Electrochemical detection of PSA.

1.5.1 L-cysteine

L-cysteine is known as an important amino acid that is needed by the human body for tissue growth and repair and the importance of monitoring the levels of L-cysteine in the body has been reported in literature [115]. L-cysteine is one of the important components found in hair, nails and skin cells thus being able to monitor the levels of L-cysteine is essential [115]. L-cysteine has been detected in the presence of MPcs [24] but it is reported for the first time in this thesis, the detection of this analyte using Pcs with QDs and its derivatives in order to enhance electrochemical sensing capabilities through current output and stability through the robustness graphene-based QDs are known to possess.

1.5.2 Prostate Specific Antigen (PSA)

Prostate specific antigen is a biomarker directly linked to prostate cancer [116]. Besides its production in cancerous cells, it can be produced in healthy cells too. However, it has been reported that the leakage volume of PSA from the prostate into the circulatory system increases with the occurrence of prostate cancer [117]. The reported concentration levels of PSA in healthy males, ranges from 0 to 4 ng.mL⁻¹ in serum [118], therefore the knowledge of acceptable PSA concentration levels in human serum, using PSA as a biomarker for the diagnosis for prostate cancer has become of great importance.

Early diagnosis of cancers is crucial to prevent premature deaths in males and avoid costly medical treatment for patients. Some diagnostic tools used for PSA detection are summarized in Table 1.4 which includes ELISA, fluorescence and electrochemical immunoassays, chemiluminescence, SPR, SERS and PCR tests [119-131]. These methods allow for high throughput and are considered reliable, but they

are very expensive and require expensive methods that can only be operated by skilled persons. Electrochemical aptasensors have the least drawbacks and are simple, efficient and can be used anywhere at any given moment. For this reason, the research reported in this thesis involves the fabrication of electrochemical aptasensors as a means to contribute to ongoing research that will allow better access to such medical resources, as well as point-of-care diagnosis preventing extended waiting periods before one can be certain of their health condition. The combination of Pcs with QDs, AuNPs and an aptamer is shown for the first time in this thesis for sensing with the aims of improving the stability, efficiency and overall functionality of the sensor.

Table 1.4: Comparative table PSA detection using electrochemical aptasensors and other reported methods.

Detection method	Advantages	Disadvantages	Reference(s)
ELISA	High throughput Very low detection limits Reliable results	Expensive, complex technologies Large sample volumes required Time consuming & Uses antibodies	[119, 120]
Fluorescence immunoassay	Sensitive and selective Low detection limits can be achieved	quenched fluorescence & Limited scope of practical application	[121, 122]
Electrochemical immunoassay	Can detect analyte in complex matrices Low detection limits	Lacks linearity and reproducibility	[123, 124]
CL	Low background signal & High sensitivity	High cost	[125]
SPR	Simple, Efficient, Specific and sensitive	Easily fouled & Poor selectivity in complex mixtures	[126, 127]
PCR	Sensitive & Identifies tumour-specific mRNA	Can give false negative results &	[128]

		poor reproducibility of analysis	
SERS	High specificity Low detection limits	Tend to be complex and uses expensive instrumentation	[129, 130]
Chromatography (2D Gel electrophoresis)	Separates different forms of the protein, PSA. (fPSA/tPSA) Low detection limits	Requires large sample volumes Narrow dynamic range for detection Multi-step protocol	[124]
Electrochemical aptasensor	High selectivity, specificity and stability Low detection limits, efficient and user friendly, Low cost & Point-of-care diagnosis	Method not suitable for follow up after clinical treatment	[124, 131]

Abbreviations: ELISA (enzyme-linked immunosorbent assay), CL (chemiluminescence), SPR (Surface plasmon resonance), PCR (polymerase chain reaction), SERS (surface-enhanced Raman scattering)

Prostate cancer screening using the Digital Rectal Examination (DRE) and PSA blood tests have been reported recently [132]. Although other tools of prostate cancer diagnosis have been developed, the monitoring of PSA concentration levels is still considered necessary as a complementary method of prostate cancer diagnosis [133]. A number of aptasensors have been fabricated for the electrochemical detection of PSA and some have shown very low detection limits [134, 135].

However, the methods of fabrication used are time consuming and quite complicated compared to the procedures developed herein. The electrochemical detection of PSA involving MPcs and QDs has also been reported in the presence of antibodies and not aptamers [136, 137]. Moreover, the studies where phthalocyanines or GQDs are used are based on enzymatic detection (ie. Detection of other cancer cell by-products) and not direct detection of PSA. The examples shown in Table 1.5 [136-140] also look at other detection methods other than electrochemical ones. As can be seen, graphene based QDs and MPcs, especially in combination, are not commonly used for PSA detection.

Table 1.5: PSA detection using Pcs, AuNPs or QDs with other molecules (no aptamer).

Electrode	Nanoconjugate/Probe	Detection method	Reference
ITO	G-CdS/CoTAPc-(anti-PSA)antibody	Photoelectrochemical	[136]
GCE	Au/Ag-rGO/Aminated-GQDs/Carboxyl-GQDs-antibody	ECL	[137]
-	g-CNQDs/Pd TPs-PA	Fluorescence	[138]
FTO	rGO-BiFeO ₃ -DNA	Photoelectrochemical	[139]
GCE	Au-CoS/graphene-TB/M-CeO ₂ /CMC/ILs-Antibody	Electrochemical	[140]

Abbreviations: G-CdS/CoTAPc-(anti-PSA)antibody (graphene-cadmium selenide/cobalt tetraamino phthalocyanine), Au/Ag-rGO/Aminated-GQDs/Carboxyl-GQDs-antibody, ECL(Electrochemiluminescence), Pd TPs-PA (palladium triangular plates-PSA aptamer), FTO (Fluorine-doped tin oxide), rGO-BiFeO₃-DNA (reduced graphene oxide- Bismuth ferrite-DNA), Au-CoS/graphene-TB/M-CeO₂/CMC/ILs (gold-cobalt sulfide/graphene-toluidine blue/mesoporous-Cerium(V) oxide/carboxymethyl chitosan/ionic liquids-antibody)

Moreover, the electrochemical detection of PSA using QDs-MPC conjugates is uncommon in literature and explored more deeply in this thesis. AuNPs have never been linked to MPCs for PSA detection as well. Click chemistry is also a new approach to sensor fabrication in this particular application. MPCs on their own with aptamers have not been employed for electrochemical detection of PSA (Table 1.6) [134, 141-146].

Table 1.6: Electrochemical PSA detection using aptamer in combination with porphyrin-type complexes, AuNPs or graphene nanomaterials.

Electrode	Conjugates	Modification method	Reference
PGE	AuNPs@GMCs-Aptamer	Adsorption	[134]
AuE	AuNPs-Aptamer	Self-assembly	[141]
SPCE	Au NPs/C ₆₀ -CS-IL/MWCNTs-Aptamer	Adsorption and electrochemical deposition	[142]
AuE	MoS ₂ QDs@g-C ₃ N ₄ @CS-AuNPs-Aptamer	Adsorption	[143]
AuE	Au nanospheres-Aptamer	Electrodeposition and self-assembly	[144]
GCE	rGO-MWCNT/AuNPs-aptamer	Adsorption and self-assembly	[145]
GCE	H-Gr/PdNPs-Aptamer	Adsorption	[146]

Abbreviations: AuE (gold electrode), SPCE (screen-printed carbon electrode), AuNPs/C₆₀-CS-IL/MWCNTs (Au nanoparticles/fullerene C₆₀-chitosan-ionic liquid/multiwalled carbon nanotubes), PGE (pyrolytic graphite electrode), AuNPs@GMCs (gold nanoparticles@graphetasizedmesocarbons), MoS₂QDs@g-C₃N₄@CS-AuNPs (Molybdenum sulfide quantum dots-graphitic carbon nitride@chitosan-gold nanoparticles), H-Gr/PdNPs (hemin-functionalized graphene-conjugated palladium nanoparticles)

1.6 Methods of electrode surface modifications

1.6.1 Adsorption by 'drop and dry' modification technique

Physical adsorption involves the interaction between the surface and the molecule without structural changes. In this work, the drop and dry method was employed by dissolving the different modifiers in a suitable solvent and applying a drop of a certain volume on the electrode surface. Herein, all electrode modifications that did not involve electrografting and click chemistry were achieved by adsorption of composites at the electrode surface. Moreover, the aptamer was placed on the electrografted and clicked surfaces using the drop-and dry method.

1.6.2 Electrodeposition & self-assembly

Using electrodeposition and self-assembly as a method of electrode modification has its advantages such as low cost, high growth rate at room temperature, reproducibility, environmental friendliness and easier control of size and shape. Electrodeposition was used to synthesize and immobilize AuNPs at the GCE surface. Thereafter, the electrode was immersed in an aptamer solution to induce self-assembly of the amine N atoms of the aptamer, as N is known to have an affinity for Au [147]. The electrode fabricated using this technique is illustrated in Fig. 1.8. Using Au surfaces for the immobilization of aptamer has been reported [141, 144, 145]. This work has taken the study further by combining AuNPs and an MPC for the first time towards the fabrication of a PSA aptasensor to study their synergistic effects towards the Electrochemical detection of PSA.

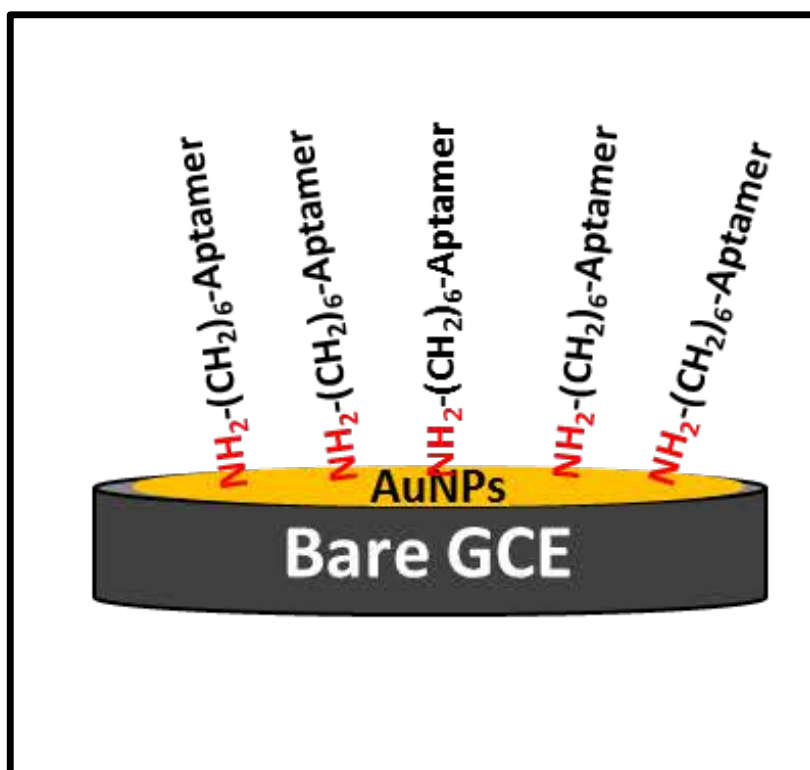


Figure 1.8: AuNPs-modified GCE with self-assembled amine-terminated aptamer molecules.

1.6.3 Electrochemical grafting by reduction and 'click' reaction

Reducing phenyl azide or phenyl acetylene diazonium salts by electrochemical methods results in the grafting of azido or ethynyl groups onto electrode surfaces [148]. Grafting involves the immobilization of molecules at the electrode surface via covalent linkage. It is achieved by electrochemical reduction of compounds in solution forming radicals which simultaneously form covalent bonds between the electrode surface and the reduced molecule. Herein, electrografting of 4-azidobenzendiazonium salt is used to obtain terminated azide groups on a glassy carbon electrode for these groups to react with the terminal alkyne groups of Complex 2. Figure 1.9 illustrates the reaction that occurs on the electrode surface during electrografting using the diazonium salt. Although the number of phenyl azide

groups on the electrode surface is unknown, attachment of molecules by covalent bonding increases the stability of the sensor which promotes the reproducibility of the electrocatalyst.

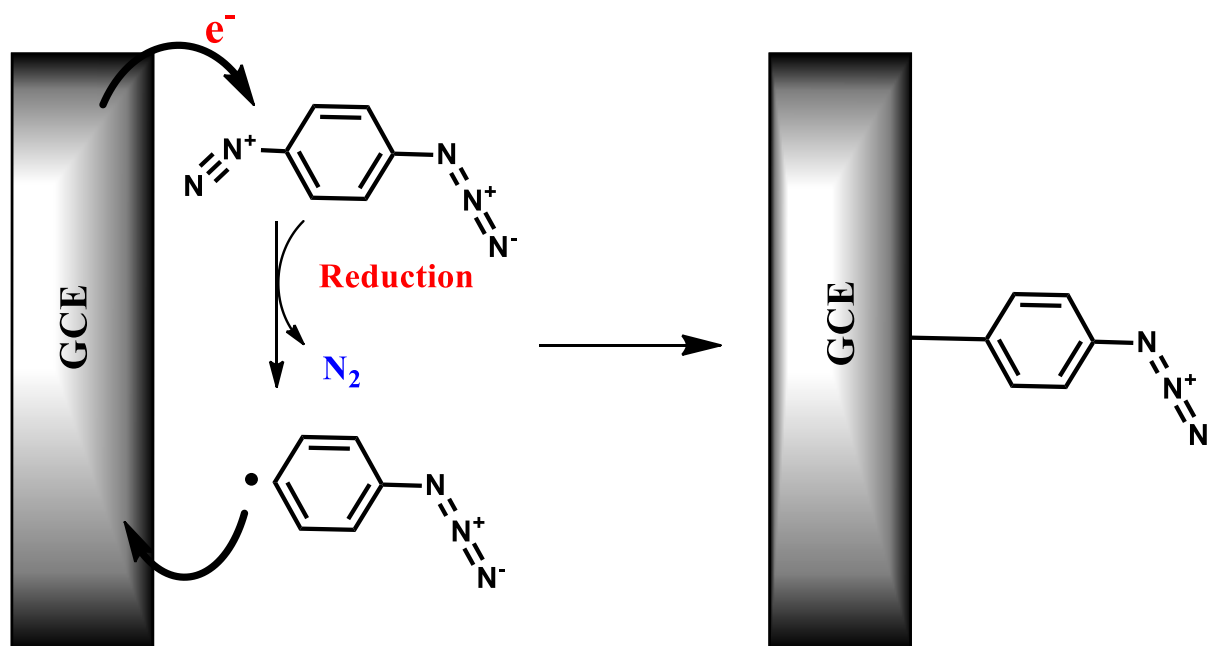


Figure 1.9: Approach to attachment of phenyl azide groups onto a GCE by electrochemical reduction.

The Sharpless Cu(I) catalyzed click reaction [149] is a useful and convenient method as it can be carried out at room temperature and does not require inert conditions, while forming strong covalent bonds with other molecules. Fig.1.10 illustrates the process of how the reaction takes place, where the copper temporarily coordinates with the terminal alkyne group displacing a ligand, followed by the azide group displacing another ligand and in turn coordinating with the copper.

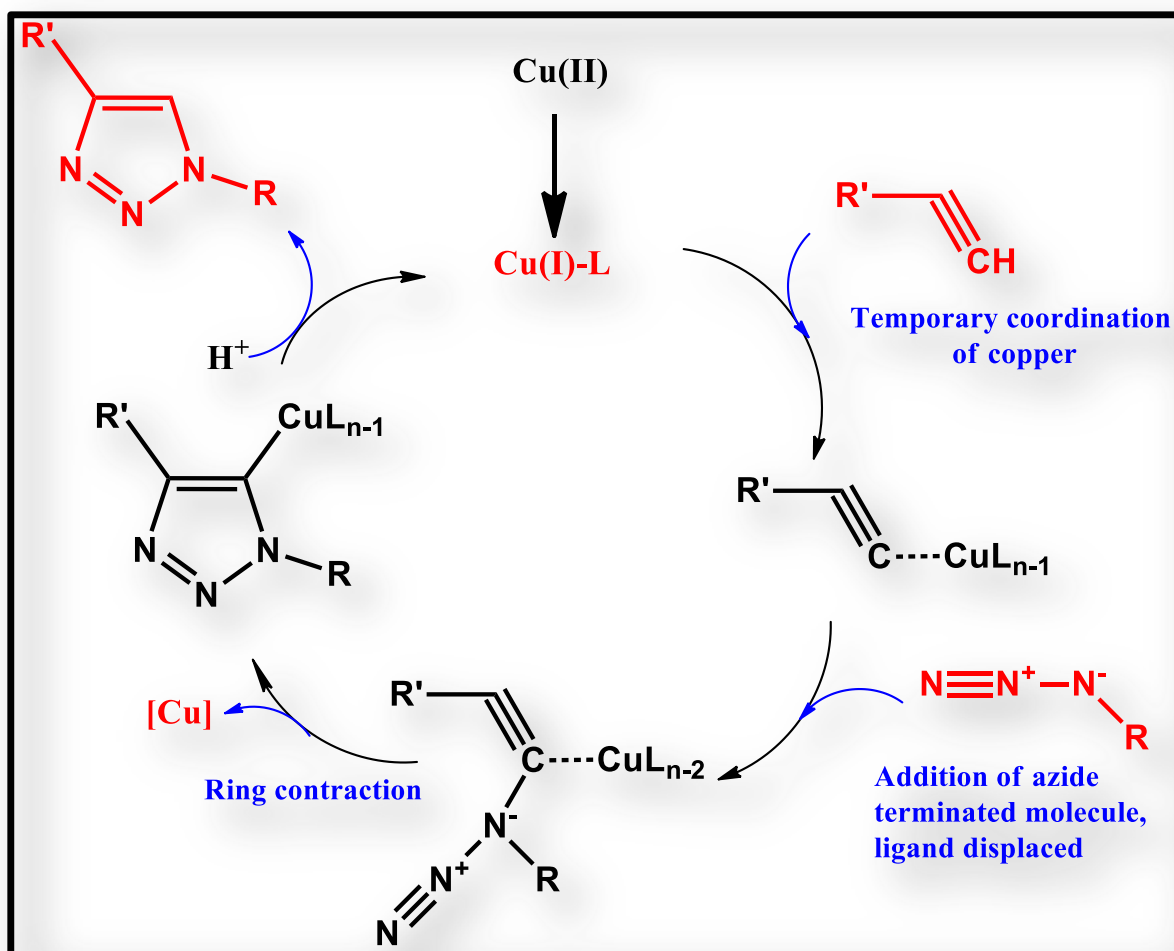


Figure 1.10: Basic illustration of Cu(I)-catalyzed Huisgen 1,3 dipolar cycloaddition.

Thereafter ring contraction takes place, forming a 1,2,3-triazole ring which is then completed by protonolysis. Initially the copper that is used is in its 2^+ state and therefore a reducing agent is used to form Cu(I). Fig. 1.11, thus illustrates the click reaction on a GCE which was done in this work. It is important to note that this is not the true representation of the electrode surface since the reaction may occur with more than one immobilized phenyl azide group.

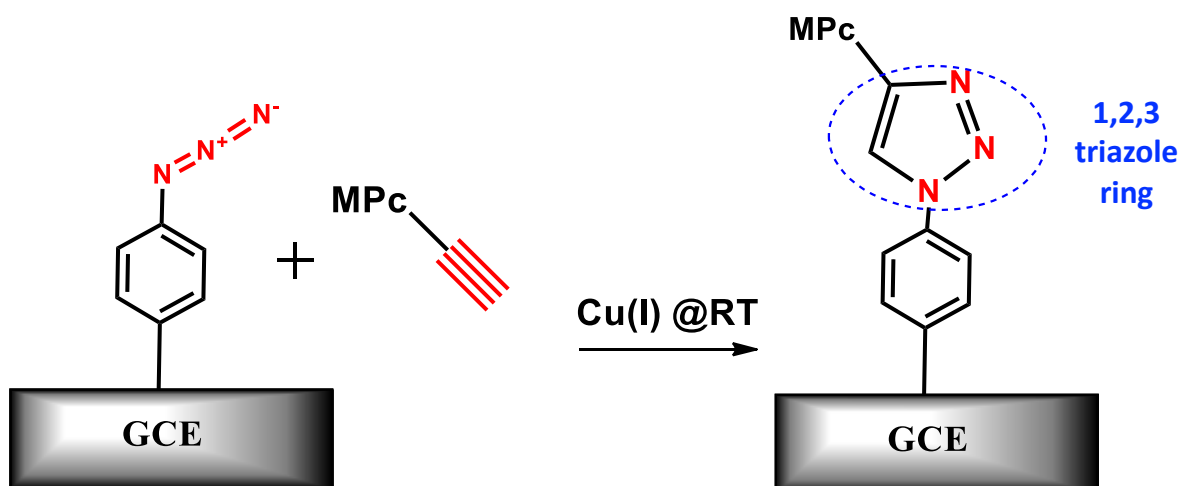
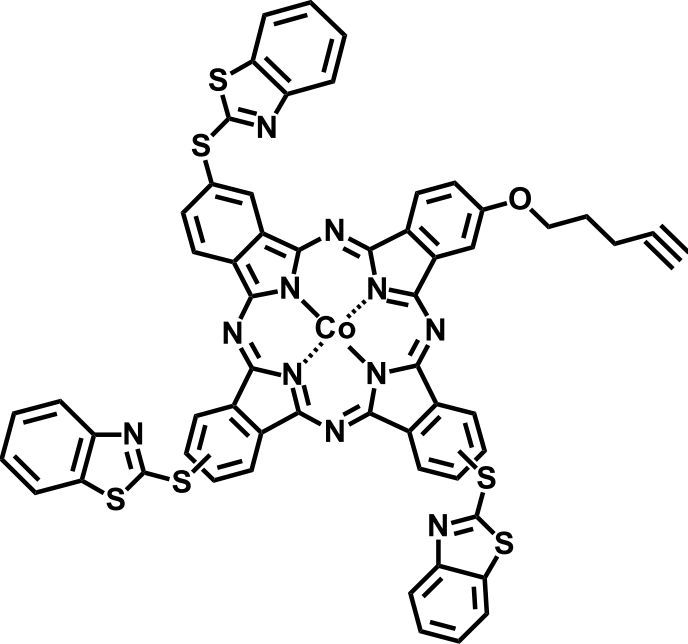
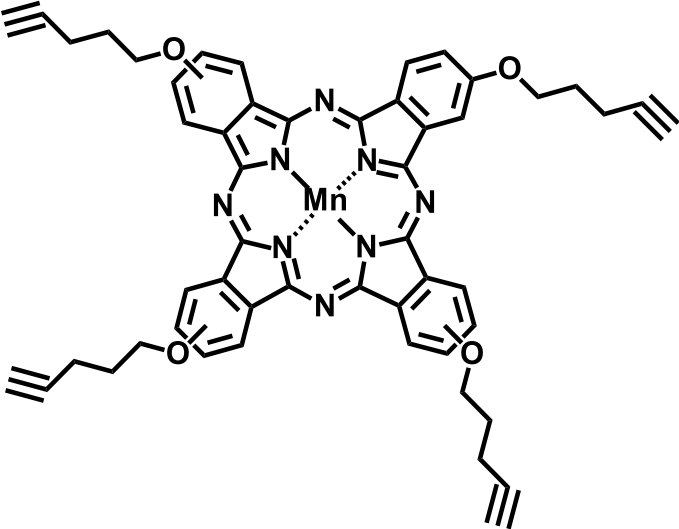


Figure 1.11: Click reaction between terminal alkyne groups of an MPC and phenyl azide groups immobilized on a GCE.

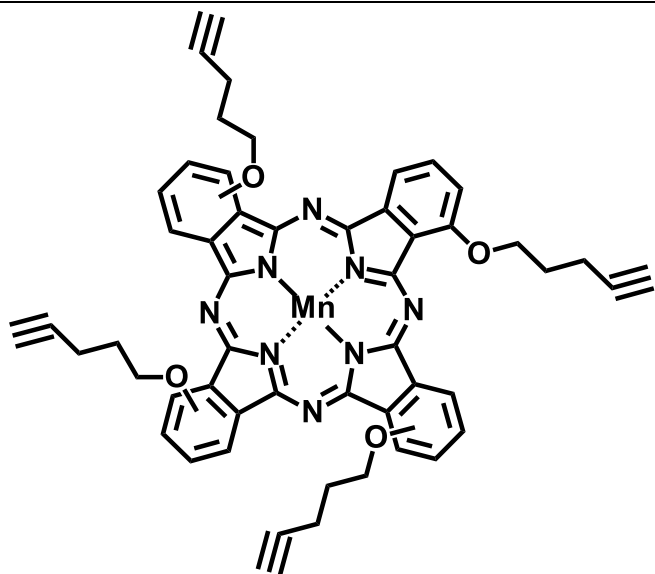
Click chemistry is used in this work to immobilize an alkyl terminated MPC onto a GCE or a GCE with AuNPs electrodeposited on the surface. Once the MPC is immobilized, the aptamer is dropped and dried on the fabricated electrodes to finally obtain the aptasensors. The electrodes are further compared to prove that the use of MPCs and AuNPs together results in the improved performance as PSA aptasensor modifiers.

Table 1.7 [150-154] illustrates the alkyne terminate phthalocyanine molecules used for electrode surface modification via click chemistry. As can be seen, this technique has rarely been used for electrode surface modification and never been used for the fabrication of PSA aptasensors leaving room to further explore its usefulness in sensor fabrication for the electrochemical detection of biomarkers.

Table 1.7: Terminal alkyne functionalized MPcs used for electrode surface modification via click chemistry

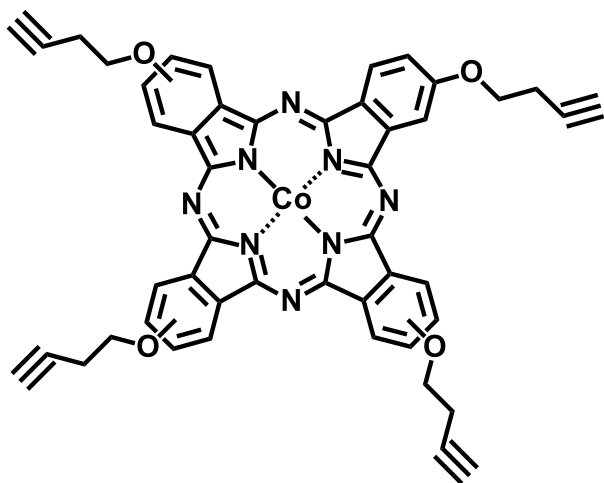
Alkynyl MPc	Analyte	reference
	Heavy metals	[150]
	Pesticides	[151]

Oxygen reduction [152]

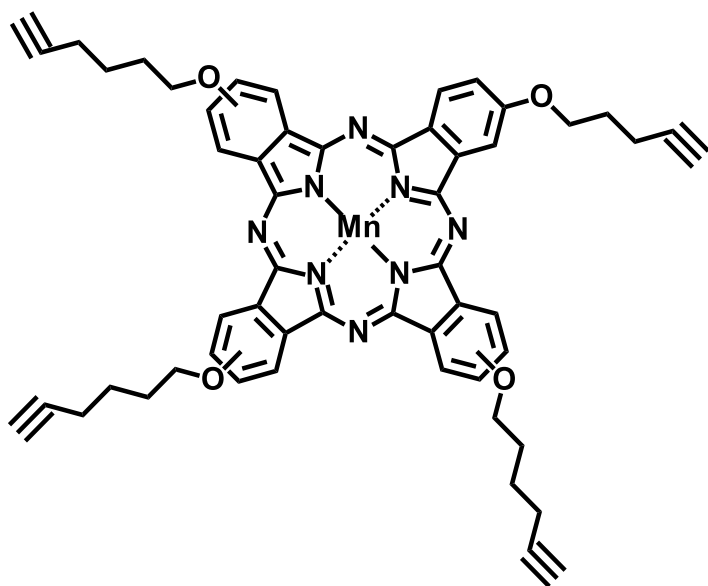


Tested in various [153]

electrolyte
systems



Hydrazine [154]



1.7 Summary of aims of this thesis

The general aims of the research conducted and reported in this thesis is to fabricate and develop efficient, low-cost, simple and stable diagnostic tools for prostate cancer, which will yield low detection limits with high specificity and selectivity. All modifiers and electrode surfaces modified were deeply physico-chemically characterized by various analytical methods, so as to verify their structure, size and charge density, as well as their stability for further applications for sensing tools. Moreover, the feasibility and reliability of the fabricated aptasensors will be determined by testing the sensors in spike serum samples. The final aims of the thesis are as follows:

1. Synergistic effects of Complex (1)-quantum dots nanoconjugates:

L-cysteine is used as test analyte to validate the effectiveness of using QDs, NGQDs and gCNQDs in combination with complex 1, as signal amplifiers and stable platforms prior to using them to fabricate aptasensors.

2. Aptasensing capabilities of complex (1)-quantum dots nanoconjugates in combination with aptamer:

QDs are used as a base point to test different combinations of the conjugates with aptamer and MPc to suite the application. The combined nanostructures are immobilized on glassy carbon electrodes using the drop-and-dry method. The best performing electrode will be used to do a comparative study of the synthesized QDs, where the NGQDs and gCNQDs replace the QDs, and then their electrochemical sensing response studied and compared.

3. Influence of quantum dots composition and structure on aptasensing capabilities-a comparative study:

A comparative study of QDs influence on aptasensing capabilities in terms of structure and composition is conducted once best adsorption combination is determined as outlined in point number 2.

4. Influence of phthalocyanine substitution on aptasensor performance:

The influence of MPc, complexes (1) and (2), on the performance of an aptasensor in terms of substituents is studied and determined.

5. Synergistic effects of complex (2) and Au nanoparticles on aptasensor performance:

Synergistic effects on the aptasensor performance of AuNPs-MPc conjugate via covalent linkage i.e., electrochemical grafting and click chemistry is studied and determined.

6. Verification of feasibility of fabricated sensors in real samples:

In each case where the aptamer is included, the best performing sensor (unless stated otherwise) is testing in spiked serum samples to verify the feasibility and potential to be used in clinical studies.

2. Materials, equipment and experimental

This chapter outlines the materials and equipment used in the work reported. It also outlines the synthesis, conjugation and electrode modification protocols followed.

2.1 Materials

2.1.1 Solvents and general materials

Chloroform and methanol (MeOH) were procured from SAARCHEM. Potassium chloride (KCl) was purchased from MINEMA. Dimethyl sulfoxide (DMSO), ethanol (EtOH), N, N-dimethylformamide (DMF) and acetonitrile (ACN) was purchased from Merck. Tetrahydrofuran (THF) was purchased from EMSURE. Potassium hexacyanoferrate (II) ($K_4[Fe(CN)_6]$), potassium hexacyanoferrate (III) ($K_3[Fe(CN)_6]$) and ethylenediaminetetraacetic acid (EDTA) were purchased from Sigma Aldrich. Ultra-pure water was obtained from a Milli-Q Water system (Millipore Corp. Bedford, MA, USA).

2.1.2 Synthesis of MPCs and conjugates

N-hydroxysuccinimide (NHS), 1-ethyl-3-(3-dimethylaminopropyl)-carbodiimide (EDC), 1,8-diazabicyclo[5.4.0]-undec-7-ene (DBU), and cobalt(II) chloride were purchased from Sigma-Aldrich.

2.1.3 Quantum dots

Sodium hydroxide, citric acid, urea, diaminomaleonitrile (DAMN) were purchased from Sigma Aldrich.

2.1.4 Biological samples

Tris-HCl, prostate specific antigen (PSA) and human serum (from male AB clotted whole blood, USA origin, sterile-filtered) were purchased from Aldrich. Magnesium chloride was purchased from SAARCHEM. The amine-functionalized aptamer was synthesized by (and purchased from) Integrated DNA technologies (IDT) and purified using high-performance liquid chromatography and its sequence is listed as follows:

single stranded DNA (ssDNA): 5'-NH₂-(CH₂)₆-TTT TTA ATT AAA GCT CGC CAT CAA ATA GCT TT-3' (235 nmol, >90% purity).

2.1.5 Capillary electrophoresis-mass spectrometry (CE-MS)

Paracetamol, dimethylformamide (DMF), ammonium carbonate, ammonium bicarbonate, sodium carbonate, sodium bicarbonate, ammonium hydroxide and triethylamine (TEA) were purchased from Sigma-Aldrich.

2.1.6 Electrode modification

4-Azidoaniline hydrochloride, tetrabutylammonium tetrafluoroborate (TBABF₄), gold salt (HAuCl₄), sodium nitrate (NaNO₃) and bromotris(triphenylphosphine)copper(I)(Cu(PPh₃)₃Br) were purchased from Aldrich.

4-Azidobenzene diazonium tetrafluoroborate was synthesized from 4-azidoaniline hydrochloride as reported in literature [155].

2.2 Solution preparation

2.2.1 Capillary electrophoresis-mass spectrometry (CE-MS)

The analyte solutions for CE-MS analyses were prepared by dissolving the quantum dots at a concentration of ca. 1mg/mL in water. Deionized water was obtained from an Alpha-Q system (Millipore, Saint-Quentin-en-Yvelines, France). The background electrolyte (BGE) was composed of 150 mM ammonium carbonate and 150 mM ammonium bicarbonate, which were mixed and diluted to make a pH 7.4 solution with an ionic strength of 10 mM. The same method applies for the sodium carbonate and sodium bicarbonate buffer used for CE-UV analysis. Electrolytes were sonicated and filtered through a 0.45 mm polyvinylidene fluoride (PVDF) membrane filters (Pall Life Sciences, MI, USA) before use.

2.2.2 Aptamer

The aptamer solution was prepared in a Tris-EDTA buffer as recommended by supplier as follows: A 100 mL stock solution of pH 8 was prepared in Tris-HCl (1 mL, 1 M) and EDTA (0.2 mL, 0.5 M) and topped up 100 mL. The stock solution was adjusted accordingly to make a 10 mM buffer solution, which was stabilized by adding 10 mM KCl, and 10 mM MgCl₂, both had a pH of 8. The solution was stored at 4°C.

2.2.3 Electrochemical detection

A phosphate buffer saline (PBS) solution of pH 7.4, 30 mM, was employed in this work. The pH of PBS was adjusted using 0.1 M HCl or NaOH where necessary. [Fe(CN)₆]^{3-/4-} solution (1 mM in 0.1 M KCl) was used for the characterization of the modified electrodes in cyclic voltammetry.

2.3 General equipment

- Ground state electronic absorption spectra were recorded on a Shimadzu UV-2550 spectrophotometer in the range of 300-800 nm.
- X-ray powder diffraction (XRD) patterns were recorded on a Bruker D8 discover equipped with a Lynx Eye detector, using Cu-K α radiation ($\lambda = 1.5405$ Å, nickel filter). Data was collected in the range from $2\theta = 10$ to 100° , scanning at 1 min with a filter time-constant of 2.5s per step and a slit width of 6.0 mm.
- Transmission Electron Microscopy (TEM) images were obtained from a Zeiss Libra TEM 120 model operated at 90 kV.
- Dynamic light scattering (DLS) measurements were done on a Malvern zetasizer nanoseries, Nano-ZS90. The assumption of a graphite structure

(carbon) refractive index of 2.417 [156] and a dispersant refractive index of 1.332 with a viscosity of 0.8872 cP was made consistently across all the dispersions. Zeta potentials were measured using a Malvern zetasizer nanoseries, Nano-ZS90. A U-shape disposable laser doppler velocimetry (LDV) determination cell (DTS1060, Malvern Instruments, Malvern, UK), with a 750 mL volume, was used.

- Infra-red spectra were collected on a Bruker Alpha model FT-IR Spectrometer with platinum-ATR.
- Raman spectrum was obtained with a Bruker Vertex 70-Ram II spectrometer (equipped with a 1064 nm Nd:YAG laser and liquid nitrogen cooled germanium detector). Solid samples were diluted with KBr.
- Scanning electron microscope (SEM) images were obtained using a JOEL JSM840 scanning electron microscope.
- Energy-dispersive X-ray spectroscopy (EDX) analysis was run using a JEOL JSM 840 scanning electron microscope (SEM)) operating at an accelerating voltage of 20 kV.
- X-ray photoelectron spectroscopy (XPS) analysis for the characterization of covalently linked conjugates was done using an AXIS Ultra DLD (supplied by Kratos Analytical) using Al (monochromatic) anode equipped with a charge neutralizer, the following parameters were used: the emission was 10 mA, the anode (HT) was 15 kV and the operating pressure below 5×10^{-9} Torr. A hybrid lens was used and resolution to acquire scans was at 160 eV pass energy in slot mode. The centre used for the scans was at 520 eV (width of 1205 eV) with steps at 1 eV and dwell time at 100 ms. The high-resolution

scans were acquired using 80 eV pass energy in slot mode. The chemically distinct peaks were resolved using a non-linear least squares curve fitting procedure. The core level binding energies (BEs) were aligned with respect to the C 1 s binding energy (BE) of 284.5 eV.

- Cyclic voltammetry (CV), differential pulse voltammetry (DPV) and chronoamperometric experiments were run using Auto lab potentiostat PGSTAT 302 (Eco Chemie, Utrecht, The Netherlands) driven by the General Purpose Electrochemical System data processing software (GPES, software version 4.9).
- Electrochemical impedance spectroscopy (EIS) experiments were run using an Autolab potentiostat PGSTAT30 equipped with Nova software version 2.1 and measurements were performed between 1 Hz and 10 KHz using a 5 mV rms sinusoidal modulation. EIS was used to measure the changes in capacitance on the substrate surface due to the binding or lack thereof of the PSA.
- Scanning electrochemical microscopy (SECM) experiments were carried out using Uniscan Model 370 equipment and a 15 μm Pt microelectrode (Uniscan) as the tip. SECM approach curves were done using the Pt microelectrode with a Pt counter electrode and Ag|AgCl wire as the pseudo-reference electrode. SECM images were obtained by maintaining the tip at a constant Z position and scanning in the X-Y plane over the desired area (constant-height mode of SECM) and monitoring changes in the steady-state current of $\text{K}_3[\text{Fe}(\text{CN})_6]$ oxidation at -0.1 V vs. Ag|AgCl (as pseudo reference electrode) as the tip travels. Approach curve analysis and constant height imaging was employed using the 15 μm Pt ultra-microelectrode (UME) together with a Pt counter

electrode and Ag/AgCl wire as the pseudo-reference electrode. For surface imaging, the microelectrode tip was maintained at a constant height (z-axis) and the desired area scanned along the X-Y plane. Changes were monitored in the steady state current of $K_3[Fe(CN)_6]$ oxidation at 0.1 V vs. Ag/AgCl as the tip travels.

- Glassy carbon plates (GCP, Goodfellow, UK) of 1×1cm and 2mm thick were also used as substrates for SECM, SEM and XPS analyses.

2.4 Capillary electrophoresis experiments

2.4.1 CE-UV experiments

CE was performed with an HP^{3D}CE instrument (Agilent Technologies, Massy, France) equipped with a UV absorbance diode array detector (DAD). Separations were achieved using bare fused- silica capillaries (Photonlines, Marly-le-Roi, France) with the following dimensions: 75 μ m internal diameter (360 μ m outer diameter), 35 cm total length and 8.5 cm effective length for UV-visible detection and 100 cm (26.5 cm effective length) when coupled to mass. HP^{3D}CE chemstation software was used for instrument control, data acquisition and data handling. Dimethylformamide (DMF) (5 mM in the ammonium carbonate buffer) was used as the neutral marker for CE-UV/Vis experiments, and Paracetamol (5 mM in the ammonium carbonate buffer) was used as neutral marker when CE coupled with MS to determine electroosmotic flow (EOF). In CE-UV, samples were injected for 5 s at 50 mbar. For MS detection, analytes were hydrodynamically injected (50 mbar, 16 s) and separation voltage was at 20 kV in positive polarity (unless otherwise specified). UV/Vis detection is

achieved through a 'window' obtained by burning (or scraping) off the polyimide external coating. The high transparency of the fused-silica capillaries wall allows the use of low UV wavelengths. New capillaries were conditioned by successive flushes with water (950 mbar, 300 s), 0.1 M NH_4OH (950 mbar, 300s), water (90 mbar, 300 s) and then the capillary filled with BGE by flushing for 600 s at 50 mbar. The temperature in the capillary cassette was set at 25 °C. The acquisition rate was 10 points/s. Analytes were detected by UV absorbance at 200 nm. Between runs, capillaries were rinsed using the same preconditioning methods. Capillaries were rinsed with 0.1 M NH_4OH and water and dried by air when not in use.

2.4.2 CE-MS experiments

The equipment employed for CE-MS experiments is shown in Fig. 2.1.



Figure 2.1: CE-ESI MS instrumentation used for the separation of the QDs synthesized in this work.

An Agilent Series 1100 MSD single quadrupole mass spectrometer (Agilent Technologies) equipped with an orthogonal electrospray ionization (ESI) source was used in the negative ionization mode. The upper mass limit of the instrument was 2000 amu. A coaxial triple-tube ESI-MS interface was used to maintain the connection between the CE and MS systems by providing the necessary sheath liquid and nebulizing gas. In the scan mode, scans were run between $m/z = 0-2000$ unless stated otherwise. In the analysis of the selected ions in single ion mode (SIM), the selected masses were used with a dwell time of 40 ms on each mass. Nitrogen was used as nebulizing gas at a temperature of 300°C (pressure in the 0 to 100 kPa range) and as drying gas at 300 °C (flow rate in the 0 to 8 L/min range). Optimized ESI voltage was 3000 V. Skimmer voltage was 10 V. Peak width and dwell time were set to 0.3 min and 880 ms, respectively. CE-MS coupling was carried out using a coaxial ESI interface (Agilent Technologies). MS detection of the compounds by direct injection was performed by hydrodynamic injection (50 mbar) of the sample from the separation capillary to the MS detector under pressure via the ESI interface. The sheath liquid (SL) (50:50 v/v MeOH: H₂O mixture containing 0.01% v/v triethylamine) was delivered by an Agilent 1100 series isocratic HPLC pump (flow rate in the 0-10 mL/min range). Some parameters are later optimized for better detection and characterization of the samples.

Prior to introducing the quantum dots samples into the CE-MS (Fig. 2.1) system for analysis, the analytical conditions needed to be optimized. The neutral marker was used as a test sample for all optimizations and introduced by an internal pressure of 50 mbar at the inlet end. The conditions optimized were the nebulizing gas pressure, electrospray voltage, drying gas flow rate, drying gas temperature, sheath liquid

flow rate, applied voltage in CE for separation and effects of changing internal pressure at a constant applied potential. The initial setpoint were varied one parameter at a time while keeping the other parameters constant. The signal to noise ratio was determined to see the effects of these parameters on measurements. Once those conditions were optimized, the samples were introduced into the CE-MS system. The optimized parameters are summarized in Table 2.1.

Table 2.1: Summary of optimized analytical conditions for ESI-MS.

ESI-MS Parameter	Set point
Nebulizing gas pressure	8 psi
Electrospray voltage	3000 V
Capillary-electrospray interface	0.2mm protrusion of capillary
Drying gas flow rate	12 l/min
Drying gas temperature	300°C
Sheath liquid flow rate	6 μ l/min

2.5 Synthesis

2.5.1 Complex (1), Scheme 3.2

The syntheses of 2,6-di-*tert*-butyl-4-methylphenoxy phthalonitrile (i) [157] and 4-(4-carboxyphenoxy) phthalonitrile (ii) [158] have been reported in literature. The synthesis of complex (1) was carried out as follows: phthalonitrile (i) (0.39 g, 1.14 mmol), phthalonitrile (ii) (0.1 g, 0.36 mmol) and CoCl₂ (0.178 g, 1.37 mmol) were dissolved in hexanol. DBU was then added, and the mixture was refluxed at 150 °C under inert conditions for 24 h. The product was then dried and subsequently purified by aluminium oxide 90 active neutral packed column chromatography with a gradient eluent mixture of methanol and CHCl₃. Since Cobalt is paramagnetic, this complex could not be characterized using nuclear magnetic resonance (NMR) analysis.

Yield: 35 % (w/w); UV-vis (CHCl₃): λ_{\max}/nm (log ϵ): 600(3.27), 665(3.05). IR [(KBr) $\nu_{\max}/\text{cm}^{-1}$]: 1600 (-C-C-), 1470 (-C-H-), 1360 (-C-N-), 1225 (-C-O-C-), 1170 (-C-O-). (Calculated for C₈₄H₈₆N₈O₆Co; (C 74.04 H 6.36 N 8.22)%, Found C 74.52 H 7.26 N 8.54) %; MS (MALDI-TOF) (m/z): calcd. for C₈₄H₈₆N₈O₆; 1361.60; found: [M]. 1361.34.

2.5.2 Complex (2), Scheme 3.3

The phthalonitriles 4-(hex-5-yn-oxy) phthalonitrile (iii) [159] and *N*-(4-(3,4-dicyanophenoxy)phenyl)acetamide (iv) [160] were also synthesized as reported in literature. The synthesis of complex (2) was carried out as follows: phthalonitrile (iv) (0.40 g, 1.4 mmol), phthalonitrile (iii) (0.065 g, 0.29 mmol) and CoCl₂ (0.094 g, 0.72 mmol) were added to dry DMF(15 mL) and DBU (0.5 mL). The mixture was refluxed over a period of 18 h in an argon atmosphere. Following the completion of the reaction, the product was allowed to cool to room temperature after which the

crude sample was precipitated using methanol and water and then dried in an oven at 120 °C. The desired compound was separated from the tetra substituted A₄ Pcs (structural isomers) and other impurities using column chromatography with a gradient eluent mixture of 9:1 tetrahydrofuran: methanol solvent system. This complex was not characterized using NMR for the same reason stated for complex 1. Yield: 0.0394 g, 12.3 % (w/w); UV/vis (DMF): $\lambda_{\text{max}}/\text{nm}$ (log ϵ): 667 (4.86), 608 (4.31), 327 (4.71). IR [(KBr), $\nu_{\text{max}}/\text{cm}^{-1}$]: 746, 795 (aromatic C-H_{str}), 1087 (C-O-C), 1258 (C-N), 1464 (C=C), 1501 (C-H), 1537 (N-H), 1662 (C=O), 2849, 2916 (aliphatic C-H_{str}), 3273 (C≡C-H). Anal. calc. for C₆₂H₄₅CoN₁₁O₇.5H₂O: C, 61.80; H, 4.57; N, 11.46. Found: C 61.70, H, 3.60; N, 10.90. MS (MALDI-TOF) (m/z): calc.: 1114.28 amu; found: 1114.34 amu [M]⁺.

2.5.3 Quantum dots, Scheme 3.1

The synthesis of gCNQDs has been reported in literature [161]. Briefly, diaminomaleonitrile (1 g, 9.25 mmol), EDTA (0.5 g, 1.34 mmol), and NaOH (5 mL of 1 M) were added to 100 mL of millipore water and the mixture stirred for 1 h to ensure complete dispersion of the compounds. The resulting mixture was then transferred to a 400 mL capacity teflon-lined hydrothermal reactor (Fig. 2.2) and was heated at 200 °C for 2, 4, 6 and 8 h. After cooling to room temperature, the resulting brown-green product was filtered through a 0.22 μm cellulose membrane, followed by the addition of ethanol. The product was centrifuged at 15000 rpm for 15 min. The collected solid was re-dispersed in Millipore water and further dialyzed against ultrapure Millipore water for 24 h to get rid of excess starting materials and by-products. The synthesis of QDs and NGQDs have been reported [162]. Briefly for QDs, citric acid (4.2 g, 1 mmol) and NaOH (2.4 g, 3 mmol) were dissolved in

100 mL water, and stirred to form a clear solution. Then the solution was transferred into a 400 mL Teflon lined stainless autoclave. The sealed autoclave was heated to 160 °C for 2, 4, 6 and 8 h. The final product was collected by adding ethanol into the solution and centrifuged at 5000 rpm for 15 min. The solid was re-dispersed into water and was dialyzed for two days using a dialysis membrane (MW 1.5 kDa) to remove excess salts. The NGQDs were prepared as described above for pristine GQDs, using urea (3.6 g, 3 mmol) in place of NaOH.



Fig. 2.2: Berghof high pressure reactor employed for the hydrothermal synthesis of the QDs used in this work.

2.5.4 Conjugation of nanocomposites

The conjugates used in this work are listed in Table 2.2.

Table 2.2: Conjugates used in this work (excluding ones directly conjugated on the electrode surface).

Modifier	Method of conjugation
GQDs-CoPc(1)($\pi\pi$)	$\pi\pi$ interactions
NGQDs-CoPc(1)($\pi\pi$)	$\pi\pi$ interactions
gCNQDs-CoPc(1)($\pi\pi$)	$\pi\pi$ interactions
CoPc(1)@Aptamer	Covalent bonding
GQDs@Aptamer	Covalent bonding
gCNQDs@Aptamer	Covalent bonding
gCNQDs@Aptamer-CoPc(1) ($\pi\pi$)	Covalent bonding and $\pi\pi$ interactions
gCNQDs@Aptamer-CoPc(2) ($\pi\pi$)	Covalent bonding and $\pi\pi$ interactions

2.5.4.1 Conjugation of QDs to CoPc(1), Scheme 3.5

Where the nature of the quantum dots used for sensor fabrication was studied, the non-covalent coordination ($\pi\pi$ stacking) between the quantum dots and the CoPc(1) derivative was achieved as follows:

CoPc(1) derivative (10 mg, 0.07 mmol) was dissolved in 2 mL of DMSO, followed by mixing with 5 mg (each) of GQDs, NGQDs, and gCNQDs, in 2 mL of water. The mixtures were then sonicated at room temperature for 1 h. Following that, the mixtures were left to stir at room temperature for 24 h. A mixture of DMSO, water

and ethanol (1:5:3) was used to repeatedly wash the products to try get rid of the excess uncoordinated QDs or CoPc(1). The conjugates are represented as GODs-CoPc(1) ($\pi\pi$), NGQDs-CoPc(1) ($\pi\pi$) and gCNQDs-CoPc(1) ($\pi\pi$), Table 2.2.

2.5.4.2 Conjugation of aptamer to QDs and CoPc(1), Scheme 3.4

Covalent linking to form an amide bond between COOH functional groups with the NH₂ group of the aptamer, was achieved by carbodiimide coupling chemistry and the method derived from literature reports [163, 164]. The CoPc(1), GODs and gCNQDs were used as examples therefore NGQDs were not covalently linked to the aptamer. Briefly, for the formation of the amide linkage, the procedure was as follows: of N-hydroxysuccinimide (NHS) (5 mL, 0.02 M) and 1-ethyl-3-(3-dimethylaminopropyl)-carbodiimide (EDC) (5 mL, 0.02 M) each, both prepared in a pH 8 Tris-HCl buffer solution were mixed together and then GODs/gCNQDs (5 mL, 20 mg/mL) were added to the mixture. These solutions were stirred for 12 h to activate the carboxylic acid groups in preparation for conjugation with the aptamer. After 12 h, aptamer (2 mL, 1.0 μ M) was added and the solution further stirred for 24 h, at room temperature, resulting in GODs@Aptamer and gCNQDs@Aptamer, Table 2.1. For the covalent linkage of CoPc(1) with aptamer, CoPc(1) (5 mL, 0.1 M) was added to the EDC/NHS mixture (same amounts as stated above) followed by the addition of aptamer (2 mL, 1.0 μ M) to form CoPc(1)@Aptamer (The '@' symbol represents covalent conjugation).

Ethanol (20 mL) was used to precipitate the conjugates out of solution which were further washed using a DMSO (10mL) and water (50 mL) to remove unreacted QDs and CoPc molecules, resulting in GODs@Aptamer, gCNQDs@Aptamer and CoPc(1)@Aptamer, Table 2.2.

2.5.4.3 Non-covalent combination of gCNQDs@Aptamer with complex (1) and (2)

The covalently linked gCNQDs@Aptamer was used for the MPc complex comparative study as examples since the $\pi\pi$ -conjugates of the QDs with complex 1 had already been extensively studied in combination with aptamer. The comparison of the MPc complexes in this work is therefore not limited to just the gCNQDs but could also be carried out with the other QDs structures. Where the nature of substituents on the asymmetrical MPcs was compared, the non-covalent coordination of the complexes with gCNQDs@Aptamer was achieved as follows: CoPc (1) (10 mg, 0.07 mmol) and CoPc (2) (10 mg, 0.01 mmol) derivatives were dissolved in 2 mL of DMSO, followed by mixing with 5 mg of the gCNQDs@Aptamer in 2 mL of water. Purification was achieved as described above. The conjugates are represented as gCNQDs@Aptamer-CoPc(1) ($\pi\pi$) and gCNQDs@Aptamer-CoPc(2) ($\pi\pi$).

2.6 Electrode modification

A three-electrode system comprising of an Ag|AgCl (3M KCl) as the reference electrode, a platinum (Pt) wire counter electrode and a glassy carbon electrode (GCE) as the working electrode was employed. Prior to modification, the electrode surface was cleaned by means of polishing on a SiC-emery paper in slurry made from alumina nano powder (Sigma-Aldrich) and rinsed with Millipore water several times. In addition, all analytical solutions were purged with argon gas for 20 min to eliminate the dissolved oxygen before each cyclic voltammetry analysis, and the argon atmosphere was maintained throughout the period of analysis to ensure that no disturbances occurred during the analyses due to oxygen.

2.6.1 Drop and dry electrode modification

Each of the conjugates listed in Table 2.2 were used to modify the electrode using the drop and dry method. Experiments where individual components of the conjugates were employed alone or in sequence to modify electrodes, were also conducted. Table 2.3 then lists the modifiers, the solvents they were prepared in and the amounts of modifier used for surface fabrication. 10 μL of each solution was placed on the GCE, followed by drying in the oven at 60°C.

Table 2.3: Summary of amounts of modifiers (2 mg of each) dispersed in different solvents in preparation for electrode surface modification.

Modifier	Solvent	Volume/ mL	Concentration/ mg/mL
QDs	H ₂ O	2	1
CoPc	DMSO	2	1
Aptamer	Tris-HCl buffer	2	1
GQDs-CoPc(1)($\pi\pi$)	H ₂ O/DMSO mixture	1	2
NGQDs-CoPc(1)($\pi\pi$)	H ₂ O/DMSO mixture	1	2
gCNQDs-CoPc(1)($\pi\pi$)	H ₂ O/DMSO mixture	1	2
CoPc(1)@Aptamer	H ₂ O/DMSO mixture	1	2
GQDs@Aptamer	H ₂ O	1	2
gCNQDs@Aptamer	H ₂ O	1	2
gCNQDs@Aptamer-CoPc(1) ($\pi\pi$)	H ₂ O/DMSO mixture	1	2
gCNQDs@Aptamer-CoPc(2) ($\pi\pi$)	H ₂ O/DMSO mixture	1	2

2.6.2 Electrodeposition and self-assembly, Scheme 4.2 (a)

The modification of GCE using gold nanoparticles was achieved by electrodeposition using literature methods [165] as follows: A de-aerated solution of 1 mM HAuCl₄ in 0.1 M NaNO₃ was cycled at a scan rate of 50 mV/s for 10 scans from 1 V to 0 V. The resulting GCE-AuNPs was then activated using 0.5 M H₂SO₄ by scanning the electrode from 0.2 V to 1.4 V for another 10 scans. The GCE-AuNPs-Aptamer was obtained by immersing the GCE-AuNPs in the aptamer solution (2 mL, 1.0 μ M) stirring for 24 h,

at room temperature to allow for the self-assembly of the aptamer at the electrode surface forming the N-Au bond [166].

2.6.3 Electrografting and click chemistry, Scheme 4.2 (b, c)

First the bare GCE surface was grafted onto the bare using 4-azidobenzene diazonium tetrafluoroborate (Scheme 4.2(b)) by reductive electrodeposition by scanning three cycles from -1.0 V to 0.2 V at 50 mV/s in a 1 mM solution of the diazonium salt (1 mM in 0.1 M TBABF₄ in 96 % ACN: 4 % HCl (0.1M)), following literature methods [167-169] to give the grafted GCE. For the electrode containing AuNPs, the AuNPs were first electrodeposited on the GCE as stated above, followed by grafting azidobenzene diazonium salt onto the AuNPs, to give grafted GCE-AuNPs. The grafted GCEs were then rinsed thoroughly with milli-Q water. The grafted electrodes were then further modified with CoPc(2) using click chemistry as reported in literature [170] by immersing them in 5 mL DMF containing alkynyl CoPc(2) (1 mM), triethylamine (10 mM) and Cu(PPh₃)₃Br (2 mM) for 18 h at room temperature, Scheme 4.2 (b) and (c). The electrodes were thoroughly rinsed using milli-Q water and are represented as GCE∅CoPc(2) and GCE-AuNPs∅CoPc(2), where ∅ represents the clicking step. The GCE∅CoPc(2)-Aptamer and GCE-AuNPs∅CoPc(2)-Aptamer were obtained by immobilizing the aptamer on the GCE∅CoPc(2) and GCE-AuNPs∅CoPc(2) using the drop and dry method (Scheme 4.2 (b) and (c)), using aptamer at 5 μL of 1.0 μM.

2.7 Electrode and solution preparation for detection of PSA

Regarding the detection of PSA using EIS and DPV, the modified electrodes were first incubated for 2 h in a 2 μM PSA solution in 10 mM phosphate buffer solution of pH

7.4 at room temperature after which the impedance measurements were performed. For concentration studies using EIS and DPV, the stock solution was further diluted to produce samples with concentrations ranging from 1.2 to 2.0 μM . The electrodes used for concentration studies were also incubated in each solution prior to EIS and DPV measurements being recorded.

3. Characterization

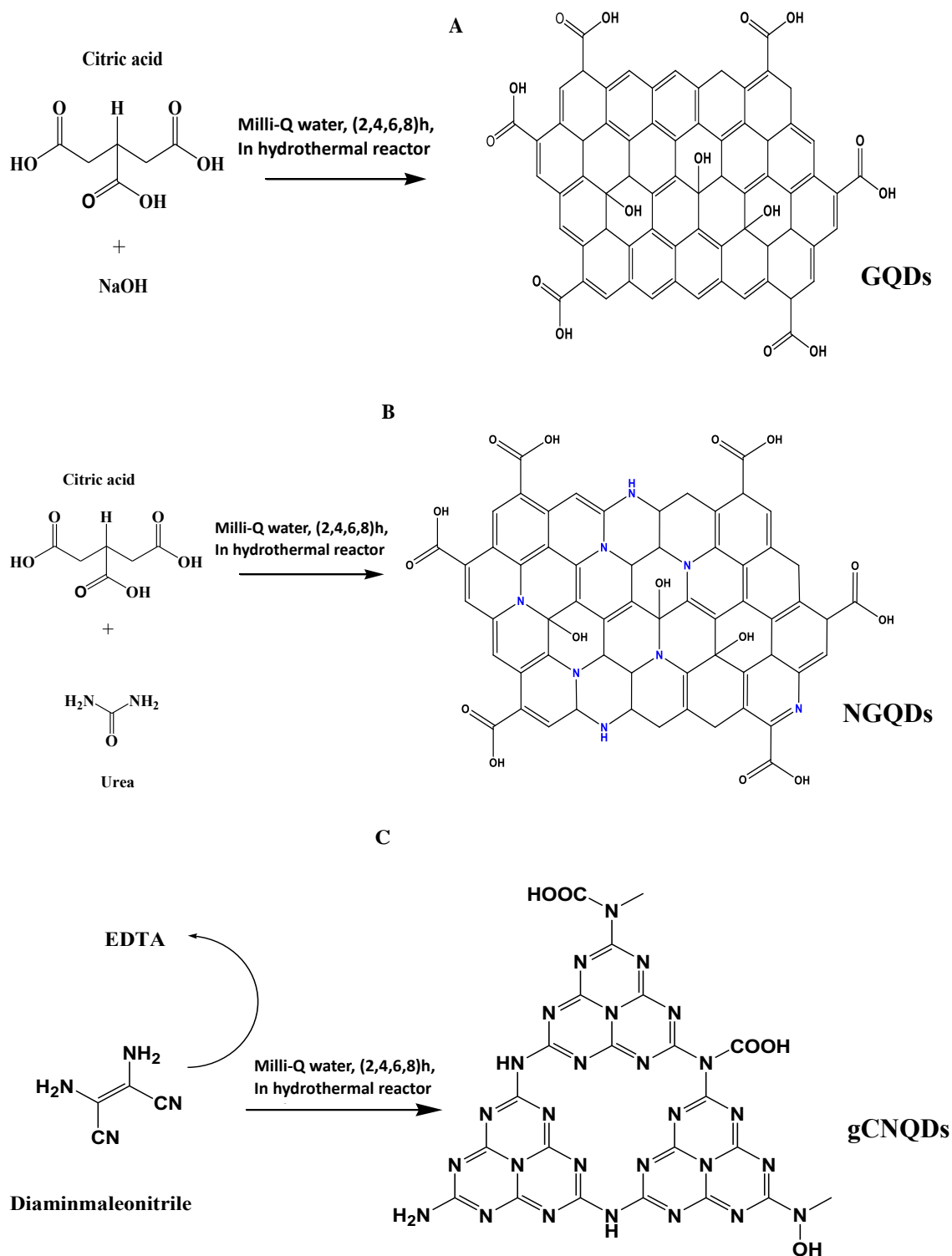
This chapter outlines the characterization of nanomaterials, MPCs and their conjugates employed in this thesis. Schematics of protocols followed are shown for illustration purposes.

3. General introduction

Initial studies showed the synthesis of quantum dots following literature protocols which resulted in sample batches that produced aggregated, polydispersed samples which would not be very suitable for further uses. An in-depth study was therefore conducted by varying one parameter (the synthesis time), to determine the synthesis duration that would produce a less polydispersed, less aggregated QDs sample batches. Thereafter, two novel phthalocyanine molecules (denoted as complexes 1 and 2) were synthesized using methods already reported and these were combined with the QDs by $\pi\pi$ interactions. These complexes were also covalently linked to the amine-functionalized aptamer via amide coupling. At each step of the design and synthesis of the GQDs and phthalocyanines, and their conjugation along with the aptamer, in-depth characterization was performed in solid state or in various solutions: to determine the best synthesis protocols and functionalized tools for further applications as aptasensors. The aptamer used had a sequence as follows: single stranded DNA (ssDNA): 5'-NH₂-(CH₂)₆-TTT TTA ATT AAA GCT CGC CAT CAA ATA GCT TT-3' (235 nmol, >90% purity).

3.1 Synthesis and characterization of GQDs, NGQDs and gCNQDs

The synthesis pathways of the three different metal-free quantum dots reported herein is shown in Scheme 3.1. The unique parameter that was varied was the reaction time, either 2, 4, 6 or 8 hours. The nanostructure batches were characterized using various techniques, which verified the success of the synthesis as well as their general structure and present functional group.



Scheme 3.1: Optimized synthetic route of (A) GQDs (B) NGQDs and (C) gCNQDs and their proposed theoretical structures.

3.1.1 Dispersity and size distribution

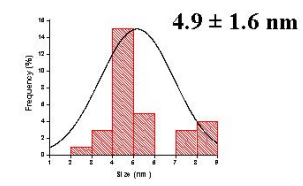
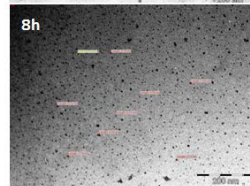
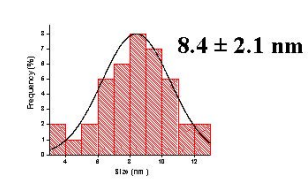
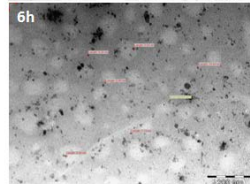
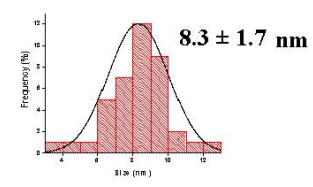
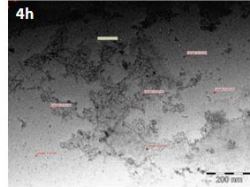
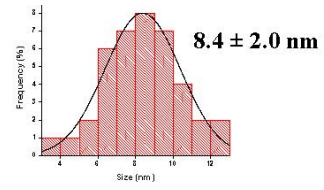
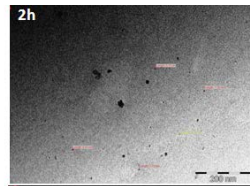
Transmission electron microscopy (TEM) and Dynamic Light Scattering (DLS) studies were employed to determine the dispersity and size distribution of the synthesized QDs.

3.1.1.1 Transmission electron microscopy (TEM) studies

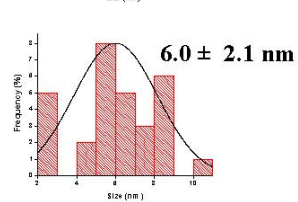
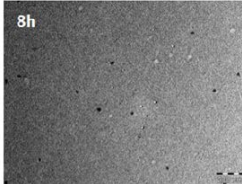
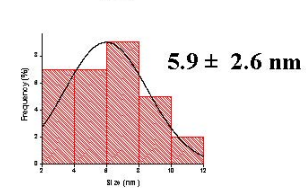
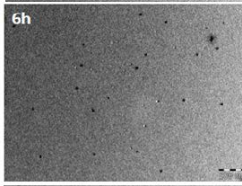
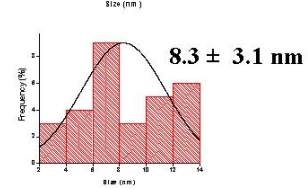
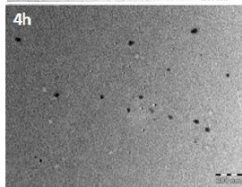
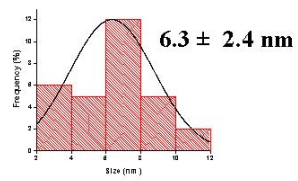
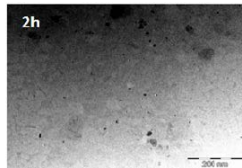
TEM images for all QDs batches were performed to get a visual representation of the dispersity of the nanostructures as well as average diameter.

The size of quantum dots can influence their physicochemical properties and behaviour in different environments and therefore it is important to determine this characteristic [171, 172]. The samples were dispersed in a EtOH: H₂O mixture, 3:1 v/v so partially dissolve the nanostructures which has been, by observation, found to increase the chance of observing QDs under the microscope as compared when dispersed in water alone. They were then dropped on copper grids where they were left to dry prior to conducting the measurements. The obtained images are shown in Figure 3.1 with their corresponding distribution curve and average diameters.

GQDs



NGQDs



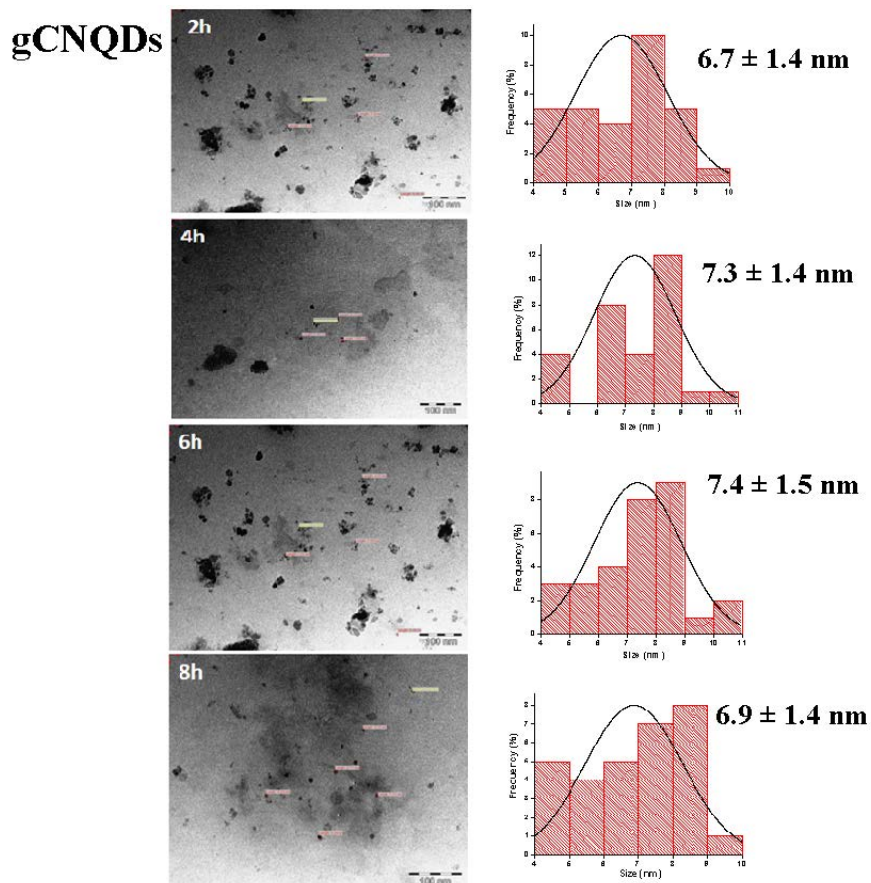


Figure 3.1: TEM images with corresponding distribution curve of GQDs, NGQDs and gCNQDs at different synthesis times. Samples prepared in EtOH: H₂O mixture (50:50) then drop-casted on a copper grid for analysis. The scale bar is at 100 nm.

For the GQDs produced after 2 and 4 h reaction times, a mixture of non-aggregated and aggregated particles was observed, making it difficult to measure the diameters. The distribution curves represent the non-aggregated particles population. At 6 h synthesis time, a better dispersity of particles was observed but there was still an occurrence of aggregation making it difficult to measure all particles in the image. The particle sizes did not vary significantly for 2 h, 4 h, 6 h synthesis times, with an average diameter being determined as of 8.4 ± 2.0 nm, Table 3.1. At a synthesis time of 8 h however, a clear spatial distribution of the GQDs is observed with an

average diameter of 4.9 ± 1.6 nm. Upon doping the pristine QDs with nitrogen atoms (NGQDs), the TEM images obtained show similar spatial distribution across all synthesis times, with minimal aggregation. The average diameters of 6.3 ± 2.4 nm at 2 h, 8.3 ± 3.1 nm at 4 h, 5.9 ± 2.6 nm at 6 h and 6.0 ± 2.1 nm at 8 h synthesis time were determined, Table 3.1.

The TEM images for gCNQDs showed aggregation of the samples at 2h, 4h and 6 h reaction times. After 8 h synthesis time, there is improved dispersity of the particles with an average diameter of 6.9 ± 1.4 nm, Table 3.1. It is evident that the optimization of the synthesis achieved by changing the synthesis time affected the dispersity and average diameters of the QDs.

From the above results, the GQDs, NGQDs and gCNQDs batches that may be pre-selected are those synthesized at 8 h, 6 h and 6 h respectively due to the small measured diameters and good observed spatial dispersion.

Table 3.1: Summary of DLS sizes and polydispersity indices (PDI) of synthesized quantum dots in water. Values in brackets are sizes from TEM.

QDs/Size (nm)	2 h	PDI	4 h	PDI	6 h	PDI	8 h	PDI
GQDs	13.5(8.4)	0.94	7.5 (8.3)	0.85	6.5 (8.4)	0.71	4.9 (4.9)	0.52
NGQDs	8.7 (6.3)	0.58	6.5 (8.3)	0.98	7.5 (5.9)	0.51	8.7 (6.0)	0.96
gCNQDs	2.0 (6.7)	0.49	11.7 (7.3)	0.63	10.1 (7.4)	0.62	13.5 (6.9)	0.65

3.1.1.2 Dynamic Light Scattering (DLS) studies

DLS was also employed in order to determine the hydrodynamic size distribution of the synthesized QDs. Contrary to TEM, these experiments are performed in solution, which can help provide the hydrodynamic radius as well as extent of aggregation in solution. As quantum dots are known to be well dispersed in water, each QDs sample was dissolved in water and sonicated to ensure homogeneity in solution. Figure 3.2 shows the DLS plots of each type of QDs samples after 2 h, 4 h, 6 h and 8 h synthesis with the particle sizes as well as the polydispersity index (PDI) values summarized in Table 3.1. For the GQDs, a decrease in the hydrodynamic radius is observed as the reaction time is increased, as well as a decrease in polydispersity indices, leading to a value close to 0.5 for 8 h, which is in accordance with what was observed in TEM. At 8 h synthesis time, the radius obtained in DLS and TEM are similar with values of 4.9 nm at the peak maxima in DLS and 4.9 ± 1.6 nm in TEM. The measurements in DLS should be higher however, due to the hydrodynamic radius which suggests that there is likely some aggregation in the TEM sample. The results obtained for the NGQDs showed no significant trend when correlating the reaction times with the particle sizes, which is in agreement with the TEM experiments. For gCNQDs, the lowest size and PDI are measured after 2 h reaction time. However, the diameter determined using TEM at 2 h synthesis is larger than that obtained from DLS experiments, which is an indication of possible aggregation. Therefore, the optimization of the synthetic routes by varying the synthesis time did result in changes of size and polydispersity.

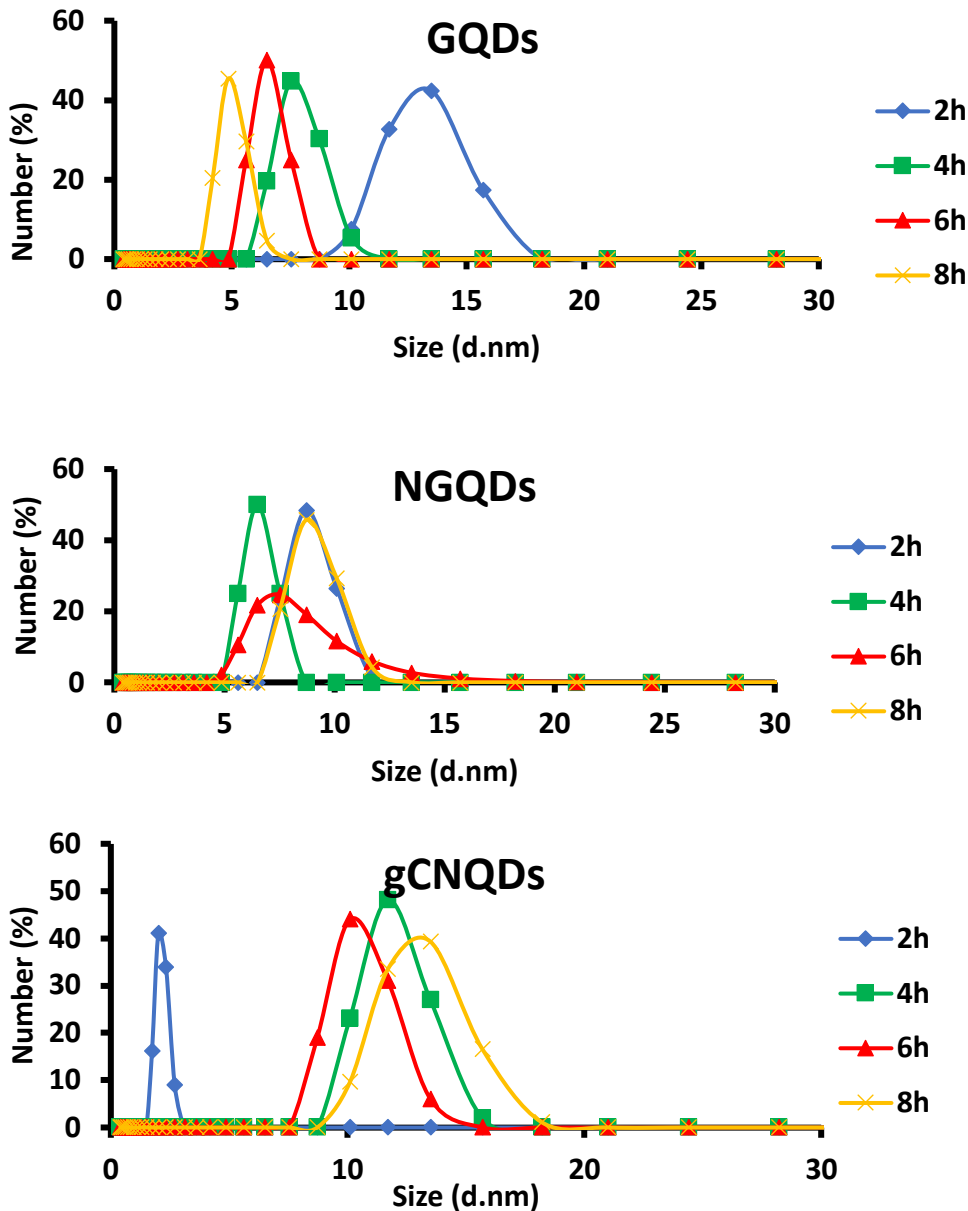


Figure 3.2: DLS plots for GQDs, NGQDs and gCNQDs dispersed in water and sonicated to promote solubilization (2mg/mL).

In conclusion, the samples that would seem preferable for further use and study would be the GQDs synthesized at 8 h synthesis, due to their lower polydispersity index, and low aggregation state visualized by TEM. Although there was no trend between the NGQDs samples, the batch synthesized at 6 h showed the lowest polydispersity index which is ideal for further applications. As already mentioned,

the gCNQDs had the lowest size and PDI values measured by DLS after 2 h reaction time. However, the diameter determined using TEM at 2 h synthesis is larger than that obtained from DLS experiments, which is an indication of possible aggregation. The next best batch therefore would be the batch synthesized at 6 h which has the lower PDI value as well as the second lowest diameter measured in DLS.

3.1.2 Elemental composition and structure

For the determination of elemental composition of the QDs, Energy dispersive X-ray (EDX) analysis was employed. Raman spectroscopy and Fourier-Transform Infra-red (FTIR) spectroscopy analysis provided structural information regarding present bonds as well as functional groups.

3.1.2.1 Energy dispersive X-ray (EDX) analysis

Figure 3.3 shows the obtained EDX results for the three QDs at the four synthesis reaction times. This technique is a qualitative measure providing the elemental composition of samples. The expected elements were carbon and oxygen for the three QDs structures and nitrogen for NGQDs and gCNQDs, which were effectively observed in the results obtained. These findings are therefore consistent with pure samples and an efficient synthesis.

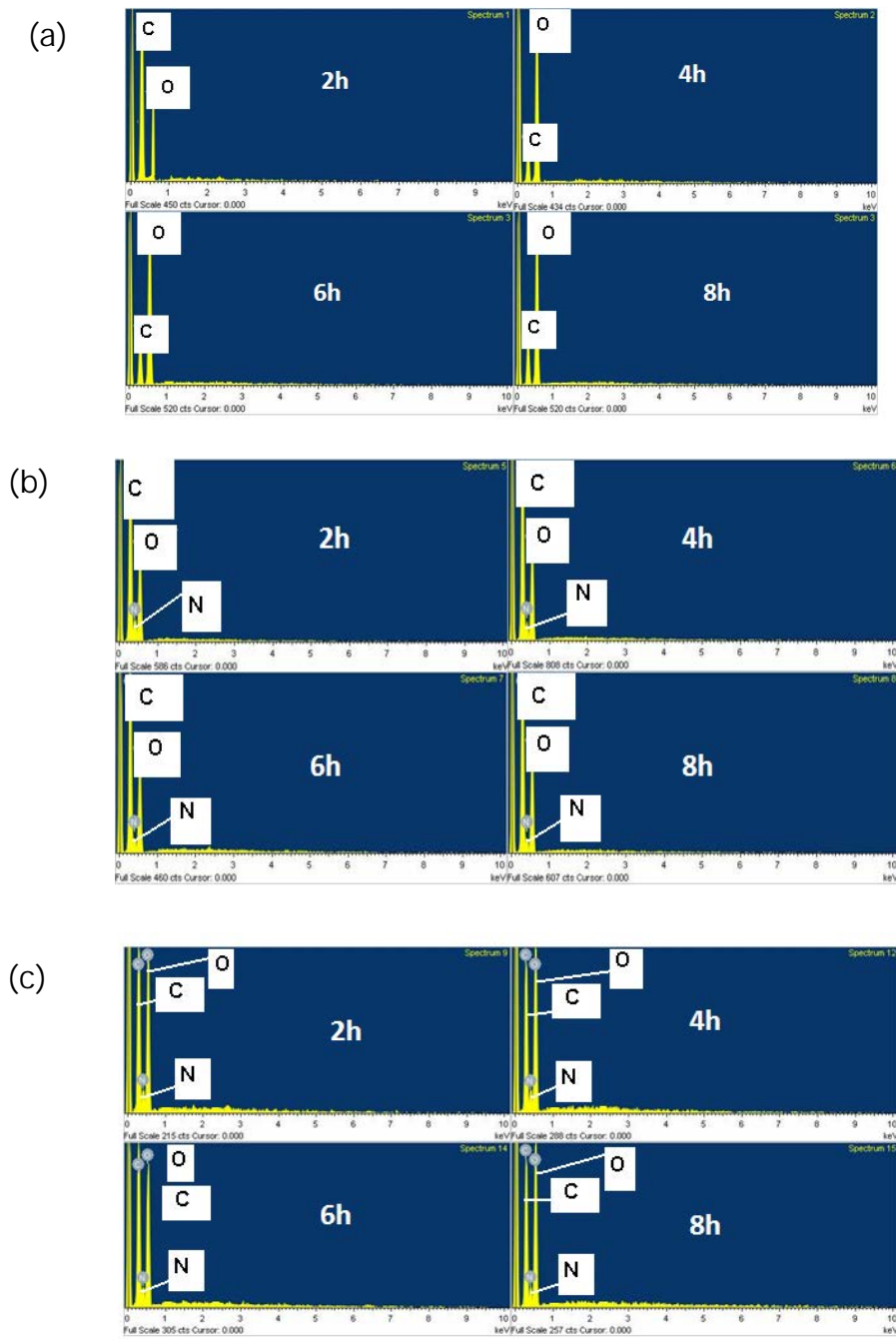


Figure 3.3: EDX spectra for (a) GQDs, (b) NGQDs and (c) gCNQDs at 2,4,6 and 8 h synthesis.

3.1.2.2 Raman spectroscopy analysis

Raman spectroscopy was employed to prove the presence of structural differences between pristine GQDs and its derivatives. Pristine GQDs are used as a reference for the NGQDs and gCNQDs as they ideally have a graphitic structure with no additional elements that could cause defects to the original structure [173]. The peaks of interest in Raman spectra are the disorder (D) sp^3 and graphitic (G) sp^2 peaks from in plane vibrations, which were observed for GQDs, gCNQDs and N-GQDs (Figure 3.4).

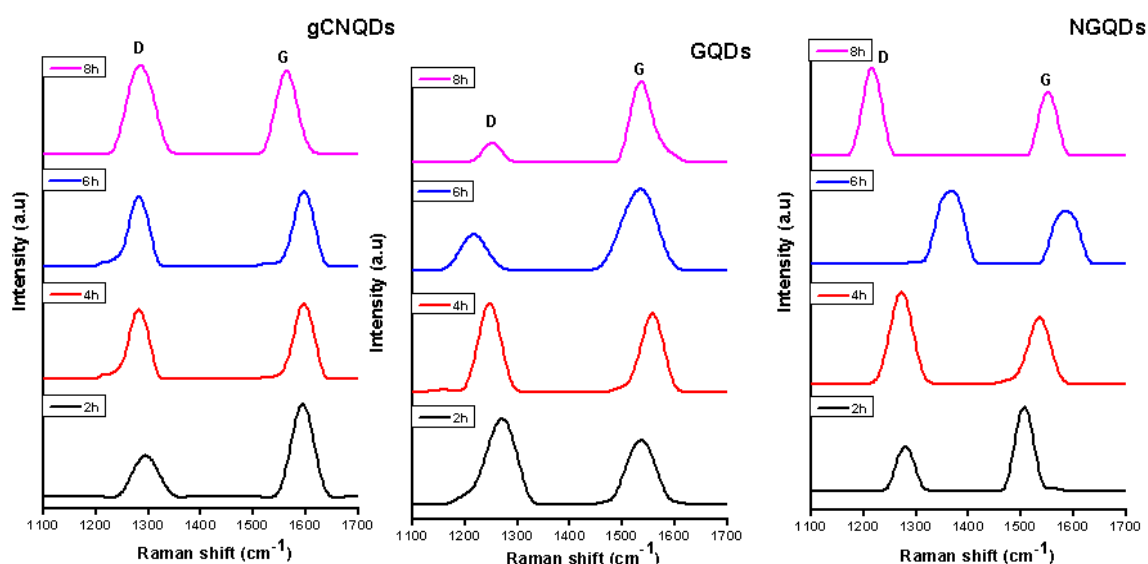


Figure 3.4: Raman spectra of synthesized GQDs, NGQDs and gCNQDs in solid state.

From these results, the $I_D : I_G$ ($sp^3 : sp^2$) ratios are calculated using peak areas, which determine the extent of functionalization of the carbon nanomaterials or introduction of heteroatoms in the pristine structure. Noticeable patterns were observed in the $I_D : I_G$ ($sp^3 : sp^2$) ratio of each type of quantum dots sample analyzed while varying the synthesis time, Table 3.2.

For the GQDs, the ratios decrease with increasing synthesis time. This is expected as it implies that with time, there is an increase in the spatial distribution of the π -conjugated structure and an increase of sp^2 carbons. The shift in wavenumber as well as decrease in intensity of the D band at 6 h and 8 h also indicates a structural change meaning with time, there are changes occurring. Pristine GQDs are used as a reference for the NGQDs and gCNQDs as they ideally have a graphitic structure with no additional elements that could cause defects to the original structure [173]. In the case of the NGQDs, the D and G bands were slightly shifted in terms of wavenumber compared to the pristine GQDs, Table 3.2. These shifts are likely due to the defective nature caused by the presence of nitrogen atoms introduced into the lattices and stretching of the graphene layers [174]. The ratios obtained for NGQDs increase with increasing synthesis time indicating an increase in the extent of doping with the nitrogen atoms. This also means there is a decrease in the spatial distribution of sp^2 carbons as the N atoms are added into the lattice structure. The longer the synthesis takes place, the greater the extent of doping of the graphene structure, resulting in greater spatial disorder.

For the gCNQDs, the ratios also increase with increasing synthesis time, indicating the presence of more triazine groups forming as the synthesis time is increased. Compared to the pristine GQDs, the D and G bands were observed in similar regions. These results are a clear indication of the QDs structural dependence on the duration of the synthesis.

Table 3.2: Summary of Raman stretches of D and G bands and I_D/I_G ratios. Analyses run in solid state.

Synthesis time	D band cm^{-1}		G band cm^{-1}	$I_D:I_G$
GQDs				
2h	1275		1525	1.33
4h	1250		1550	1.14
6h	1220		1525	0.34
8h	1250		1525	0.17
NGQDs				
2h	1280		1500	0.56
4h	1280		1550	1.33
6h	1375		1600	1.50
8h	1225		1560	1.56
gCNQDs				
2h	1300		1590	0.50
4h	1300		1590	0.83
6h	1300		1590	0.83
8h	1280		1550	1.31

3.1.2.3 Fourier-Transform Infra-Red (FTIR) spectroscopy analysis

FTIR provides information on the bonds present within each GQD structure, and for instance the functional groups the QDs possess. Figure 3.5 presents the spectra of the three GQDs at the four reaction times.

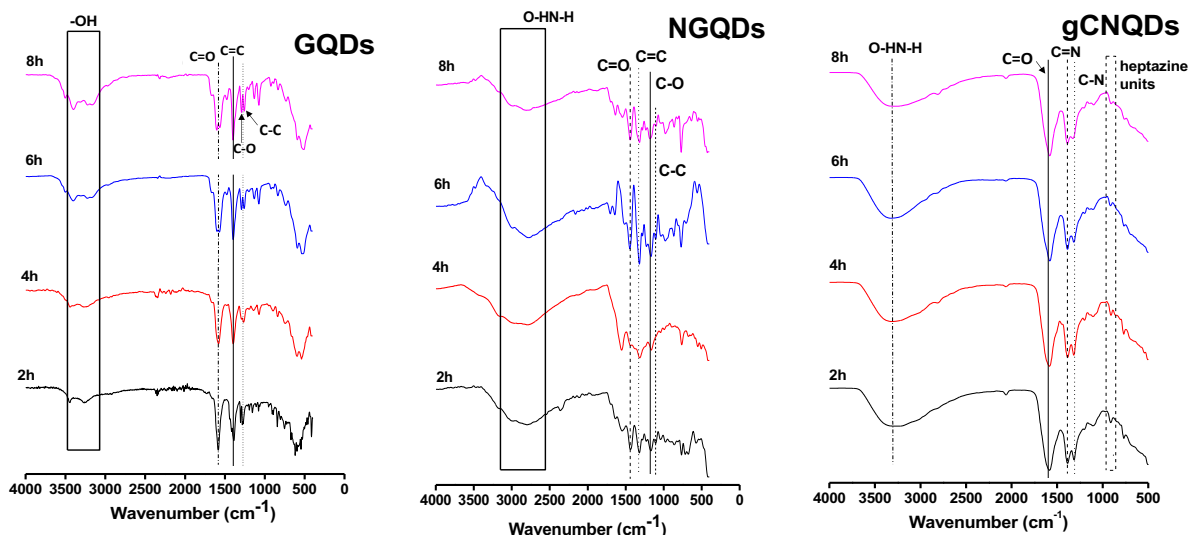


Figure 3.5: FTIR spectrum of GQDs, NGQDs and gCNQDs synthesized at varying times for optimization of synthetic routes. Analyses run in solid state.

The spectra of GQDs show the presence of different vibrational peaks characteristic of these nanostructures. Vibrations observed between 3000-3500 cm^{-1} , are typical of the O-H vibration [51]. The vibrations at 1250 cm^{-1} and 1262 cm^{-1} are attributed to the C-C and C-O bonds respectively, and the vibration at 1430 cm^{-1} is characteristic of the C=C bond. The vibration identified at 1620 cm^{-1} characterizes the C=O bond which confirms the presence of the expected carboxylic acid groups as well. The spectra of the NGQDs are characterized by vibrations observed in regions of 2500-3500 cm^{-1} which is a broader window compared to GQDs. These vibrations are typical of the O-H/N-H vibration. At 1400 cm^{-1} and 1430 cm^{-1} are the C=O and C=C vibrations respectively and at 1210 cm^{-1} and 1125 cm^{-1} are vibrations due to C-O and C-C respectively. These findings also correspond to those reported in literature [175]. As stated in the introduction, the gCNQDs have a different base structure compared to the other quantum dots. Therefore, there will be differences

in the FTIR spectrum of these nanostructures. Vibrations observed at around 774 cm^{-1} are characteristic of the heptazine units, which the other quantum dots do not possess. At 1415 cm^{-1} and 1315 cm^{-1} vibrations are characteristic of the C=N and C-N bonds respectively as the structure of these quantum dots is predominantly nitrogen based and the 1627 cm^{-1} stretch is characteristic of the C=O of the carboxylic acid groups. Finally, the broad peak between 2750 and 3750 cm^{-1} is characteristic of the N-H/O-H groups. Literature reports also show similar findings and therefore in agreement with the peak assignments made in this work [176, 177]. These results confirm the presence of the expected functions on each of the three QDs synthesized herein.

3.1.2.4 X-ray photoelectron spectroscopy (XPS) analysis

XPS is another technique that provides information on the types of bonds and atoms present in the molecular structure, which allows for the determination of extent of functionalization. The wide scan analyses allow for the determination of the general elemental composition of the sample. Thereafter, the peaks due to the elements of interest are deconvoluted in order to determine the exact bonds that exist within the structure and what functional groups are present. Figure 3.6 shows the wide scans for all the synthesized dots at 2 h, 4 h, 6 h and 8 h reaction times. These survey scans confirm the presence of the expected elements comprised within the QDs structures.

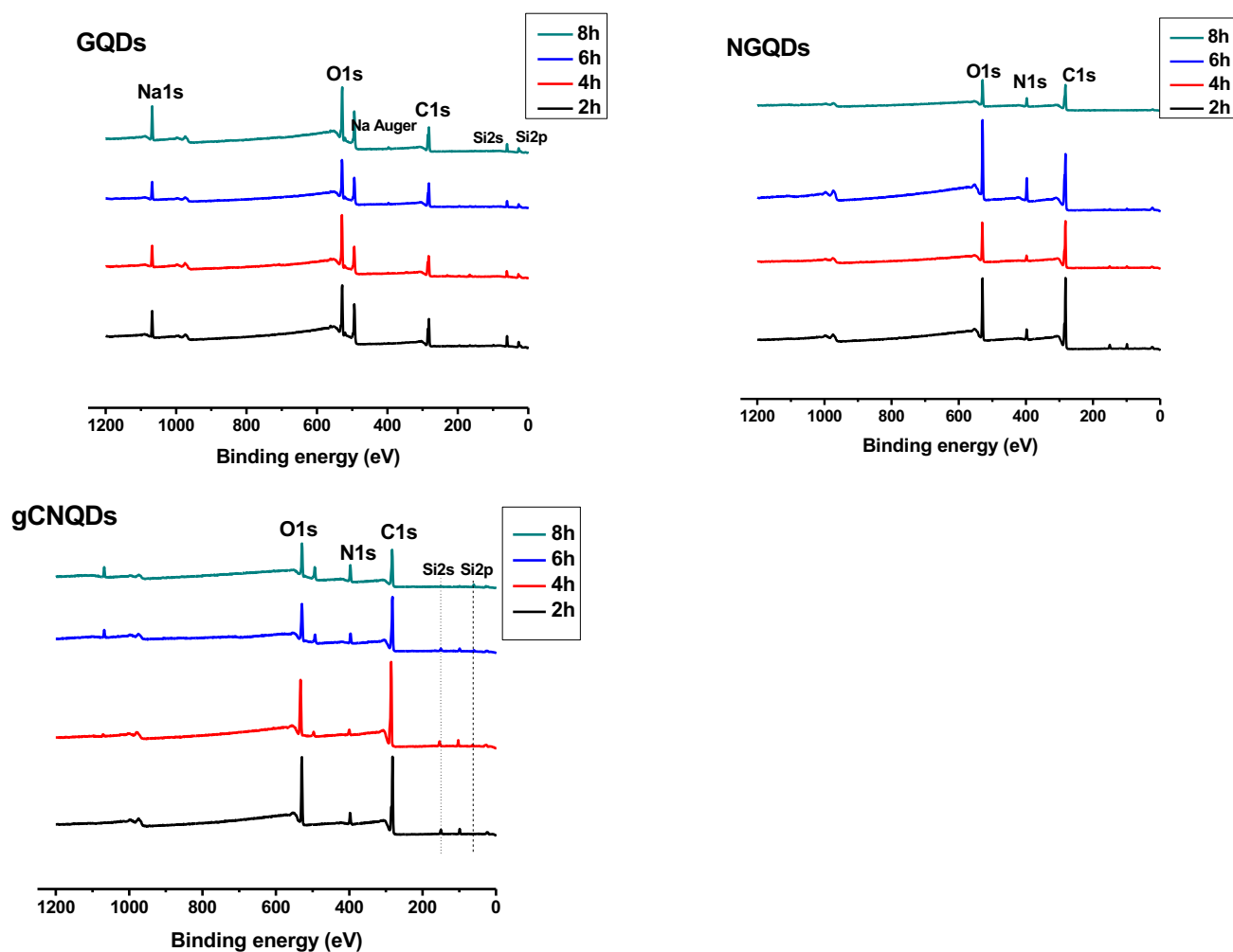


Figure 3.6: XPS wide scans of GQDs, NGQDs and gCNQDs.

For GQDs, the expected carbon (C1s) and oxygen (O1s) peaks were observed with an additional sodium (Na) peak, probably due to excess NaOH used during synthesis. It is unclear where the silica peaks come from as there is no silica used in the starting materials and no silica was observed in the EDX spectra already discussed. Therefore, the assumption is that the impurity was picked up during XPS analysis. High-resolution scans were then obtained and deconvoluted and the results are summarized in Table 3.3. The C1s spectra were deconvoluted in order to confirm

which other atoms the carbon atoms were bonded to, as well as to prove the presence of the -COOH groups. At all GODs synthesis times, three peaks were observed at binding energies of about 294 eV, 292 eV and 290 eV corresponding to C=C/C-C which are the sp^2 and sp^3 carbons respectively, C-O which are the sp^3 carbons and C=O, Table 3.3(a). The C-O and C=O peaks also confirm the presence of -COOH groups [176]. While varying the synthesis time, no effect on the binding energies was observed. For the NGQDs samples, the wide scans only showed peaks corresponding to the nitrogen (N1s), carbon (C1s) and oxygen (O1s) with no peak due to possible contaminants. The C1s (Table 3.3(a)) and N1s (Table 3.3(b)) peaks were further analyzed by plotting and deconvoluting the high-resolution scans. Under the C1s scan, three prominent peaks were observed at binding energies of 286 eV, 284 eV and 282 eV corresponding to O-C=O, C-N/C=N and the sp^2 hybridized C-C/C=C [176]. For the high resolution N1s scan, four peaks were observed at binding energies of 401 eV, 400 eV, 399 eV and 398 eV corresponding to N-C=O, N-H, C=N and C-N-C bonds [176]. Thus, for the NGQDs the synthesis time did not affect the binding energies of the peaks. The wide scans for the gCNQDs show the expected O1s, N1s and C1s peaks. Very weak signals corresponding to Si are observed. However, no Si was used in the synthesis of the QDs indicating that this contamination did not come from these nanostructures. The deconvoluted C1s scans of the gCNQDs samples synthesized at 2h, 6h and 8h revealed three peaks at binding energies of 294 eV, 293 eV and 291eV which correspond to C-O, C=N and C-C/C-N respectively. The binding energies of the peaks observed for the sample at 4h synthesis time were observed at 289 eV, 287 eV and 285 eV. The same trend is observed for the N1s deconvoluted scans where for, the samples obtained at 2h, 6h and 8h synthesis time, peaks were observed at binding energies of 399 eV, 397 eV and 396 eV corresponding to C-N-H,

$N(C)_3$ and $C-N=C$ [160]. For the sample reacted for 4h, the peaks were observed at 390, 401 and 404 eV. The peak at 404 eV corresponds, according to reported works [178], to N-oxide, the charging effects in the cyano group and heterocycles or π -excitations, 401 eV corresponds to the quaternary nitrogen bonded terminal amino group (C-H-N) and 399 eV corresponds to the tertiary nitrogen bonded to carbon atoms in the form of $N(C)_3$ bonds.

These results confirmed the presence of the synthesized quantum dots in greater details than FTIR did, providing more information on the structural formation of these nanostructures.



Table 3.3(a): **C1s** deconvoluted peak assignments (binding energy/BE) of GQDs, NGQDs and gCNQDs.

GQDs	C=C/C-C	C-O	C=O
2-8h	294	292	290
NGQDs	O-C=O	C-N/C=N	C-C/C=C
2-8h	286	284	282
gCNQDs	C-O	C=N	C-C/C-N
2h, 6h, 8h	294	293	291
4h	289	287	285

Table 3.3(b): **N1s** deconvoluted peak assignments of NGQDs and gCNQDs.

NGQDs	N-C=O	N-H	C=N	C-N-C
2-8h	401	400	399	398
gCNQDs	C-N-H	N(C)₃	C-N=C	-
2h, 6h, 8h	399	387	396	-
	N-oxide	C-H-N	N(C)₃	-
4h	404	401	399	-

Moreover, the percentage of oxygen and carbon present in the GQDs, NGQDs and gCNQDs synthesized at 2, 4, 6 and 8 h were also determined (Table 3.4). For the GQDs and NGQDs samples, there was no trend observed that could help in differentiating the structures at the different synthesis times. However, the gCNQDs showed an increase in percentage of oxygen and a decrease in percentage of carbon, as synthesis time increased. This may imply an introduction of more triazine groups within the gCNQDs structure as well as more -COOH groups in the periphery.

Table 3.4: Summary of % Oxygen and Carbon present in the GQDs, NGQDs and gCNQDs synthesized at 2, 4, 6 and 8 h.

Synthesis time	Atomic conc. % Carbon	Atomic conc. % Oxygen
GQDs		
2h	55.51	44.49
4h	63.09	36.91
6h	51.77	48.23
8h	60.25	39.75
NGQDs		
2h	73.80	26.20
4h	76.90	23.10
6h	66.42	33.58
8h	72.96	27.04
gCNQDs		
2h	83.75	16.82
4h	81.07	18.93
6h	80.67	19.33
8h	75.88	24.12

3.1.3 Dispersity, charge density and colloidal stability

Zetametry was used to determine the charge density and colloidal stability of the QDs in solution. Capillary electrophoresis (CE) allowed for an electrophoretic separation of the batches, prior to UV or MS detection. CE provides information on the colloidal stability of the batches, the dispersity of the QDs as well as the ratio surface charge/size.

3.1.3.1 Zeta potential (ζ) determination

Zetametry provides information on the charge density of the QDs in solution, which relates to their surface functionalization as well as their colloidal stability in solution [179]. In other words, the higher the zeta potential value, the more stable the particles are in solution. Water was used as the analysis medium. The obtained data is summarized in Table 3.5 alongside the mobility obtained from the zetametry instrumentation.

Table 3.5: Summary of Zeta (ζ) potential data and mobility of synthesized quantum dots in water.

Synthesis time	Zeta (ζ) potential/mV	Mobility/ $10^{-4} \text{ cm}^2 \cdot \text{V}^{-1} \cdot \text{s}^{-1}$
GQDs		
2h	-20.9	-1.76
4h	-26.4	-1.70
6h	-27.6	-1.61
8h	-30.1	-1.71
NGQDs		
2h	-18.4	-1.54
4h	-19.7	-1.60
6h	-24.5	-2.76
8h	-37.5	-3.02
gCNQDs		
2h	-31.8	-2.50
4h	-33.2	-2.60
6h	-40.0	-3.14
8h	-26.1	-2.0

The literature reports a pKa value of 4.3 for COOH near -OH in graphene oxide (GO) [180] and 5.2 for -NH₂ [181]. These values are low suggesting overall negatively charged nanostructures. All synthesized quantum dots were negatively charged at all synthesis times in the -18 to -40 mV range (Table 3.5) which is therefore expected. For the QDs and NGQDs, there is a tendency of increasing zeta potential values with extended synthesis time which implies more COOH when reaction time increases for the QDs and more COOH compared to NH for the NGQDs. When these functional groups are deprotonated, they generate an overall negative charge. Whereas QDs and NGQDs present equivalent values, the zeta potential for gCNQDs is in a higher range, which can be correlated to the different composition of this QDs, and a possible higher functionalization at the QDs surface.

The lower negative value at 8h synthesis is however unexpected. This could be caused by aggregation if the NH₂ groups are protonated while COOH or OH groups deprotonated in this sample (but also for NGQDs). Indeed, the classical proposed structure in the literature of gCNQDs contains NH₂ groups at their periphery and possibly COOH or OH groups, Scheme 3.1. The difference with NGQDs could be explained by a less accessible NH function at the periphery.

The negative values obtained in zetametry measurements therefore indicate the presence of negatively charged particles in solution. The QDs appeared stable, especially at 8 h synthesis with the highest zeta potential value which is in agreement with TEM and DLS data. The NGQDs and gCNQDs showed highest zeta potential values at 8 h and 6 h synthesis times respectively which should lead to better stability. The results for the QDs and gCNQDs are in agreement with the samples pre-selected from TEM and DLS data. However, the NGQDs pre-selected in

previous studies were synthesized at 6 h and therefore further characterization will determine which NGQDs batch will be used for further study in CE analysis.

Zetametry analysis also provides mobility measurements which have been recorded in Table 3.5. These measurements are achieved by laser doppler velocimetry [182]. The main differences between this method of determining electrophoretic mobility and that used in CE are the following [182]:

- LDV determination is performed on a microtube composed of polycarbonate or polystyrene with an internal diameter of millimetre scale. The CE determination is carried out on a capillary with an internal diameter of micrometre scale made up of fused silica. This means that the particles being analysed may also interact with the walls of the channel they move through differently.
- LDV measurements are usually made by detecting the phase or frequency shift of an incident laser beam, while the CE is coupled with UV detection for example as done in this work, which is based on optical absorbance.
- In CE, the capillary is filled with a buffer solution of specific ionic strength which affects the overall surface charge of the particles and therefore affects their migration through the capillary.

These differences then are expected to affect the mobility values obtained. The fundamental principal is that of CE where particles with an overall surface charge migrate to the oppositely charged electrode at a given velocity which also relates to particle size. A classical micro-electrophoresis system in this method is a cell with electrodes at either end to which a potential is applied. The values obtained from

the zetasizer will therefore be compared later in the text, with the mobility values determined from CE.

3.1.3.2 Electrophoretic separations and characterization

Capillary electrophoresis (CE) is an electrokinetic method that was proved a powerful analytical tool to separate and characterize nanostructures, allowing for their separation in size, surface charge density and functionalization as well as for understanding their behavior in different environments to allow for further applications [54, 172, 183].

The first GQDs batches characterized by CE were the ones at a 10h synthesis time, which was the classical time for the synthesis, at the beginning of the PhD work. The initial CE separation was performed with UV detection at 200 nm and DMF was used as the neutral marker. Figure 3.7 shows the electropherogram of the GQDs as an example in time scale (other results not shown). Separation was achieved in a 10 mM (ionic strength) sodium carbonate buffer (pH 7.4). As can be seen, a number of populations within the sample batch was obtained indicating a heterogeneity of the sample, i.e., a high polydispersity, different families of GQDs more or less functionalized or possibility of stacking between different sheets of GQDs. The electrophoretic profiles therefore clearly showed that the batches were very polydisperse, and further optimization of the synthesis was undergone in terms of synthesis time.

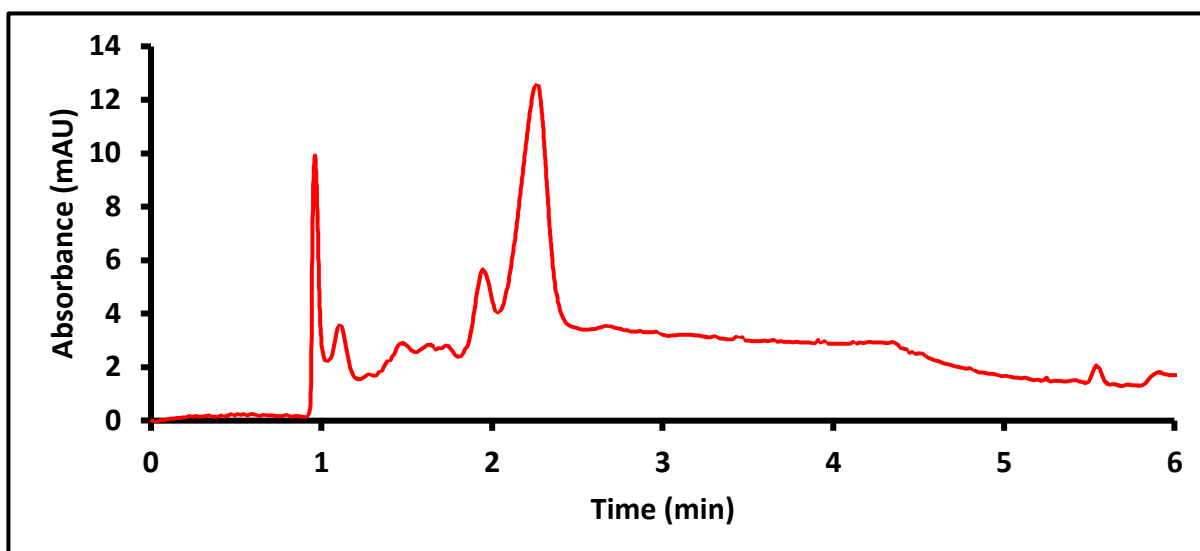


Figure 3.7: Electropherogram of neutral marker and GQDs simultaneous injected, in time scale. Experimental conditions ; hydrodynamic injection (5 s, 50 mbar) of 1 mg.mL⁻¹ synthesis batch sodium carbonate buffer (pH 7.4) ; electrokinetic separation under a -10kV potential in 10 mM Na₂CO₃/NaHCO₃ buffer (pH = 7.4) BGE ; UV detection at 200 nm. Capillary total length = 35 cm; effective length to the detector = 26.5 cm.

From the results obtained after optimizing the synthesis of the QDs, the samples used for further studies throughout this thesis were GQDs 8 h, NGQDs 6 h and gCNQDs 6 h.

The GQDs batch at the above-mentioned synthesis time was chosen as it showed the lower PDI value in DLS which is ideal for CE analysis. It was also clear from the TEM images that this batch is not as aggregated and the particles are fairly homogenous in size compared to the other batches. It also showed a zeta potential value of -30.1 mV at this time which was an indicator of potential better colloidal stability in solution thanks to inter-particle repulsive forces compared to the other batches synthesized for different lengths of time which had less negative values. Note that

by observing with the naked eye, the batches at other synthesis times did not dissolve completely when dispersed in solution which is an indicator of instability (data not shown).

The NGQDs also showed the lowest PDI value and hydrodynamic size in DLS at 6 h synthesis time compared to the other batches and therefore was chosen for further studies. Moreover, in XPS, it showed the highest percentage of oxygen at 6 h synthesis which suggests more COOH groups available for amide bonding in later studies.

Although the gCNQDs showed the lowest PDI value and size in DLS at 2 h synthesis time, the batch synthesized for 6 h was chosen for further studies as it showed the highest value of -40.0 mV in zeta potential measurements. In-solution stability is crucial for further studies and applications. In addition, DLS and TEM were in agreement at these reaction times.

An attempt was therefore made to further characterize the selected QDs by electrophoretic methods, that improve the characterization process by separation of the sample, which was not the case with the previous presented analyses.

In the first step after optimization, the detection was performed by UV-Vis analysis at 200 nm detection wavelength (CE-UV) in a 10 mM ammonium carbonate buffer (pH 7.4). The injection of the sample made of neutral marker and GQDs evidenced peaks overlapping. Therefore, an original injection procedure was developed, where NM and GQDs were injected at the inlet and outlet of the capillary, respectively. Electropherograms are presented in time scale. The conversion from time to mobility (m) can be achieved according to Equation 3.1(a) as follows:

$$m = \frac{l_{eff}L}{Vt_{migration}} \quad 3.1(a)$$

Where l and L are the effective and total capillary length, respectively in cm, V is the applied voltage in volts V and t is the migration time in seconds. The electrophoretic mobility therefore may be determined using Equation 3.1(b) as follows:

$$m_{EP} = m_i - m_{EOF} \quad \mathbf{3.1(b)}$$

Where m_i is the apparent mobility (calculated by Eq.3.1a) and m_{EOF} is the electroosmotic flow or the electroosmotic mobility calculated for the neutral marker using again the Eq. 3.1a.

Fig. 3.8 shows the electropherogram of the QDs as an example. First of all, the peak dispersity was drastically diminished thanks to the synthesis time optimization study.

Then the electropherogram allows to determine the electrophoretic mobility of the QDs as $-7.5 \times 10^{-4} \text{ cm}^2 \cdot \text{V}^{-1} \cdot \text{s}^{-1}$. This negative value is coherent with negatively charged QDs. This value is however higher than the one calculated by zetametry measurements ($-1.7 \times 10^{-4} \text{ cm}^2 \cdot \text{V}^{-1} \cdot \text{s}^{-1}$). This difference, as already mentioned may be caused by the difference in mode of detection, the solutions used for analysis (water for zetametry and BGE for CE) as well as the difference between the microtube and the capillary.

This study by CE allows to go deeper in the validation of the optimization of the QDs synthesis. Compared to the CE results obtained before optimization, the

profile is much more monodisperse, which is coherent with an homogeneous population within the optimized batch which is promising.

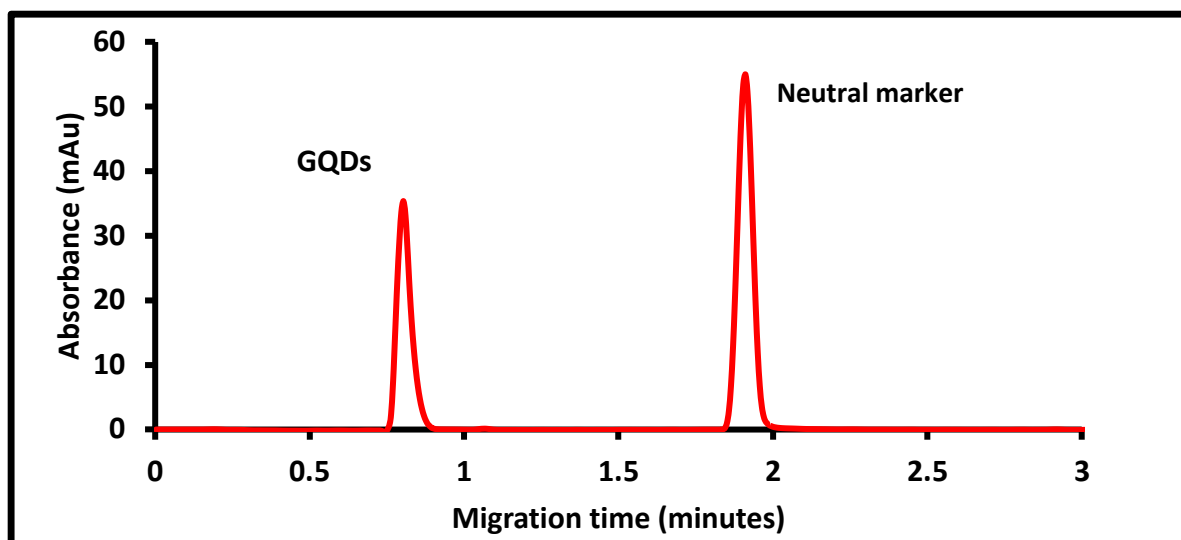


Figure 3.8: Electropherogram of neutral marker and GQDs simultaneous injection. Experimental conditions ; $1 \text{ mg}\cdot\text{mL}^{-1}$ synthesis batch in ammonium carbonate buffer; hydrodynamic injection of neutral marker (paracetamol) through the inlet vial (5s, 50 mbar) and QDs through the outlet vial (5s, 50 mbar); electrokinetic separation under a 18 kV potential in the 10 mM Ammonium carbonate buffer (pH 7,4) BGE ; UV detection at 200 nm ; capillary total length = 35 cm; effective length to the detector = 26.5 cm.

After CE-UV characterization of the QDs, preliminary results were performed while coupling CE to mass spectrometry, via an electrospray interface (CE-ESI-MS). The three types of GQDs were characterized for the first time in CE-ESI-MS in this work. The objective was to determine a more precise structure of the GQDs than the theoretical scheme classically presented in literature (Scheme 3.1). Indeed, after

the successful separation of the QDs in CE-UV, the coupling with MS required further optimization for the efficient separation and detection of the GQDs. This optimization was focused on the parameters of the electrospray ionization (ESI) interface between CE and MS, that allows for sample ionization and transfer to gaze phase, and to make up the difference in fluid velocity between CE and MS, so as to reach sensitive detection. This optimization process was first undergone with paracetamol (further used as neutral marker). The optimized parameters are summarized in Chapter 2 as part of the methods applied to carry out the studies. Then the CE-ESI-MS optimization was undergone with the three GQDs allowing to determine an efficient CE separation and MS detection with nitrogen as nebulizing gas at a temperature of 300 °C (pressure in the 0 to 100 kPa range) and as drying gas at 300 °C (flow rate in the 0 to 8 L/min range). Optimized ESI and skimmer voltage were 3000 V and 10V, respectively. Peak width and dwell time were set to 0.3 min and 880 ms, respectively. The sheath liquid (SL) (50:50 v/v MeOH:H₂O mixture containing 0.01% v/v triethylamine) was delivered by an Agilent 1100 series isocratic HPLC pump (flow rate in the 0-10 mL/min range). Capillaries were rinsed with 0.1 M NH₄OH and water in between runs to remove any particles that could have potentially interacted with the capillary.

As no literature exists for CE-MS GQDs characterization, a first step consisted in the optimization of the MS detection of the compounds via the ESI interface. For this purpose, the sample was injected as a large zone (hydrodynamic injection at 50 mbar for 16 s) and pushed by pressure (50 mbar) till the ESI-MS, so as to estimate the MS sensitivity for these GQDS.

So as to optimize the detection sensitivity, the effect of pH was one of the parameters studied as it plays a role in the surface charge of the nanostructures in solution and therefore their electrophoretic mobility, which can lead to separation and ionization differences, that can improve their MS detection. The pH range was chosen as 7 to 10 . Figure 3.9 shows the electropherograms obtained in these experimental conditions at increasing pH from 7 to 10, and the MS spectra in scan mode are presented at each pH. The mass to charge ratios below 1000 were observed when injecting the BGE alone. Above $m/z = 1000$, an attempt could be made to assign the m/z values to possible QDs populations/structures. The ion mass spectra observed however, are of low intensity which may indicate poor ionization of the nanostructures thus making it difficult to deeply characterize the batches.

The mobilization of the QDs in the capillary by pressure can provide profiles that depend on differences in their diffusion coefficient along with the phenomenon of dispersion due to the large zone injected.

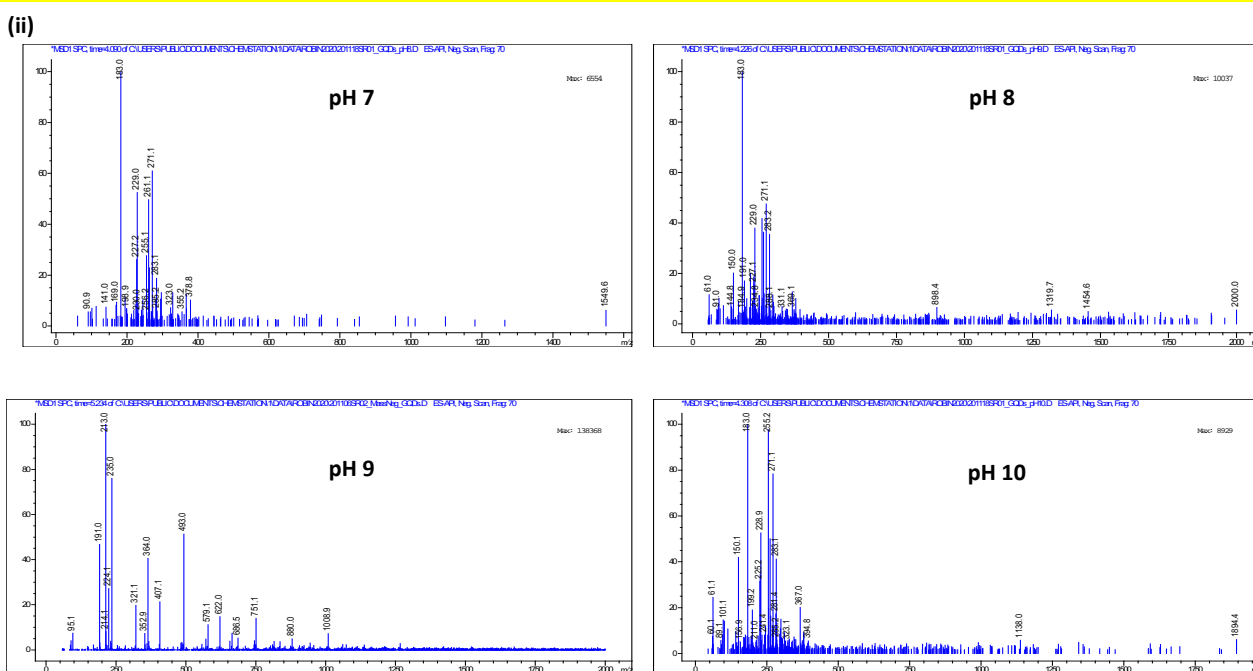
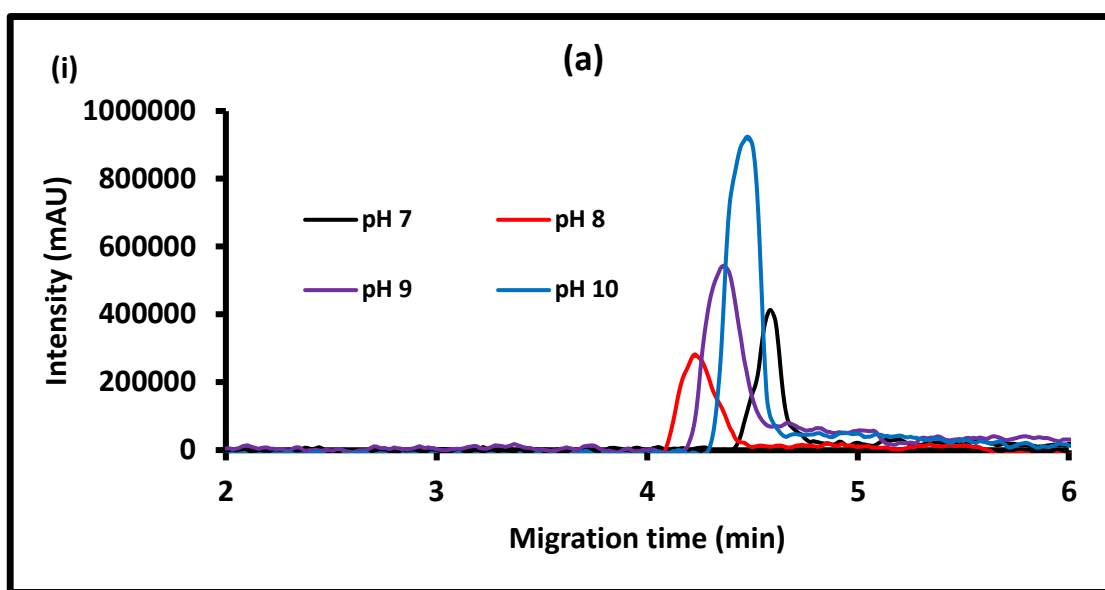
The three types of QDs are detected in the same range of time (4-6 minutes) in the four pHs studied. For each QD, the difference according to pH of the BGE does not seem significant, probably due to the low pressure value applied for QDs mobilization.

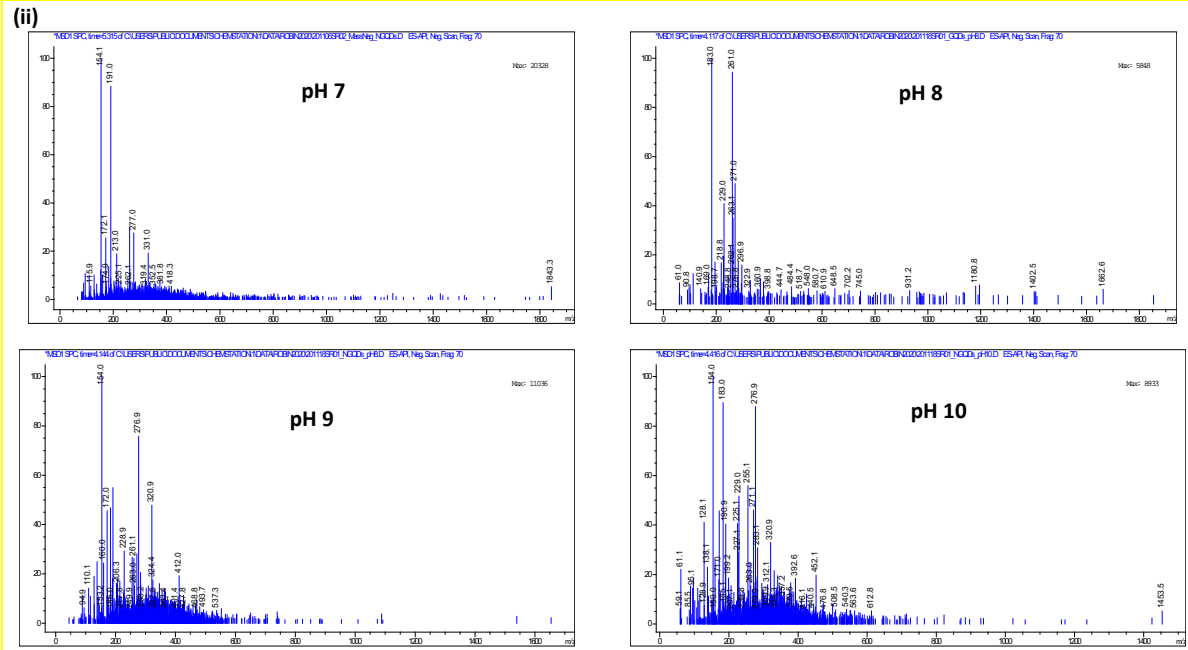
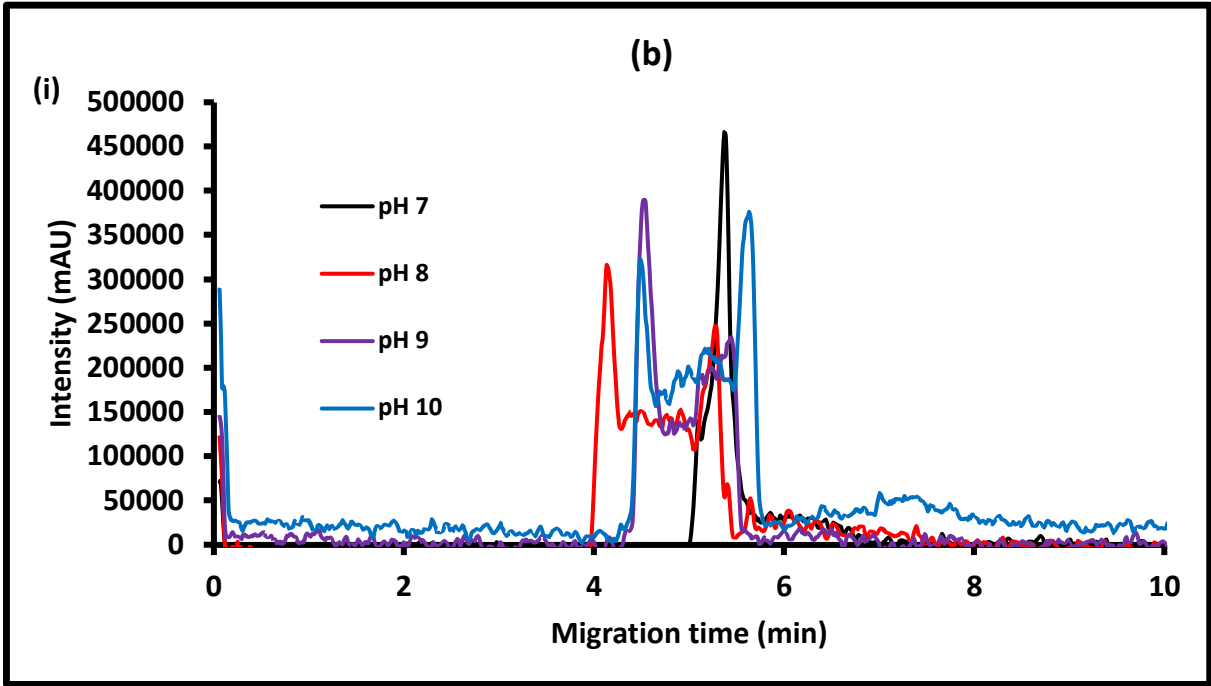
The peaks obtained for QDs at all pH values (Fig. 3.9(a)) are quite well defined in a quasi-gaussian profile.

For the NGQDs, Fig.3.9(b), the profile at pH 7 is similar to the one of QDs. But for the other pHs (8 to 10), the profiles are much more distorted, with a larger footprint made of a plateau surrounded by two peaks. This can be a sign of sample evolution due to pH.

Regarding the gCNQDs, the profiles (Fig. 3.9(c)) are equivalent to those for GQDs. These results indicate a lower polydispersity for both GQDs and gCNQDs compared to NGQDs.

Concerning the mass spectra, the too low intensity at the expected m/z values did not allow to go further in possible peak attribution.





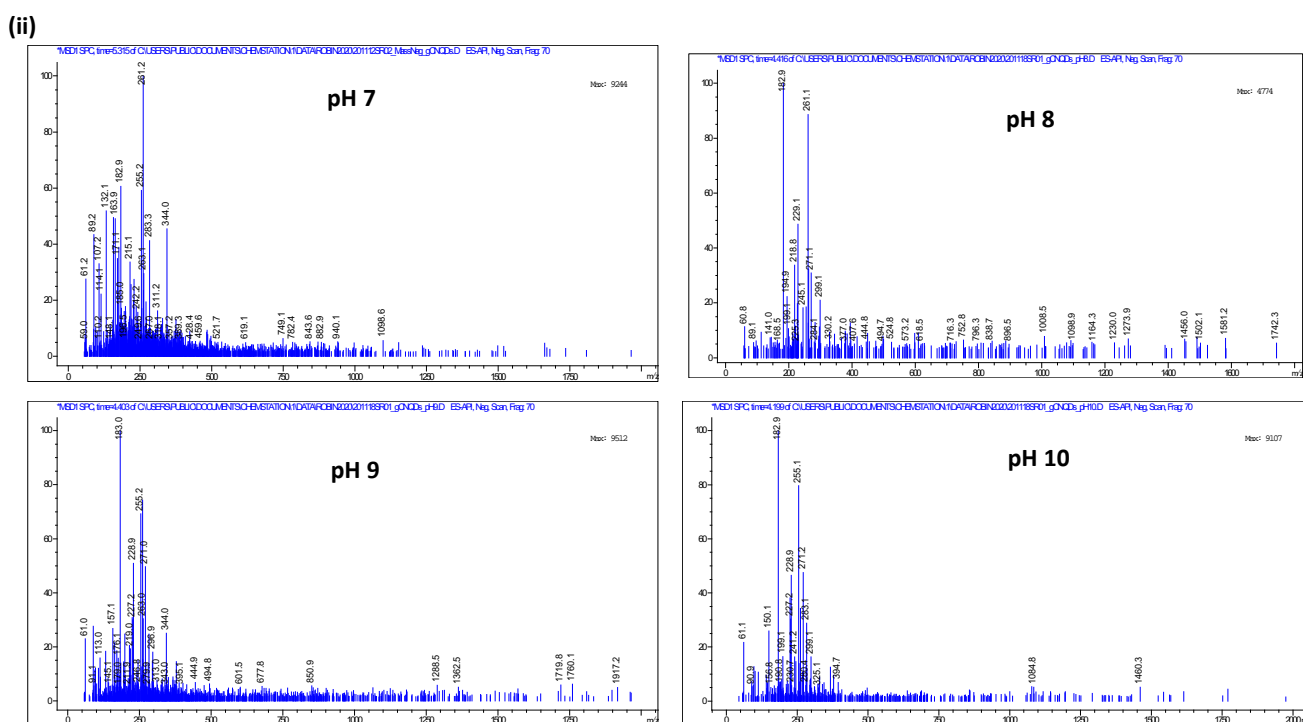
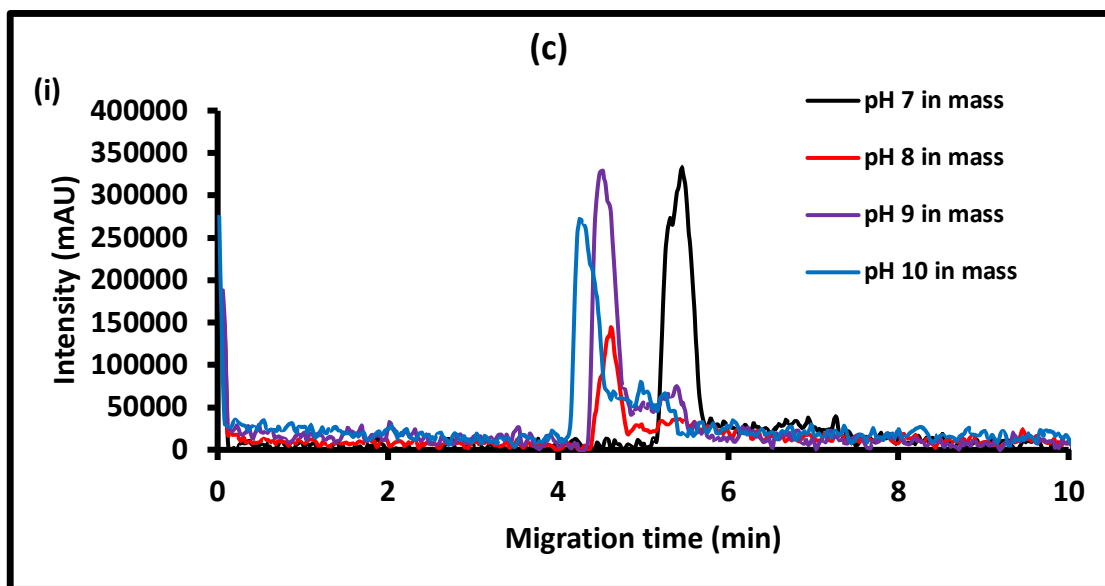


Figure 3.9: Electropherograms of (a) GQDs, (b) NGQDs and (c) gCNQDs (1mg/mL in BGE). Injections done at 50 mbar for 16 s for QDs. Pressure applied for mobility till the MS detector : 50 mbars. (i) MS electropherograms and (ii) corresponding ion mass spectra in scan mode, negative ion mode within a m/z window of 0-2000).

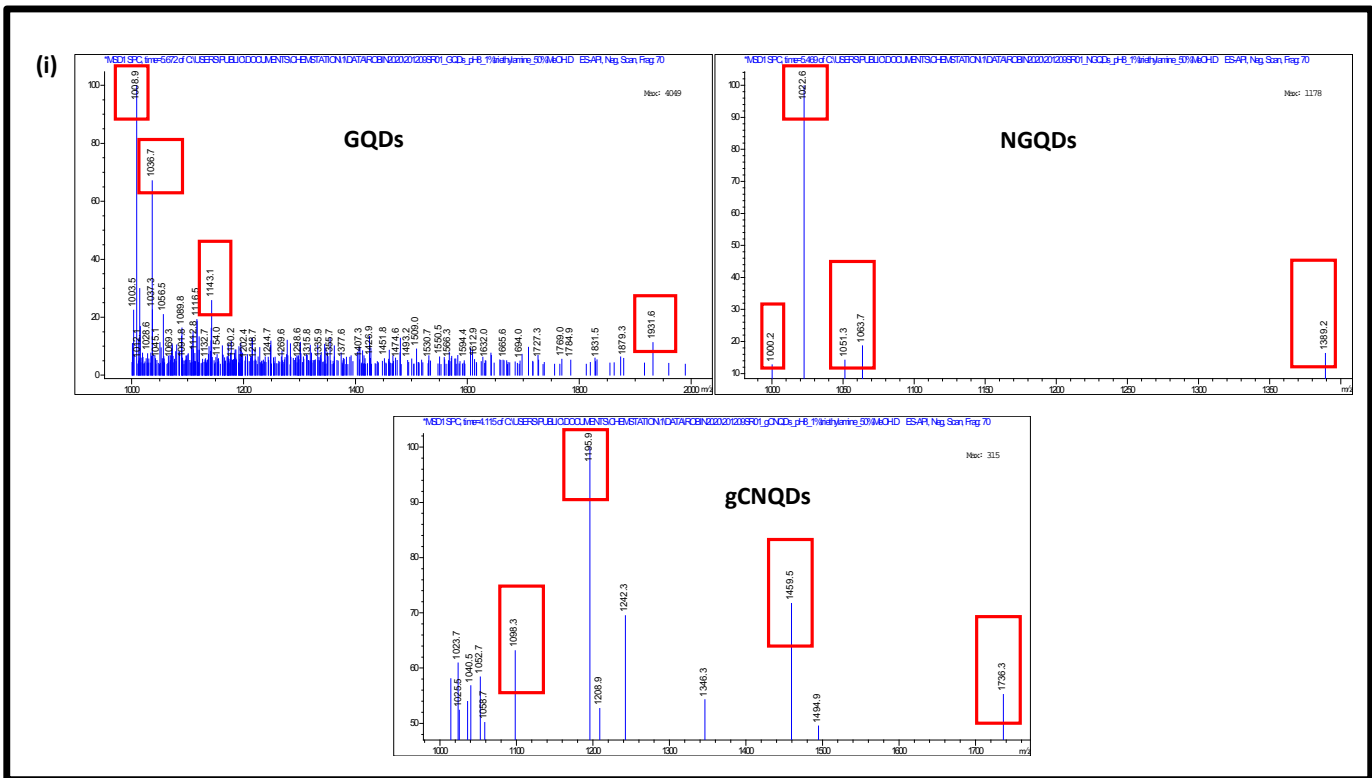
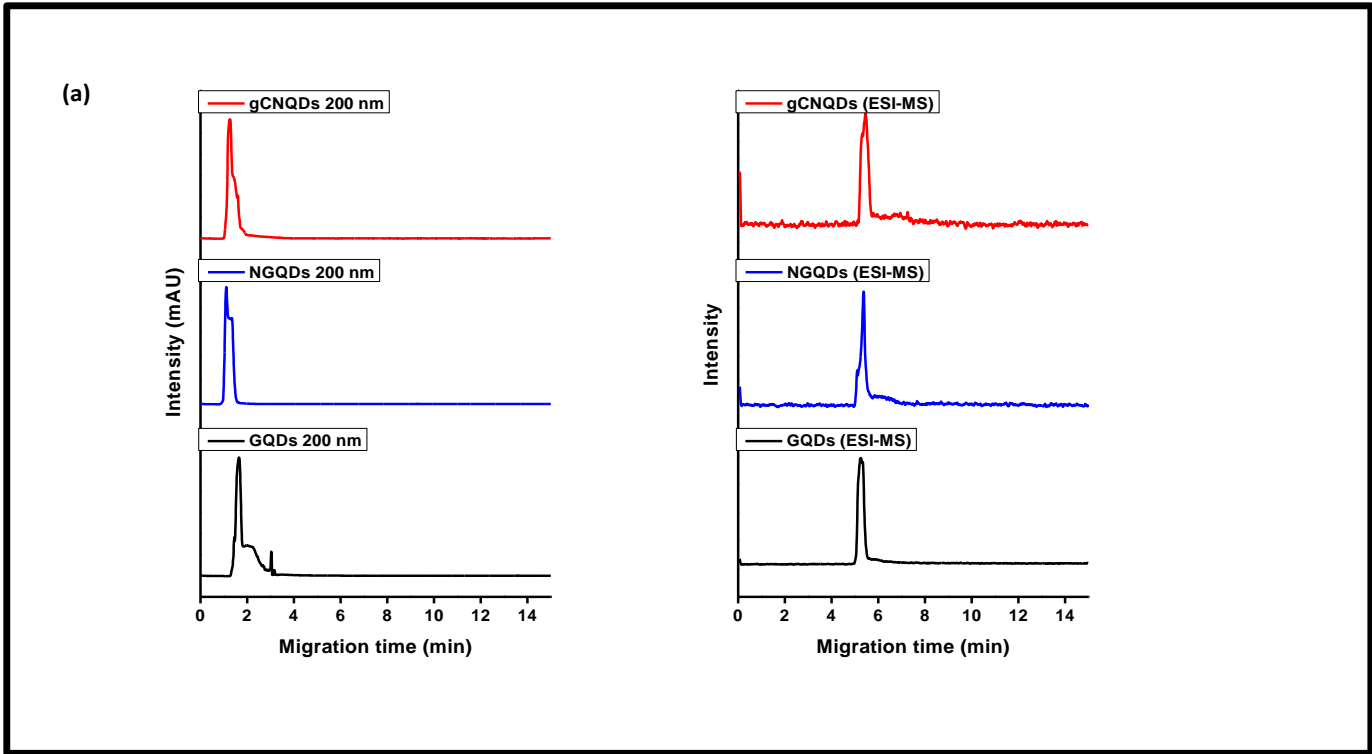
So as to increase the intensity of the mass spectra, the ionization rate of the QDs should be improved. Therefore, two different studies were performed and compared (1) injection of a small zone of sample prepared in the BGE, (2) continuous injection in the frontal mode of the sample prepared in the sheath liquid.

Dissolving the sample in the sheath liquid rather than in the BGE (is not classical but should help to increase the ionization of the sample and therefore its detection. Indeed, the sheath liquid is optimized so as to help for sample ionization and desorption.

The continuous injection of sample (figure b) should help to increase the signal as the integration can be performed on a large time range.

The ion mass plots extracted from electropherograms obtained after introducing the samples in the capillary by injection are shown in Fig. 3.10 (i) and those extracted from the frontal mode are shown in Fig. 3.10 (ii). These ion mass plots are clearer but still show the low intensity and possibly poor ionization of the samples analyzed in this work.

Using these masses obtained, an attempt was then made to predict possible structures and extent of functionalization of the quantum dots (Table 3.6 and Table 3.7). Most of the predicted structures can be deprotonated. However, some of the structures predicted for the NGQDs and the gCNQDs indicate no possible ionization as the theoretical masses are equivalent to the ion masses found from the analyses which agrees with the thought that the functional groups on these nitrogen-rich nanostructures are not as easily accessible as those on the pristine QDs.



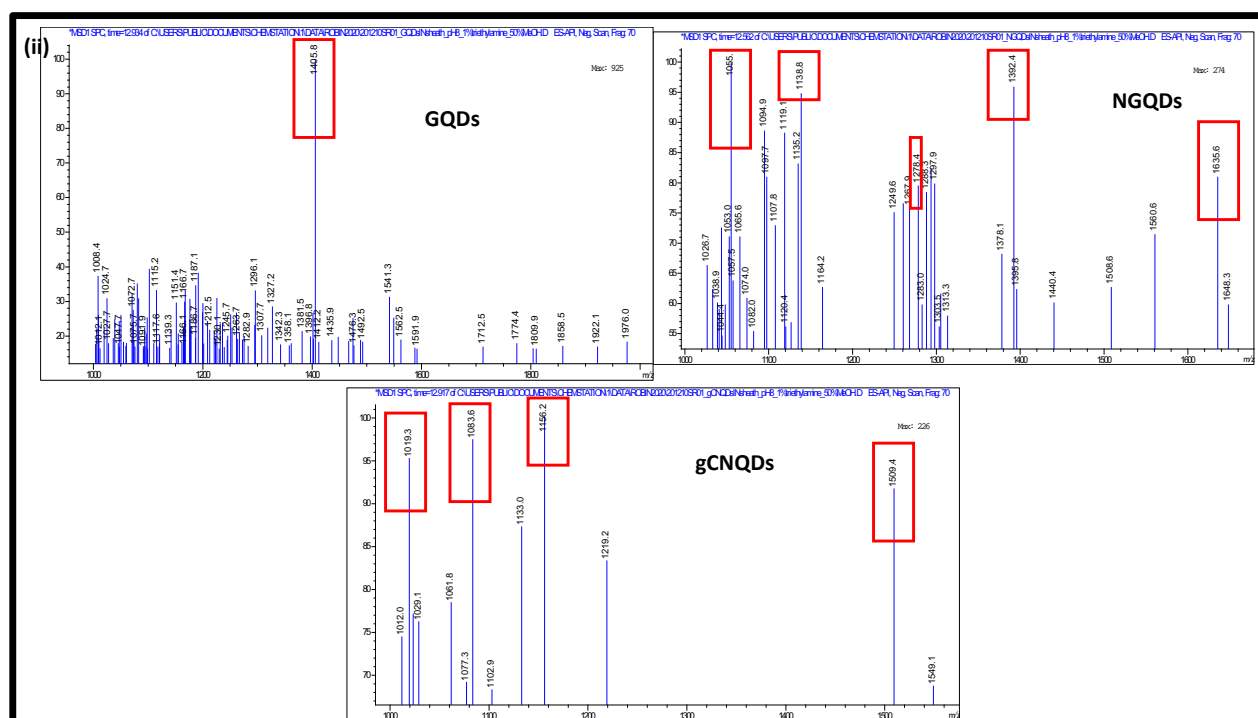
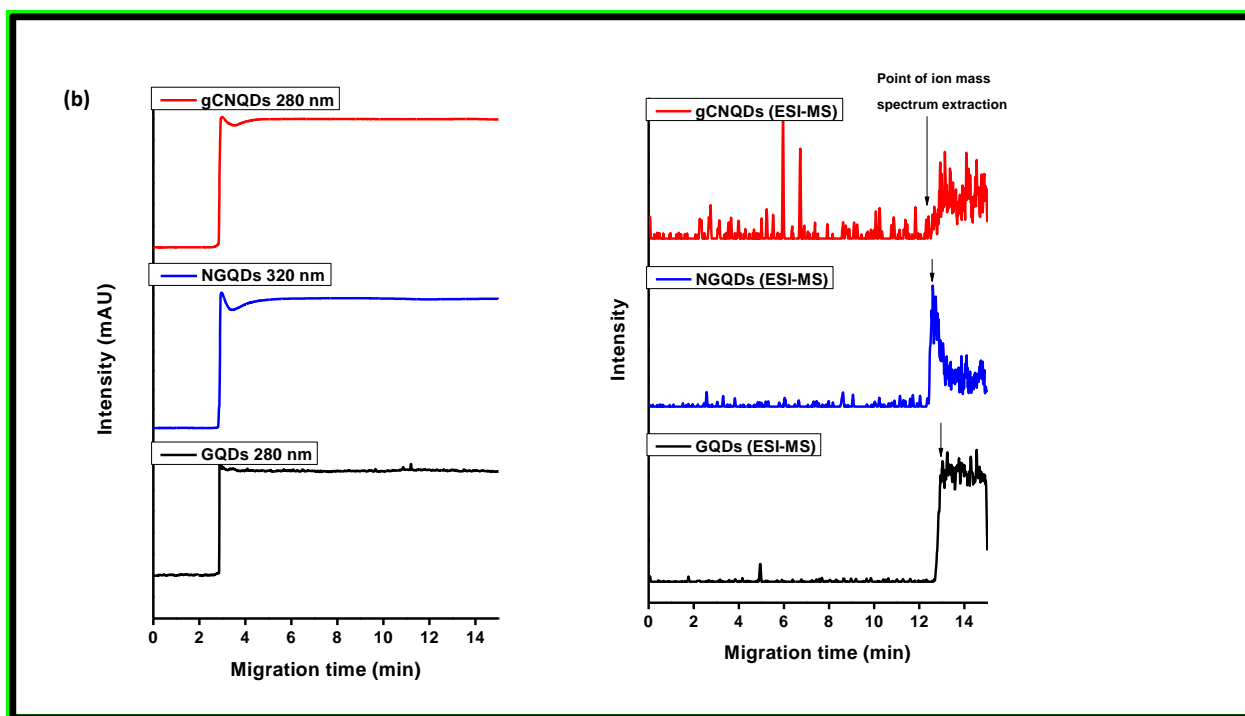
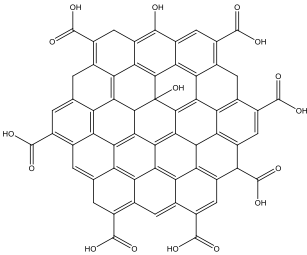
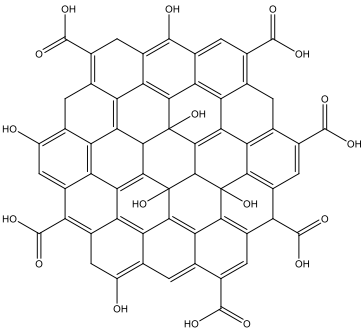
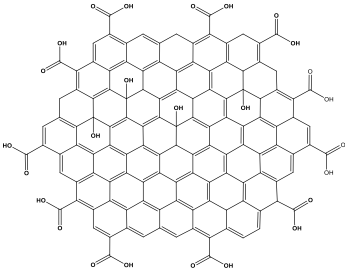
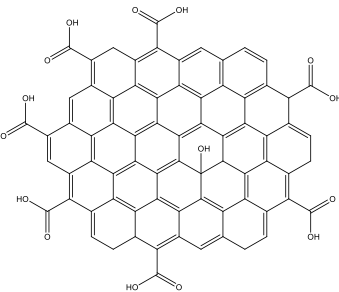
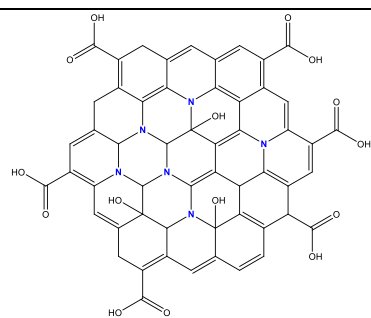


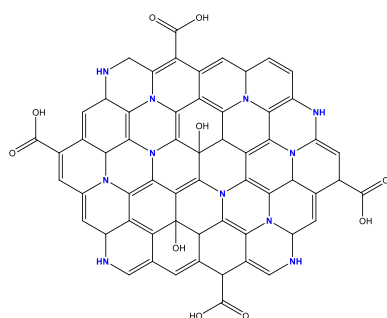
Figure 3.10: Electropherograms of (a) 1mg GQDs, NGQDs and gCNQDs in 1 mL BGE (Injections done at 50 mbar for 16 s) with (i) extracted ion mass plots recorded in scan mode and (b) 1 mg GQDs, NGQDs and gCNQDs in 1 mL sheath liquid (introduction of sample by pressure 50 mbar) with (ii) extracted ion mass plots recorded in scan mode. m/z window = 1000-2000 in negative ion mode.

Table 3.6: Predicted structures and possible deprotonation determined according to obtained ion masses in CE-MS analyses for the samples injected in a sample zone in BGE.

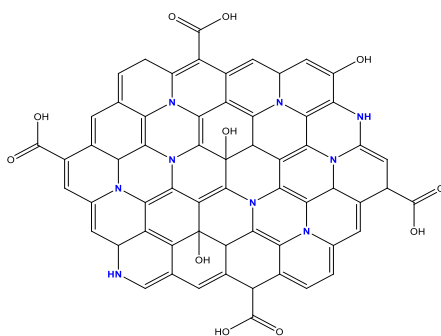
Structure	Possible ionization
GQDs	
	$1014.85 - 6[H]^+ = 1008.9$
	1036.13 predicted 1036.7 found
	$1144.14 - [H]^+ = 1143.1$
	$1935.2 - 4[H]^+ = 1931.6$
NGQDs	



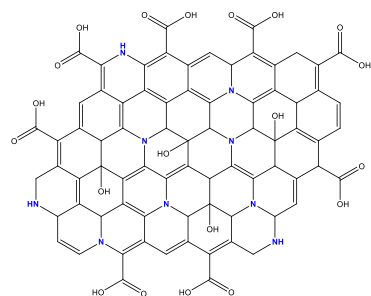
$$1002.18 - 2[\text{H}]^+ = 1000.2$$



$$1055.24 - 4[\text{H}]^+ = 1051.3$$

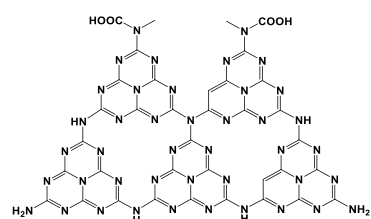


$$1065.21 - 2[\text{H}]^+ = 1063.7$$

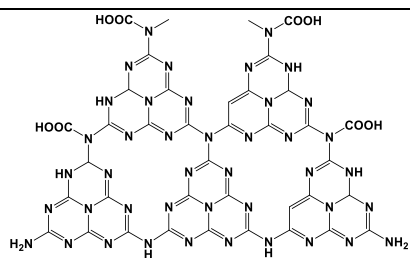


1389.26 predicted
1389.2 obtained
(no ionisation)

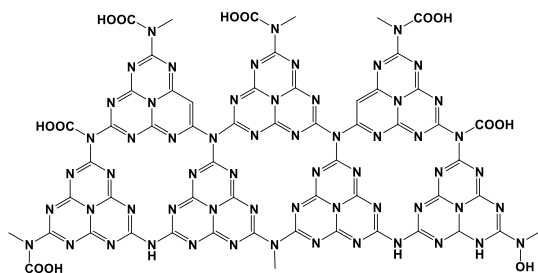
gCNQDs



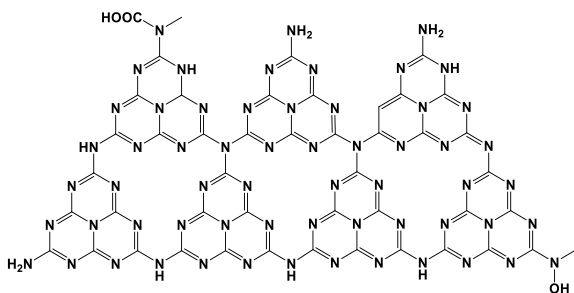
$$1102.25 - 4[\text{H}]^+ = 1098$$



$$1198.29 - 3[\text{H}]^+ = 1195.9$$

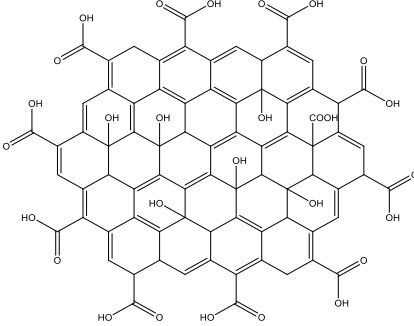
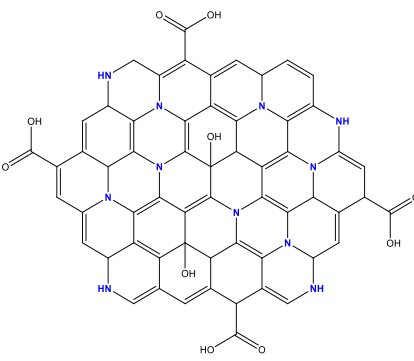
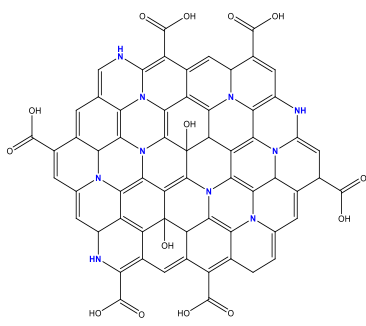


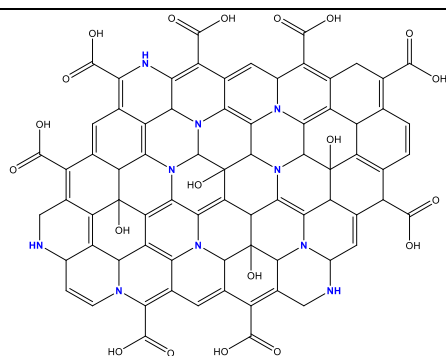
$$1737.36 - [\text{H}]^+ = 1736.3$$



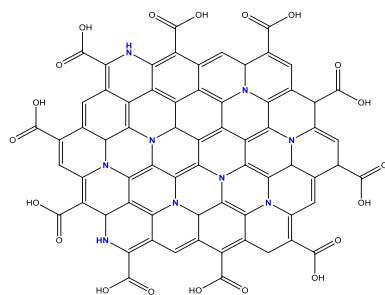
$$1462.34 - 3[\text{H}]^+ = 1459.5$$

Table 3.7: Predicted structures and possible deprotonation determined according to obtained ion masses in CE-MS analyses for the samples dissolved in sheath liquid and continuously introduced (frontal mode)

Predicted structure	Possible ionization
GQDs	
	$1412.17 - 6[H]^+ = 1405.8$
NGQDs	
	<p>1055.24 predicted 1055.1 obtained (no ionization)</p>
	<p>1138.19 predicted 1138.8 obtained (no ionization)</p>



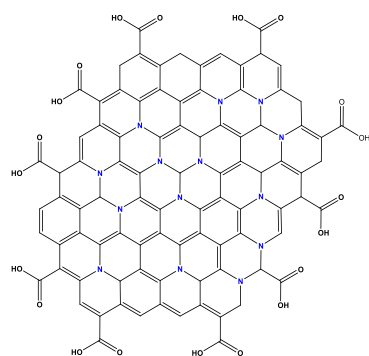
$$1279.15 - [\text{H}]^+ = 1278.4$$



1392.27 predicted

1392.4 obtained

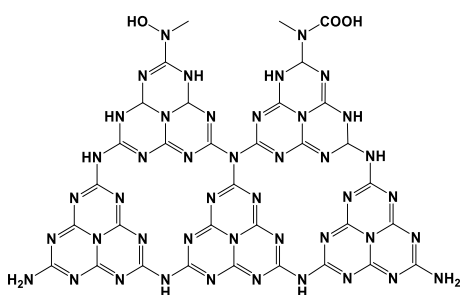
(no ionization)



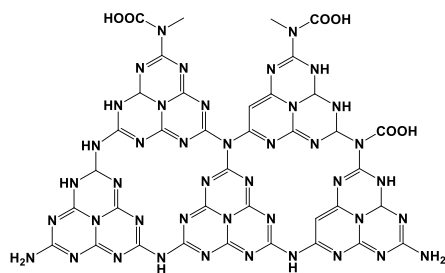
$$1637.26 - 2[\text{H}]^+ =$$

1635.6

gCNQDs



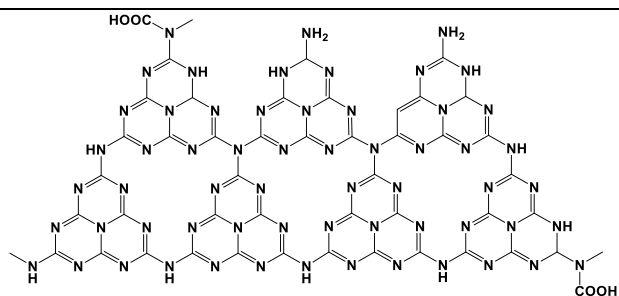
$$1084.31 - [\text{H}]^+ = 1083.6$$



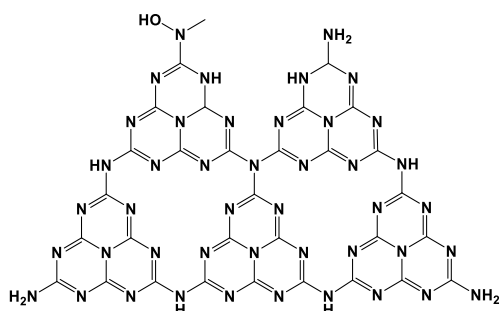
1156.32 prediction

1156.2 obtained

(no ionization)



$$1511 - 2[\text{H}]^+ = 1509.4$$



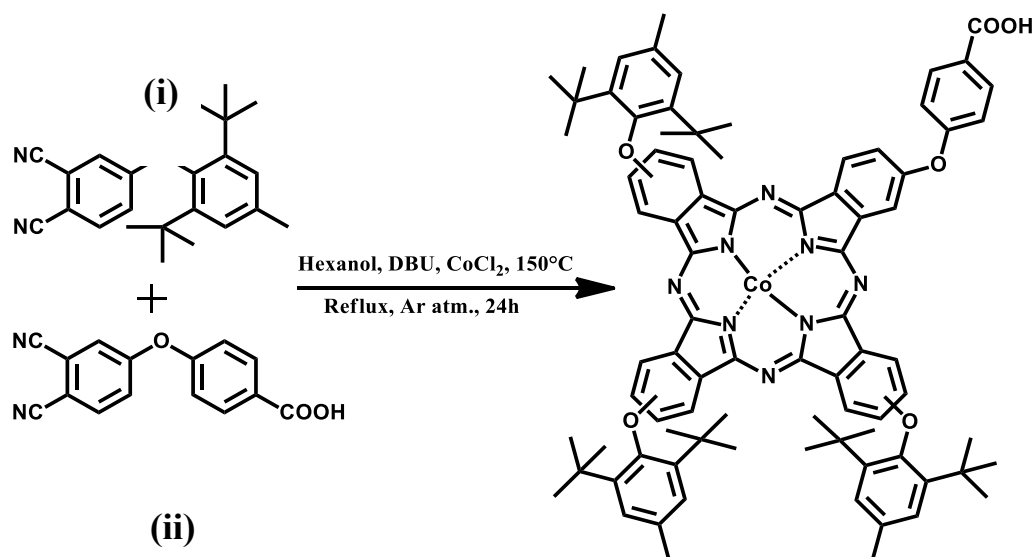
$$1022.27 - 3[\text{H}]^+ = 1019.3$$

These preliminary results allow to identify some layer structures, and further work should take into account that interactions between layers could be modified according to the GODs environment in solution.

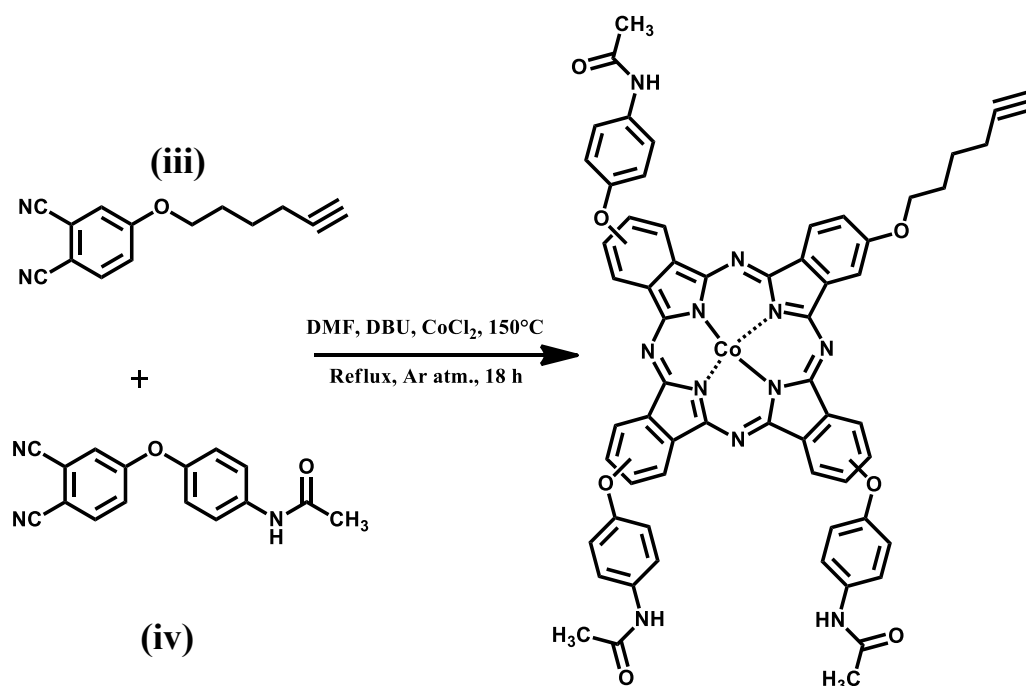
In conclusion, these preliminary results highlight that CE-MS seems a very interesting analytical methodology to go deeper in the understanding of the GODs structures. Indeed, the separative mode by electrophoresis allows to evidence the polydispersity of the sample, and we showed for the first time that the coupling to MS allows to propose some structures which are completely compatible with what is expected from the synthesis pathway. Deeper studies would then allow to obtain more precise identifications, and

3.2 Synthesis and characterization of MPcs, Complex (1) and complex (2)

Complexes 1 and 2 were synthesized by a statistical cross-condensation reaction using two phthalonitriles illustrated in Schemes 3.2 and 3.3.



Scheme 3.2: Synthesis of complex 1.



Scheme 3.3: Synthesis of complex 2.

The obtained products were characterized using various analytical techniques such as UV/vis, FTIR, MALDI-TOF as well as elemental analysis, which gave an indication of the success of the reaction. Complexes 1 and 2 gave a mass of 1361.34 for [M] and 1114.34 for [M]⁺ respectively, verifying the success of the syntheses. Fig. 3.11 shows the absorption spectra of MPc complexes 1 and 2 in DMF. The Q band is broad probably due to aggregation for complex 1. A broad or split Q band indicates aggregation in Pc complexes, with the low energy band being due to the aggregate and the high-energy band being due to the monomer [184]. Q bands (corresponds to the absorption band due to the transition from ground state to first excited state) and B bands (attributed to the transition from ground state to second excited state) associated with metalated Pcs are observed, where complex 2 achieves its Q band maximum at 667 nm while the B band is the most pronounced at 327 nm. The Q band of complex 1 was observed at 665 nm in DMF.

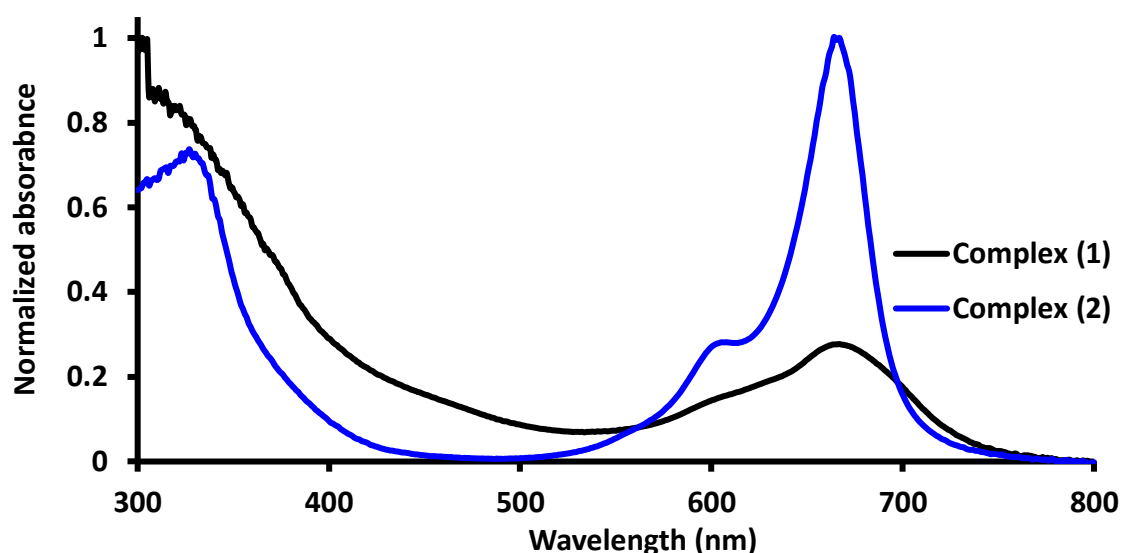


Figure 3.11: Absorption spectrum of complex 1 and 2 in DMF ($\sim 10^{-5}$ M).

3.3 Synthesis and characterization of covalent conjugates between QODs, MPcs complexes and aptamer.

Two-component systems were formed in this work prior to combining the QODs, MPcs and aptamer to finally form the three-component systems. The conjugates formed are listed in Table 3.8 with some data summarized, which will be further elaborated on in this sub-section.

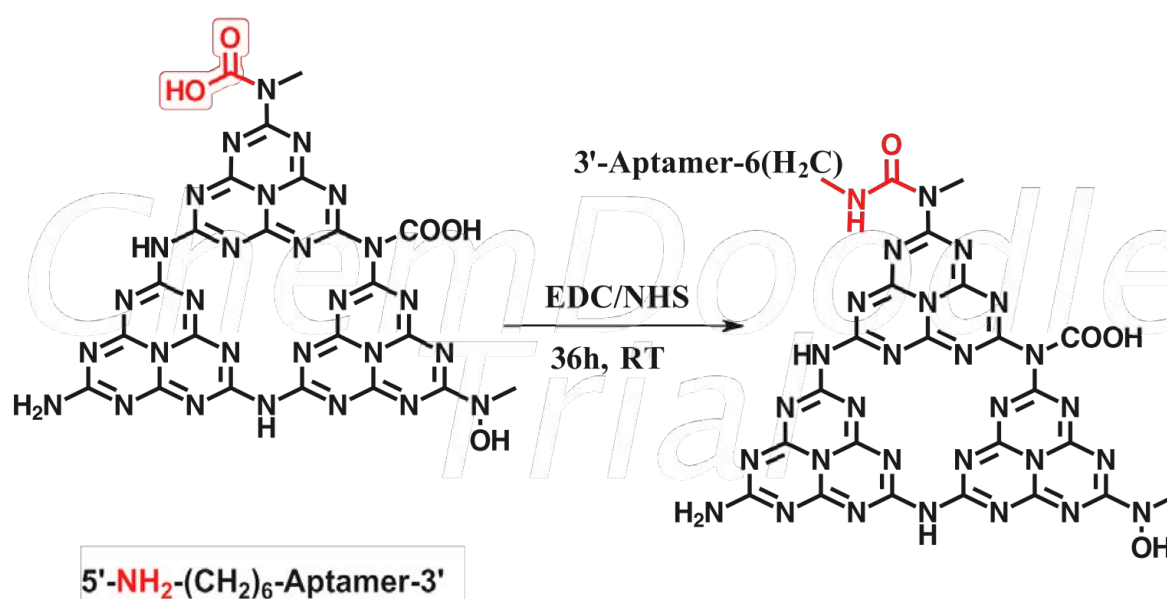
Table 3.8: Summarized spectral, DLS and zeta potential data of quantum dots, phthalocyanine and their conjugates with aptamer.

Sample	Loading (mg/mg)	λ_{\max} (nm)	Hydrodynamic size/ nm (PDI) ^d	Zeta (ζ) potential/mV
GQDs, 8 h	-	348 ^a	4.9 (0.52)	-30.1
NGQDs, 6 h	-	344 ^a	7.5 (0.51)	-24.5
gCNQDs, 6 h	-	378 ^a	10.1 (0.62)	-40.0
CoPc(1)	-	660 ^b	Unstable in solution	Unstable in solution
CoPc(2)	-	667 ^b	Unstable in solution	Unstable in solution
Aptamer	-	622 ^a	-	-
GQDs-CoPc(1) ($\pi\pi$)	0.08	639 ^c	18.2 (0.66)	-33.9
NGQDs-CoPc(1) ($\pi\pi$)	0.39	629 ^c	15.7 (1.0)	-34.7
gCNQDs-CoPc(1)($\pi\pi$)	0.21	660 ^c	18.2 (0.67)	-76.0
CoPc(1)@Aptamer	-	400, 625 ^c	37.8 (0.97)	-46.4
GQDs@Aptamer	-	629 ^a	68.1 (0.74)	-39.3
gCNQDs@Aptamer	-	620 ^a	58.8 (1.0)	-51.2

^ain water, ^bin DMSO, ^cin DMSO/water (3:1 v/v) mixture, ^dPDI in brackets

3.3.1 Verification of covalently linked conjugates QDs@Aptamer, gCNQDs@Aptamer and CoPc(1)@Aptamer

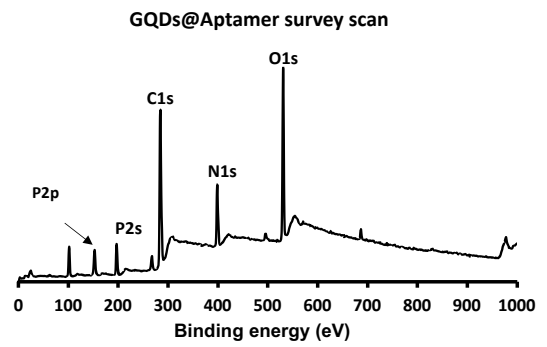
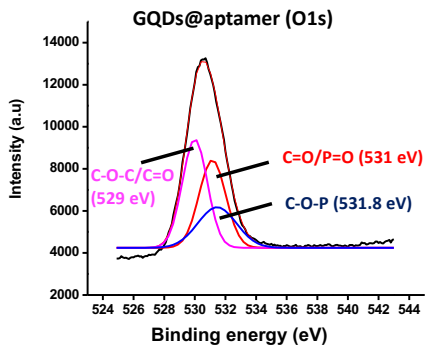
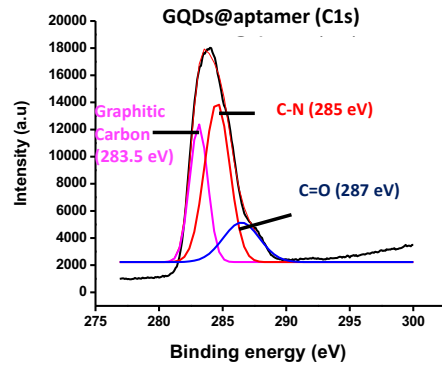
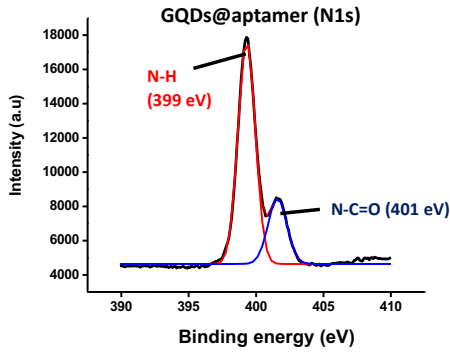
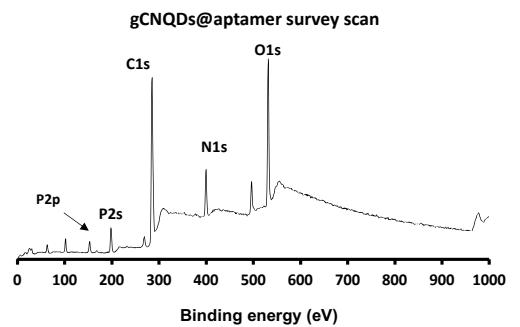
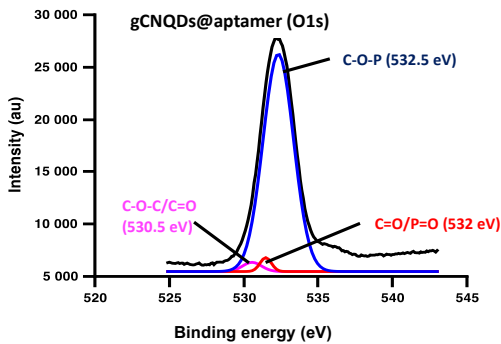
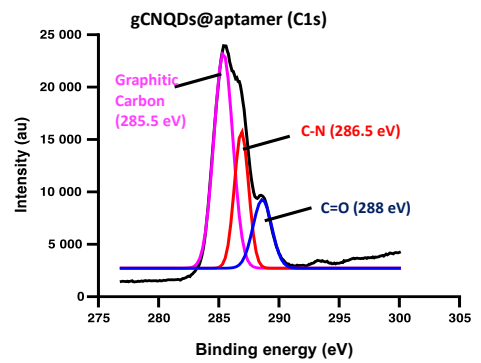
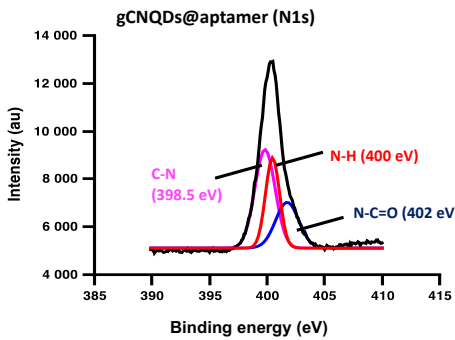
The covalent conjugation of the QDs or CoPc(1) with aptamer was achieved via amide coupling which is illustrated in Scheme 3.4 using gCNQDs as the example. This subsection highlights various analytical techniques used to fully characterize these composites.



Scheme 3.4: Amide coupling procedure of gCNQDs and amine-terminated aptamer.

3.3.1.1 XPS analysis

XPS was used to verify the success of covalent linking of the aptamer with the chosen quantum dots samples or the CoPc(1). The XPS results obtained are shown in Figure 3.12. The analyzed samples are QDs@Aptamer, gCNQDs@Aptamer and CoPc(1)@Aptamer ('@' representing covalent amide linking of molecules).

A**B**

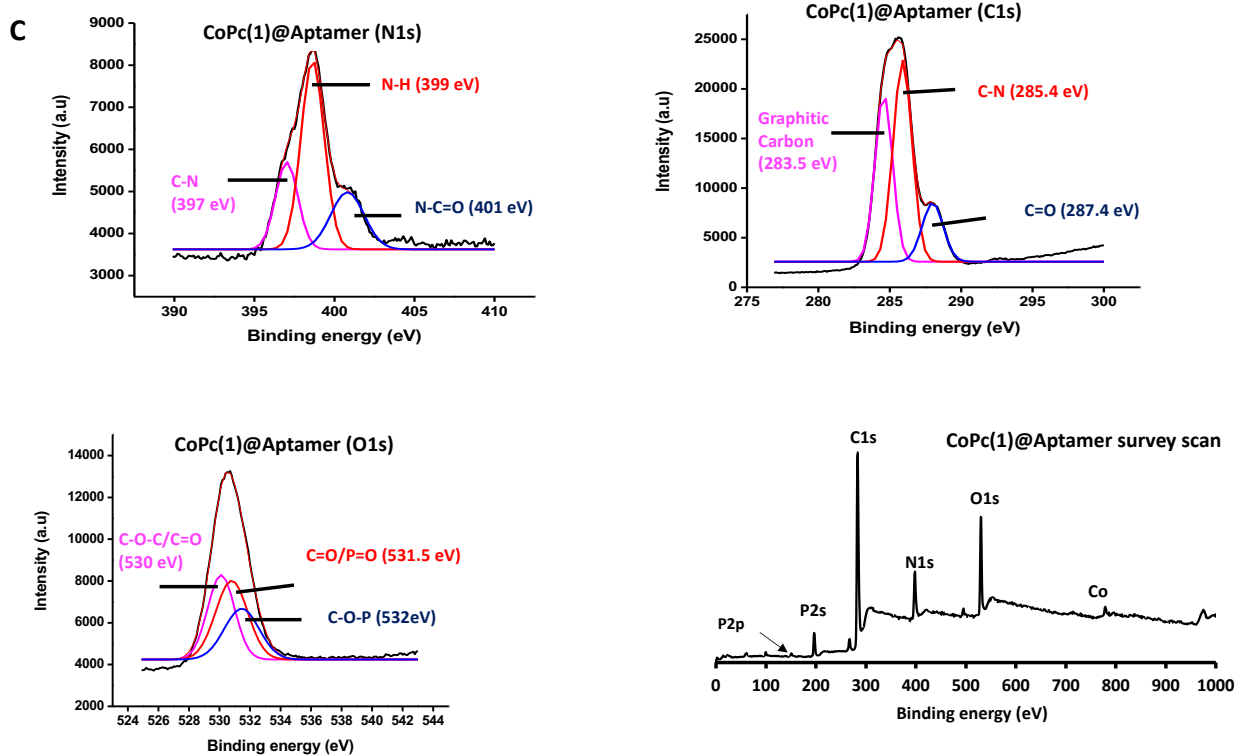


Figure 3.12: XPS survey and high-resolution scans for GQDs@Aptamer, gCNQDs@Aptamer and CoPc(1)@Aptamer for the verification of covalent bonding.

The wide survey scans showed the expected peaks which were attributable to the covalent conjugates synthesized in this work. The observed peaks on the wide scan were the N1s at 400 eV, C1s at 300 eV, O1s around 550 eV, P2s at 197 eV and P2p around 150 eV all wide scans. The difference in the survey scans was just the peak due to cobalt, which is the central metal of the phthalocyanine used, observed at around 791 eV which is the region where Co is observed on XPS analyses of CoPc(1)@Aptamer [185]. The P is said to be due to the DNA phosphate group [186]. P has been observed at binding energies of 150-200 eV [186].

The peaks due to nitrogen, carbon and oxygen were further studied as high-resolution scans and deconvoluted to confirm the covalent conjugation of the aptamer with the QDs and CoPc(1). All data from deconvoluted spectra are summarized in Table 3.9.

Table 3.9: Summary of binding energies determined from deconvoluted high-resolution spectra, corresponding to bonds forming the structures reported and their conjugates.

Peak assignments	N1s			C1s			O1s		
	C-N	N-H	N-C=O	Graphitic carbon	C-N	C=O	C-O-C/ C=O	C=O/P=O	C-O-P
GQDs@Aptamer	-	399.0	401.0	283.5	285.0	287.0	529.0	531.0	531.8
gCNQDs@Aptamer	398.5	401.0	402.0	285.5	286.5	289.0	530.5	532.0	533.0
CoPc(1)@Aptamer	397.0	399.0	401.0	283.5	285.4	287.4	530.0	531.5	532.0

For the GQDs@Aptamer conjugate, the deconvoluted N1s spectrum showed two main peaks underneath the original peak at binding energies of 399 eV and 401 which are attributable to N-H and N-C=O respectively, as reported at these binding energies [187]. The presence of N-C=O confirms the formation of an amide bond. The C1s spectrum showed three peaks after deconvolution at binding energies of 283.5 eV, 285.0 eV and 287.0 eV attributable to graphitic carbon, C-N and C=O respectively, Table 3.9. The O1s spectrum showed three peaks under the main peak at binding energies of 529.0 eV, 531.0 eV and 531.8 eV which may be attributed to C-O-C/C=O, C=O/P=O and C-O-P respectively. A similar finding for aptamer-based work has been

reported in literature [188]. For the gCNQDs@Aptamer conjugate, the deconvoluted N1s spectra showed three peaks at binding energies of 398.5 eV, 401.0 eV and 402.0 eV which may be attributed to C-N, N-H and N-C=O respectively [187]. The C1s spectra for this samples showed three peaks after deconvolution at binding energies of 285.5, 286.5 eV and 288.0 eV attributable to graphitic carbon, C-N and C=O respectively. The O1s spectrum showed three peaks under the main peak at binding energies of 530.5 eV, 532.0 eV and 533.0 eV which may be attributed to C-O-C/C=O, C=O/P=O and C-O-P respectively. Compared to the QDs, the other QDs samples have the nitrogen atoms present within their structures and thus contain more defects than the QDs which may be the cause of shifts in binding energies. For the CoPc(1)@Aptamer conjugate, the deconvoluted N1s spectrum showed peaks at binding energies of 397.0 eV, 399.0 eV and 401.0 eV which may be attributed to C=N, N-H and N-C=O respectively [189]. For the C1s and O1s spectra, similar results were observed as was for QDs@Aptamer which confirms the presence of the new amide bond formed by covalent linkage as well as presence of N-C=O bond.

3.3.1.2 DLS and zetametry studies

Figure 3.13 shows the profiles obtained for the QDs and their conjugates with aptamer dispersed in a carbonate buffer solution. For the QDs (Fig. 3.13(a)), (Tables 3.1 and 3.8) the size determined in DLS was 4.9 nm for the sample synthesized for 8 h. Upon covalently linkage to the aptamer (QDs@Aptamer), a very broad peak is observed with a size of about 68.1 nm at the peak maxima, Table 3.8. Sizes this large in DLS analyses are an indication of high aggregation of these conjugates in the buffer solution. The gCNQDs (Fig. 3.13(b)), were found to be 10.1

nm for the sample synthesized for 6 h, with its conjugate with aptamer being 58.8 nm, Tables 3.1 and 3.8. As aptamers are non-spherical and small in size, they could not be analyzed by DLS. However, when conjugated to the QDs, the conjugated nano-architectures could be analyzed by DLS, providing negative values. The zeta potential values of the GQDs and gCNQDs prior to conjugation were -30.1 and -40.0 mV, Table 3.8. When conjugated to the aptamer, the structures showed a colloidal stability, and their zeta potential values were measured as -39.3 and -51.2 mV respectively. The higher zeta potentials for the covalently conjugated molecules is coherent with the negative charge of the conjugated aptamers in these experimental conditions. Indeed, the phosphate groups in DNA have a pKa of 2 and are negatively charged due to the bonds formed between O atoms and P atoms [190]. The CoPc(1)@Aptamer conjugate in particular showed a colloidal stability (compared to the CoPc(1) alone which was unstable in solution) and a hydrodynamic radius of 37.8 nm (Figure 3.13 (c)) with a zeta potential value of -46.4 mV.

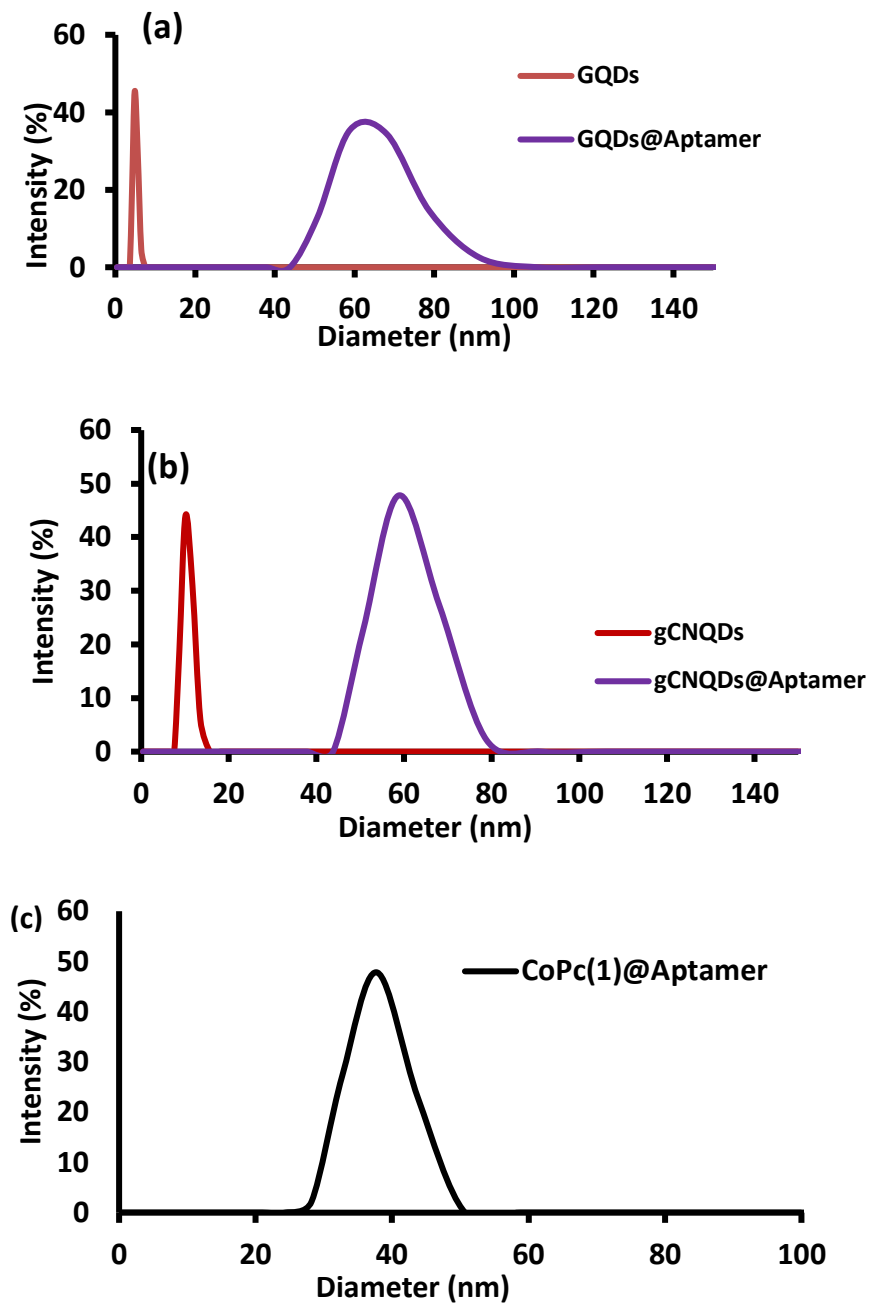


Figure 3.13: DLS plots of (a) GQDs and (b) gCNQDs and their conjugates with aptamer.

3.3.1.3 FTIR analysis

The presence of aptamer within the covalent conjugate was also validated using FTIR analysis. The conjugation between the GODs and aptamer was used as an example to illustrate the results obtained for all covalent conjugates reported in this thesis. These results are shown in Figure 3.14. The stretches due to the backbone of the aptamer are identified in the region of 1084/1225 cm^{-1} where they are expected. These peaks are not observed in the GODs spectrum. More importantly, in the region between 3000-3500 cm^{-1} of the conjugate a distinct peak at 3300 cm^{-1} due to N-(C=O) can be seen, as well as spectral shift which are an indication of amide bond formation [191]. For the CoPc@Aptamer conjugate, the same stretches due to the amide bond as well as the phosphate backbone of the aptamer were observed (data not shown), confirming the covalent conjugation of these molecules.

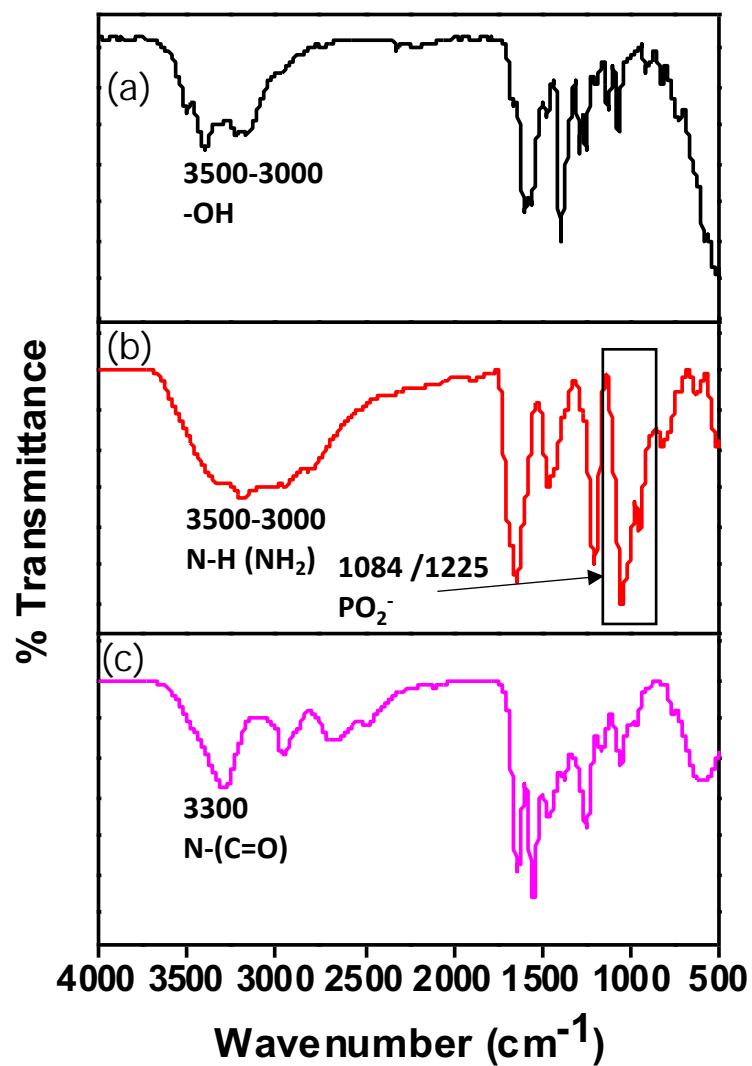


Figure 3.14: FTIR spectra of (a) GQDs, (b) aptamer and (c) their covalent conjugates.

3.3.1.4 Raman spectroscopy analysis

Raman results are shown in Fig. 3.15 for the GQDs, aptamer and GQDs@Aptamer.

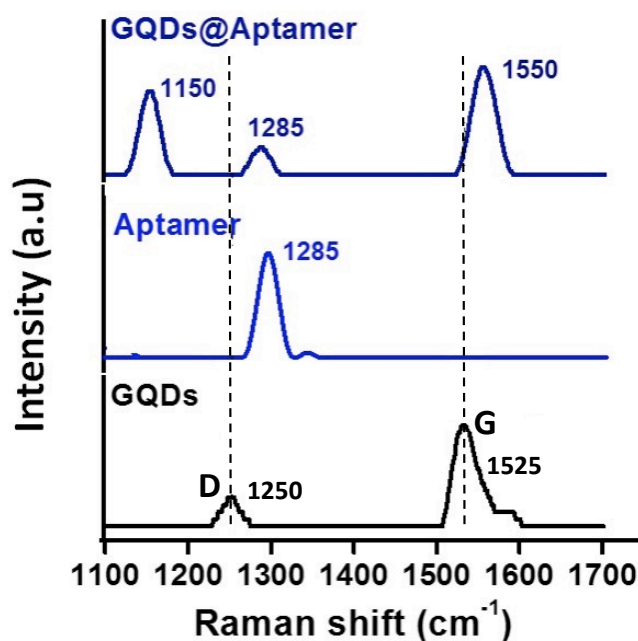


Figure 3.15: Raman of aptamer with its covalent conjugates with selected QDs.

The peak due to the aptamer was observed at 1285 cm⁻¹ that has been reported in literature to occur in this region [192, 193]. The effect of covalently conjugating the QDs to the aptamer is discussed using GQDs@Aptamer as an example. When the GQDs are covalently bonded to the aptamer, there is a shift of the D band to a lower frequency and G band of the GQDs to a higher frequency. The aptamer peak still appears at 1285 cm⁻¹. The D band of the GQDs also intensifies upon conjugation of the aptamer with the GQDs, indicating an interaction between the two molecules. The I_D/I_G ratio of GQDs@Aptamer was found to be 0.67 which is an increase from the ratio determined for the GQDs alone, determined as 0.17 (Table 3.10). This is one

of the indicators that there is interaction between the aptamer and the QDs as the increase in ratio means there is defectiveness in the pristine QDs.

Table 3.10: Aptamer and its covalent conjugates with selected QDs.

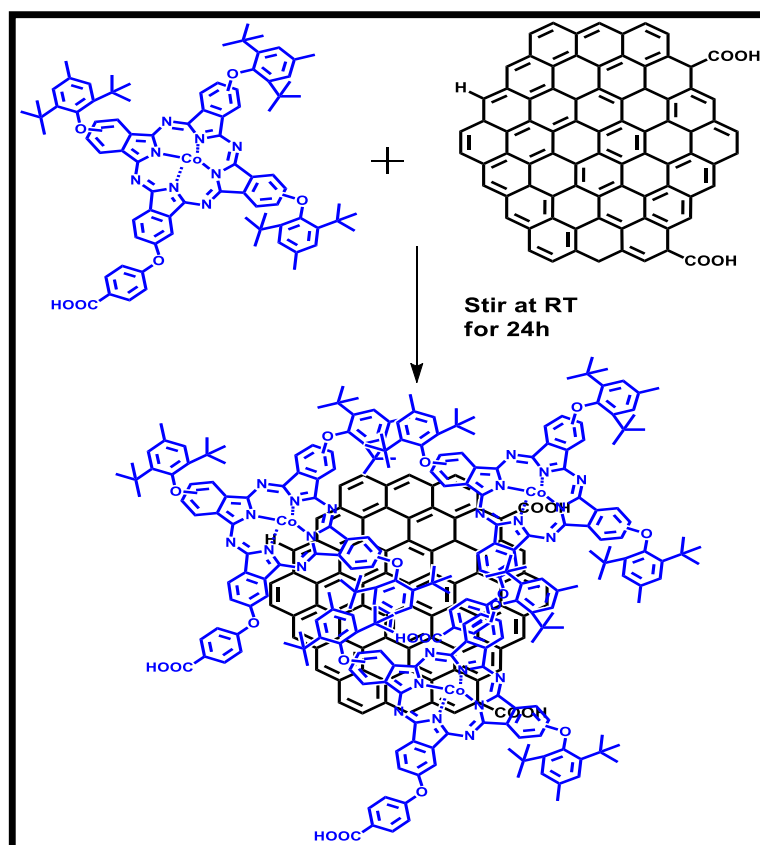
Electrode modifier	Raman D (cm^{-1})	Raman G (cm^{-1})	Aptamer Raman (cm^{-1})	Raman (I_D/I_G)
GQDs (8 h)	1250	1525	-	0.17
NGQDs (6 h)	1375	1600	-	1.50
gCNQDs (6 h)	1300	1590	-	0.83
GQDs-CoPc(1) ($\pi\pi$)	1300	1623	-	0.50
NGQDs-CoPc(1) ($\pi\pi$)	1280	1550	-	0.40
gCNQDs-CoPc(1) ($\pi\pi$)	1325	1600	-	0.50
Aptamer	-	-	1285	-
GQDs@Aptamer	1150	1550	1285	0.67
gCNQDs@Aptamer	1650	1750	1400	0.86

3.3.2 Conjugation between GQDs and MPcs by $\pi\pi$ interactions

The conjugates formed between GQDs and MPcs are listed in Table 3.6 with some data summarized, which will be further elaborated on in this sub-section. These conjugates are characterized using UV/vis to see how their combination affects their optical properties. They are also characterized using DLS to observe the possible changes that would occur in solution upon their conjugation as well as Raman which is run in solid state and indicates how the nanocomposites are affected structurally when combined.

3.3.2.1 UV/vis spectroscopy

The $\pi\pi$ interaction between the CoPc(1) and QDs of interest is illustrated in Scheme 3.5 using GQDs as an example.



Scheme 3.5. The $\pi\pi$ conjugation of CoPc(1) with GQDs to form GQDs-CoPc(1) ($\pi\pi$).

The NGQDs and gCNQDs were combined with the CoPc(1) in the same manner. The UV/vis spectra are shown in Figure 3.16 where comparative plots show how the CoPc(1) spectrum changes when conjugated to the QDs. QDs alone were dissolved in water (5 mg/mL), the Pc in DMSO (5 mg/mL) and the conjugates (2 mg/mL) in DMSO and water solvent mixture (3:1 v/v).

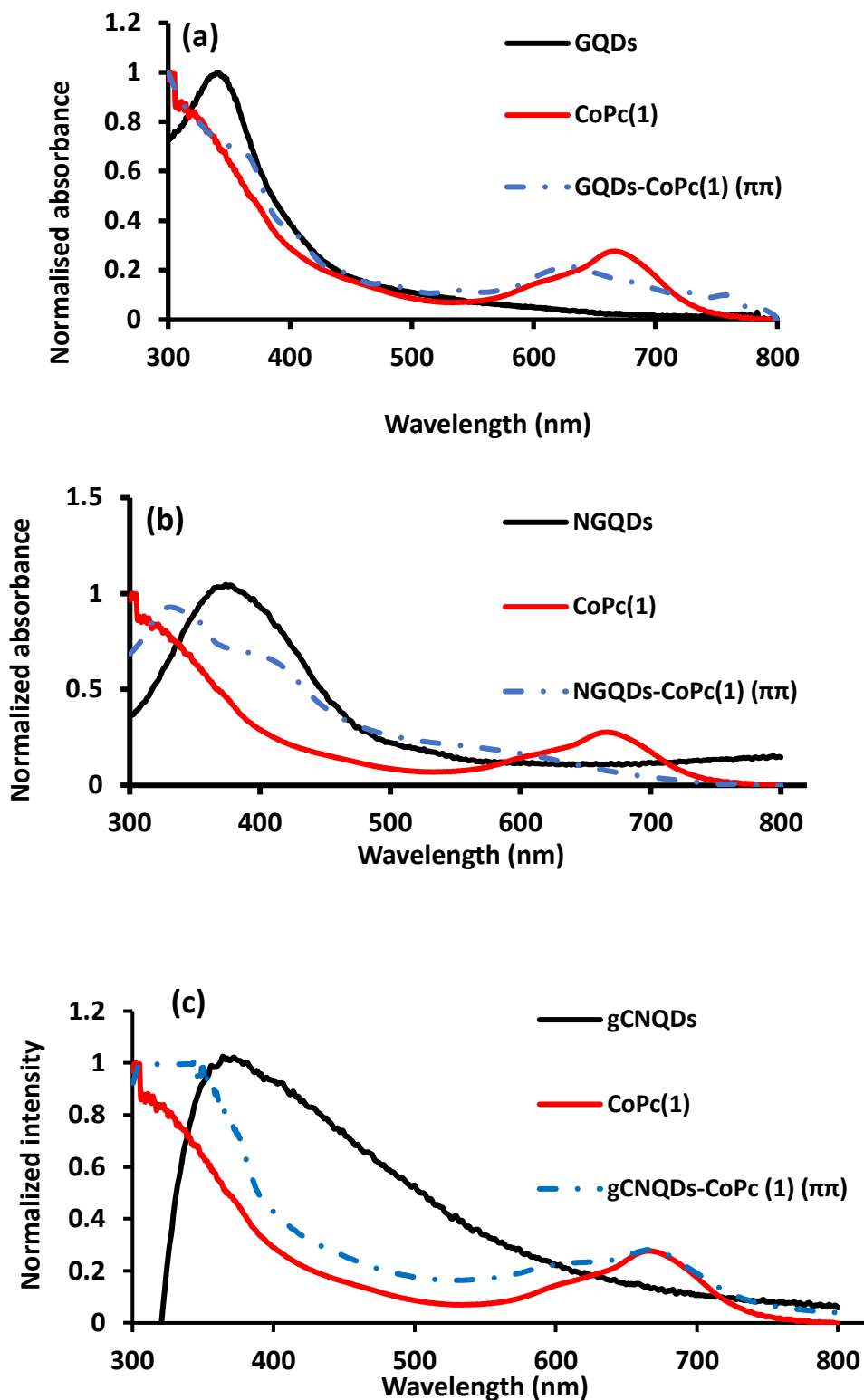


Figure 3.16: UV/vis spectra of (a) GQDs, (b) NGQDs and (c) gCNQDs and their conjugates with CoPc(1). All QDs were dispersed in water, CoPc(1) was dispersed in DMSO and the conjugates were dispersed in a DMSO/water (3:1 v/v) mixture.

The quantum dots synthesized in this work showed absorption peaks at 348 nm (GQDs), 344 nm (NGQDs) and 378 nm (gCNQDs), Table 3.8. GQDs-CoPc(1) ($\pi\pi$) and NGQDs-CoPc(1)($\pi\pi$) showed extensive aggregation indicated by blue shifting and broadness of peaks with only the peak due to the aggregate being observed. These peaks are also blue shifted. For gCNQDs-CoPc(1) ($\pi\pi$), both the CoPc(1) monomer (670 nm) and aggregate peaks (small shoulder peak on left of monomer peak) are observed and there is no change in peak position of the monomer following conjugation.

The loading of the CoPc(1) onto the QDs (amount of MPc on a QD since QDs are larger than MPc molecules) was investigated following previous studies using absorption instead of fluorescence [194]. This involves comparing the Q band absorbance intensities of the conjugate (QDs-CoPc(1)($\pi\pi$)) with that of the CoPc(1) before the conjugation. Equal masses (mg) for CoPc(1) and QDs-CoPc(1)($\pi\pi$) conjugates were weighed and separately dissolved in the same volume of the solvent. The loading values were determined to be 0.08, 0.39 and 0.21 mg/mg for the GQDs-CoPc(1) ($\pi\pi$), NGQDs-CoPc(1)($\pi\pi$) and gCNQDs-CoPc(1)($\pi\pi$), respectively. The low loading of the Pc on the GQDs could be due to repulsion in solution of deprotonated carboxylic acid groups on the Pc and on the GQDs. The NGQDs and gCNQDs have NH and NH₂ functions respectively, which, upon deprotonation become positively charged. Should this occur in solution, there is a possible attraction between the deprotonated COOH groups of the Pc and the protonated NH and NH₂ groups of the NGQDs and gCNQDs, hence increasing the loading.

3.3.2.2 DLS and zetametry studies

Figure 3.17 illustrates the change in DLS distribution curve from the unconjugated quantum dots to the QDs-MPc conjugate. For analysis, the QDs were dispersed in water and their conjugates with CoPc(1) dispersed in a DMSO/water mixture. The profiles observed are broad indicating high polydispersity (PDI values and hydrodynamic radii shown in Table 3.8). Moreover, the conjugation of the QDs with the MPc resulted in an increase in the hydrodynamic radius measured for the QDs alone. For the GQDs (Fig. 3.17(a)), the size determined in DLS was 4.9 nm as stated above, Table 3.8. Upon conjugation with the CoPc(1), the hydrodynamic size increased to about 18.2 nm. The NGQDs (Fig. 3.17(b)), showed hydrodynamic sizes of 7.5 nm for the QDs alone and 15.7 nm when $\pi\pi$ conjugated to the CoPc(1). The gCNQDs, (Fig. 3.17(c)), measured a hydrodynamic size of 10.1 nm with its CoPc(1)($\pi\pi$) conjugate measured at 18.2 nm. The increase in hydrodynamic size is likely due to aggregation which was also observed in UV/vis analysis as well as contribution from the hydrodynamic radius.

The zeta potential values of the GQDs, NGQDs and gCNQDs prior to conjugation were -30.1, -24.5 and -40.0 mV. When $\pi\pi$ conjugated to the CoPc(1), the zeta potential was increased to -33.9, -34.7 and -76.0 mV respectively. The increase in zeta potential values to more negative values could be a result of deprotonation of the COOH terminal group of the phthalocyanine molecules stacked on the larger QDs nanostructures. The higher values also show improved stability in DMSO/water solution upon conjugation of the QDs to the MPc.

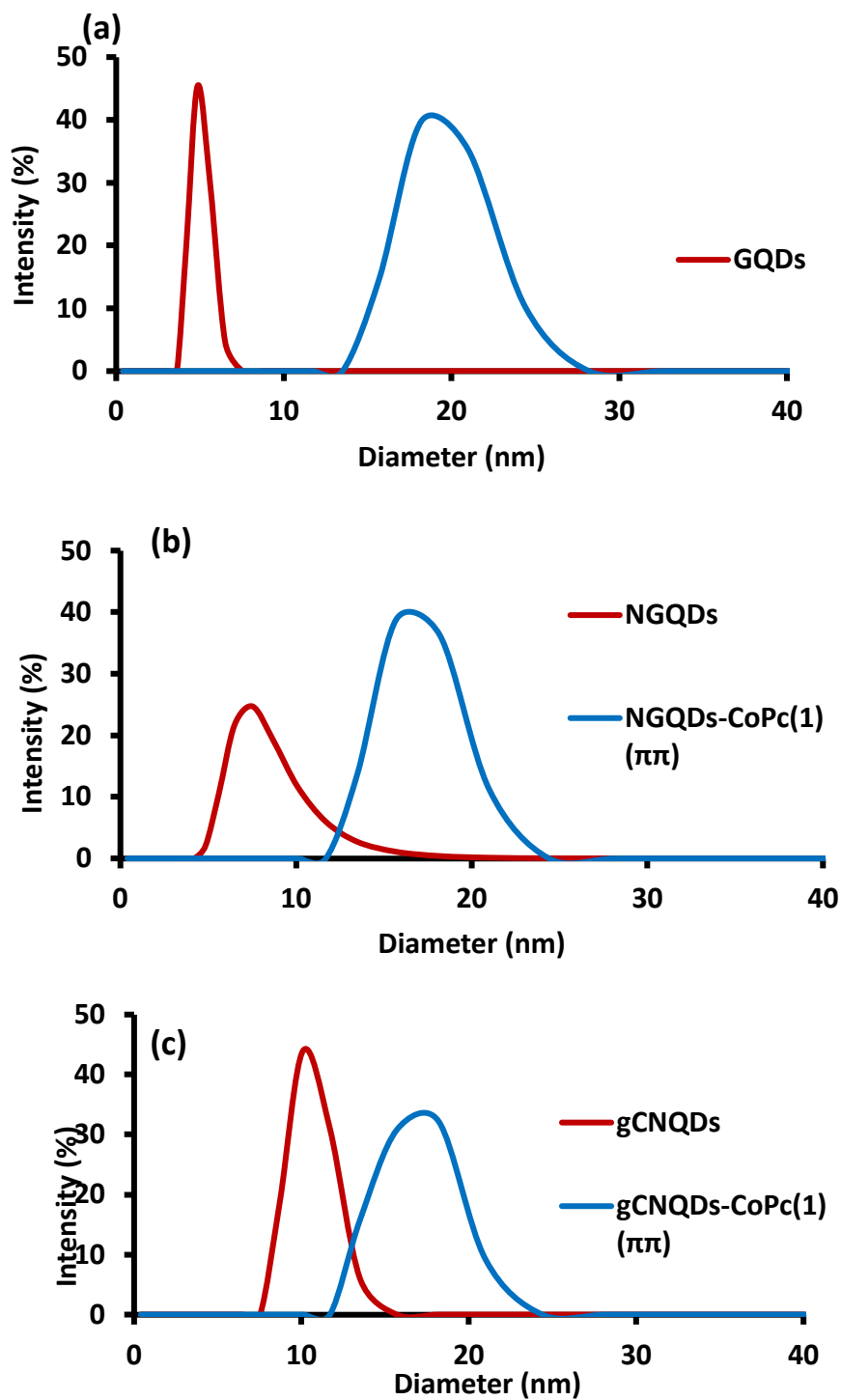
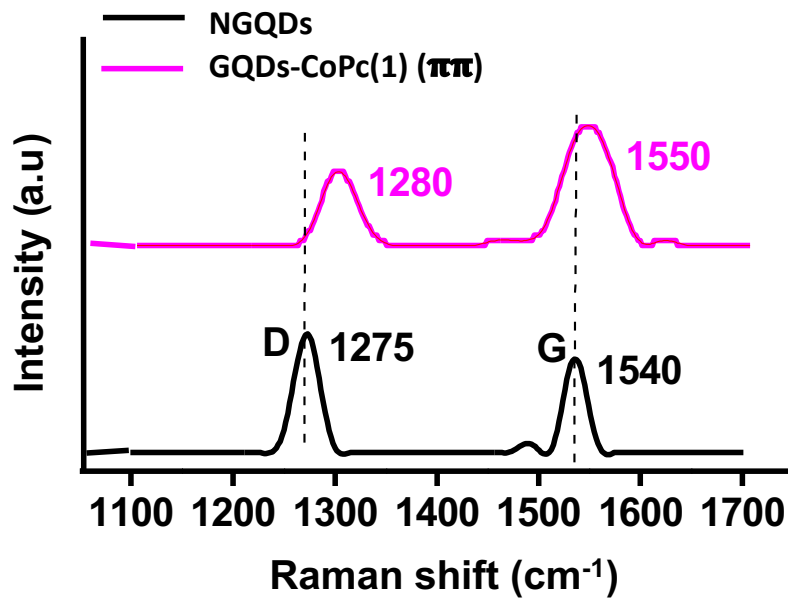
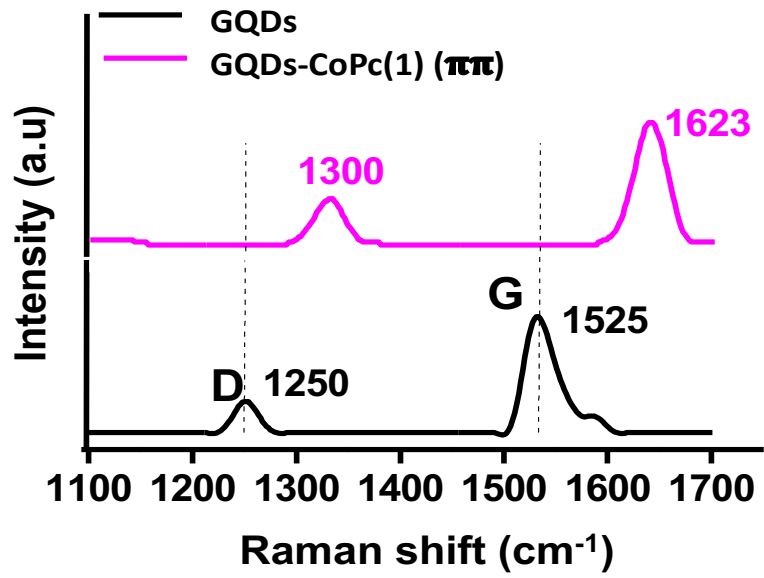


Figure 3.17: DLS plots of (a) GQDs, (b) NGQDs and (c) gCNQDs and their conjugates with CoPc (1).

3.3.2.3 Raman spectroscopy analysis

Raman was used to characterize the QDs and their conjugates with Complex 1. The spectra are shown in Figure 3.18. For the GQDs, the D band is observed at 1250 cm^{-1} and the G band at 1525 cm^{-1} with an I_D/I_G ratio of 0.17, Table 3.10. Upon conjugation with the CoPc(1) by $\pi\pi$ interactions, there is a shift to higher frequencies of 1300 cm^{-1} and 1623 cm^{-1} for the D and G bands, respectively with the I_D/I_G ratio determined as 0.50. The shift in frequency is a result of strong interactions between the composites. The D and G bands of the NGQDs are observed at 1275 cm^{-1} and 1540 cm^{-1} respectively with an I_D/I_G ratio of 1.50, shifting to higher frequencies of 1280 cm^{-1} and 1550 cm^{-1} upon $\pi\pi$ conjugation with the CoPc(1). The G band intensity increases, however which is not expected when conjugation of the composites occurs. The I_D/I_G ratio for NGQDs-CoPc(1) ($\pi\pi$) was determined as 0.40. Regarding the gCNQDs, the D and G bands for this sample are observed at 1300 cm^{-1} and 1590 cm^{-1} respectively. Upon $\pi\pi$ conjugation with the CoPc(1) shifts of the peaks to higher frequencies of 1325 cm^{-1} and 1600 cm^{-1} are observed. As already mentioned, the higher frequencies are a result of strong interactions between the phthalocyanine and QDs. The I_D/I_G ratio decreased from 0.83 to 0.50. This increase is an indicator of more defects occurring on the QDs structure.



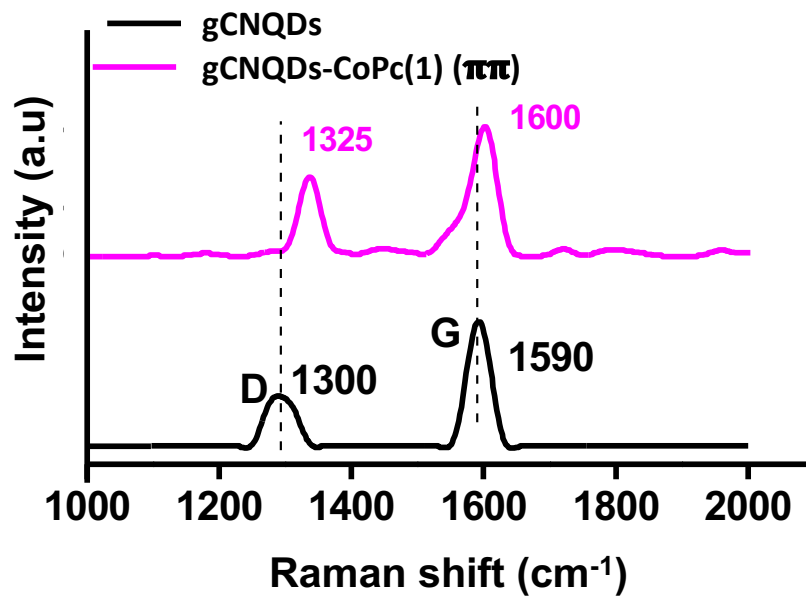


Figure 3.18: Raman spectra of QDs and their conjugates with CoPc(1).

3.4 Conclusion

The MPc complexes 1 and 2 were successfully synthesized, purified, and characterized using various techniques. Besides their obvious structural differences, their optical properties differed as well as seen in UV/vis spectral analyses. The synthesized gCNQDs, QDs and NGQDs were characterized in their physical dry form and in solution. The optimization of the synthesis time proved useful in obtaining well dispersed nanostructures which could be further analyzed and characterized using electrophoretic separation analyses. The obtained results provided proof of the presence of the expected functional groups as well as overall structures. TEM images showed samples of differing dispersity but helped in deciding on the best dispersed samples to use going forward in this work. Moreover, the behavior of these nanostructures in solution such as their hydrodynamic size, surface charge and mobilities agreed with the presence of functional groups determined from structural characterization techniques. Capillary electrophoresis was used to further characterize the synthesized QDs with regards to surface charge, size and extent of polydispersity of the samples in solution. However, the initial results showed the presence of a number of populations within one batch. The results obtained also showed that the samples had a high polydispersity which affected the separation efficiency. The synthetic protocols were then optimized focusing only on synthesis time. The synthesis optimization studies also showed that the synthesis time influences the quantum dots size, extent of functionality as well as in-solution behavior.

In addition, the QDs were conjugated and characterized successfully to the MPc molecules by $\pi\pi$ interactions as well as covalent bonding with regards to gCNQDs

and GQDs. These two-component systems will further be used to modify electrode surfaces as part of the process of developing the proposed aptasensors.

4. Electrode modification and characterization

This chapter outlines the electrode modification protocols as well as the characterization of these electrodes using surface characterization techniques and electrochemical methods. Methods of electrode modification include adsorption, electrodeposition, electrochemical grafting and click chemistry.

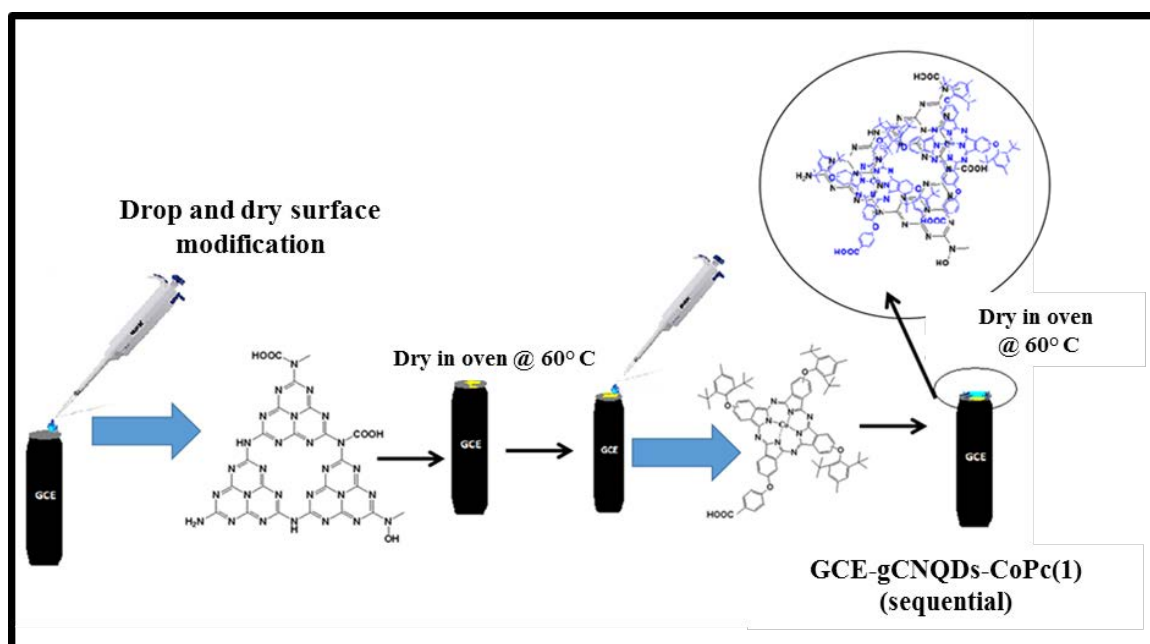
Table 4.1: List of modifiers and conjugates used for electrode fabrication.

Conjugates	ΔE (mV)	Γ ($\times 10^{-10}$ mol.cm⁻²)
Bare GCE	77	-
GQDs-CoPc (1) ($\pi\pi$)	161	0.09
<ul style="list-style-type: none"> • GQDs • CoPc(1) • GQDs-CoPc(1) (sequential) 	321 158 107	1.59 0.33 6.50
NGQDs-CoPc (1) ($\pi\pi$)	100.1	15.5
<ul style="list-style-type: none"> • NGQDs • NGQDs-CoPc(1) (sequential) 	466 615	3.1 8.2
gCNQDs-CoPc (1) ($\pi\pi$)	100	30.2
<ul style="list-style-type: none"> • gCNQDs • gCNQDs-CoPc(1) (sequential) 	90.4 174	39.3 12.0
GQDs-CoPc (1) ($\pi\pi$)-aptamer	361.5	2.99
NGQDs-CoPc (1) ($\pi\pi$)-aptamer	139.1	28.1
gCNQDs-CoPc (1) ($\pi\pi$)-aptamer	202.6	39.6
CoPc(1)@Aptamer	166	0.96
<ul style="list-style-type: none"> • CoPc(1)-Aptamer (sequential) • CoPc(1)-Aptamer (premixed) 	300 262	3.00 0.55
GQDs@Aptamer	617	1.99
<ul style="list-style-type: none"> • aptamer • GQDs-Aptamer (sequential) • GQDs-Aptamer (premixed) 	178 68 262	0.11 1.57 0.009
gCNQDs@Aptamer	292	-
gCNQDs@Aptamer-CoPc(1) ($\pi\pi$)	288	0.151
gCNQDs@Aptamer-CoPc(2) ($\pi\pi$)	356	0.215
<ul style="list-style-type: none"> • CoPc(2) 	169	0.066

4.1 Electrode modification by adsorption: Table 4.1

This method of electrode modification applies to the composites listed in Table 4.1 and depicted in Scheme 4.1 for gCNQDs-CoPc(1) (sequential) as an example. This includes the individual components as well as the covalently linked and $\pi\pi$ conjugated modifiers. Individual components were placed sequentially, by first placing the QDs on the electrode surface followed by the CoPc(1) or the aptamer. The components with aptamer were also premixed in addition to their sequential deposition onto the electrode surface. Literature has shown electrode modification using premixed composites, as well the sequential immobilization of nanostructures [195].

Preliminary studies of this work involved the study of the synthesized QDs and complex 1 as individual modifier and in combination, to determine the changes in current output. This was to validate the use of these nanocomposites as signal enhancers for the fabricated sensors towards the electrochemical detection of PSA.



Scheme 4.1: Example of GCE fabricated in this work using sequential drop-dry electrode modification.

4.1.1 Cyclic voltammetry

Cyclic voltammetry was used to characterize the electrode surface to better observe the electrochemical sensing capabilities of the modified electrodes. Peak separations are recorded in Table 4.1, which indicate that there has been a change on the electrode surface compared to that of the bare electrode.

To avoid congestion within one plot, only some of the cyclic voltammograms are shown in Fig. 4.1(a) where electrodes are tested in a 0.1 M KCl solution containing 1 mM ferricyanide (pH 7.5). Peaks near a potential of -0.5 V (I) are due to electrode modifiers associated with the redox processes of GQDs and have been observed before for modified electrodes containing GQDs [196]. GQDs possess oxygen-rich groups at the surface, which may result in their oxidation, making them good redox

mediators. Moreover, their tunability allows them to act as multivalent redox species. Moreover, peaks in the -0.5 V (I) region for electrodes containing CoPc(1) could be due to the $\text{Co}^{\text{II}}\text{Pc}^{-2}/\text{Co}^{\text{I}}\text{Pc}^{-2}$ redox couple [197]. The DNA also show the peaks in this region [198], hence a peak is observed for the aptamer alone. The peaks labelled (II) are due to $[\text{Fe}(\text{CN})_6]^{3-/4-}$ redox couple. Peaks at 0.70 V (III) can be assigned to ring based process in electrodes containing CoPc(1) [197]. However, the oxidation of amino acids such as guanine, which constitute the aptamer also occur in this region [199]. Although it may be of low intensity, the electrode containing aptamer alone also shows this peak (III). The lower ΔE_p is related to better charge transfer processes.

Comparing the different combinations of electrodes using GQDs and aptamer, the increase in ΔE_p is as follows: GCE-GQDs-Aptamer (sequential) (68 mV) < GCE-GQDs-Aptamer (premixed) (262 mV) < GCE-GQDs@Aptamer (617 mV), Table 4.1. These results show an improvement in charge transfer when the electrode is modified sequentially. The ΔE_p for GCE-GQDs-Aptamer (sequential) is near the Nernstian value. The GCE-GQDs@Aptamer with a higher ΔE_p , suggests bonding of the aptamer to more than one carboxylic acid functional group around the GQDs, hindering the GQDs from being able to mediate the transfer of electrons as it usually would when used to modify the electrode surface, therefore allowing for less electron transfer between the analytical solution and electrode. The GCE-GQDs-Aptamer (premixed) (262 mV) showing the second highest ΔE_p in this group indicates strong adsorption of aptamer on the GQDs thus hindering the electron transfer process compared to the sequentially modified electrode with the same components. The combination of the CoPc(1) with the aptamer showed a reverse trend where the increase in ΔE_p is as

follows: CoPc(1)-Aptamer (sequential) (300 mV) < CoPc(1)-Aptamer (premixed) (262 mV) < CoPc(1)@Aptamer (166 mV). This trend suggests that the CoPc(1) may not be lying flat on the electrode surface for the covalently linked molecule (CoPc(1)@Aptamer), leaving unmodified spaces to for charge transfer to take place. Thus, it can be said that the bonded aptamer does not passivate the electrode surface due to its orientation, as much as the aptamer on the surfaces of the premixed and sequential combinations does.

Of the QDs alone, the largest ΔE_p is observed for NGQDs (466 mV), showing poor charge transfer in ferricyanide, Table 4.1. The CoPc(1) alone has a ΔE_p of 158 mV, which improves in the presence of NGQDs when conjugated by $\pi\pi$ interactions. Moreover, in ferricyanide, the electrodes modified with combinations of QDs and MPcs by $\pi\pi$ interactions, compared to the sequentially combined modifiers, show a lower peak potential difference indicating better electrochemical sensing activity, in the absence of any analyte. Therefore, in ferricyanide, GCE-GQDs-CoPc(1)($\pi\pi$), GCE-NGQDs-CoPc(1)($\pi\pi$) and GCE-gCNQDs-CoPc(1)($\pi\pi$) perform as better electrocatalysts compared to GCE-GQDs-CoPc(1) (sequential), GCE-NGQDs-CoPc(1) (sequential) and GCE-gCNQDs-CoPc(1) (sequential).

It is also important to test all electrodes in the absence of the analyte to ensure there are no interferences with the detection of the analyte of interest in solution. Fig. 4.1(b) shows the responses of the selected electrodes in the buffer in the absence of analytes. The peaks observed in these studies can then be used to determine surface coverages of the fabricated electrodes. When determining the electrochemical properties of a modified electrode surface, non-specific adsorption is one of the factors that need to be considered, hence the determination of the

electrode surface coverage values (amount of modifier per square centimeter) in this work.

The Randles-Sevcik Eqn.4.1 can be applied on $[\text{Fe}(\text{CN})_6]^{3-/4}$ redox couple (Fig. 4.1(a)) to determine the effective electrode area.

$$I_p = 2.69 \times 10^5 n^{3/2} A C D^{1/2} v^{1/2} \quad (4.1)$$

where I_p , A , C , D , n , and v are the peak current, the effective surface area, concentration of $[\text{Fe}(\text{CN})_6]^{3-/4}$, diffusion coefficient of $[\text{Fe}(\text{CN})_6]^{3-/4}$, the number of electrons involved, and scan rate, respectively. The literature value for $D = 7.6 \times 10^{-6} \text{ cm}^2\text{s}^{-1}$ [200] for $[\text{Fe}(\text{CN})_6]^{3-/4}$ was used. By using the effective area of the modified electrodes determined using Eqn. (4.1) above, and the total charge determined by integrating the anodic peak area of peaks (ii) in Fig. 4.1(b) and then by employing Eqn. (4.2), surface coverages were calculated.

$$\Gamma = \frac{Q}{nFA} \quad (4.2)$$

where n is the number of electrons transferred (~ 1), F the Faraday constant ($96,485 \text{ C mol}^{-1}$), A is the effective surface area obtained from Eqn. (4.1) and Γ is the surface coverage. The surface coverages calculated are shown in Table 4.1 and were generally higher than the reported value for phthalocyanines lying flat on the surface of the electrode ($1 \times 10^{-10} \text{ mol cm}^{-2}$) [201]. The higher surface coverages imply the increase in the electrode surface area, which offers more sensing surface. For

CoPc(1) $\pi\pi$ linked with QDs, the GQDs containing electrodes show the lowest coverages followed by NGQDs, with the gCNQDs containing electrodes showing the highest values. This then means that the gCNQDs are expected to perform better. The NGQDs are expected to perform better than the GQDs due to the addition of heteroatoms (nitrogen atoms) to the pristine graphitic structure, which is known to enhance electrochemical sensing capabilities. Therefore, higher signal amplification is expected from the NGQDs-based electrode compared to the GQDs-based electrode. At first glance, better performance would be expected from the gCNQDs due to their predominantly nitrogen rich structure, as observed by the largest surface coverage value of the gCNQDs-CoPc(1)($\pi\pi$) modified electrode.

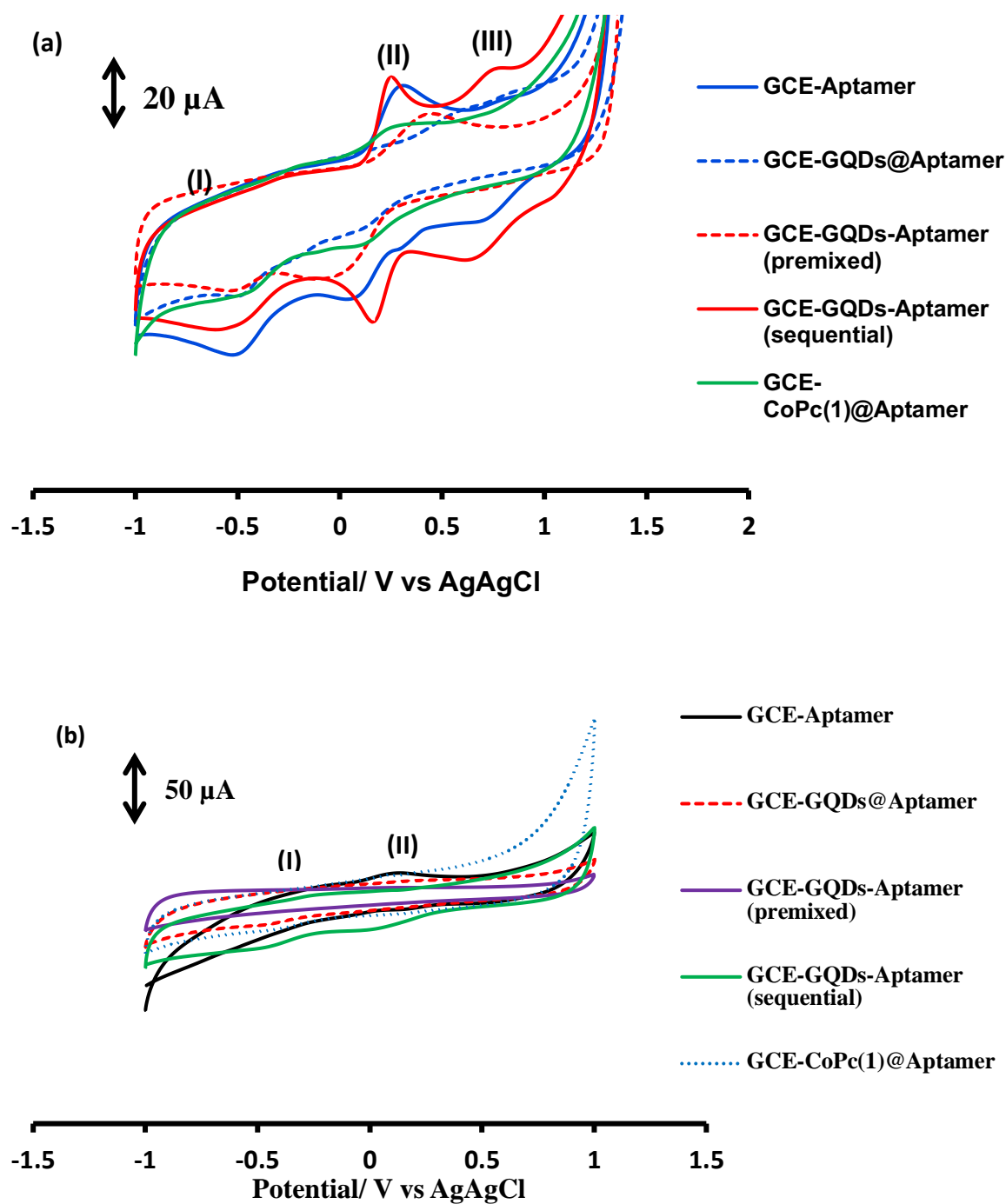


Figure 4.1: Electrodes in (a) 0.1M KCl containing 1mM $[\text{Fe}(\text{CN})_6]^{3-/4-}$ and (b) 30 mM PBS solution of pH 7.4. Scan rate =100 mV/s. (Starting potential of scans = -1.0 V).

Following the study of the effects of QDs structure on composition on the behavior of the aptasensor, complex 2 was introduced to determine the effects of MPC substitution on the aptasensor behavior while keeping the nature of the QDs constant. As an example, covalently linked gCNQDs@Aptamer was used as the constant and complex 1 and complex 2 incorporated onto the modifier by $\pi\pi$ interactions. These composites were immobilized on the electrode surface using the drop-dry method. The modified electrodes for this part of the study are listed in Table 4.1. A higher surface coverage was obtained for GCE-gCNQDs@Aptamer-CoPc(2) ($\pi\pi$).

4.1.2 SECM

SECM was used for further probing of the behaviour of the modified surfaces. The CoPc(1), QDs and aptamer composites are used as examples. The analyses were done in a ferricyanide solution as was done for cyclic voltammetry. Fig. 4.2 shows the approach curves which provide information on the changes in tip current as the ultra-micro electrode (UME) tip approaches the substrate glassy carbon plate (GCP) in a feedback mode experiment in the presence of $\text{Fe}^{2+}/\text{Fe}^{3+}$ redox mediator. The current generated at the tip of the electrode is determined by the substrate, the distance between the tip of the electrode and the substrate as well as the composition of the redox mediator. When the tip is closer to a conductive substrate surface, an increase in the current is observed while an insulating substrate is accompanied by a decline in the current [202].

The approach curves show an enhancement in current output of the QDs-CoPc(1)($\pi\pi$) compared to the bare GCP which contradicts the trends observed in ΔE_p values where

the bare GCE has a lower ΔE_p value which implies better conductivity. This contradiction may arise due to the nature of electrodes being used as well as the area in which the analysis is taking place, where greater aggregation may have occurred on the GCE surface compared to the analyzed area on the GC plate. In SECM, a GC plate is modified and a UME is used to analyze the conductivity of a specific area on the substrate in solution. With CV, the electrode is modified and used as the working electrode to determine extent of electron transfer between substrate and solution. These differences may be the reason contradictions are observed.

In summary, the approach curves obtained for the different surfaces show that the bare GCP as well as the surface modified with the QDs-CoPc(1)($\pi\pi$) conjugate are conducting, with increasing normalized current as the UME approaches the GCP surface. Once the aptamer is incorporated in all cases, a drop in current is observed. The aptamer evidently has a passivating effect on the electrode surface.

The area scans are shown in Fig. 4.3 for the bare GCP, GCP-QDs-CoPc(1)($\pi\pi$) and the GCP-QDs-CoPc(1)($\pi\pi$)-Aptamer. For QDs-CoPc(1)($\pi\pi$), there is a slight reduction in current of the modified region compared to the bare GCP, which may indicate passivation of the GCP surface upon modification, confirming ΔE_p values. When the aptamer is immobilized at the surface, the surface conductivity is further passivated which correlates with the results obtained for the approach curves. For NGQDs-CoPc(1)($\pi\pi$), and gCNQDs-CoPc(1)($\pi\pi$), there is an enhancement in surface conductivity compared to bare GCP, contradicting ΔE_p values as discussed for the approach curves as well. The current decreased however, upon immobilization of the aptamer, which was expected as the same trend was observed on the approach curves.

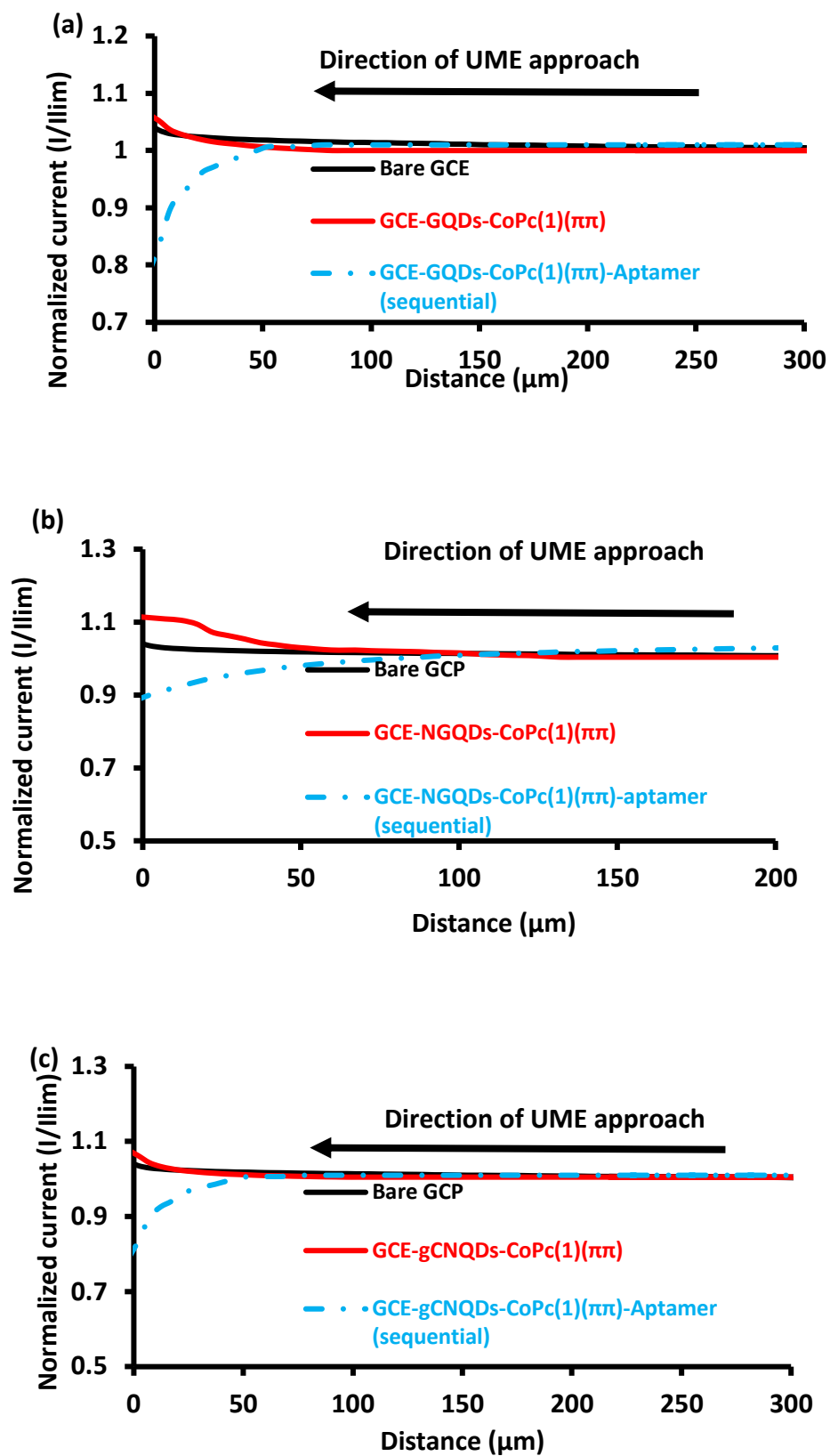


Figure 4.2: Approach curves of bare GCEs with (a) GQDs, (b) NGQDs and (c) gCNQDs based conjugates.

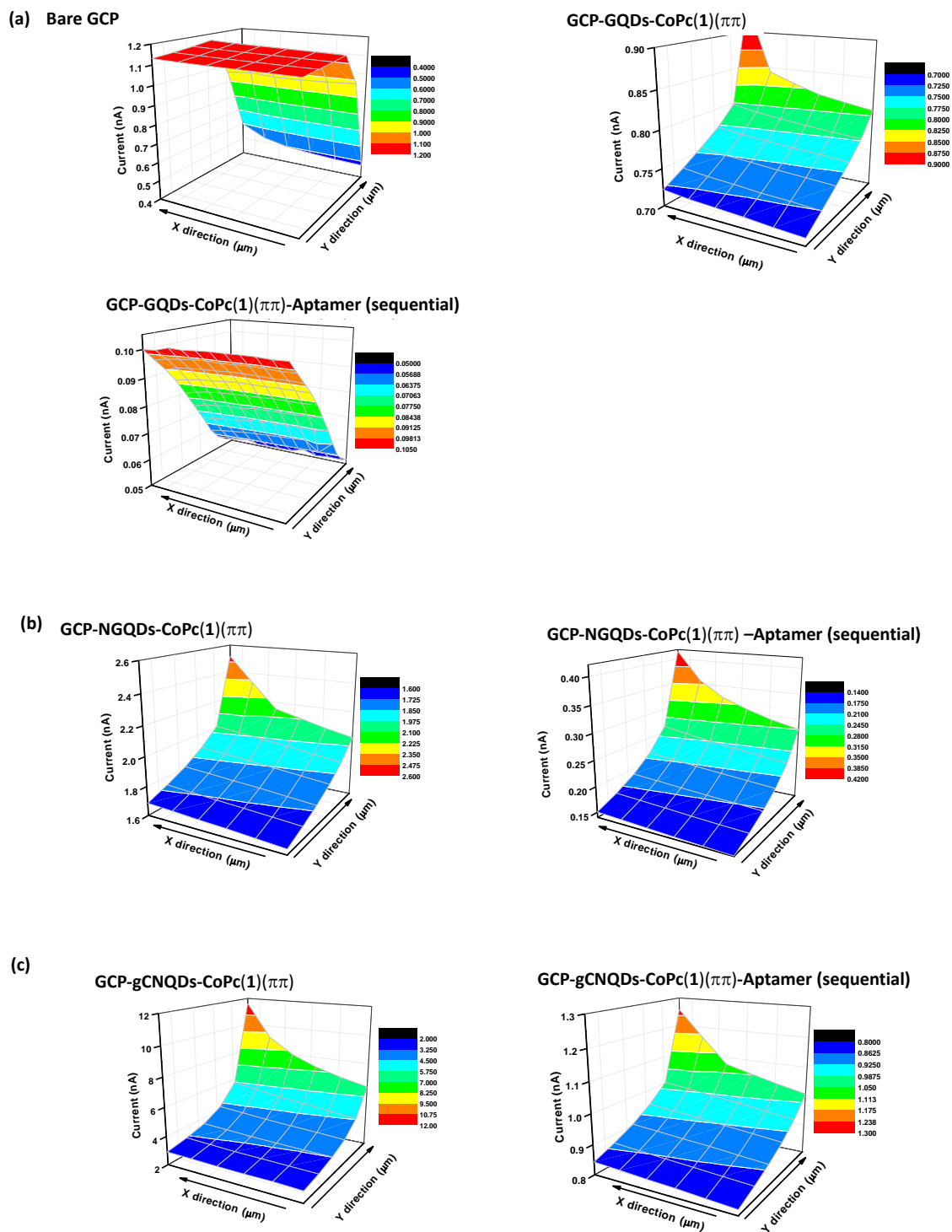
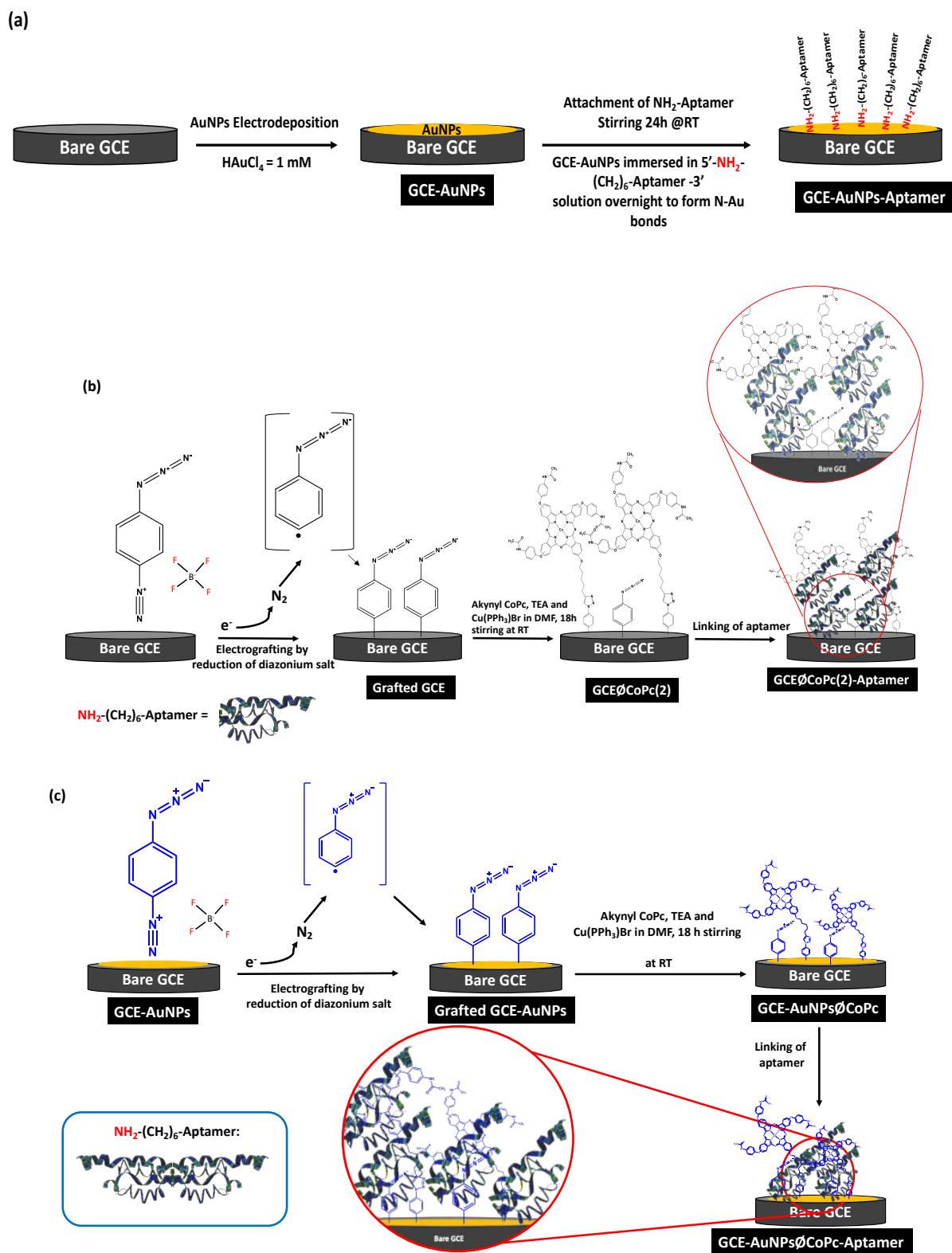


Figure 4.3: Area scans of bare GCPs with (a) GQDs, (b) NGQDs and (c) gCNQDs based conjugates.

4.2 Preparation and characterization of AuNPs, CoPc(2) and aptamer-based electrodes

This section shows the use of complex 2 and Au nanoparticles (AuNPs) as nanoplatforms for the immobilization of an aptamer to prepare novel aptasensors. The synergistic effects of these complex 2 and AuNPs are studied. Literature has shown the use of AuNPs-containing nanoconjugates as platforms for the immobilization of PSA-binding aptamer towards the detection of PSA [134, 141-144, 203]. These nanoconjugates have aided in improving the stability and sensitivity of the fabricated devices. Although these aptasensors have shown good promise as potential early diagnostic tools for PSA, the combination of electrodeposited AuNPs and phthalocyanines with aptamer, has not been studied, thus introducing another novel aspect to this thesis. Moreover, electrochemical grafting and click chemistry are employed, in order to fabricate these aptasensors. This technique has not been used to fabricate PSA aptasensors before. Scheme 4.2 Illustrates the fabricated aptasensors as well as the protocol followed in achieving this.

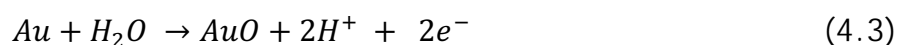


Scheme 4.2: Fabrication process of (a) GCE-AuNPs-aptamer, (b) GCE∅CoPc(2)-Aptamer and (c) GCE-AuNPs∅CoPc(2)-Aptamer.

4.2.1 Electrodeposition of AuNPs, Scheme 4.2(a)

4.2.1.1 Cyclic voltammetry

AuNPs were obtained via the electroreduction of the gold salt in 0.1 M NaNO₃ by cyclic 10 scans using the cyclic voltammetry technique shown in Fig. 4.4. After cycling, the electrode surface appeared gold in color confirming the success of the deposition (Fig. 4.4). The formation AuNPs is represented in Fig. 4.5. The forward scan shows the reduction of Au(III) to Au(0) with a cathodic peak at 0.41 V, resulting in the deposition of AuNPs onto the GCE surface (GCE-AuNPs), Fig. 4.4. Literature reports have recorded a value of 0.48 V, which is close to the value obtained in this work [165]. The decrease in current following electrodeposition has also been reported [165], which is due to the consumption of the gold salt. The electrodeposited AuNPs were then activated, following literature methods [165] using 0.5 M H₂SO₄ by cyclizing (10 scans) from 0.2 V to 1.4 V. Fig. 4.4(b) shows the cyclic voltammogram of the 10th scan. The anodic and cathodic peaks increased with the increase of the number of scans. The anodic peaks between 1.0 and 1.3 V correspond to Au oxidation. The presence of two oxidation peaks suggests the formation of different types of Au oxides. However, AuO is formed as the main oxide according to Eqn. (4.3):



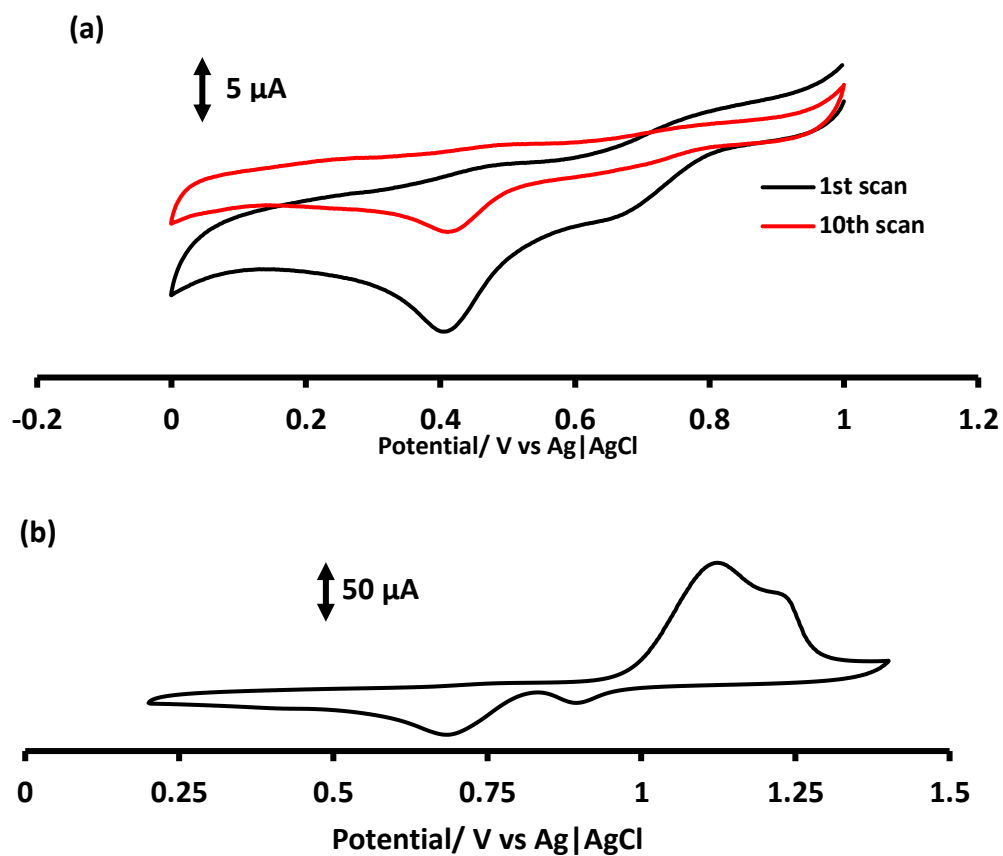


Figure 4.4: Cyclic voltammograms of (a) the first and the last scan of 1 mM HAuCl₄ in 0.1 M NaNO₃ (scan rate 50 mV/s) and (b) GCE-AuNPs in 0.5 M H₂SO₄ solution (activated AuNPs at scan rate= 100 mV/s).



Figure 4.5: Images of a bare GCE and the GCE after cycling in 1 mM HAuCl_4 in 0.1 M NaNO_3 .

4.2.1.2 Energy dispersive X-ray (EDX) spectroscopy and scanning electron microscopy (SEM)

To verify the formation of AuNPs on glassy carbon surfaces, scanning electron microscopy (SEM) was used to analyze a bare glassy carbon plate as well as the one modified with AuNPs. The GCP was modified in the same manner as the GCE was. Verification of the elemental composition at the substrate surface was achieved using EDX, illustrated by Fig. 4.6. In Fig. 4.6(a), the bare plate is shown with the EDX spectrum showing only carbon which is due to the carbon surface. The EDX spectrum in Fig. 4.6(b), shows the presence of Au. Fig. 4.6(b) also shows the SEM image of the electrodeposited AuNPs which appear well distributed spherical. The EDX spectrum confirms the presence of the AuNPs thus proving the success of the electrodeposition of these nanostructures on a glassy carbon plate.

The AuNPs formed by electrodeposition on the electrode surface were thereafter collected for UV characterization by sonicating the electrode in DMF. The color in DMF was pale purple as expected [204]. The absorption spectrum was obtained and is shown in Fig. 4.7. The absorption peak is recorded at 436 nm, which is surface plasmon resonance band.

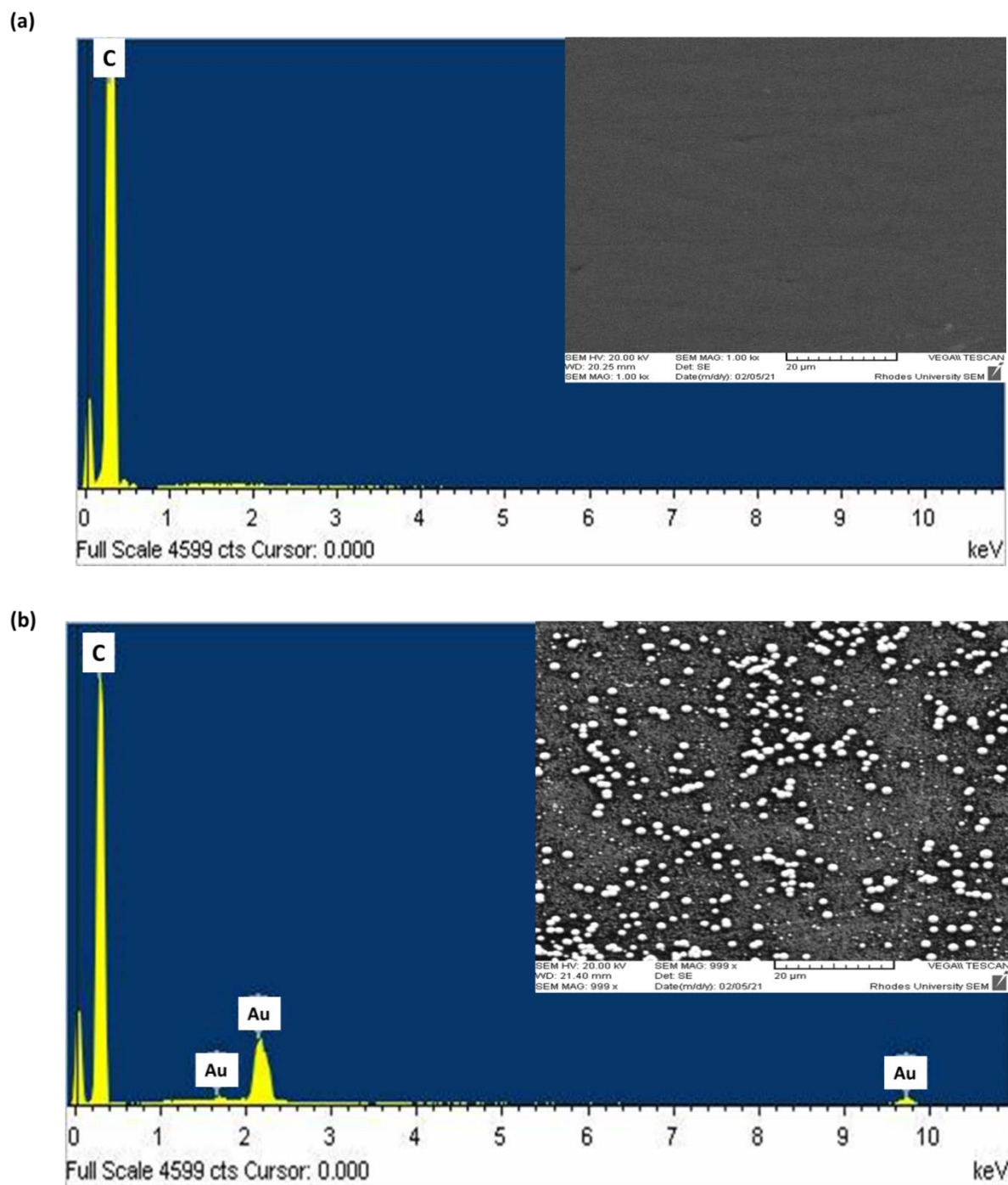


Figure 4.6: EDX analysis spectra of (a) Bare GCP and (b) GCP-AuNPs. Inserts: Corresponding SEM images.

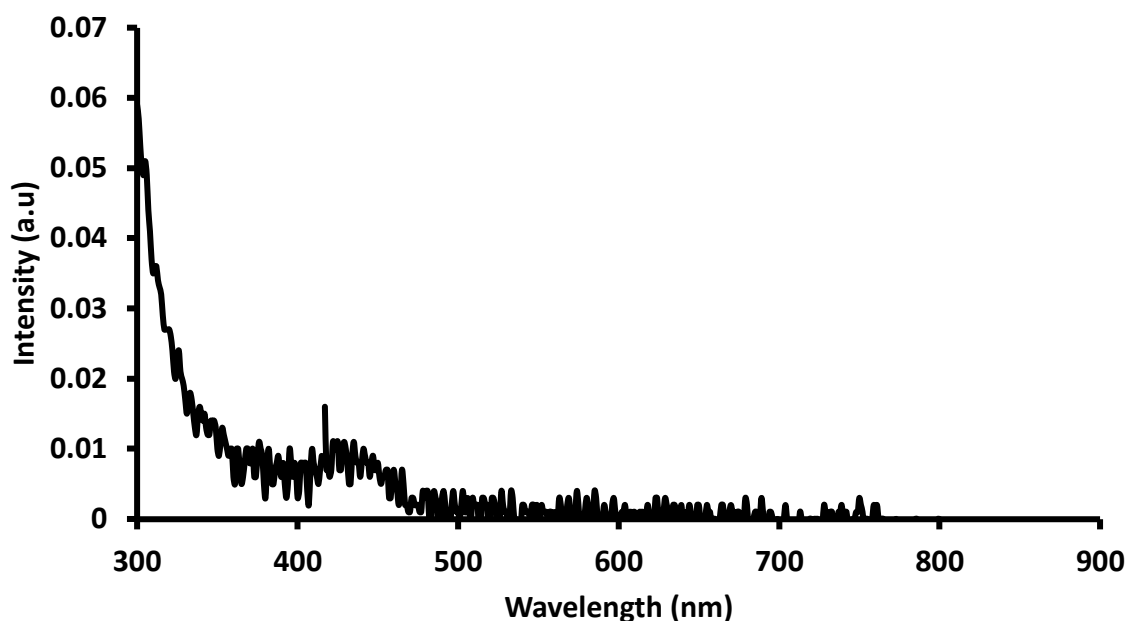


Figure 4.7: Absorption spectrum of AuNPs in DMF.

4.2.2 Self-assembly (Scheme 4.2(a)), electrochemical grafting and click chemistry, Scheme 4.2 (b, c)

The GCE-AuNPs was then linked to aptamer via the NH_2 functional group by self-assembly, as nitrogen is known to have an affinity for Au. Scheme 4.2(a) illustrated the fabrication of GCE-AuNPs-Aptamer. The evolution of the cycling voltammograms due to the electrografting of the GCE is shown in Fig. 4.8. This was achieved in a solution of 1 mM 4-azidobenzenediazonium tetrafluoroborate in 0.1 M TBABF_4 in acetonitrile, within a potential window of -1.0 V to 0.2 V at 50 mV/s. A reduction peak is observed at -0.79 V on the first cycle of the bare GCE and completely disappears on the 3rd cycle confirming passivation of the electrode surface by azide groups [205]. The gold surface was also electrografted the same way the bare GCE was. For the GCE-AuNPs, the reduction peak is also observed at around -0.79 V but the peak only disappears on the 5th cycle which is not uncommon [206]. The electrografting of gold surfaces has been reported in literature, however, the

reduction peak observed at -0.35 V [167]. Both the grafted GCE and the GCE-AuNPs were then linked to CoPc(2) via click chemistry to form GCE \emptyset CoPc(2) and GCE-AuNPs \emptyset CoPc(2). To immobilize the aptamer on these surfaces, the aptamer was adsorbed at the GCE \emptyset CoPc(2) and GCE-AuNPs \emptyset CoPc(2) surfaces to give GCE \emptyset CoPc(2)-Aptamer (Scheme 4.2 (b)) and GCE-AuNPs \emptyset CoPc(2)-Aptamer (Scheme 4.2(c)). Both electrodes were tested in an electroactive solution to confirm the passivation of their surface and the data reported in the next section.

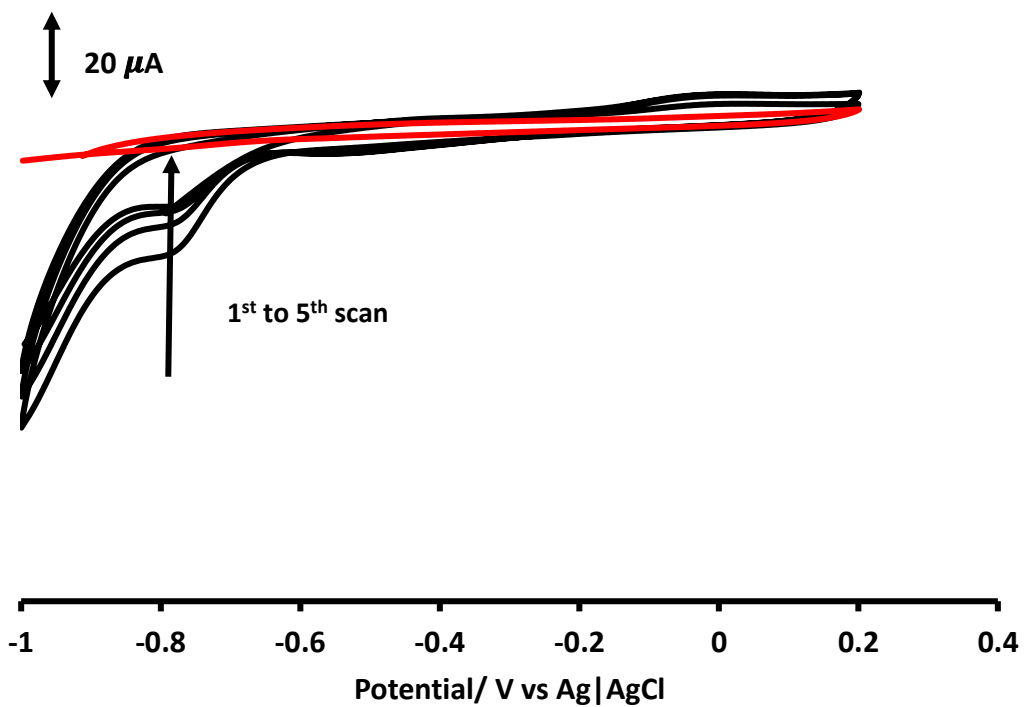
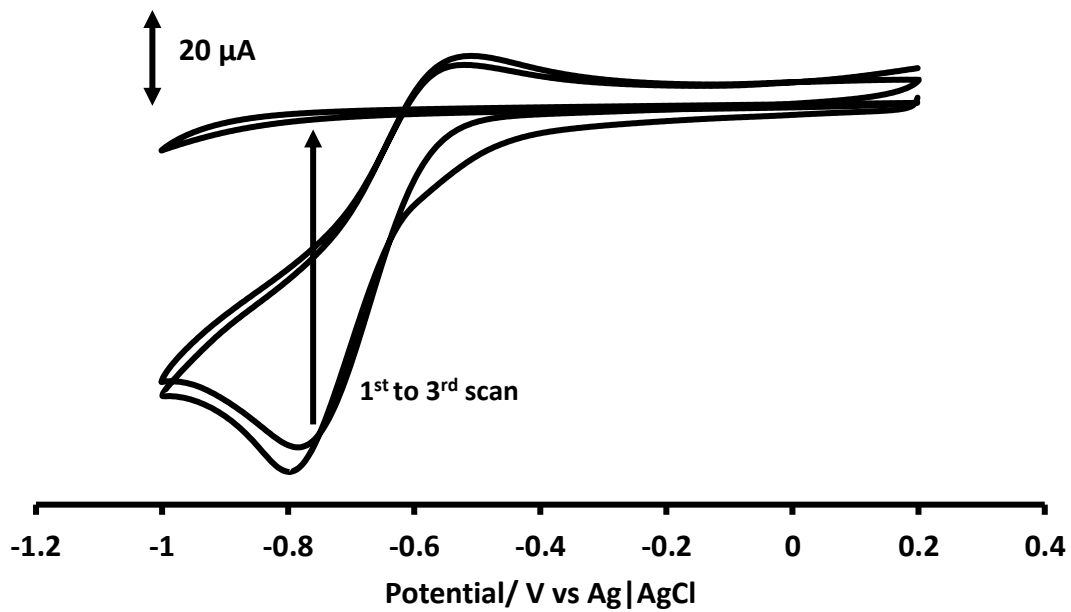


Figure 4.8: Cyclic voltammograms evolving during electrografting of (a) bare GCE and (b) GCE-AuNPs.

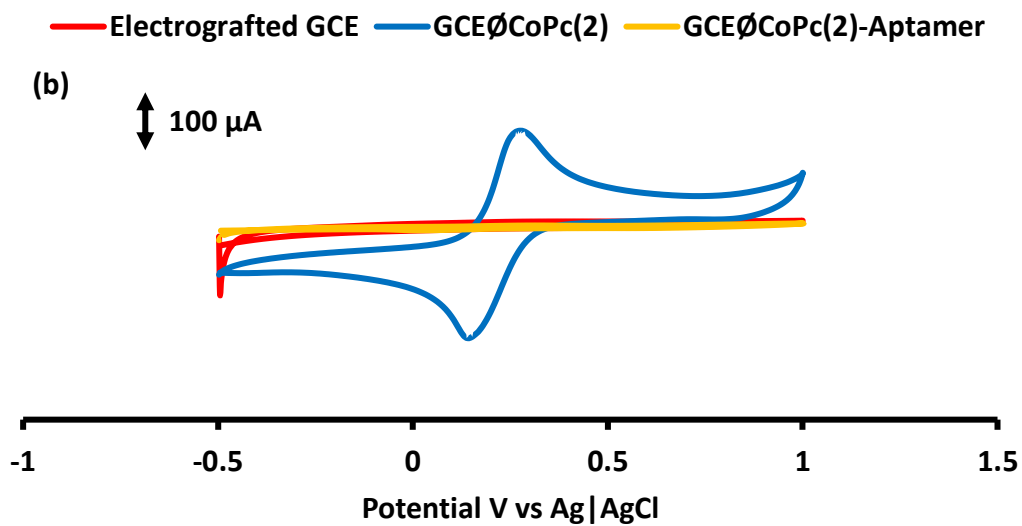
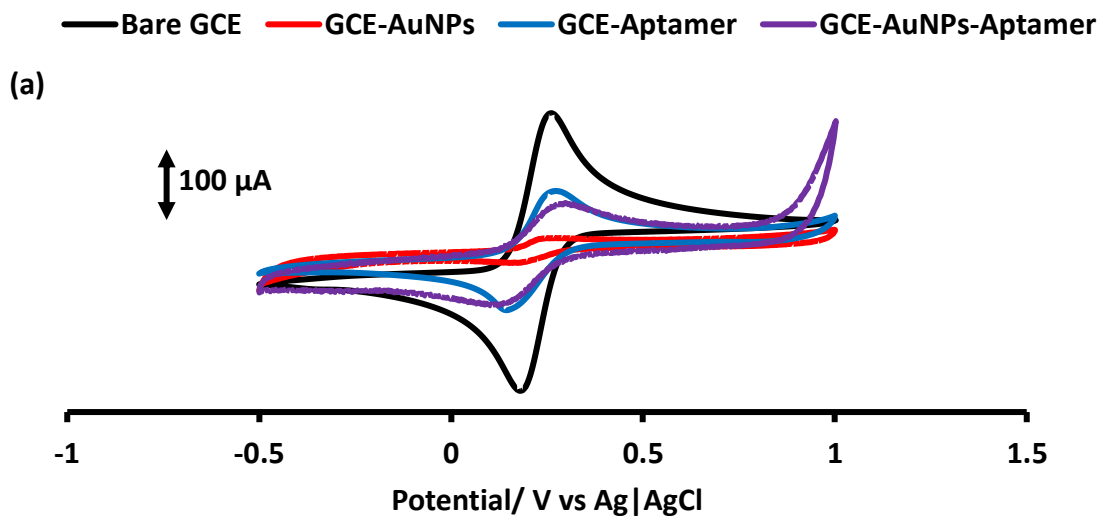
4.2.3 Cyclic voltammetry characterization

All the electrode surfaces were tested using cyclic voltammetry analysis in a 0.1 KCl solution containing 5 mM $K_3[Fe(CN)_6]$ and the results are shown in Fig. 4.9(a-c). From these figures, the peak separation values, ΔE , are recorded in Table 4.2. The modified electrodes were also tested in a buffer solution (PBS pH 7.4) before addition of the analyte and the selected CVs are shown in Fig. 4.9(d).

When looking at the results obtained from characterizing the electrodes in the ferricyanide solution, the aptamer was expected to passivate the electrode completely; however, results showed that there was still some current output, which is indicative of some exposed areas of the GCE after the modification of the surface, Fig. 4.9(a). Fig. 4.9(b) shows complete passivation due to grafting the electrode surface as well as when the aptamer is immobilized at the surface of the electrode. Fig. 4.9(c) shows that the combination of AuNPs and CoPc(2) enhances current output, and upon immobilization of the aptamer there is a significant decrease in the peak current indicating the success of immobilization of the aptamer on the electrode surface. From these cyclic voltammograms, ΔE values were determined. As previously mentioned, an increase in this value implies a decrease in current output due to blocking of electroactive sites at the electrode surface. The highest value was determined for GCE-AuNPs \emptyset CoPc(2)-Aptamer and the lowest value was obtained for the GCE-AuNPs \emptyset CoPc(2) which agree with what is observed in the voltammograms.

When the electrodes were studied in the buffer solution, no peaks were observed for the bare GCE, GCE-Aptamer, GCE \emptyset CoPc(2)-aptamer and GCE-AuNPs \emptyset CoPc(2)-Aptamer. The electrografted GCE showed very broad flattened peaks (data not shown) which indicated that there were still ungrafted parts of the electrode

surface. The peaks in the circled part of Fig. 4.9(d) could be due to $\text{Co}^{\text{III}}\text{Pc}^{-2}/\text{Co}^{\text{II}}\text{Pc}^{-2}$ processes in CoPc(2) containing electrodes. These peaks observed were quite broad and flattened but attempts to integrate them were made to estimate the surface coverage. The effective electrode area and surface coverages were calculated as done for the electrodes already mentioned in this chapter. The calculated parameters are summarized in Table 4.2. The highest surface coverage value was obtained for GCE-AuNPs/CoPc(2) indicating that the combination of the AuNPs with the phthalocyanine enhances the surface area of the electrode, which is what is needed in order to achieve the maximum output and efficiency of the sensor.



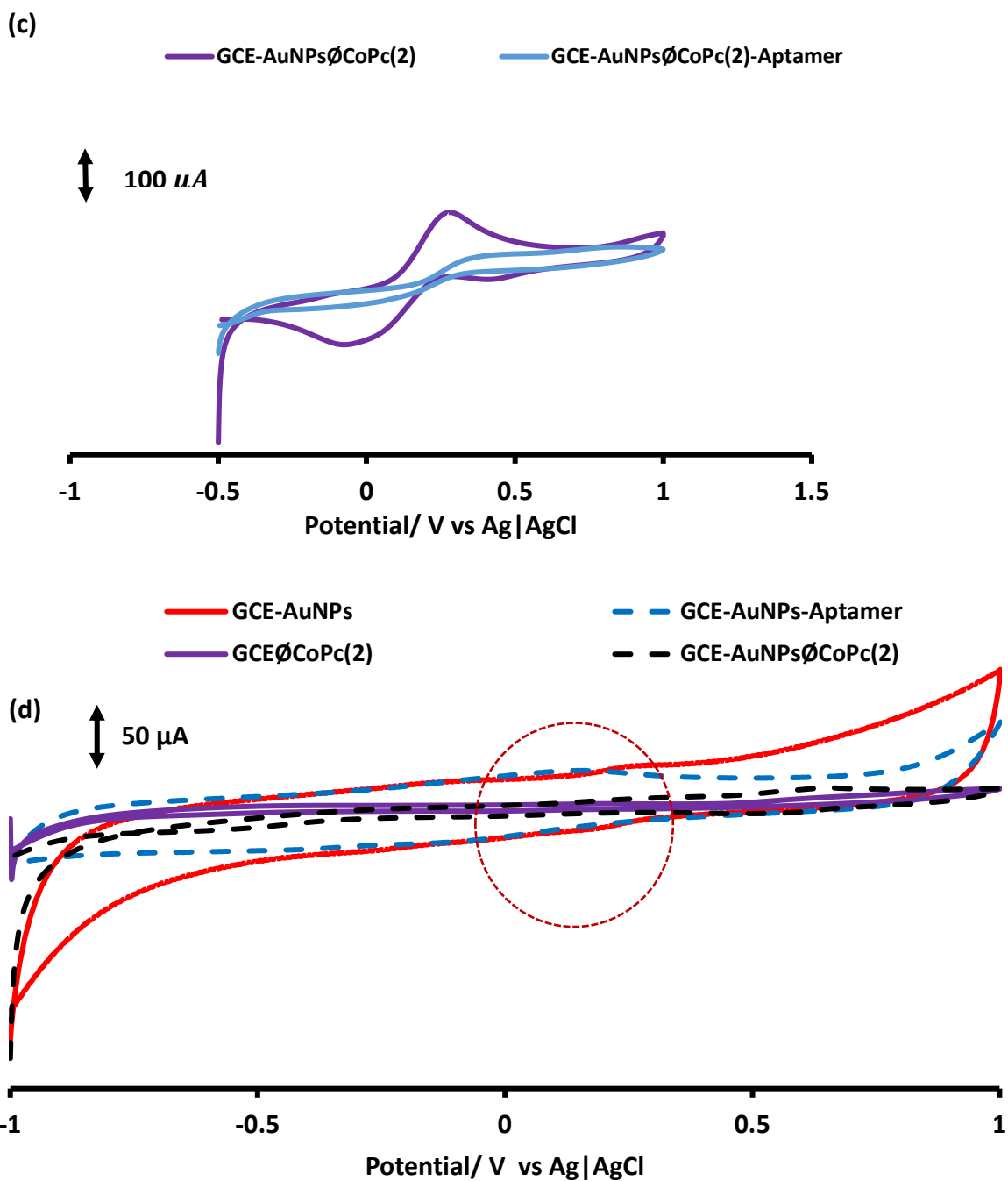


Figure 4.9: Cyclic voltammograms of bare and modified electrodes in (a), (b) and (c) 5 mM $K_3[Fe(CN)_6]$ containing 0.1 KCl solution containing and (d) in PBS solution pH 7.4. Scan rate = 100 mV/s.

Table 4.2: Summarized cyclic voltammetry data for the electrodes in 0.1M KCl containing 1mM $[\text{Fe}(\text{CN})_6]^{3-/4-}$ solution.

Electrode	$\Delta E/ \text{mV}$	$\Gamma \text{ mol.cm}^{-2} (\times 10^{-9})$ in K ₃ [Fe(CN) ₆] in 0.1 M KCl pH 7.4 buffer
Bare GCE	77	-
GCE-AuNPs	83	1.19
GCE-Aptamer	134	-
GCE-AuNPs-Aptamer	164	1.23
GCE \emptyset CoPc(2)	147	2.34
GCE \emptyset CoPc(2)-Aptamer	273	-
GCE-AuNPs \emptyset CoPc(2)	56	7.12
GCE-AuNPs \emptyset CoPc(2)-Aptamer	573	-

4.2.4 Scanning electrochemical microscopy (SECM) characterization

Further characterization of the modified surfaces was done using SECM. The studies were done in ferricyanide, as it is a conductive solution. Approach curves were recorded and are shown in Fig. 4.10. The bare and electrodes modified with AuNPs, CoPc(2) and AuNPs \emptyset CoPc(2) were conducting. The grafted electrodes showed a drop in normalized current as the UME approached the surface. This was expected and in agreement with the results obtained in the same solution using cyclic voltammetry as the analytical technique. The introduction of the aptamer also indicated a passivated surface.

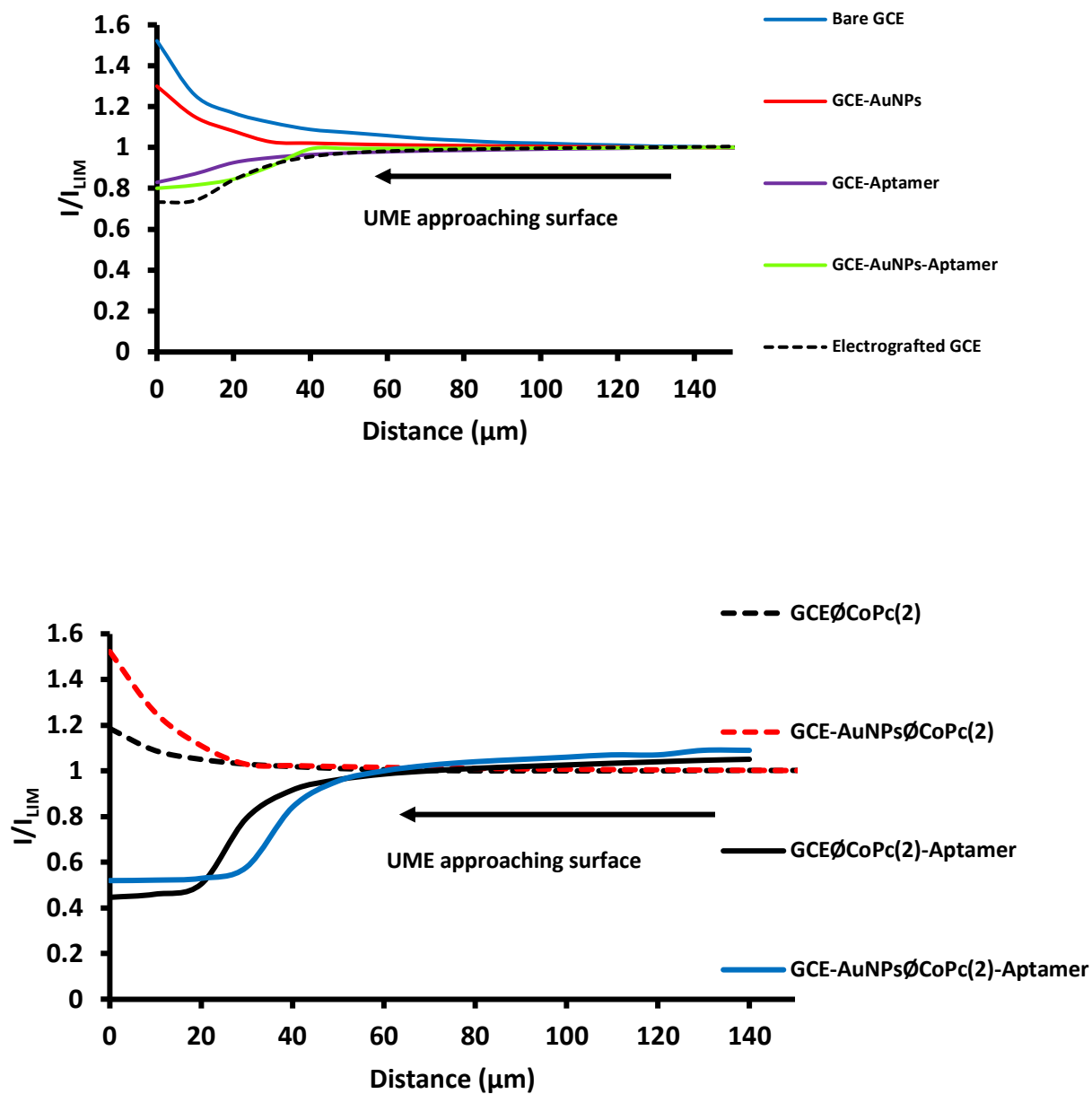


Figure 4.10: Approach curves of bare and modified electrodes in 0.1 KCl solution containing 5 mM $\text{K}_3[\text{Fe}(\text{CN})_6]$. Curves are plotted separately to avoid crowding on one plot.

4.2.5 XPS spectra

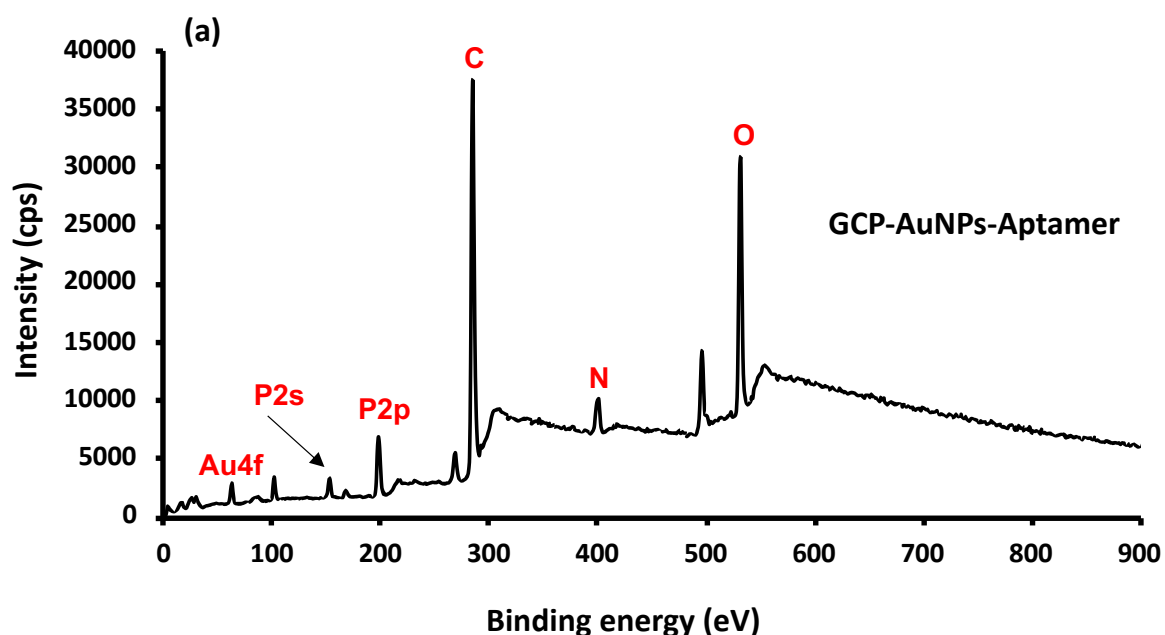
XPS analyses was carried out to validate some of the conjugations performed in the electrode fabrication process. Initially, wide scans were obtained to see if all expected elements were present on each fabricated surface. The survey scans of the fabricated aptasensors are shown in Fig. 4.11. The analyzed surfaces are the GCP-AuNPs-Aptamer, grafted AuNPs surface, grafted GCP, the GCP-AuNPs \emptyset CoPc(2)-Aptamer and the GCP \emptyset CoPc(2)-Aptamer. Fig. 4.11(a) shows the survey scan for GCP-AuNPs-aptamer sensor. All expected elements were observed as also reported in literature [207]. The nitrogen peak is likely due to the amine groups on the aptamer. The Au4f high resolution scan for GCP-AuNPs-Aptamer (Fig. 4.12(a)) was deconvoluted to assign the peaks associated with the expected AuN bond since N (in the aptamer) has an affinity for Au. Four peaks were extracted at binding energies of 84.0, 86.0, 87.5 and 89.6 eV, Table 4.3(a). These peaks have been assigned to AuN (Au4f_{5/2}), Au⁰ (Au4f_{5/2}), Au⁰ (Au4f_{7/2}) and Au4f_{7/2} (AuN) respectively [208]. The presence of AuN confirms that the aptamer is linked to AuNPs through the N groups on the aptamer.

Fig. 4.11(b) shows the survey scans for the electrografted GCP and GCP \emptyset CoPc(2)-aptamer. The presence of Co in the clicked surface at 683.8 eV was an indication of the presence of the CoPc(2) at the GCP surface. The P atom from the backbone of the aptamer, confirmed the adsorption of aptamer at the electrode surface. The high-resolution spectra of the N1s peaks (Fig. 4.12(b)) from the grafted and clicked electrode were extracted and deconvoluted to verify the success of the click reaction. The identified peaks and their assignments are summarized in Table 4.3(b) with the spectra shown in Fig. 4.12(b). The N1s spectrum of the grafted GCP showed

two peaks after deconvolution at binding energies of 399.5 and 402.5 eV which have been assigned to the azide nitrogen atoms of the terminal azide groups. The lower intensity peak at higher binding energy is due to the electron deficient central nitrogen [209]. The clicked surface showed four peaks after deconvolution at binding energies of 398.5, 399.5, 401.0 and 402.5 eV, Table 4.3 (b). The peaks due to the azide groups at 399.5 eV and 402.5 eV are still visible showing that not all azide groups were part of the click reaction. However, they were reduced to intensities of 7000 cps and 7400 cps respectively, compared to the intensities observed for the grafted GCP which were at 10800 cps and 8900 cps respectively. The lower intensities prove that some of the azide groups were 'clicked' to the alkynyl group of the MPc. The peaks at 398.5 and 401 eV have been assigned to N-N and N-C respectively [210].

Fig. 4.11(c) shows the survey scans of the grafted gold surface as well as the GCP-AuNPs/CoPc(2)-aptamer and grafted GCP-AuNPs. Herein, the appearance of Co on the clicked surface confirms the presence of the CoPc(2) on the electrode surface. However, the high intensity of the peaks due to Au over-shadow the peak expected after grafting due to nitrogen at 400 eV. The presence of nitrogen on the gold surface due to electrografting is only confirmed upon obtaining high-resolution scans shown in Fig. 4.12(c) for the grafted GCP-AuNPs with the peak assignments summarized in Table 4.3(c). To validate the success of the grafting process, the C1s spectra were extracted and deconvoluted for grafted GCP-AuNPs, Fig. 4.12(c). For the C1s spectrum, peaks were observed at 285.5, 287 and 289 eV. These peaks are attributed to C-N, C-Au bond, and C-C respectively [211]. The C-Au bond confirms the success of the electrografting process. The deconvoluted N1s spectrum was too broad to provide useful information.

Fig. 4.12(d) then shows the N1s spectrum of the clicked gold surface, with the peak assignments summarized in Table 4.3(c) for AuNPs@CoPc(2)-Aptamer. The N1s spectrum showed peaks at 400.0, 402.5 and 407.0 eV after deconvolution. The peaks at 400.0 (10 600 cps) and 402.5 eV (8500 cps) have been earlier assigned to azide peaks which also shows that not all azide groups were clicked to the MPC. The peak at 407 eV can be assigned to N=C which may be a contribution from the CoPc(2) at the surface. The N1s spectrum of the grafted gold surface also showed very high intensities of about 23 900 cps at around 400 eV (data not shown) therefore it can also be noted that the highly reduced N1s intensities from the grafted electrode to the clicked electrode indicates the success of the click reaction.



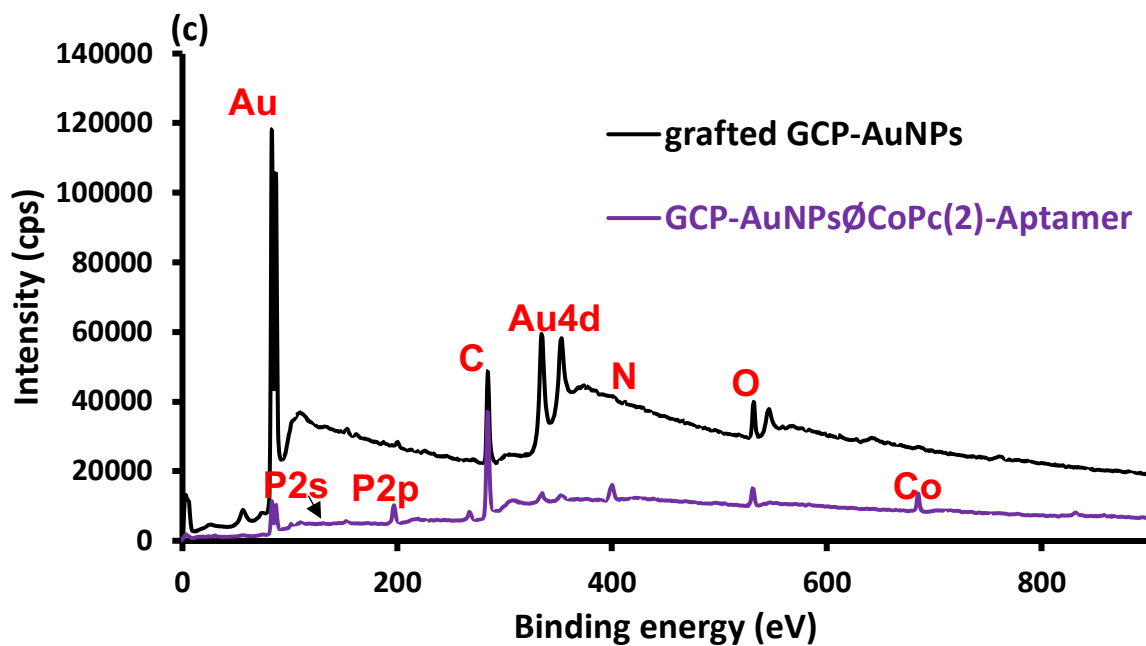
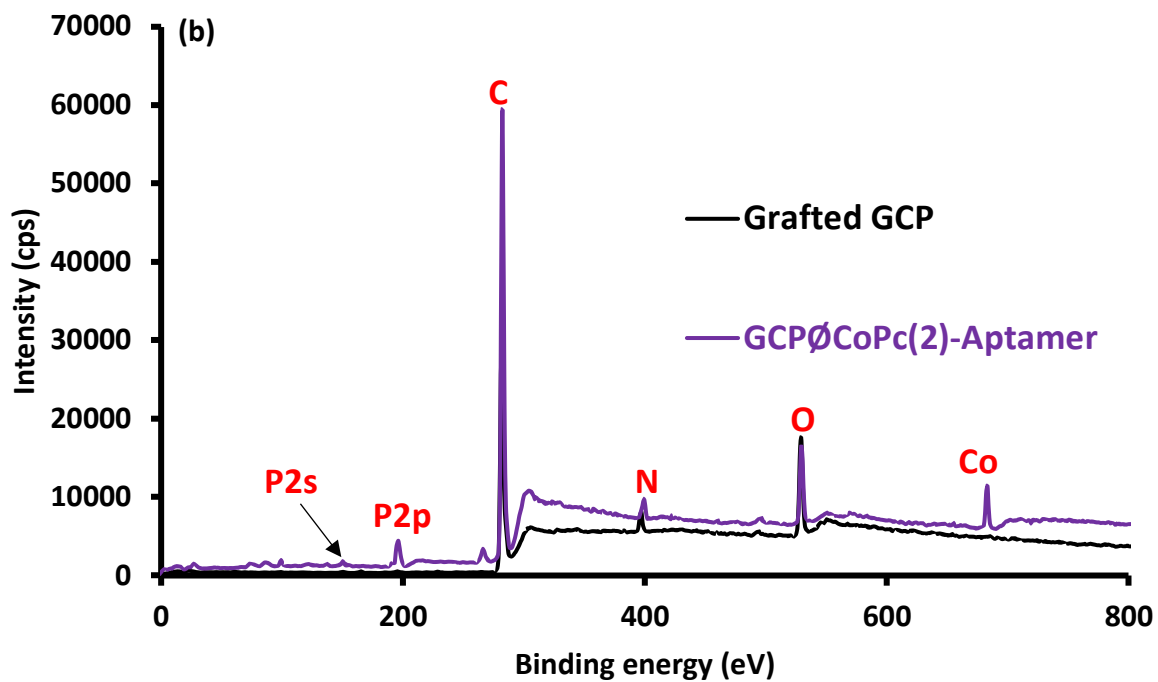
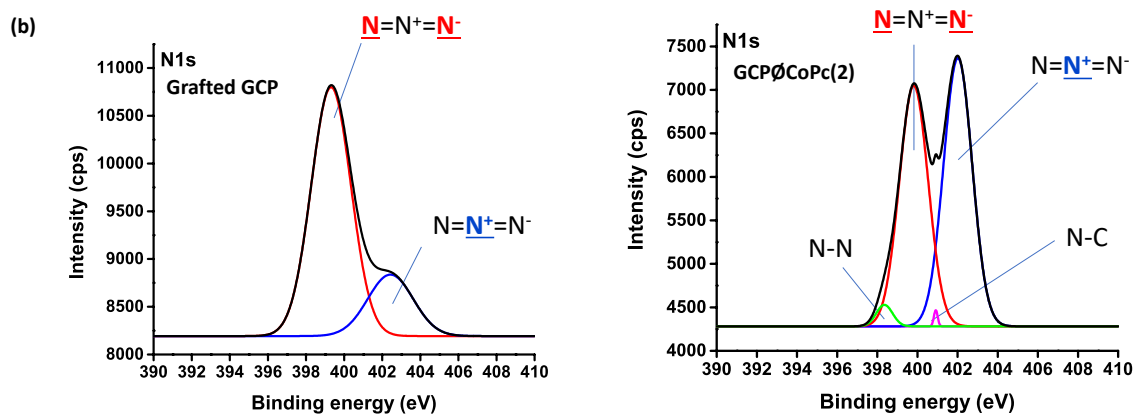
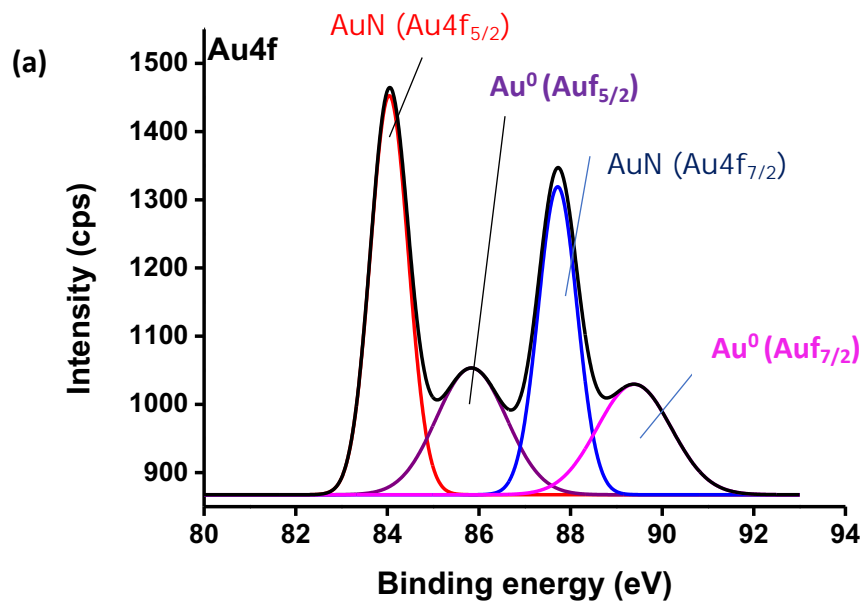
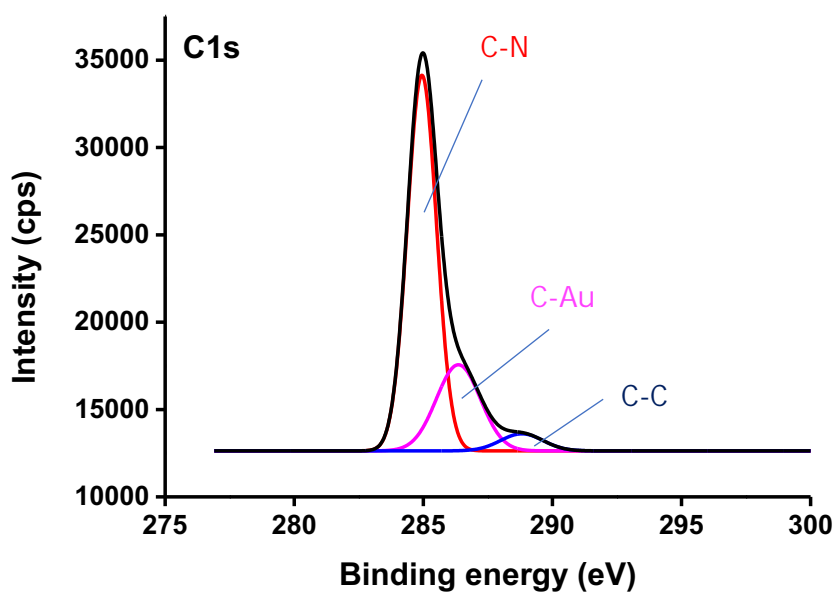


Figure 4.11: Survey scans of (a) GCP-AuNPs-Aptamer, (b) grafted GCP and GCP∅CoPc(2)-Aptamer and (c) grafted GCE -AuNPs and GCP-AuNPs∅CoPc(2)-Aptamer.



(c)



(d)

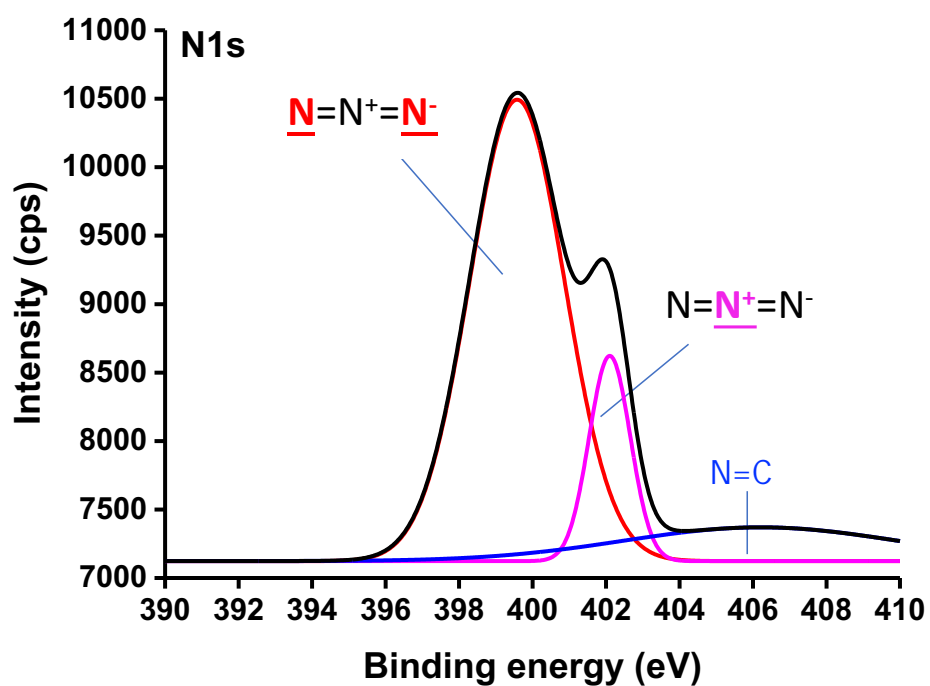


Figure 4.12: High resolution scans obtained for (a) Au4f of GCP-AuNPs-Aptamer, (b) N1s of Grafted GCP and GCP \emptyset CoPc(2) (c) C1s of grafted GCP-AuNPs and (d) N1s of GCP-AuNPs \emptyset CoPc(2).

Table 4.3(a): XPS peak assignments for electrode modification verification for GCP-AuNPs-Aptamer.

Surface	Element	Binding energy/ eV	Assignment
GCP-AuNPs-Aptamer	Au4f	84.0	AuN (Au4f _{5/2})
		86.0	Au ⁰ (Au4f _{5/2})
		87.5	AuN (Au4f _{7/2})
		89.6	Au ⁰ (Au4f _{7/2})

Table 4.3(b): XPS peak assignments for electrode modification verification for GCPØCoPc(2)-Aptamer

Surface	Element	Binding energy/ eV	Assignment
Grafted GCP	N1s	399.5	<u>N</u> =N ⁺ = <u>N</u>
		402.5	N= <u>N</u> ⁺ =N ⁻
GCPØCoPc(2)	N1s	398.5	N-N
		399.5	<u>N</u> =N ⁺ = <u>N</u>
		401.0	N-C
		402.5	N= <u>N</u> ⁺ =N ⁻

Table 4.3(c): XPS peak assignments for electrode modification verification for GCP-AuNPsØCoPc(2)-Aptamer.

Surface	Element	Binding energy/ eV	Assignment
Grafted GCP-AuNPs	C1s	285.5	C-N
		287.0	C-Au
		289.0	C-C
GCP-AuNPsØCoPc(2) (Clicked GCP-AuNPs)	N1s	400.0	<u>N=N⁺=N</u>
		402.5	N= <u>N⁺</u> =N ⁻
		407.0	N=C

4.3 Conclusions

GCEs and GCPs were used as immobilization platforms for composites with the aims of fabricating electrochemical sensors. Moreover, it was also proven that using QDs and AuNPs in combination with MPcs rather than individually resulted in enhanced signal output. The nature of the QDs affected the performance of the modified electrode. When AuNPs were combined with Complex 2 directly on the electrode surface, the synergistic effects were observed when the electrode surface was characterized. The electrode surfaces were successfully coated with AuNPs and complex 2 successfully clicked onto the bare GCE and GCE-AuNPs, followed by the adsorption of the PSA binding aptamer. When complex 1 and complex 2 were compared, they also showed different behavior, suggesting that the substituent of the MPc complexes does have an effect on the functionality of the sensor.

5. Electrochemical detection

Successful sensor fabrication was achieved by adsorption, electrodeposition, electrografting and click chemistry as discussed in Chapter 4. These fabricated sensors were then employed for the electrochemical detection of L-cysteine and PSA. The electrochemical detection of L-cysteine was carried out to prove the signal enhancement capabilities of the QDs-MPc conjugates rather than using these nanocomposites on their own. This is the first time an MPc or QDs are linked to an aptamer for the detection of PSA and it is the first time where all three (MPc, aptamer and QDs) are employed together for sensing. Moreover, the combination of AuNPs and MPc using electrografting and click chemistry for PSA sensing is employed here for the first time using complex 2.

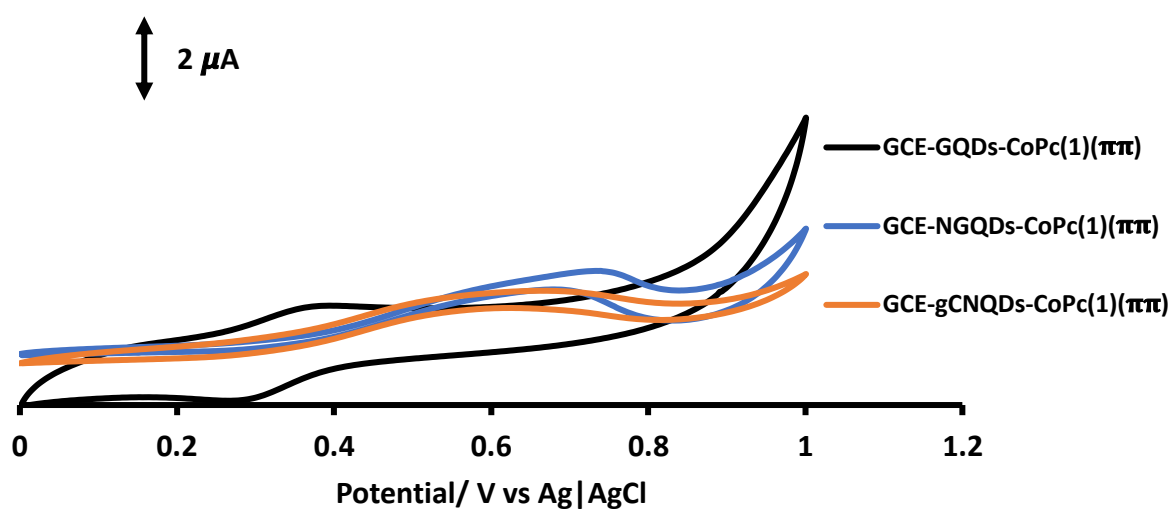
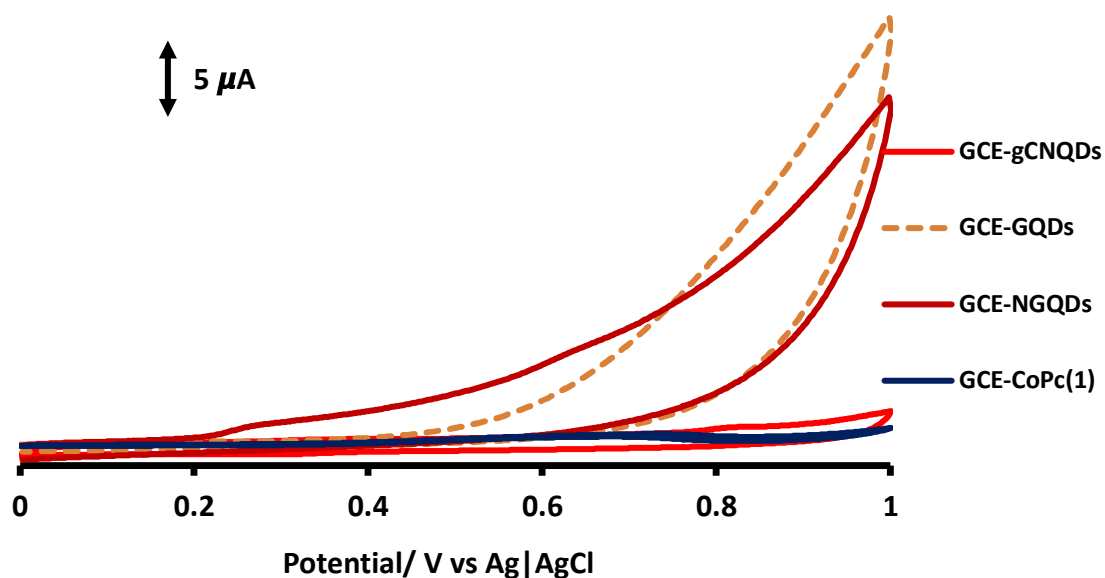
5.1 Electrochemical detection of L-cysteine

Complex (1), the selected QDs and their conjugates were immobilized on a GCE and tested in a buffer solution containing L-cysteine to further prove the improved electrochemical sensing capabilities or signal response, as opposed to using them as individual components. These results are also shown to validate the use of these conjugates as signal amplifiers for the PSA aptasensors and determine the best QDs for this application. L-cysteine is used as a test analyte since it is also later used for selectivity studies using the mixed solutions methods.

5.1.1 Cyclic voltammetry

In this study, L-cysteine is analyzed in a buffer solution of pH 4 due to good solubility of analyte at this pH. Fig. 5.1 shows the responses of the modified electrodes in the presence of 2 mM L-cysteine. Double oxidation peaks were observed for GCE-CoPc(1) as well as the electrodes modified sequentially using the NGQDs, gCNQDs and CoPc(1). The gCNQDs show a small peak at a potential of 0.83 V, Table 5.1, which is attributable to the electrochemical sensing of L-cysteine. The NGQDs also show an oxidation peak at 0.28 V with the GQDs showing no interpretable peaks in the presence of the analyte. As explained in previous studies, the oxidation on both the forward and reverse scans is attributed to regeneration of the active catalyst responsible for the oxidation of L-cysteine [212]. The GCE-GQDs-CoPc(1)($\pi\pi$), GCE-NGQDs-CoPc(1)($\pi\pi$) and GCE-gCNQDs-CoPc(1)($\pi\pi$) showed peak potentials at 0.38, 0.76 and 0.61 V, respectively. Compared to the sequentially modified electrodes, the drastic shift was observed for the GQDs-based electrode where the peak potential was 0.61 V but shifted to 0.38 V when the GQDs and CoPc(1) were combined by $\pi\pi$ interactions. The sequentially modified electrodes in general, show

a higher current response than their counterparts combined by $\pi\pi$ interactions. The mechanism behind the electrochemical sensing of L-cysteine by CoPc's has been reported in literature [213].



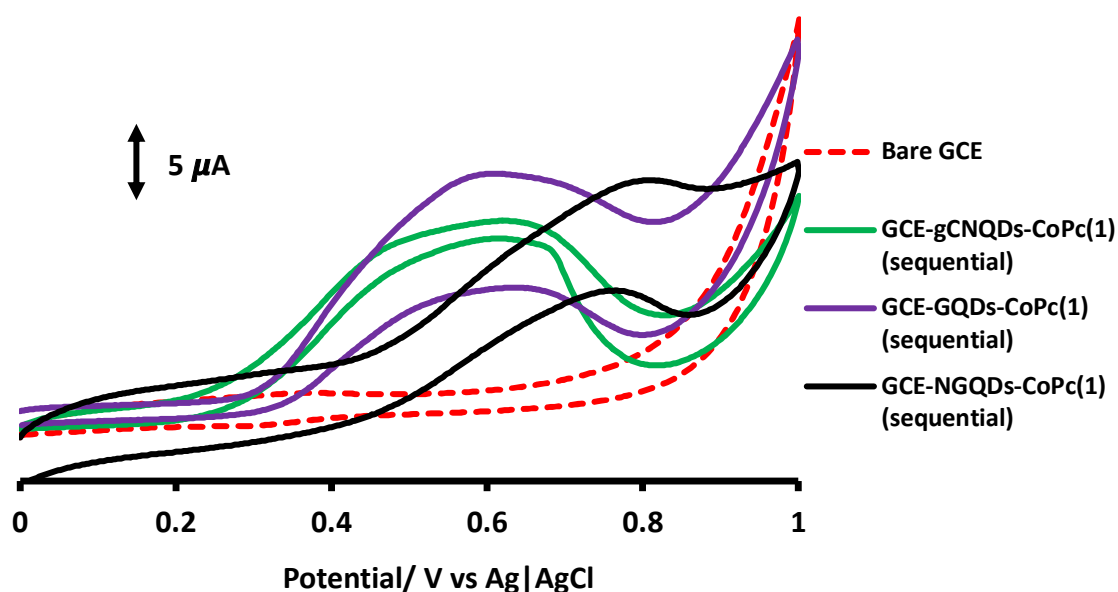


Figure 5.1: Cyclic voltammograms of de-aerated pH 4 buffer solution in the presence of 2 mM L-cysteine. Scan rate= 100 mV/s.(Plots separated for better visibility of peaks).

5.1.2 Chronoamperometry

Chronoamperometry allows for the determination of the behavior of the electrocatalysts employed in the presence of the analyte at different concentrations and how the sensing effects evolve with increasing concentration of the analyte of interest.

Fig. 5.2(a) shows the chronoamperograms obtained from electrochemical sensing responses of gCNQDs-CoPc(1) (sequential) as an example, in the presence of L-cysteine at different concentrations. The potential was held constant at 0.6 V vs Ag/AgCl for the gCNQDs and GQDs based electrodes and at 0.8 V vs Ag/AgCl for the electrode containing NGQDs, based on Fig. 5.1. Linear responses of concentration vs current response are observed as illustrated in Fig. 5.2(b). The limits of detection (LOD) were obtained using $3\delta/\text{slope}$ ratio notation, where δ is the standard deviation

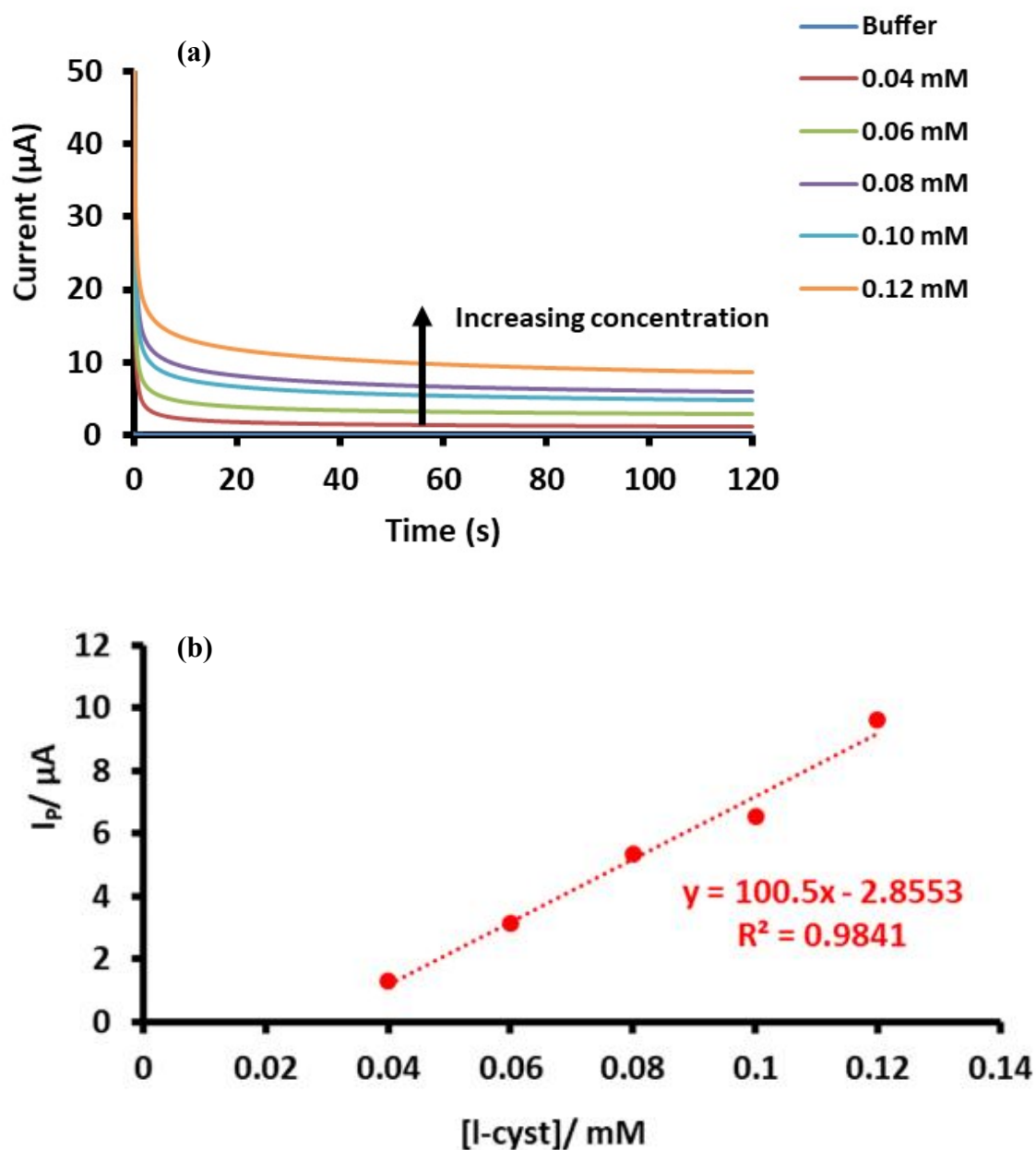
and 3 is a recommended factor that gives a practical confidence of 90 % to 99.7 % [214]. The sensitivity of the sensors were determined as 38.2 $\mu\text{A}\cdot\text{mM}^{-1}$ and the limit of detection (LoD) as 0.16 μM for GCE-GQDs-CoPc(1) (sequential), 39.9 $\mu\text{A}\cdot\text{mM}^{-1}$ and 0.11 μM for GCE-NGQDs-CoPc (1) (sequential) and 100.5 $\mu\text{A}\cdot\text{mM}^{-1}$, 0.02 μM for GCE-gCNQDs-CoPc(1) (sequential), 12.4 $\mu\text{A}\cdot\text{mM}^{-1}$ and 1.09 μM for GCE-GQDs-CoPc(1)($\pi\pi$), 18.6 $\mu\text{A}\cdot\text{mM}^{-1}$ and 0.52 μM for GCE-NGQDs-CoPc(1)($\pi\pi$) and 23.4 $\mu\text{A}\cdot\text{mM}^{-1}$ and 0.41 μM for GCE-gCNQDs-CoPc(1)($\pi\pi$). It is evident that the sequentially modified surfaces performed better than their $\pi\pi$ counterparts. Table 5.2. The LoD is the lowest on GCE-gCNQDs-CoPc(1) (sequential). Fig. 5.2(c) shows plots of I_{cat}/I_{buf} versus $t^{1/2}$ for the sequentially modified electrodes that are useful for the determination of the rate constant according to Eqn. (5.1) [215]:

$$\frac{I_{cat}}{I_{buf}} = \gamma^{1/2} \pi^{1/2} = \pi^{1/2} (k_{cat} C t)^{1/2} \quad (5.1)$$

where I_{cat} and I_{buf} are currents in the presence and absence of L-cysteine respectively, k_{cat} is the catalytic rate constant, C is the concentration of L-cysteine and t is the time elapsed in seconds. By plotting the square of the slopes obtained from Fig. 5.2(c) for GCE-gCNQDs-CoPc(1) (sequential) versus concentration of the analyte, a linear relationship may be observed (Fig. 5.2(d)) and is represented by Eqns. (5.2):

$$y = 2, [L\text{-cysteine}](s^{-1}mM) - 0.4238s^{-1}, R^2 = 0.8545 \quad (5.2)$$

where the slope of this plot is equivalent to πk . The value of k_{cat} in this work was found to be $1.3 \times 10^5 \text{ M}^{-1} \text{ s}^{-1}$ for GCE-GQDs-CoPc(1) (sequential), $3.9 \times 10^5 \text{ M}^{-1} \text{ s}^{-1}$ for GCE-NGQDs-CoPc(1) (sequential) and $1.0 \times 10^7 \text{ M}^{-1} \cdot \text{s}^{-1}$ for GCE-gCNQDs-CoPc(1) (sequential), Table 5.1. Here again, the electrode containing the gCNQDs shows better results than the other surfaces.



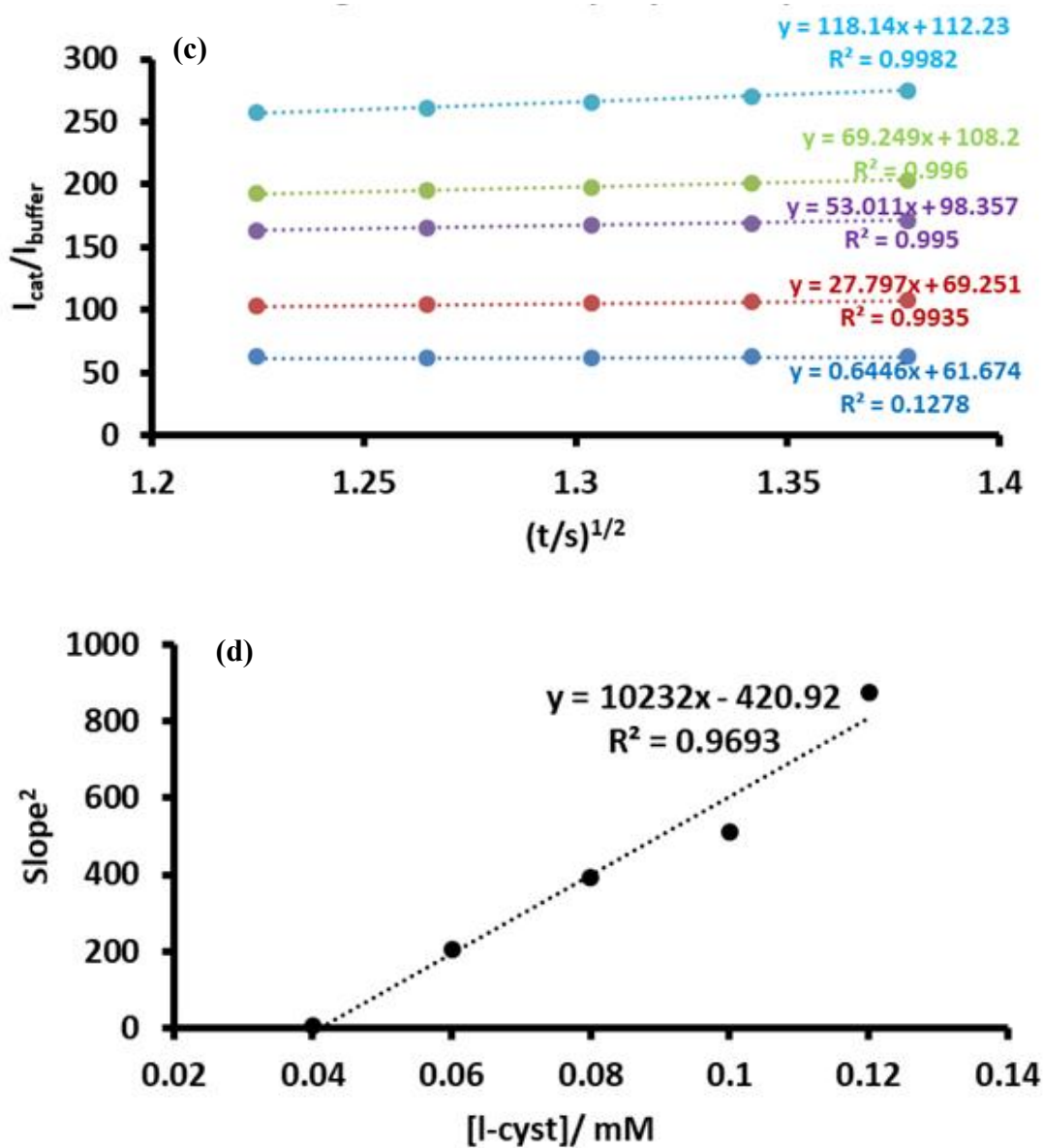


Figure 5.2: (a) Chronoamperograms of modified electrodes in pH₄ buffer with L-cysteine concentration ranging from 0.04-0.12 mM, and plots of [L-cysteine] vs I_p . Scan rate= 100 mV/s. (b) I_{cat}/I_{buffer} vs \sqrt{t} and plots of $Slope^2$ vs concentration of analyte. GCE-gCNQDs-CoPc(1) (sequential) used as an example.

Table 5.2 then compares the best electrode surface obtained in this work used for the electrooxidation of L-cysteine with other fabricated electrodes for the detection of L-cysteine reported in literature [195, 216-218]. To highlight an important difference, one report [216] has used multiwalled carbon nanotubes (MWCNTs) and a tetrasubstituted phthalocyanine (symmetrical) whereas in this work gCNQDs quantum dots with a predominant nitrogen rich structure and an asymmetrical phthalocyanine. As stated in the introduction of this work, asymmetry improves electrochemical sensing behavior of porphyrin-type complexes and the presence of nitrogen in the gCNQDs results in an electron rich structure which is expected to enhance the electrochemical sensing activity of MPCs to a larger extent than QDs which are also carbon based nanostructures, therefore it is expected that the combination of the novel asymmetric CoPc(1) and the gCNQDs to be an improved electrocatalyst for the electrooxidation of L-cysteine compared to some literature reports.

Table 5.1: Summary of determined characteristics of fabricated electrodes for L-cysteine detection in this work.

GCE surface	E_p (V) (L-cysteine)	Background corrected current (μA)	$k_{\text{cat}}/\text{M}^{-1}\text{s}^{-1}$	LoD/ μM	Sensitivity/ $\mu\text{A}\cdot\text{mM}^{-1}$
CoPc(1)	0.74	1.53	1.9×10^4	0.96	0.65
GQDs	No peak	No peak	1.3×10^3	112.1	2.5
GCE-GQDs-CoPc(1) (sequential)	0.61	8.64	1.3×10^5	0.16	38.2
GCE-GQDs-CoPc(1) ($\pi\pi$)	0.38	3.38	5.4×10^5	1.09	12.4
NGQDs	0.28	2.92	2.01×10^3	109.3	2.9
GCE-NGQDs-CoPc(1) (sequential)	0.80	8.62	3.9×10^5	0.11	39.9
GCE-NGQDs-CoPc(1) ($\pi\pi$)	0.76	3.95	4.2×10^5	0.52	18.6
gCNQDs	0.83	1.85	3.1×10^3	101.3	3.5
GCE-gCNQDs-CoPc(1) (sequential)	0.63	8.46	1.0×10^7	0.02	100.5
GCE-gCNQDs-CoPc(1) ($\pi\pi$)	0.61	3.62	2.2×10^6	0.41	23.4

Table 5.2: Comparison of results obtained for L-cysteine electrochemical sensing by sequentially modified electrode surfaces in this work and those reported in literature.

Electrode surface	LoD/ μM	Sensitivity/ $\mu\text{A.mM}^{-1}$	Reference
GCE-gCNQDs-CoPc(1) (sequential)	0.02	100.5	This work
GCE-GQDs-CoPc(1) (sequential)	0.16	38.2	This work
GCE-NGQDs-CoPc(1)(sequential)	0.11	39.9	This work
CoTAPc-MWCNTs-GCE(sequential)	0.28	0.0007×10^{-6}	[195]
MWCNT-FeTsPc-GCE	1.00	0.175	[216]
PPy- MWCNT-CoPc	200	1.15	[217]
CoPc-SPEs	4.00	0.78	[218]

Abbreviations: Multiwalled carbon nanotubes (MWCNTs), polypyridine (PPy), screen printed electrodes (SPEs)

5.1.3. Kinetics: Scan rate studies

The response of the modified electrodes was observed as the scan rate was increased. An increase in current response was observed with increasing scan rate, Fig. 5.3(a). From these results, the peak current was plotted against the scan rate (I_p vs v), the peak potential against the log of scan rate (E_p vs $\log v$) and the peak current was plotted against the square root of the scan rate (I_p vs $v^{1/2}$) shown by Fig 5.3 (b). The linear relationship observed in the plot of I_p vs $v^{1/2}$ suggests that the catalytic response of the electrode is an irreversible diffusion-controlled process [216].

The plot of E_p vs $\log v$ gave a linear relationship (for which is a characteristic of an irreversible diffusion-controlled process) and allows for the determination of the Tafel slope, Eqn. (5.3) [217]:

$$E_p = \frac{b}{2} \log v + K \quad (5.3)$$

Where b is the Tafel slope and v is the scan rate. The gradient of the slope can be defined as $\frac{b}{2}$. The Tafel slopes for the electrodes modified with GODs-CoPc(1) ($\pi\pi$), NGQDs-CoPc(1)($\pi\pi$) and gCNQDs-CoPc(1)($\pi\pi$) were determined as 143, 217 and 73 mV/decade respectively. The determined value for the gCNQDs based electrode lies in the expected range of 30-120 mV/decade since it has shown the best performance throughout the studies conducted in this work. Moreover, low Tafel slopes are an indication of high current density at low potentials which is ideal for a good electrocatalyst.

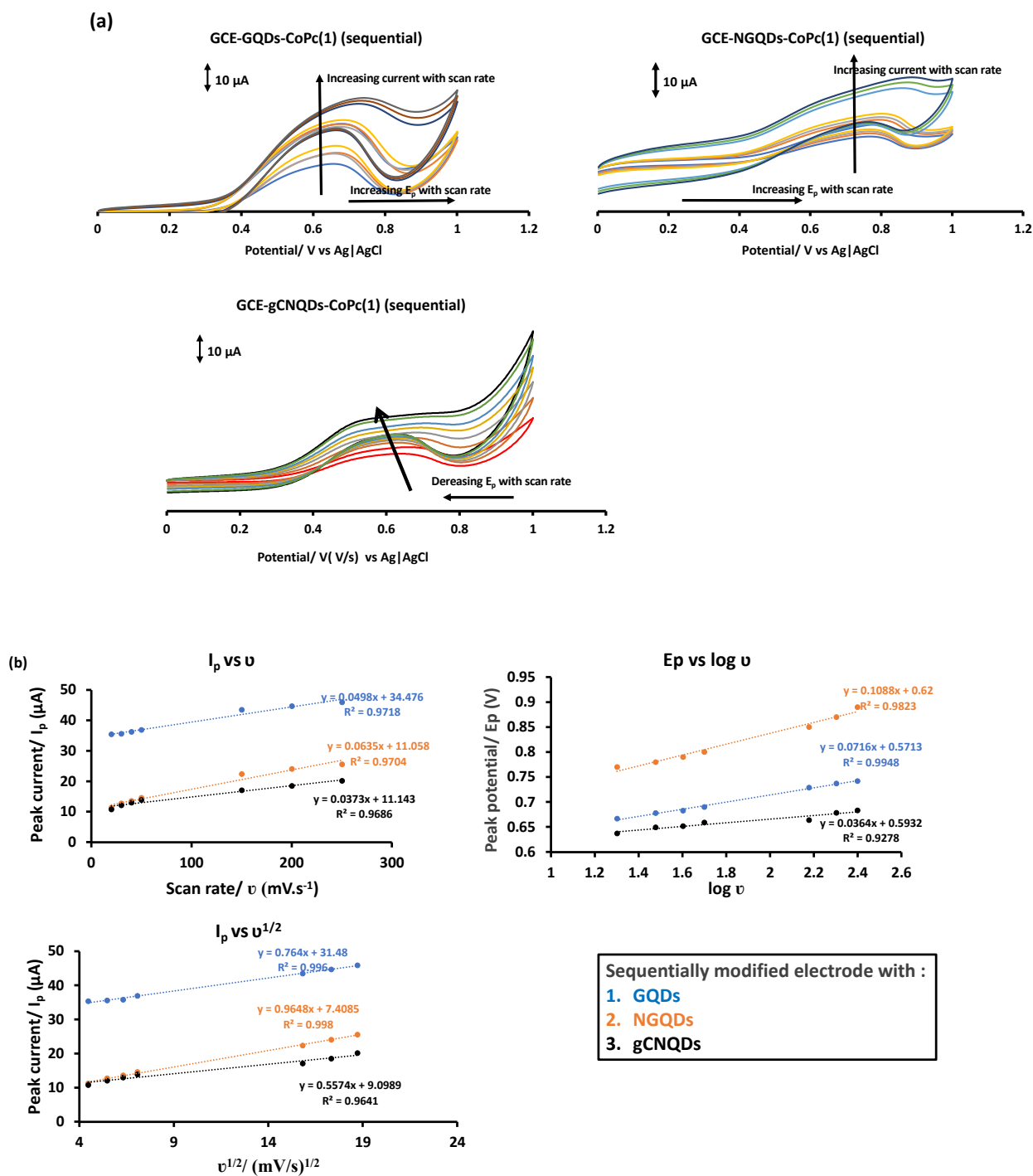


Figure 5.3: (a) Cyclic voltammograms of sequentially modified electrodes at changing scan rates (20, 30, 40, 50, 150, 200, 250 mV/s) and (b) I_p vs ν , E_p vs $\log \nu$ and I_p vs $\nu^{1/2}$ for the sequentially modified electrodes in de-aerated pH 4 buffer solution in the presence of 2 mM L-cysteine.

5.1.4 Stability

The modified electrodes were continuously cyclized in the presence of L-cysteine to test the stability of the electrocatalyst on the electrode surface as well as the repeatability of the detection. The more cycles run on the electrode, the more enhanced the current response as shown in Fig. 5.4, using the sequentially modified electrodes as examples. These results also prove that the electrode surfaces are resistant to fouling and passivation.

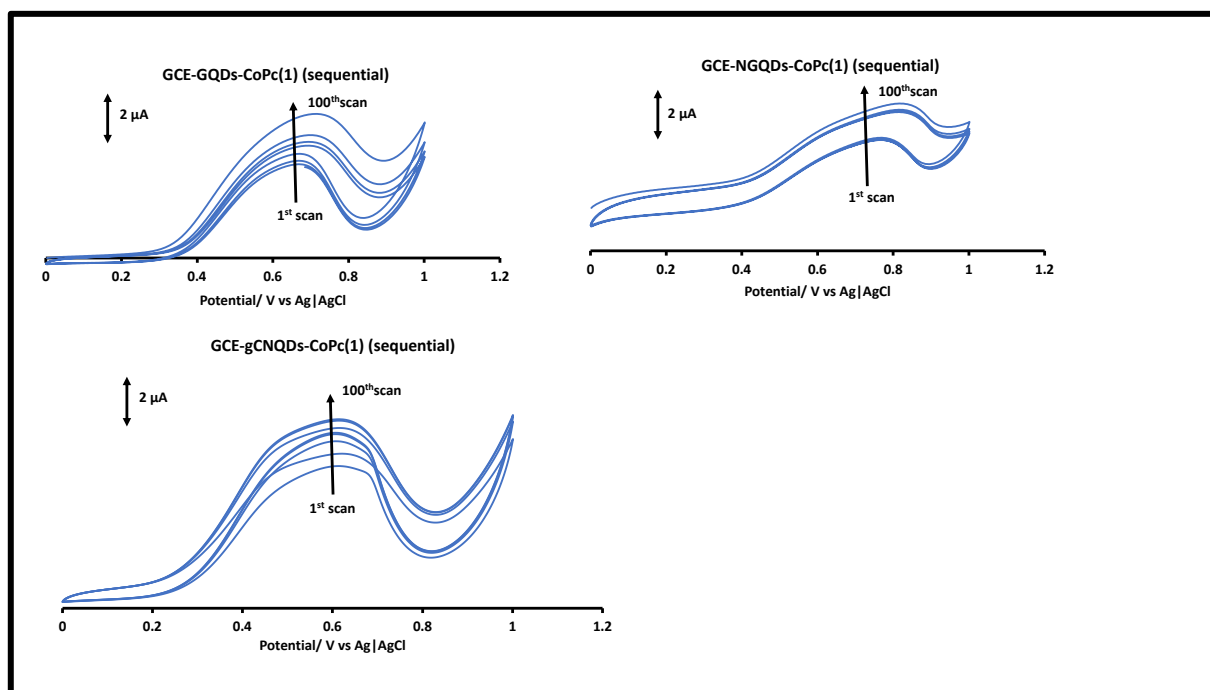


Figure 5.4: Continuous cyclization of sequentially modified electrodes in de-aerated pH₄ buffer solution in the presence of 2 mM L-cysteine. Scan rate = 100 mV/s, 100 cycles.

5.2 The electrochemical detection of PSA

Various aptasensors were fabricated in this work to determine the combinations of nanocomposites and aptamer that would generate low detection limits and good sensitivity. From these results, the best performing sensors would be used to determine sensor characteristics such as stability, selectivity, repeatability and reproducibility. Moreover, these sensors would also be used to determine their feasibility and potential use in clinical applications by detecting PSA in spiked serum samples. It should be noted that QDs were used for the initial study to determine the combination sequence of the modifiers that would yield the best results for the electrochemical detection of PSA.

5.2.1 QDs-CoPc(1)-Aptamer conjugates

5.2.1.1 EIS

Although this section focuses on PSA sensing and should only focus on aptamer-based electrodes, the behaviour of individual components of QDs-CoPc(1)($\pi\pi$) are included. Electron transfer kinetics in the presence of PSA were determined using EIS. Nyquist plots (Fig. 5.5(a)) were used to determine R_{ct} values by fitting the Randles equivalent circuit (Fig. 5.5(b)). The impedance spectra were fitted using a Randles electronic equivalent circuit, which is often used in diffusion-controlled electrochemical systems [219, 220] where a well-defined semi-circle followed by a linear segment is observed. This model includes the solution resistance (R_s), the electron transfer resistance (R_{ct}), the double-layer capacity element (C_{dl}) and a Warburg element (Z_w) to quantify the diffusion processes of the ionic species. However, the results obtained in this work showed suppressed semi-circles and thus a constant phase element (CPE) was used following the observation of similar

behaviour in literature reports [220]. It is also reported that using a CPE, accounts for the irregularities on the electrode surface that are a result of roughness and inhomogeneities on the modifiers [220], where the plot starts to appear more linear than the semi-circle with a defined linear segment [219].

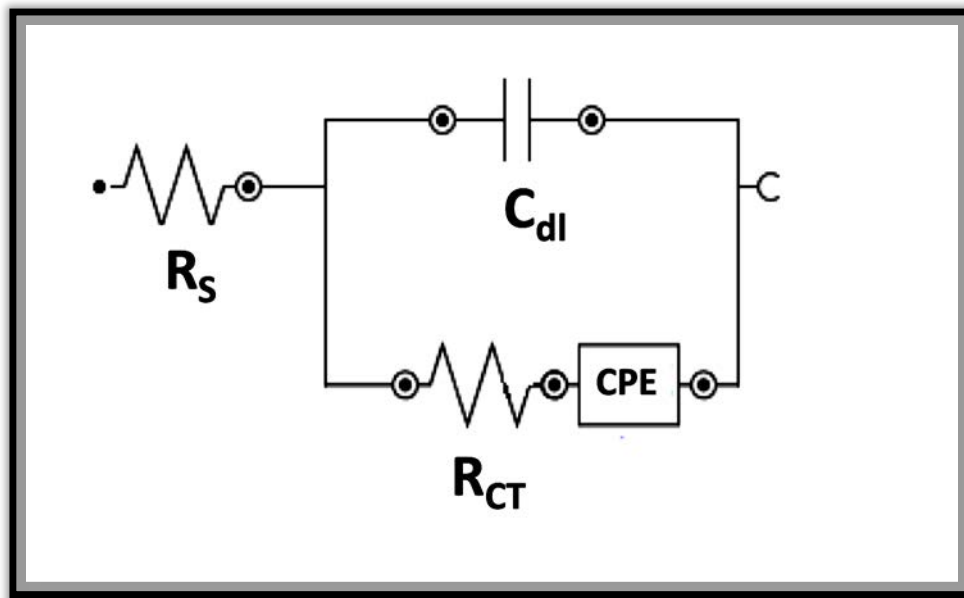
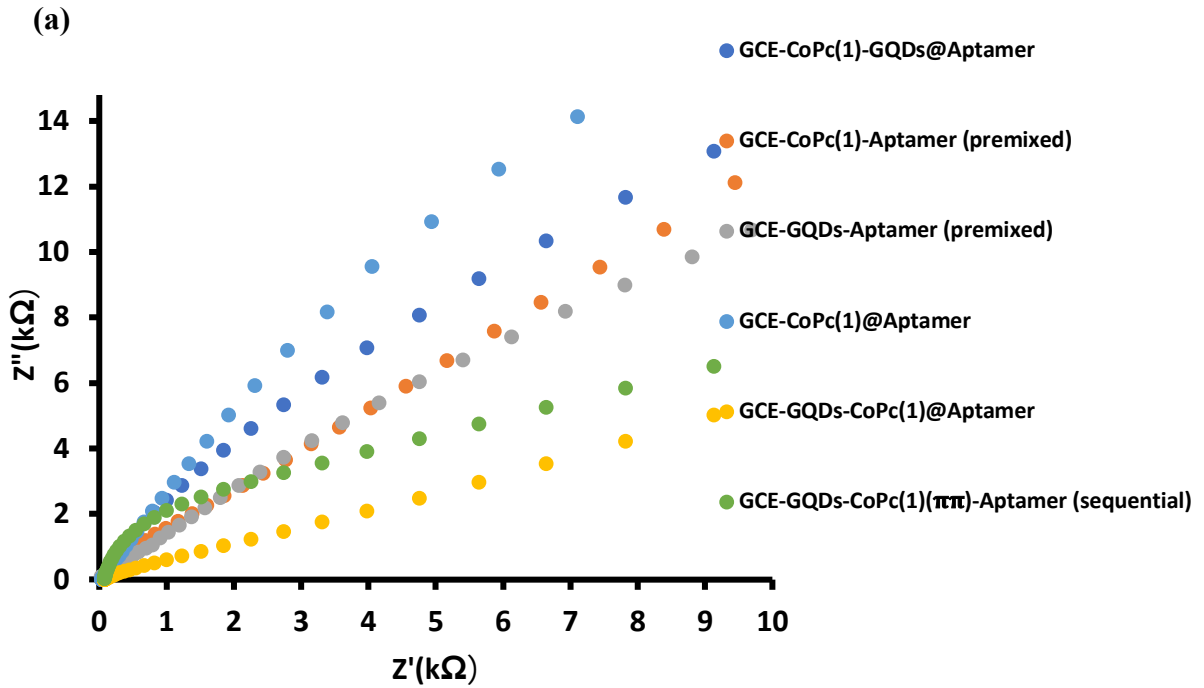


Figure 5.5: (a) Nyquist plots of some aptamer-modified electrodes in a 2 μM PSA solution in 30 mM phosphate buffer solution of pH 7.4. Plots separated into three groups for ease of comparison. (b) Circuit fitting model used.

The R_{ct} values are summarized in Table 5.3. The highest R_{ct} values were observed for the bare GCE, GCE-GQDs, GCE-CoPc(1) and the GCE-GQDs-Aptamer (sequential). For the bare GCE and the GCE-GQDs, the R_{ct} values decrease slightly for the latter, possibly due to only a slight enhancement in electron transfer caused by the GQDs. The slight increase in R_{ct} at the GCE-GQDs-Aptamer (sequential) surface may possibly be a result of how the adsorbed aptamer is assembled at the GCE surface, which only causes a slight increase in resistance to charge transfer.

Comparing the combinations of electrodes using GQDs and aptamer only, the R_{ct} values increase as follows:

GCE-GQDs-Aptamer (sequential) > GCE-GQDs@Aptamer > GCE-GQDs-Aptamer (premixed). The GCE-GQDs-Aptamer (sequential) sensor performed poorly in the presence of PSA even though it showed good charge transfer in terms of ΔE_p when the electrodes were characterized in the $[\text{Fe}(\text{CN})_6]^{3-/4-}$ solution, Table 4.1. The large R_{ct} suggest faster passivation, hence better binding of PSA to aptamer and better detection. Thus, the electrode surface modified with GCE-GQDs-Aptamer (sequential) showing poor charge transfer in the presence of PSA is an indication of good binding of PSA to the aptamer, which hinders electron transfer. The combination of CoPc(1) and aptamer (CoPc(1)-Aptamer (sequential)) showed the largest R_{ct} value, followed by CoPc(1)-Aptamer (premixed), with CoPc(1)@Aptamer being the least resistant. Lower R_{ct} values suggest less binding of PSA to aptamer. The orientation of the electrocatalyst on the electrode surface may explain this in terms of how well the aptamer at the surface may be exposed, to be able to bind to the PSA in solution.

The apparent charge transfer rate constant (k_{app}) was also calculated using Eqn. 5.4 [221] and the results are summarized in Table 5.3.

$$k_{app} = \frac{RT}{F^2 AR_{ct}C} \quad (5.4)$$

where C is the concentration of the PSA, A = real surface area in cm² and other symbols retain their usual scientific meaning. The real surface area was obtained using Eqn. 4.1. The k_{app} values are inversely proportional to R_{ct} , which validates the results obtained where high k_{app} values corresponded to low R_{ct} values.

Table 5.3: Summary of determined R_{ct} and k_{app} values determined from Nyquist plots (in order of increasing R_{ct} values). (Modified electrodes in the presence of PSA).

Electrode	$R_{CT}/ k\Omega$	$k_{app} (cm/s)^2/s$
Bare GCE	77.64	5.14×10^{-3}
GCE-GQDs	74.84	5.75×10^{-3}
GCE-CoPc(1)	85.87	4.37×10^{-3}
GCE-Aptamer	10.31	3.64×10^{-1}
GCE-GQDs-CoPc(1)($\pi\pi$)	12.44	2.79×10^{-1}
GCE-GQDs-CoPc(1) (sequential)	8.13	4.61×10^{-1}
GCE-GQDs@Aptamer	16.10	1.46×10^{-1}
GCE-GQDs-Aptamer (premixed)	10.62	3.53×10^{-1}
GCE-GQDs-Aptamer (sequential)	79.12	4.74×10^{-3}
GCE-CoPc(1)-GQDs@Aptamer (sequential)	41.68	1.11×10^{-2}
GCE-CoPc(1)@Aptamer	13.90	2.54×10^{-1}
GCE-CoPc(1)-Aptamer (premixed)	27.50	5.11×10^{-2}
GCE-CoPc(1)-Aptamer (sequential)	30.20	4.98×10^{-2}
GCE-GQDs-CoPc(1)@Aptamer (sequential)	26.30	5.23×10^{-2}
GCE-GQDs-CoPc(1)($\pi\pi$)-Aptamer (premixed)	3.15	1.19
GCE-GQDs-CoPc(1)($\pi\pi$)-Aptamer (sequential)	19.13	8.34×10^{-2}
GCE-GQDs@Aptamer-CoPc(1)@Aptamer (premixed)	11.41	2.98×10^{-1}

Note: Sequential modification involves placing the QDs first on the electrode surface. For premixed ($\pi\pi$ interactions), the CoPc(1) and GQDs are mixed with aptamer then placed on the electrode surface.

5.2.1.2 Concentration studies: DPV and EIS

A stock solution of PSA with a concentration of 2 μM was diluted to concentrations ranging from 1.2-2.0 pM to determine the effects concentration of the analyte would have on the current output or resistance to charge transfer. Electrodes with the PSA specific aptamer at the surface were selected for this study. Although several electrodes were tested, the DPV and EIS of the best performing electrodes are shown in Fig. 5.6. The DPV plots of the electrode containing aptamer alone (GCE-Aptamer) is illustrated by Fig. 5.7. As can be seen, this plot shows two peaks near 0 V (III), which are known for DNA [198]. These peaks are observed on all electrodes containing aptamer. Peaks near zero will overlap with the $\text{Co}^{\text{III}}\text{Pc}^{-2}/\text{Co}^{\text{II}}\text{Pc}^{-2}$ processes for electrodes containing CoPc(1). For all electrodes containing GQDs, there is a peak near -0.65 V (I), which has been assigned to GQDs. DPV peaks near -0.65 V (due to GQDs) and the sharp one near -0.25 V (II) due to $\text{Co}^{\text{III}}\text{Pc}^{-2}/\text{Co}^{\text{II}}\text{Pc}^{-2}$ were used for the determination the detection limits.

The DPV results illustrated in Fig. 5.6(a), showed that the peak currents decreased with increasing PSA concentration. Fig. 5.6(b) showed an increasing in resistance to charge transfer with increasing concentration. It is reported that the immobilized aptamer undergoes a conformation change upon PSA binding such that the double stranded DNA is formed with simultaneous binding to (and covering with) PSA that decrease the charge transfer rate, between redox probe and electrode surface [144]. Therefore, there is an expected increase in resistance and decrease in current as PSA concentrations increase. The calibration plots (inserts) were linear in the ranges from 1.2 to 2.0 pM (0.2 pM increments) and the detection limits were calculated.

The electrodes GCE-GQDs-Aptamer (sequential) and GCE-GQDs-CoPc(1)($\pi\pi$)-Aptamer (sequential) gave the lowest detection limits compared to the other electrodes tested, Table 5.4. Similar values were obtained in EIS analyses with the same electrodes showing better detection limits. The detection limit of the best surface tested using EIS, GCE-GQDs-CoPc(1)($\pi\pi$)-Aptamer (sequential), was determined as 1.79 pM (0.051 ng/mL). The best performing surface in DPV was GCE-GQDs-CoPc(1)($\pi\pi$)-Aptamer (sequential) with LoD values of 0.66 (0.018 ng/ml) and 0.73 pM (0.021 ng/mL) determined using peaks (I) and (III). Again, sequential modification proved superior, with the combination of MPC and QDs showing the best performance overall.

A three-component system showing higher detection limits than the one developed in this work is reported by Liu et al. [134] where AuNPs are also used and fabrication involves multiple steps whereas the fabrication process reported in this work is much simpler and shorter for the best performing aptasensor developed. Another aptasensor reported in literature is one developed by Hu and co-workers [135] where PSA was detected at femtomolar level concentrations by cleavage-based electrochemical detection using eATRP-based (eATRP = electrochemically mediated atom transfers radical polymerization) method for signal amplification. The major drawback, however, is that the fabrication process is quite time consuming and the use of gold electrodes in their method is at a cost higher than that of carbon electrodes which are used in this work. Amongst good sensitivity and low detection limits, cost effectiveness as well as ease of use are important when developing biosensors so that they may be more accessible and user friendly.

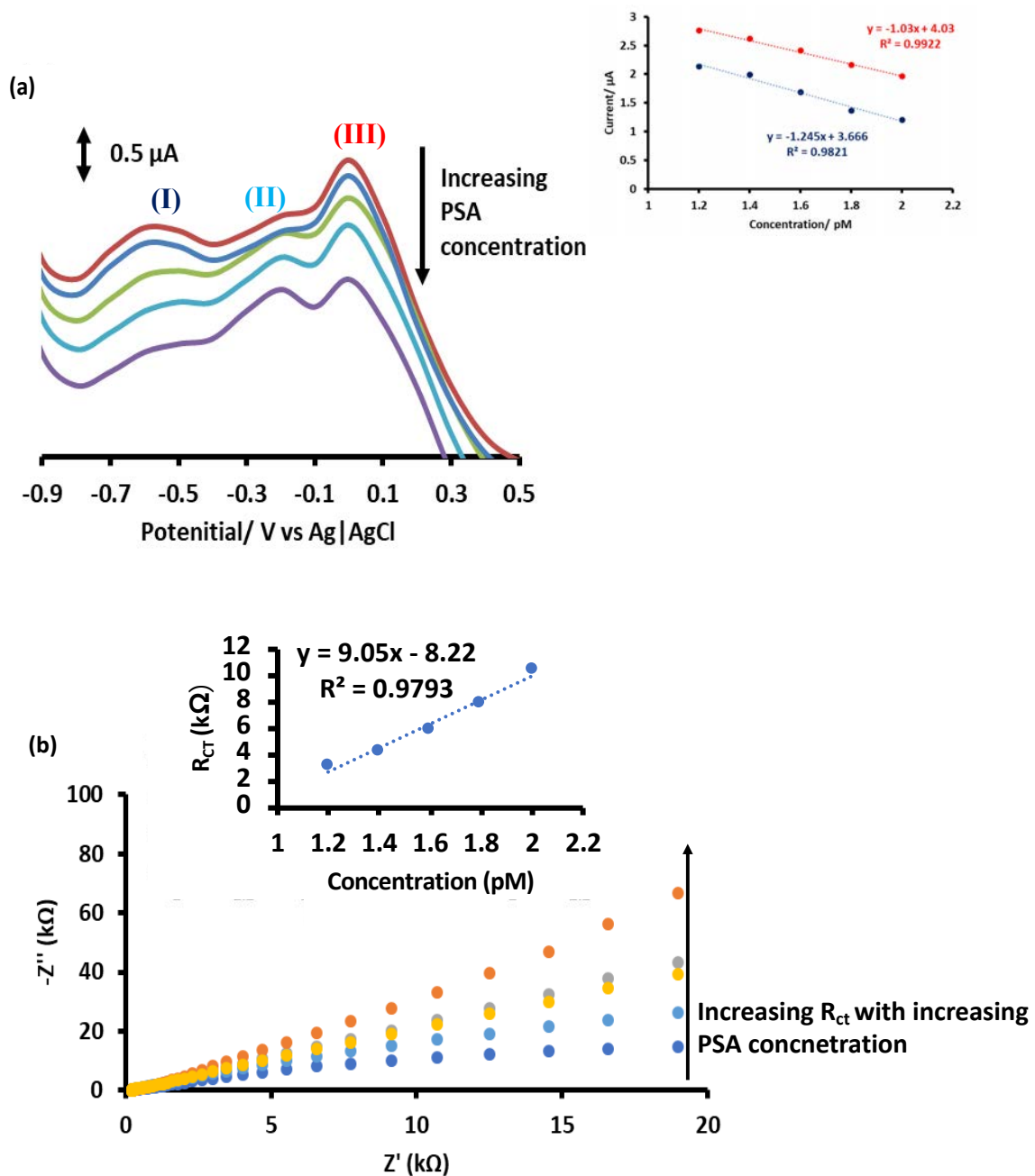


Figure 5.6: (a) Differential Pulse Voltammograms (DPV) and (b) Electrochemical impedance (EIS) Nyquist plots of GCE-GQDs-CoPc(1)($\pi\pi$)-Aptamer (sequential) in a 30 mM phosphate buffer solution of pH 7.4 with PSA concentrations ranging from 1.2-2.0 pM. Inserts: Linear responses of currents and resistance to changing concentrations.

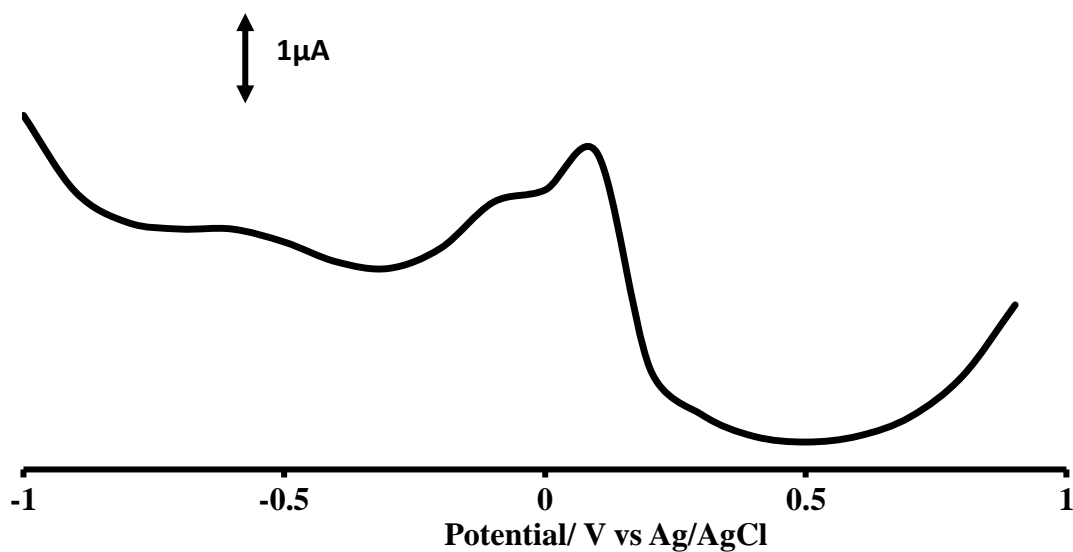


Figure 5.7: DPV of GCE-aptamer in PSA.

Table 5.4: Summary of limits of detection (LoD) of selected electrode surfaces determined from EIS and DPV measurements (Linear detection range: 1.2-2 pM).

Electrode	LoD (EIS)/ pM	Peak (I)LoD (DPV) / pM	Peak (III)LoD (DPV) / pM
GCE-Aptamer	4.15	4.02	5.10
GCE-GQDs@Aptamer	4.18	2.27	4.36
GCE-GQDs-Aptamer (sequential)	2.51	-	2.23
GCE-CoPc(1)@Aptamer	22.40	24.7	-
GCE-GQDs-CoPc(1)@Aptamer (sequential)	17.41	21.6	16.8
GCE-GQDs-CoPc(1)($\pi\pi$)-Aptamer (sequential)	1.79	0.73	0.66

5.2.1.3 Stability, selectivity, and reproducibility studies

The stability, selectivity, and reproducibility of the proposed electrochemical aptasensor were also investigated by DPV using a 2 pM PSA in PBS solution of pH 7.4 (30 mM). The electrode GCE-GQDs-CoPc(1)($\pi\pi$)-aptamer is used as an example.

The same electrode was fabricated on three different occasions and tested in the PSA solution of same concentration (2 pM). The results are illustrated in Fig. 5.8. There were slight differences in current output, however no changes were observed in terms of peak potential. The relative standard deviations (RSD %) were determined from peaks at -0.6 V and at 0 V, and were found to be 4.43 % and 3.77 %, respectively. After incubation in the PSA solution, the DPV scans were run for 50 cycles and the change in current response was monitored (Fig. 5.9). The first and the last scan were compared and it was found that the current response at the most prominent peak (0 V) decreased by only 3.9 %. When the electrode was not in use, it was stored at 4 °C. After a week of storage, the final scan in the repeatability test was compared to an initial run done at the same scan rate (Fig. 5.10). By looking at the difference between peak currents at -0.6 V and 0 V, this electrode maintained approximately 89 % of its performance ability proving to be quite stable in that time frame.

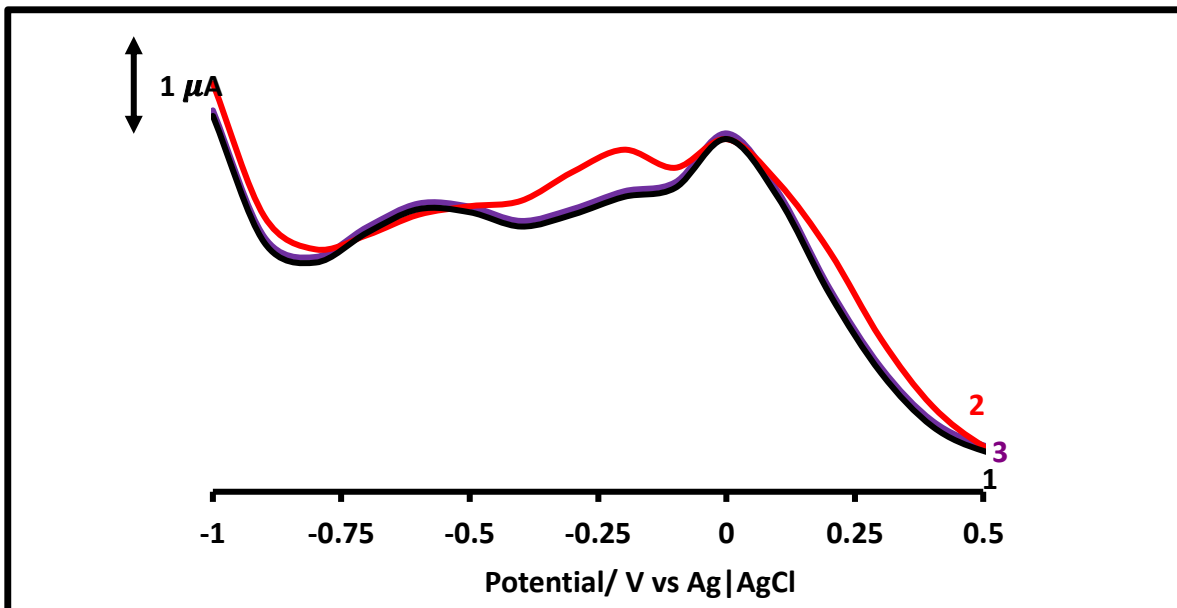


Figure 5.8: Differential pulse voltammograms of three different GCE-GQDs-CoPc(1)($\pi\pi$)-Aptamer (sequential) in a PSA solution of concentration 2.0 pM to determine reproducibility.

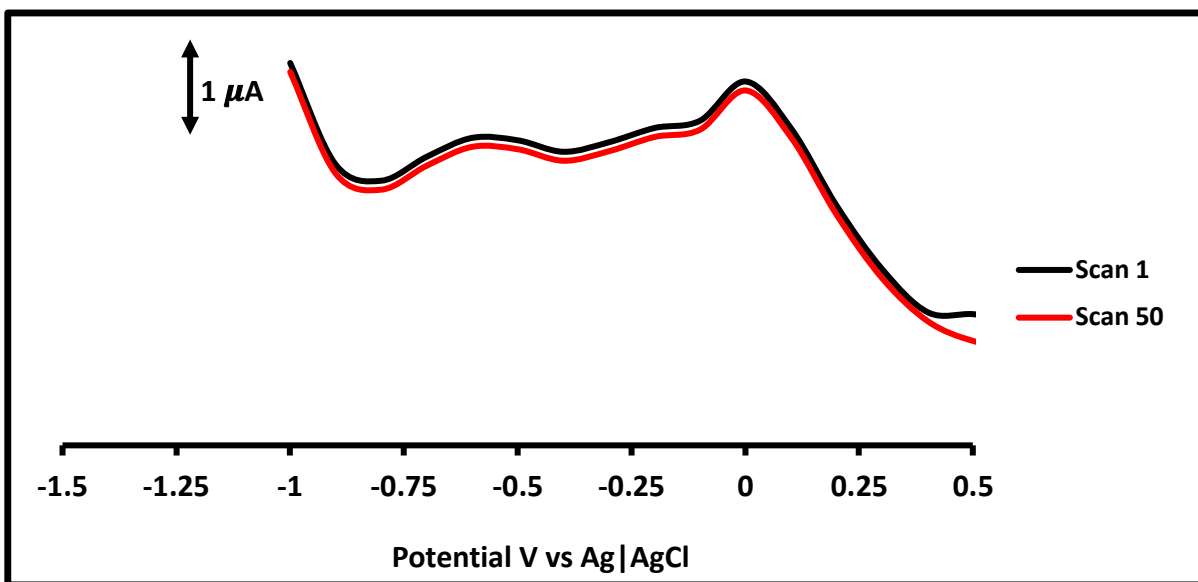


Figure 5.9: Differential pulse voltammograms of GCE-GQDs-CoPc(1)($\pi\pi$)-Aptamer (sequential) in a PSA solution of concentration 2.0 pM before and after 50 cycles to test electrode repeatability.

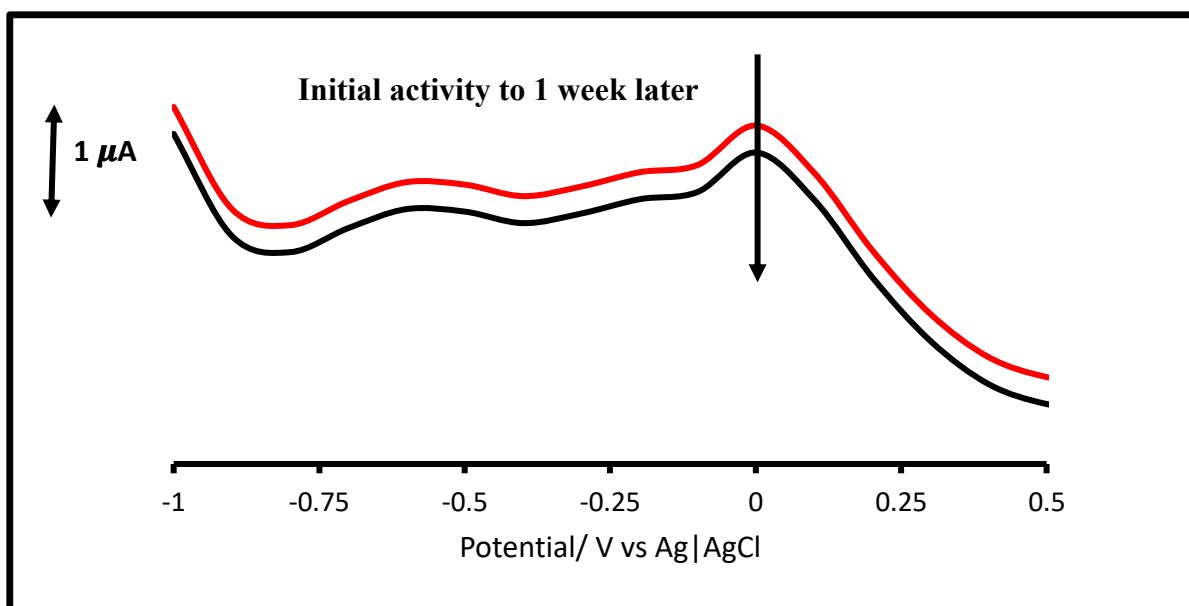


Figure 5.10: Differential pulse voltammograms of GCE-GQDs-CoPc(1)($\pi\pi$)-Aptamer (sequential) tested in a PSA solution of concentration 2.0 pM 1 week apart to determine stability of electrode.

Biological samples exist as complex mixtures therefore the fabricated sensors need to be tested against potential interferences in order to validate their reliability to target a specific analyte, irrespective of what other analytes may be present in a sample. The mixed solution method [222] and DPV (Fig. 5.11) was used to determine the selectivity of the best performing electrode towards PSA, in the presence of other analytes that could possibly be detected in a real sample with PSA, namely bovine serum albumin (BSA), L-cysteine and glucose. The chosen test analytes BSA, L-cysteine and glucose were mixed in excess, in the buffer solution with PSA. Other than being easily accessible in the laboratory, BSA was chosen so as to determine how other proteins expressed in biological samples could affect the aptasensor functionality. Glucose was chosen as it is possible to detect it in seminal samples and the level may vary depending on the health of the patient. L-cysteine was

chosen as a test analyte as it is an amino acid, which can be found in the human body, or a variant thereof may be ingested as a supplement to enhance sperm quality [223]. The concentration of PSA used was 2.0 pM and 2.0 nM of interfering analyte was added for non-specific binding determination. The interferants were added in excess ($\times 10^{-3}$ higher than analyte) to ensure a high enough concentration for the sensor to pick up should it be sensitive to the interferences. The fabricated electrodes were incubated in the solutions as was done for PSA studies in earlier sections. Eqn. (5.5) was used to determine values of the selectivity coefficients (K_{amp}) which will give a measure of the degree of interference.

$$K_{AMP} = \left(\frac{I_{MIXTURE}}{I_{PSA}} - 1 \right) \frac{[PSA]}{[INTERFERANT]} \quad (5.5)$$

where $I_{mixture}$ and I_{PSA} are background corrected current responses of PSA in the presence and absence of the interferent, respectively. A K_{amp} value in the order of magnitude higher than 10^{-2} indicates strong interference and a value close to 10^{-3} indicates weak interference [224]. From the peaks observed at about -0.6 V (Fig. 5.11(I)), a K_{amp} value of 0.17×10^{-3} , 0.08×10^{-3} and 0.04×10^{-3} were obtained for BSA, glucose and L-cysteine, respectively. At the potential close to 0 V (Fig. 5.11 (II)) where the more prominent peak is observed, K_{amp} value of -0.46×10^{-3} , -0.64×10^{-3} and 0.68×10^{-3} were obtained for BSA, glucose and L-cysteine, respectively. Therefore, this sensor platform can be applied without any pre-separation procedures for the determination of PSA in the presence of the tested interferents with no need for pre-treatment of sample.

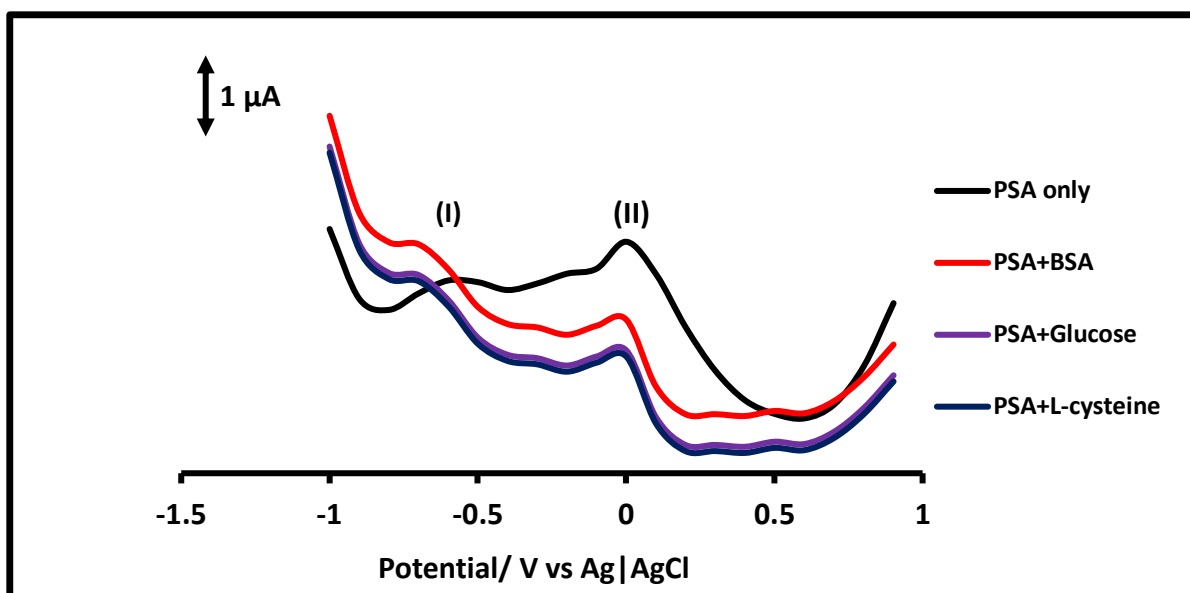


Figure 5.11: Differential pulse voltammograms of GCE-GQDs-CoPc($\pi\pi$)-Aptamer (sequential) in the absence and presence of interferents (2 nm of BSA, glucose, and L-cysteine) in a PSA solution of concentration 2.0 pM.

The best performing aptasensor showed one of the lowest detection limits using DPV and comparable reproducibility and repeatability relative standard deviations (RSD) % compared to other similar works reported in literature [134, 142, 144, 145, 225, 226]. Table 5.5 summarizes this data and the data from the above-mentioned literature reports related to the detection of PSA.

Table 5.5: Summary of results obtained in this work for GCE-GQDs-CoPc(1)($\pi\pi$)-Aptamer (sequential) compared to electrochemical PSA aptasensors reported in literature (units used in this work converted from pM to pg/mL for ease of comparison with literature values).

Electrode	Linear range	LoD	Repeatability (RSD%)	Reproducibility (RSD%)	Reference
Biotin-Aptamer/strept avidin/AuNPs@ GMCs on polygraphite electrode	0.005-20 ng/mL	1.0 ng/mL	4.7	4.40	[134]
APT/AuNPs/C ₆₀ -CS-IL/MWCNTs/SPCE	0.05-5 ng/mL	13 pg/mL	-	5.00	[142]
AuE-nAu-Aptamer	0.25-200 ng/mL	0.25 ng/mL	4.2	5.40	[144]
GCE- rGO-MWCNT/AuNPs/Aptamer	0.14-11.6 ng/mL	0.14 ng/mL	3.0	4.50	[145]
GCE-GS-MB-CS film	0.125-200 ng/mL	50 pg/mL	4.5	5.50	[225]
IDE/APTES/EDC-NHS/anti-PSA aptamer	2.5-90 ng/mL	1.5 ng/mL	3.3	3.10	[226]
GCE-GQDs-CoPc(1)($\pi\pi$)-Aptamer (sequential)	0.035-0.057 ng/mL	0.018 ng/mL	3.9	3.77	This work

Abbreviations: Reduced graphene oxide (rGO), multi-walled carbon nanotubes (MWCNTs), gold nanoparticles (AuNPs), GMCs (graphitized mesoporous carbon), gold nanospheres (nAu), graphene sheets-methylene blue-chitosan (GCE-GS-MB-CS), Au nanoparticles/fullerene C₆₀-chitosan-ionic liquid/multiwalled carbon nanotubes/screen printed carbon electrode (APT/Au NPs/C₆₀-CS-IL/MWCNTs/SPCE), Interdigitated electrode/ Aminopropyltrimethoxysilane / EDC-NHS/anti-PSA aptamer (IDE/APTES/EDC-NHS/anti-PSA aptamer)

5.2.2 The effects of QDs composition and structure: Comparing GQDs, NGQDs and gCNQDs

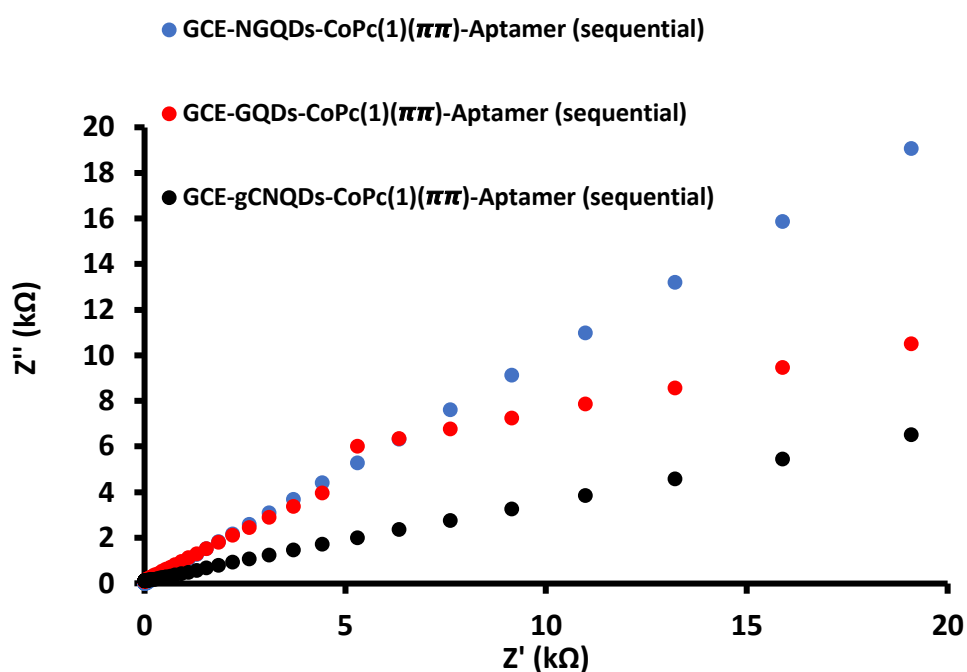
Once the best modification approach was determined, the nature of the QDs used was changed and the aptasensors compared. The aim of this sub-study was to verify the influence the structure and composition of the QDs has on the overall performance of the aptasensors fabricated herein.

5.2.2.1 EIS

The electrodes used for this sub-study were GCE-GQDs-CoPc(1)($\pi\pi$)-Aptamer (sequential), GCE-NGQDs-CoPc(1)($\pi\pi$)-Aptamer(sequential) and GCE-gCNQDs-CoPc(1)($\pi\pi$)-Aptamer (sequential). The Nyquist plots Fig. 5.12(a) were used to determine R_{ct} values by fitting the Randles equivalent circuit (Fig. 5.5(b)) as previously carried out. The R_{ct} values are summarized in Table 5.6. The highest R_{ct} values were observed for the NGQDs-based electrode followed by the GQDs-based electrode, with the gCNQDs-based electrode having the lowest values. A higher R_{ct} suggests more PSA binding hence better detection activity. Thus, the electrode containing NGQDs show better PSA detection. This electrode also had a low ΔE (Table 4.1) in the 1 mM $[\text{Fe}(\text{CN})_6]^{3-/4-}$ solution before incubation with PSA which further validates the result obtained.

The apparent charge transfer rate constant (k_{app}) was calculated using Eqn.5.4. The gCNQDs-CoPc(1)($\pi\pi$)-Aptamer (sequential) combination had the highest k_{app} value (1.78×10^{-1} cm/s) which implies a less passivated electrode surface compared to the other two electrodes hence minimal binding of PSA to the aptamer or more exposure of the conductive regions of the electrode surface compared to the GQDs and

NGQDs-based surfaces. This means the gCNQDs-CoPc(1)($\pi\pi$)-Aptamer is less effective at detecting PSA, even though it has a larger surface coverage, Table 4.1. A plot of phase-shift against log frequency Fig. 5.12(b) provides further characteristic information on the frequency, which cannot be obtained from the Nyquist plot. All electrodes showed the phase angle less than the ideal 90° indicative of a true capacitor (Table 5.6) [227]. Shift of phase angles towards lower frequencies in the Bode plots are an indication that the electrocatalyst gives more efficient catalytic activity [228]. The Bode plots show broad peaks suggesting complicated relaxation behavior. This has been observed before and related many factors including film thickness [229], which could result in different diffusion processes within the film.



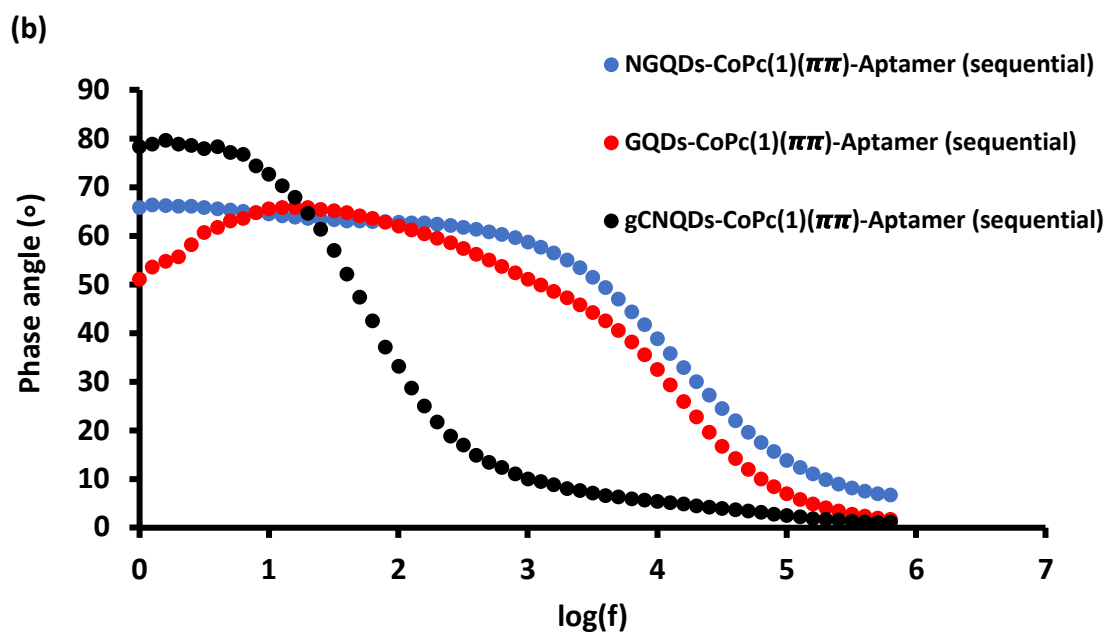


Figure 5.12: (a) Nyquist plots and (b) Bode plots of modified electrodes in a 2 μ M PSA solution in 30 mM phosphate buffer solution of pH 7.4.

Table 5.6 :EIS parameters for PSA detection.

Electrode	$R_{CT}/ k\Omega$	$k_{app} (cm/s)^2/s$	-Phase angle ($^{\circ}$)
GCE-GQDs-CoPc(1)($\pi\pi$) -Aptamer (sequential)	19.13	8.34×10^{-2}	58.7
GCE-NGQDs-CoPc(1)($\pi\pi$) -Aptamer (sequential)	29.1	6.72×10^{-2}	77.1
GCE-gCNQDs-CoPc(1)($\pi\pi$) -Aptamer (sequential)	7.53	1.78×10^{-1}	65.4

5.2.2.2 Concentration studies using EIS and DPV

For the determination of limits of detection (LoD), the aptamer-containing electrodes were tested in a 30 mM phosphate buffer solution of pH 7.4 with PSA concentrations ranging from 1.2-2.0 pM. The analytical techniques used were EIS, Fig. 5.13(a) and DPV, Fig. 5.13(b). The results shown are for the NGQDs-based electrode as an example. Nyquist plots of the electrodes in PSA solutions of different concentrations are shown in Fig. 5.13(a). The detection limits determined in EIS are also summarized in Table 5.7 alongside other determined characteristics of the aptasensors fabricated. The GQDs, NGQDs and gCNQDs-based electrodes showed detection limits of 0.051, 0.046 and 0.035 ng/mL in EIS, respectively. The gCNQDs shows the highest LoD in EIS with the NGQDs performing the best using this technique. The DPV technique gave LoD values of 0.018, 0.044 and 0.053 ng/mL for the GQDs, NGQDs and gCNQDs-based electrodes respectively, therefore showing that the GQDs-based electrode produced the best results using DPV. In EIS and DPV, the detection limits obtained for the NGQDs and gCNQDs based electrodes were in similar. The LoD values obtained for the GQDs based electrode suggested that using DPV as the analytical technique produces better results.

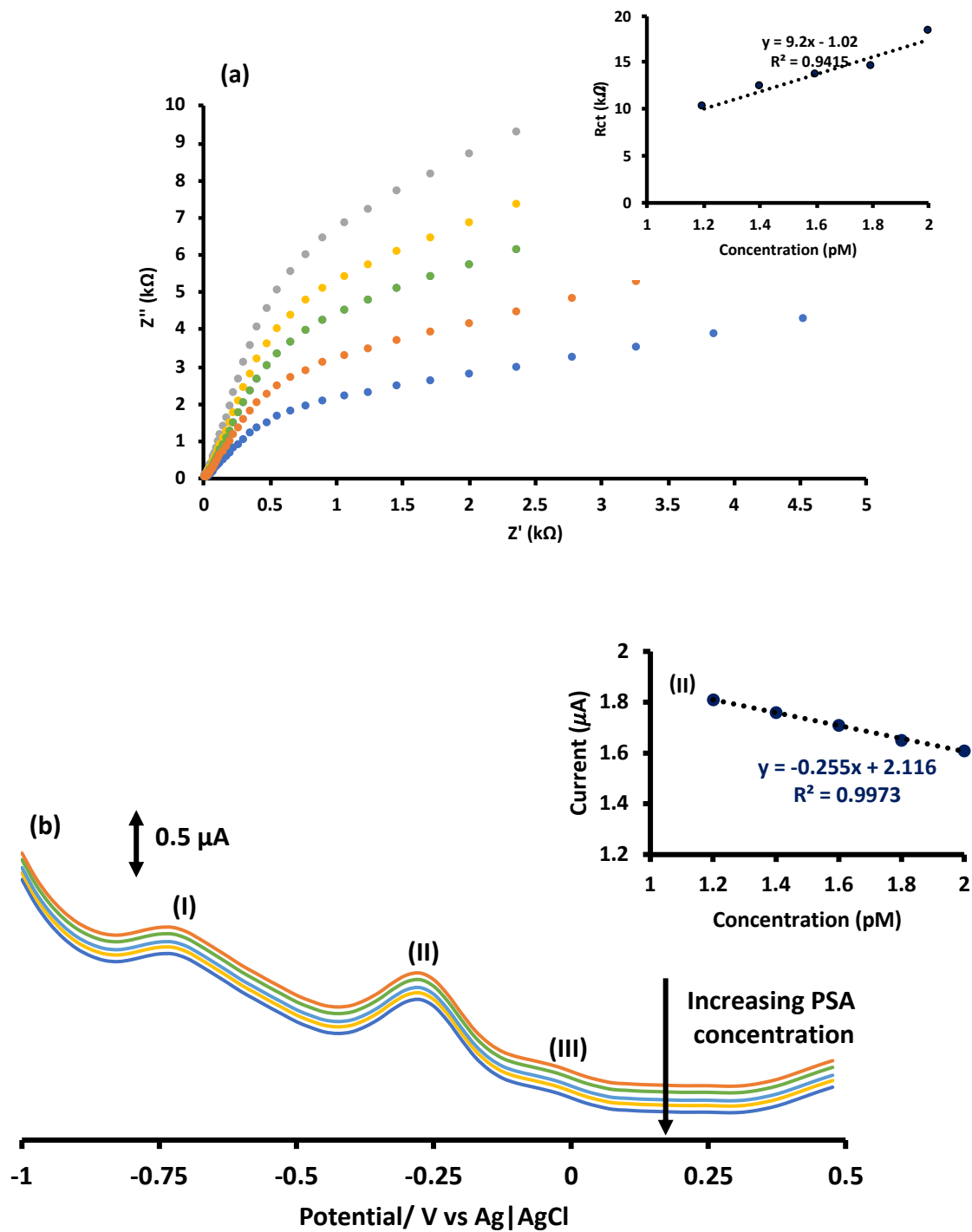


Figure 5.13: (a) Electrochemical impedance (EIS) Nyquist plots and (b) differential pulse voltammograms (DPV) of GCE-NGQDs-CoPc(1)($\pi\pi$)-Aptamer in a 30 mM phosphate buffer solution of pH 7.4 with PSA concentrations ranging from 1.2-2.0 pM. Inserts: Linear responses of resistance to changing concentrations.

5.2.2.3 Selectivity, stability, and reproducibility studies

The selectivity, stability and reproducibility of the fabricated electrochemical aptasensors were investigated using DPV. The results shown are for the NGQDs and gCNQDs electrodes since the GQDs based electrode has already been discussed in the previous sub-section. However, for the sake of comparison, the data for the GQDs-based electrode is included in the tables containing the NGQDs and gCNQDs data. The obtained voltammograms for reproducibility and stability studies are similar to those shown in Fig. 5.8- 5.10. The calculated results are summarized in Table 5.7. For reproducibility studies, the same electrode was fabricated on three different occasions (as done in Fig. 5.8) and tested in the PSA solution. The relative standard deviation (RSD (%)) was determined from peaks at 0 V for GQDs and was found to be 3.8 %. For the NGQDs based electrode, the RSD (%) was determined from peaks at -0.25 V and was found to be 6.2 %, Table 5.8. For the gCNQDs based electrode, the RSD (%) was determined from peaks at 0 V and was found to be 6.7 %. When the electrode was not in use, it was stored at 4 °C. After a week of storage, the aptasensors were used to detect PSA in PBS solution which allowed for the determination of the stability of the aptasensors. By looking at the difference between peak currents, the GQDs, NGQDs and gCNQDs based electrodes maintained approximately 89.0 %, 95.3 % and 92.2 % of their performance ability respectively (Table 5.7), proving to be quite stable in that time frame. Table 5.7 summarizes the LoD, repeatability and reproducibility results obtained in this work, which are further compared to other literature reports related to the detection of PSA [134, 230-234]. The aptasensor reported in this work showed one of the lowest detection limits and one of the lowest reproducibility RSD %. The values determined were

comparable to literature. From this, it can be concluded that these aptasensors have good potential to be used in clinical studies.

Table 5.7: Summary of results obtained in this work for GCE-GQDs-CoPc(1)($\pi\pi$)-Aptamer, GCE-NGQDs-CoPc(1)($\pi\pi$)-Aptamer and GCE-gCNQDs-CoPc(1)($\pi\pi$)-Aptamer (determined from EIS) compared to electrochemical PSA aptasensors reported in literature (units used in this work converted from pM to ng/mL for ease of comparison).

Electrode	Linear range/ ng/mL	LoD in EIS ^a / ng/mL	Stability (% retention)	Reproducibility (RSD %)	Reference
PGE/AuNP@GMC /aptamer	0.25-200	0.25	92.8	Not reported	[134]
Au/MSF/Aptamer	1-300	0.28	98	2.4	[230]
SPCE-Ag/GO- Aptamer	0.75-100	0.27	77	5.3	[231]
GCE-CNTs- Chitosan-Aptamer	0.85-12.5	0.75	Not reported	3.9	[232]
CdS-Cu ₂ OTM/NAs- CdS-Cu/Aptamer	0.1-100	0.26	>99	Not reported	[233]
Graphene-PEDOT: PSS modified Whatman paper with aptamer	0.77-14	0.45	Not reported	0.26	[234]
GCE-GQDs- CoPc(1)($\pi\pi$)- Aptamer	0.034-0.057	0.104 (0.018)	89.0	3.8	This work
GCE-NGQDs- CoPc(1)($\pi\pi$)- Aptamer	0.034-0.057	0.046 (0.044)	95.3	6.2	This work
GCE-gCNQDs- CoPc(1)($\pi\pi$)- Aptamer	0.034-0.057	0.055 (0.053)	92.2	6.7	This work

Abbreviations: Au (Gold), MSF (mesoporous silica thin films), SPCE (screen printed carbon electrode), Ag (silver), GO (graphene oxide), CNT (carbon nanotubes), PGE/AuNP@GMC (pyrolytic graphite electrode/gold nanoparticles@graphitized meso- porous carbon), CdS-Cu₂OTM/NAs-CdS-Cu (cadmium selenide cuprous oxide titanium mesh/ nanorod arrays), PEDOT: PSS (poly (3,4-ethylenedioxythiophene):poly(styrenesulfonate)).

^aLoD values from DPV in brackets

The mixed solution method discussed above, and DPV (Fig. 5.14) were used to test the selectivity of the developed aptasensors in complex mixtures, to prove their selectivity towards PSA. The interferences used and protocols followed were the same as those used for the QDs-based aptasensor. The fabricated electrodes were incubated in the solutions and calculations carried out to determine the K_{amp} values. The peak potentials employed to calculate the K_{amp} values were -0.25 V (II) (for NGQDs and gCNQDs) and 0 V (III) (for QDs and gCNQDs) since they were more resolved. The calculated values were summarized in Table 5.8 which indicate low interference and high selectivity of the fabricated sensors towards PSA detection. The gCNQDs-based electrodes also seem to show no interference at the most negative potential which indicates excellent potential as early detection devices towards PSA and thus reliable early diagnosis of prostate cancer.

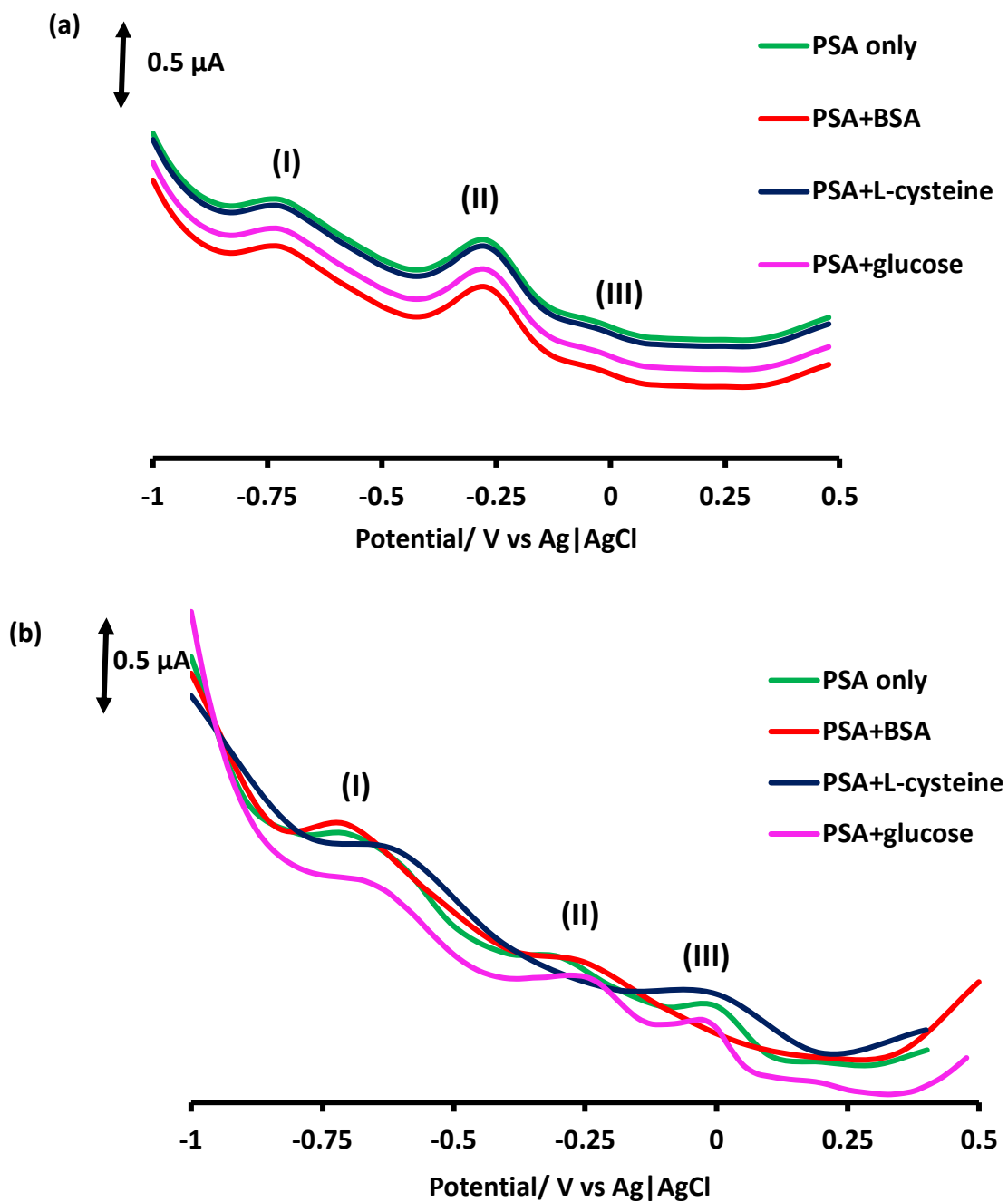


Figure 5.14: Differential pulse voltammograms of (a) GCE-NGQDs-CoPc(1)($\pi\pi$)-Aptamer and (b) GCE-gCNQDs-CoPc(1)($\pi\pi$)-Aptamer in the absence and presence of interferents in a PSA solution of concentration 2.0 pM.

Table 5.8: Comparative table of selectivity results obtained for the developed aptasensors.

	GQDs-CoPc(1)(($\pi\pi$) -	NGQDs-CoPc(1)(($\pi\pi$)	gCNQDs-CoPc(1)(($\pi\pi$)	-
	Aptamer	-Aptamer	Aptamer	
Potential/	0.0	-0.25	-0.25	0.0
K_{amp} BSA	-4.60×10^{-4}	-1.75×10^{-4}	4.14×10^{-5}	-1.00×10^{-3}
K_{amp} Glucose	-6.40×10^{-4}	-1.11×10^{-4}	2.37×10^{-5}	-1.27×10^{-4}
K_{amp} I-cysteine	6.80×10^{-4}	2.96×10^{-5}	-1.42×10^{-4}	-1.27×10^{-4}

5.2.3 Influence of MPC substituents

5.2.3.1 EIS

The effects of substituents on the MPC complexes were studied using EIS, by $\pi\pi$ -stacking gCNQDs@Aptamer with complex 1 and complex 2. Sequential modification was not used here as placing MPC complexes first on the electrode surface is not as efficient as placing QDs on the surface first. Moreover, placing the CoPc on top of the QDs-aptamer conjugate may lead to blocking of the binding sites of the aptamer. Therefore, premixing the components, which would lead to $\pi\pi$ conjugation of the modifiers was the best option for the fabrication of these aptasensors. Nyquist plots were obtained from analyzing all modified surfaces in the PSA solution (Fig. 5.15). The R_{ct} values obtained from EIS analyses are summarized in Table 5.9. The highest R_{ct} values were observed for the GCE-gCNQDs@aptamer-CoPc(2)($\pi\pi$) (104.3 k Ω) followed by the GCE-gCNQDs@aptamer-CoPc(1)($\pi\pi$) (98.6 k Ω) supporting cyclic voltammetry results in terms of ΔE (Table 4.1). The large R_{ct} suggest faster passivation, hence better binding of PSA to aptamer and better detection. The GCE-

gCNQDs@aptamer sensor showed slightly lower resistance to charge transfer compared to the bare electrode, which was not expected. However, this could imply that the gCNQDs enhanced the electron transfer slightly. For this section, the influence of the MPc complexes is the main focus.

Using the R_{ct} values obtained in the impedance studies, the apparent charge transfer rate constant (k_{app}) was calculated using Eqn.5.4 and the results are summarized in Table 5.9. The surface area was obtained as previously described and k_{app} values were high where R_{ct} were low as expected.

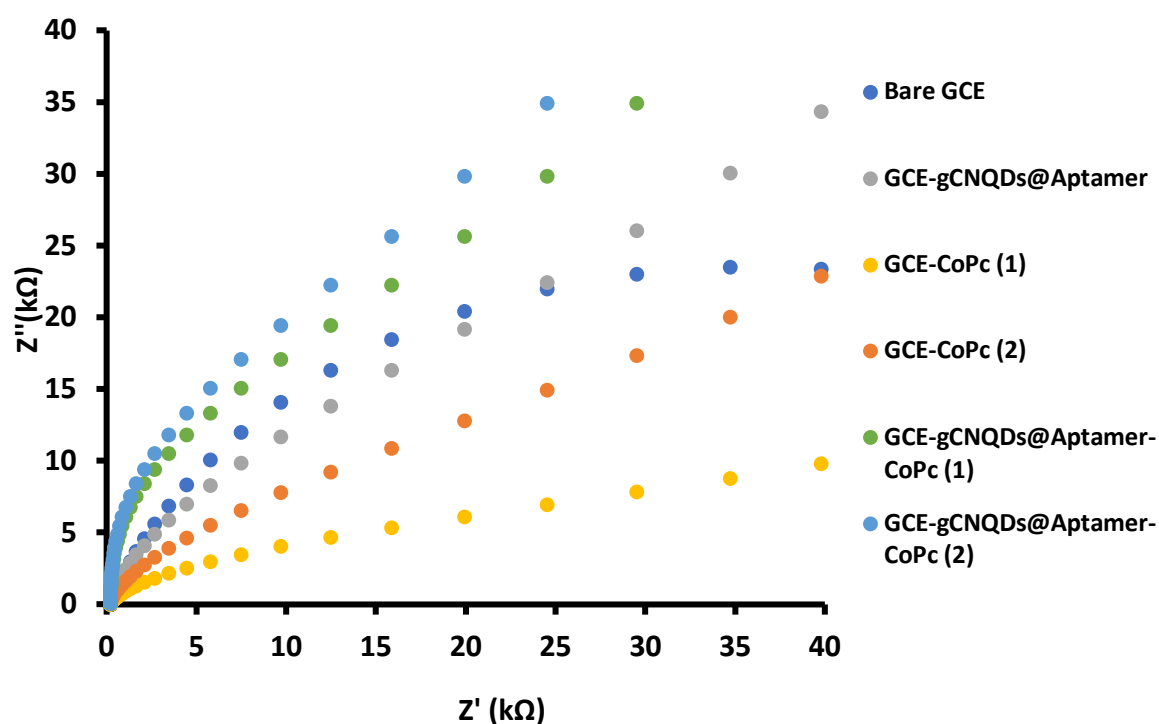


Figure 5.15: Nyquist plots of modified electrodes in a 2 μ M PSA solution in 30 mM phosphate buffer solution of pH 7.4.

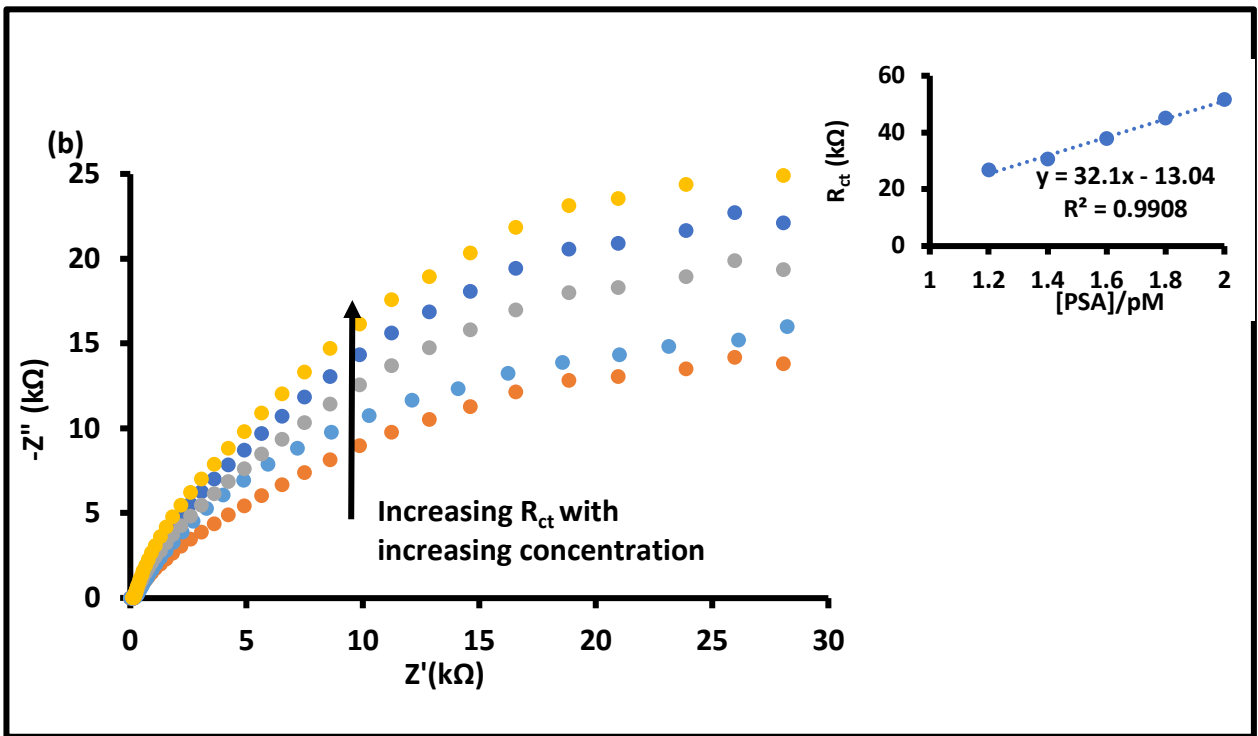
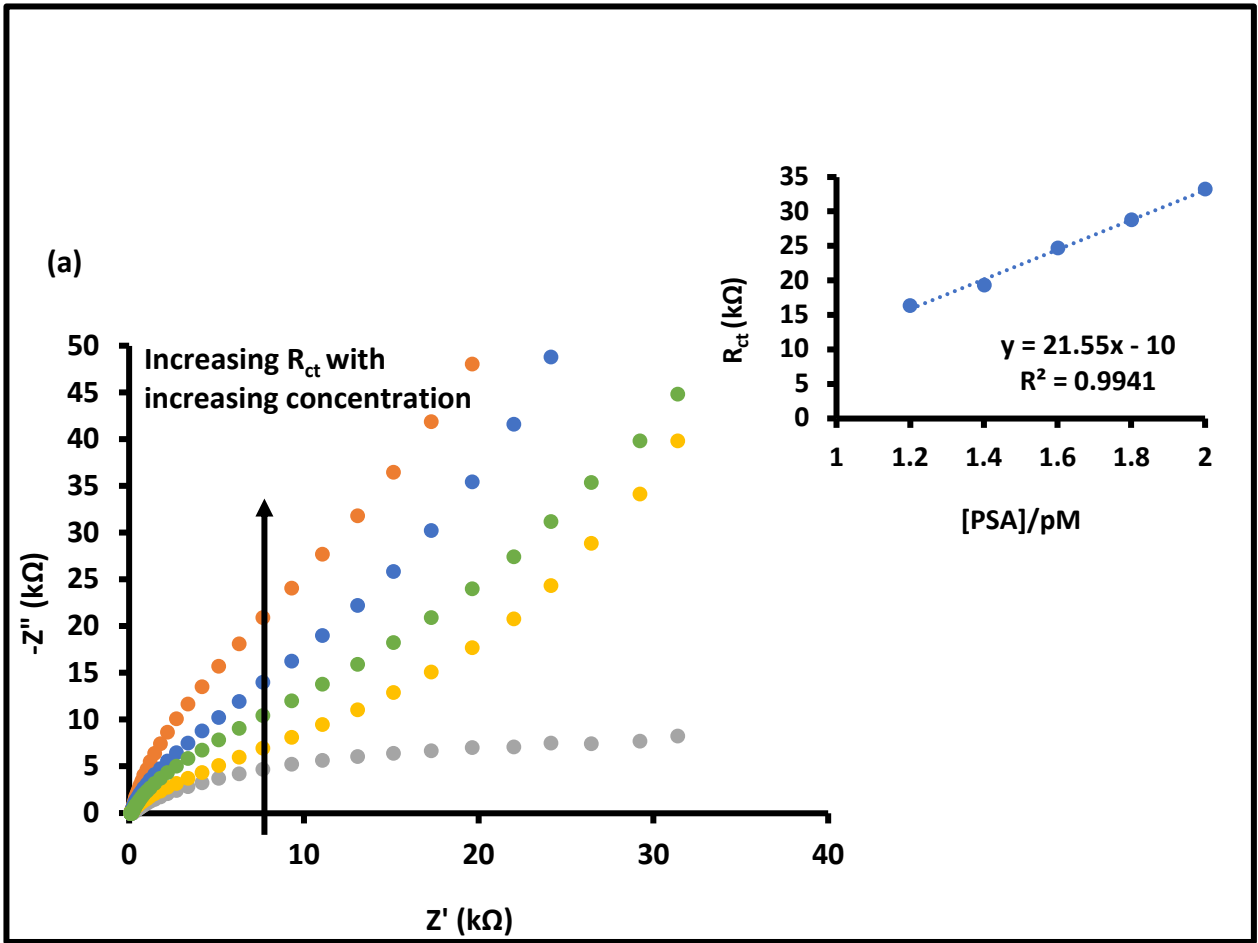
Table 5.9: Summary of determined R_{ct} and k_{app} values determined from Nyquist plots (in order of increasing R_{ct} values).

Electrode	$R_{ct}/ k\Omega$	$k_{app} (cm/s)^2/s$	LoD (ng/mL)
Bare GCE	77.6	5.14×10^{-3}	-
GCE-gCNQDs@aptamer	69.5	5.75×10^{-3}	0.042
GCE-CoPc(1)	22.3	3.01×10^{-2}	-
GCE-CoPc(2)	24.1	2.98×10^{-2}	-
GCE-gCNQDs@aptamer-CoPc(1) ($\pi\pi$)	98.6	6.3×10^{-4}	0.031
GCE-gCNQDs@aptamer-CoPc(2) ($\pi\pi$)	104.3	6.0×10^{-4}	0.023

5.2.3.2 Concentration studies using EIS

The aptamer-based electrodes were all compared to further show the significance of incorporating the phthalocyanine complexes to the gCNQDs@aptamer. Concentration studies were then carried out in buffer to see if the detection limits of the gCNQDs@Aptamer-based sensor is improved when linked to the phthalocyanine complexes. Detection limits were measured in a 30 mM phosphate buffer solution of pH 7.4 with PSA concentrations ranging from 1.2-2.0 pM. The obtained results are summarized in Fig. 5.16 with the inserts showing a linear relationship where the resistance to charge transfer increases with concentration of PSA. The detection limits obtained for the detection of PSA in buffer solutions using the GCE-gCNQDs@Aptamer, GCE-gCNQDs@Aptamer-CoPc(1)($\pi\pi$) and GCE-gCNQDs@Aptamer-CoPc(2)($\pi\pi$) were 0.042, 0.031 and 0.023 ng/mL respectively

(Table 5.9), which are all lower than the reported dangerous levels of PSA in males [118]. Although the addition of the asymmetric phthalocyanine complexes improved the detection limit of the gCNQDs@Aptamer conjugate, complex 2 produced better results than complex 1, proving that the nature of the functional groups present in the complexes plays a role in its electrochemical sensing and influence. The better performance of complex 2 when compared to complex 1 may be explained as follows: Complex 2 has three acetaminophen substituents and an electron donating alkoxy group terminated by an alkyne group. The dominant acetaminophen substituent has a push-pull effect (electron donating-electron withdrawing) through resonance [235] that is independent of the MPc ring. This contributes greatly to the electrochemical sensing ability of CoPc(2). Moreover, alkoxy groups lower oxidation potentials which results in a lower potential difference, which implies better electron transfer [236]. The substituents of CoPc(2) also possess nitrogen atoms which are known to enhance electrochemical sensing ability of composites which was earlier observed for the N-doped GQDs compared to the pristine GQDs.



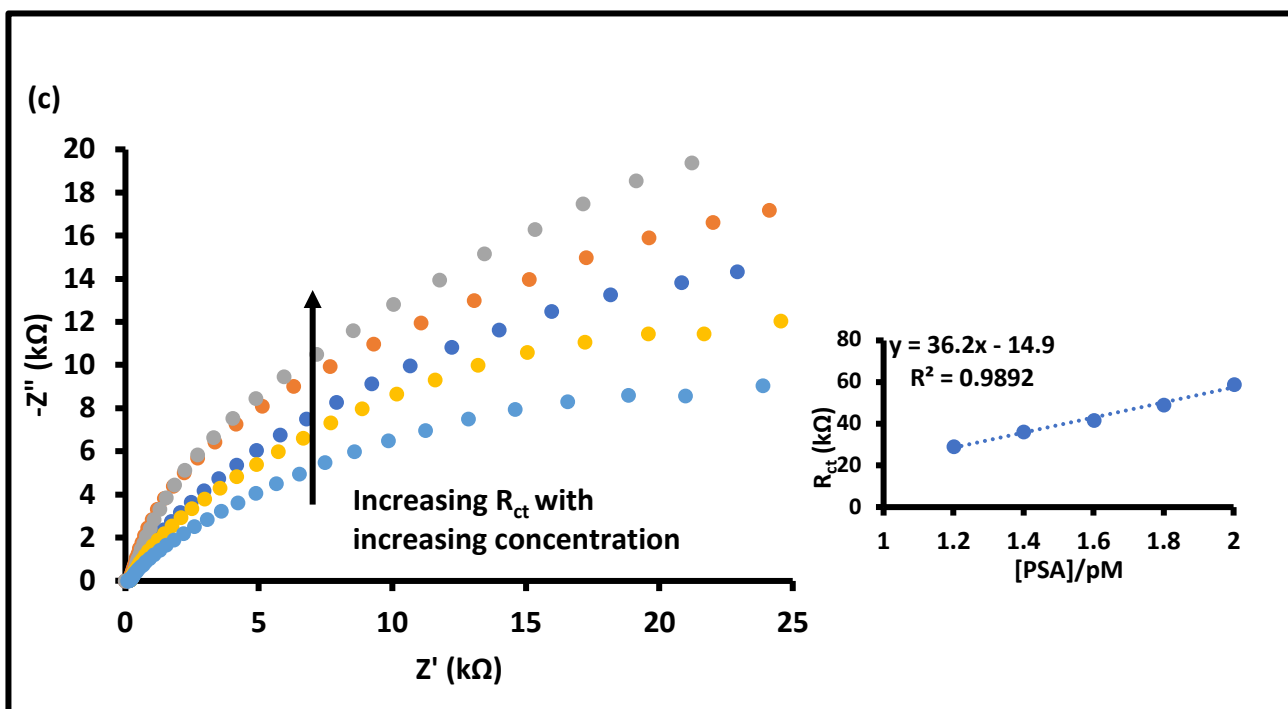


Figure 5.16: Electrochemical impedance (EIS) Nyquist plots of (a) GCE-gCNQDs@Aptamer (b) GCE-gCNQDs@Aptamer-CoPc(1) and (c) GCE-gCNQDs@Aptamer-CoPc(2) in a 30 mM phosphate buffer solution of pH 7.4 with PSA concentrations ranging from 1.2-2.0 pM. Inserts: Linear responses of resistance to changing concentrations.

5.2.3.3 Stability, reproducibility, and repeatability

The best performing aptasensor (GCE-gCNQDs@Aptamer-CoPc (2)) was further used as an example to determine the stability, reproducibility, and repeatability of the fabricated sensor. These tests were run using EIS as this has been the technique used throughout the studies conducted (Table 5.10). For stability, the aptasensor was stored for a week at 4 °C and then tested again. The sensor managed to retain 96.5 % of its performance. The reproducibility was determined by fabricating the same aptasensor three different times and determining the behavior in the buffer solution containing PSA after incubation. The RSD % was determined as 2.5 % validating the reproducibility of this sensor. The aptasensor was tested 10 times over to determine if the same aptasensor could be used for multiple PSA tests (repeatability). The repeatability RSD % was determined as 4.8 % which is quite low. These studies therefore show that this fabricated aptasensor with low detection limits is reliable and efficient as it is stable, reproducible and can be reused for several tests before a new one is required.

Table 5.10: Raw data recorded for the determination of Stability, reproducibility and repeatability for the GCE-gCNQDs@Aptamer-CoPc(2)($\pi\pi$) aptasensor. All measurements were run in triplicate. Repeatability measures were recorded for 10 analyses.

STABILITY			
Rct values in $k\Omega$			
	DAY 0	DAY 7	
	106.2	94.8	
	98.3	100.1	
	99.8	98.6	RETENTION %
AVERAGE	101.4	97.8	96.5

REPRODUCIBILITY			
	Electrode 1	Electrode 2	Electrode 3
Run 1	102.2	104.2	95.4
Run 2	101.3	100.4	89
Run 3	99.4	98.6	105.9
Average	101.0	101.1	96.8
Mean of means	99.6		
SD of means	2.5		
RSD %	2.5		

REPEATABILITY		
Run		
1		103.2
2		101.5
3		97.5
4		90.5
5		99.1
6		101.3
7		102.5
8		91.8
9		103.2
10		104.1
	average	99.5
	SD	4.8
	RSD	4.8

5.2.4 AuNPs-MPc conjugates

5.2.4.1 EIS

A selection of Nyquist plots is shown in Fig. 5.17 and were fitted using a Randles electronic equivalent circuit fitted with a constant phase element (CPE) due to the suppressed semi-circles. As previously stated, using a CPE takes into account the irregularities on the electrode surface that are a result of roughness and inhomogeneities on the modifiers, where the plot starts to appear more linear as opposed to appearing as a semi-circle with a defined linear segment. The apparent charge transfer rate constant (k_{app}) was also calculated using Eqn. 5.4 and summarized in Table 5.11. The R_{ct} value is highest for the GCE-AuNPs \emptyset CoPc(2)-Aptamer with the lowest corresponding apparent charge transfer which is expected as R_{ct} and K_{app} are inversely proportional.

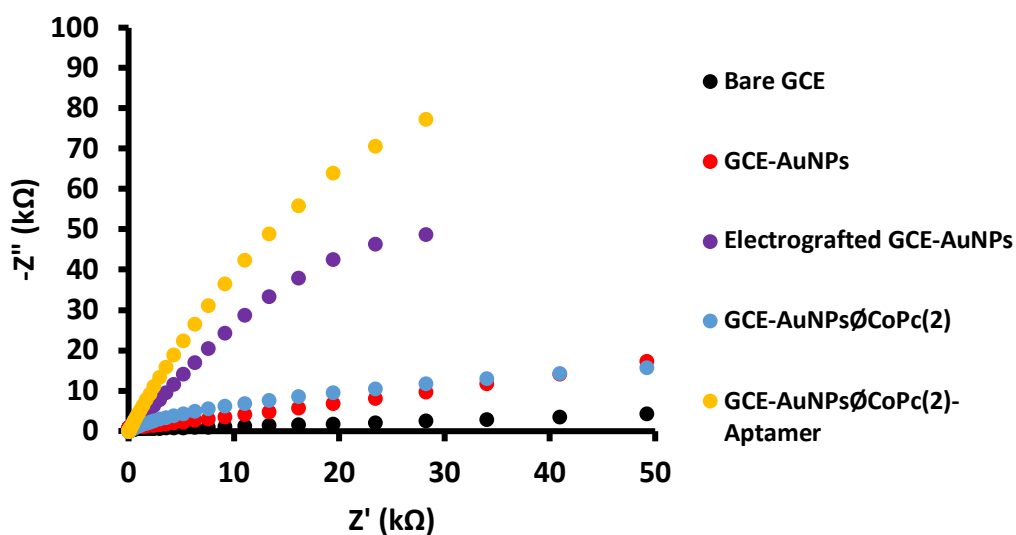


Figure 5.17: Nyquist plots of electrodes in a 2 μM PSA solution in 30 mM PBS solution of pH 7.4.

Table 5.11: Summary of results determined from PSA detection using EIS in 2 μM PSA.

Electrode	$R_{CT}/ \text{k}\Omega$	$k_{app} (\text{cm/s})^2/\text{s}$
Bare GCE	0.46	8.42×10^{-4}
GCE-AuNPs	0.68	5.80×10^{-4}
GCE-Aptamer	3.66	4.8×10^{-5}
GCE-AuNPs-Aptamer	2.58	8.8×10^{-5}
GCE \emptyset CoPc (2)	2.46	9.02×10^{-5}
GCE \emptyset CoPc(2)-Aptamer	4.18	2.09×10^{-5}
GCE-AuNPs \emptyset CoPc(2)	1.14	2.68×10^{-4}
GCE-AuNPs \emptyset CoPc(2)-Aptamer	9.62	1.82×10^{-6}

5.2.4.2 Concentration studies using EIS and DPV

Fig. 5.18, representing GCE-AuNPs \emptyset CoPc(2)-Aptamer as an example, shows the Nyquist plots of the electrodes in solutions containing different concentrations of PSA. All electrodes show a linear response to changing PSA concentration after incubation in the PSA solutions. The slopes of each fabricated aptasensor represents the sensitivity of the sensor and the highest sensitivity is observed in the insert of Fig. 5.18, recorded for the GCE-AuNPs \emptyset CoPc(2)-Aptamer. The LoDs were also determined (Table 5.12) and the lowest was for the GCE-AuNPs \emptyset CoPc(2)-Aptamer as expected, was found to be 0.92 pM (0.026 ng/mL), determined from EIS results and 0.89 pM (0.025 ng/mL) determined from DPV studies.

Table 5.12: Summary of LoD determined from the detection of PSA in buffer and in spiked serum samples.

Electrode	LoD in PBS (pM)	reference
GCE-AuNPs-Aptamer	1.24 (EIS)	This work
	1.09 (DPV)	
GCE \emptyset CoPc(2)-Aptamer	1.83 (EIS)	This work
	1.10 (DPV)	
GCE-AuNPs \emptyset CoPc(2)-Aptamer	0.92 (EIS)	This work
	0.89 (DPV)	

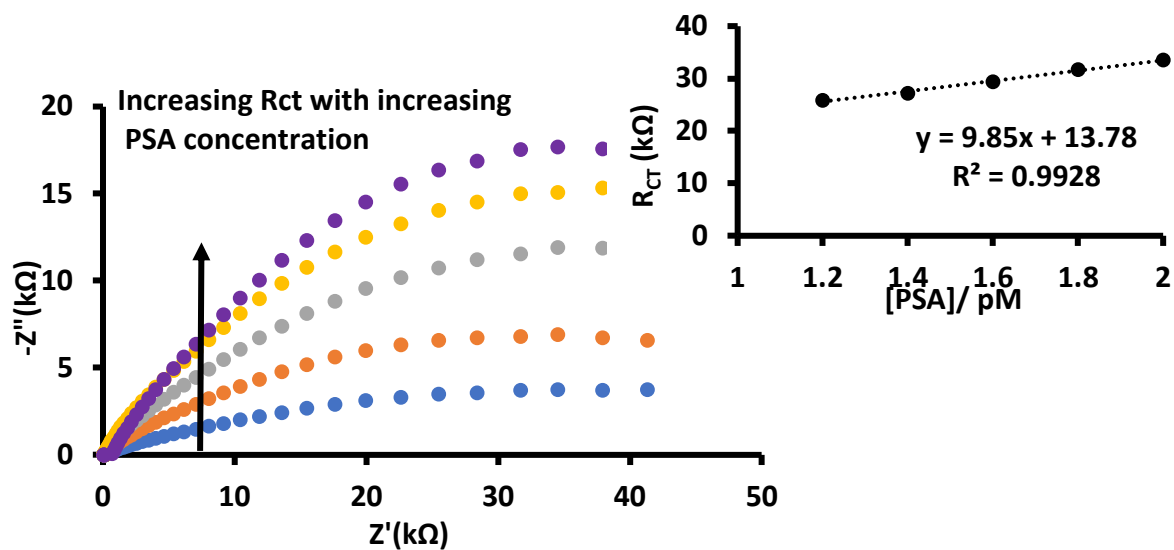


Figure 5.18: Electrochemical impedance (EIS) Nyquist plots of GCE-AuNPs \emptyset CoPc(2)-Aptamer in a 30 mM PBS solution of pH 7.4 containing PSA concentrations ranging from 1.2-2.0 pM. **Insert:** Linear responses of resistance to changing concentrations.

The DPV results are illustrated in Fig. 5.19. Linear responses to change in concentration were also observed where the peak current decreased with increasing PSA concentration due to PSA binding during incubation. The LoD was determined from the peak at 0 V for the GCE-AuNPs-Aptamer aptasensor, 0.0 V for the GCE \emptyset CoPc(2)-Aptamer aptasensor and at -0.25 V for the GCE-AuNPs \emptyset CoPc(2)-Aptamer aptasensor. In DPV (Fig. 5.19) the GCE-AuNPs \emptyset CoPc(2)-Aptamer aptasensor produced a LoD of 0.89 pM. These detection limits will later be compared to those that will be determined in human serum to test the reliability of the studies reported in this work.

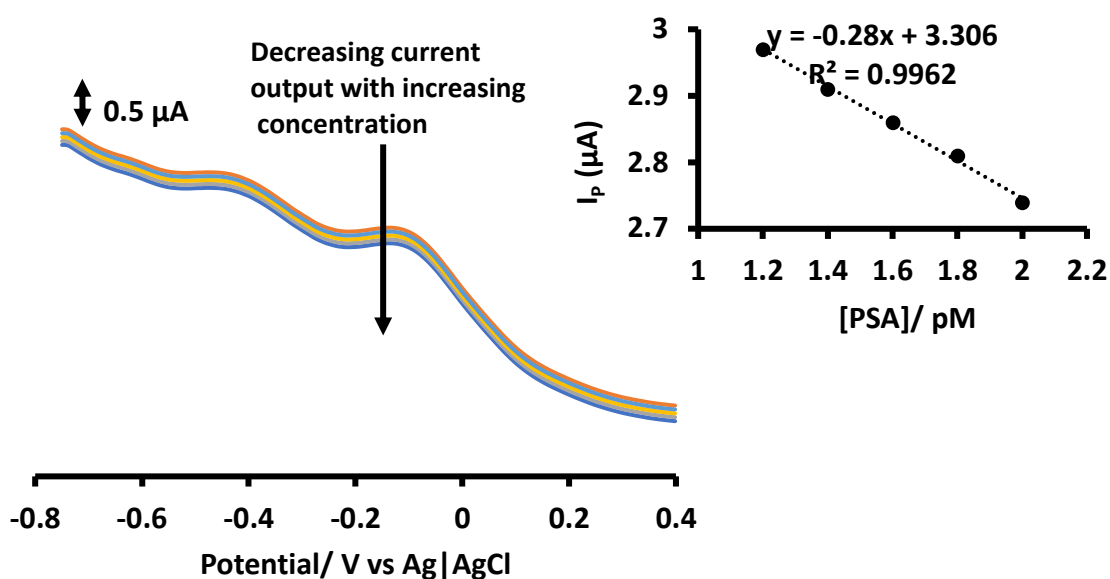


Figure 5.19: Differential pulse voltammograms (DPV) of GCE \emptyset CoPc(2)-Aptamer in a 30 mM PBS solution of pH 7.4 containing PSA concentrations ranging from 1.2-2.0 pM. **Insert:** Linear responses of resistance to changing concentrations.

5.2.4.3 Effects of scan rate

The scan rate studies were conducted using DPV and scan rates of 0.625, 1.25, 2.5, 5, 15 and 20 V/s. The results obtained are summarized in Fig. 5.20 using GCE \emptyset CoPc(2)-Aptamer as an example. The general trend observed was an increasing in peak current with increasing scan rate. However, this increase was not linear and did not pass through the origin when scan rate was plotted against peak current as well as peak current vs the square root of scan rate. This has been reported to be characteristic of an electrodic process (i.e., reactions occurring at the electrode surface) preceded by an electrochemical reaction, followed by a homogenous

chemical reaction [196]. Thus, it can be concluded that the process occurring between solution and sensor are mainly adsorption controlled.

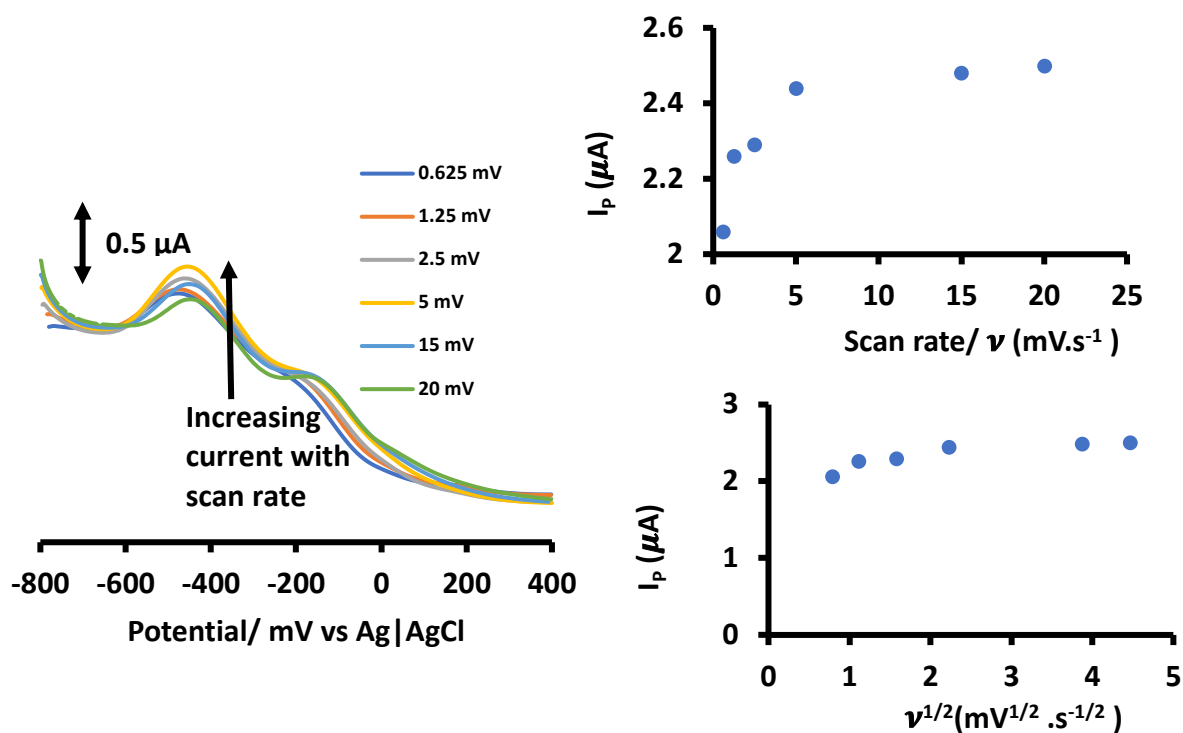


Figure 5.20: Differential pulse voltammograms of scan rate studies of GCE@CoPc(2)-Aptamer in a 30 mM phosphate buffer solution of pH 7.4 with PSA concentration of 2.0 pM. Inserts: Plots of peak current (I_p) vs ν and peak current (I_p) vs $\nu^{1/2}$.

5.2.4.4 Selectivity, stability, repeatability, and reproducibility studies

Selectivity studies were achieved by using the mixed solution method and DPV. The PSA samples were mixed with BSA, L-cysteine and glucose as interferants as done for other fabricated aptasensors already discussed and (K_{amp}) values determined in the same manner as above. The results obtained are summarized in Table 5.13 with the potentials at which the K_{amp} values were calculated. The values determined were very low implying that these sensor platforms could be applied without any pre-separation procedures for the determination of PSA in the presence of the interferents with no need for pre-treatment of sample.

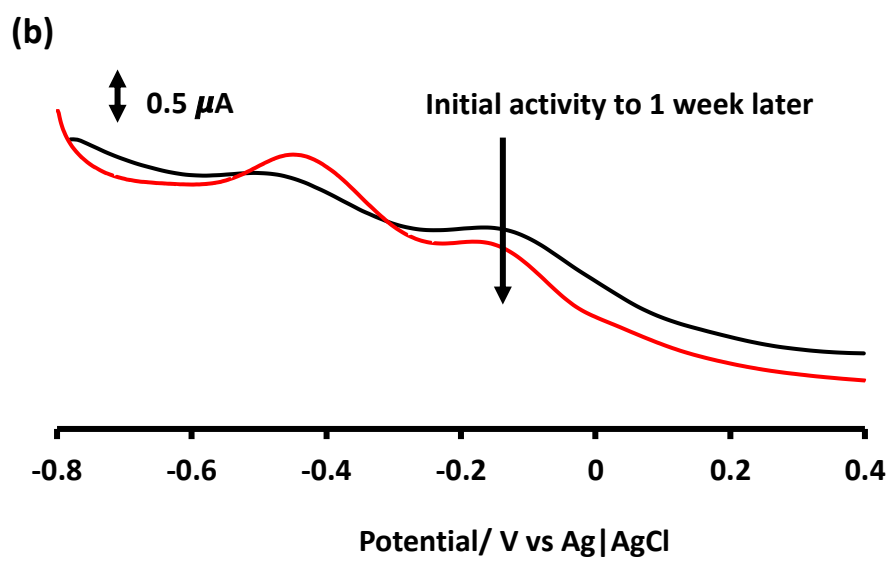
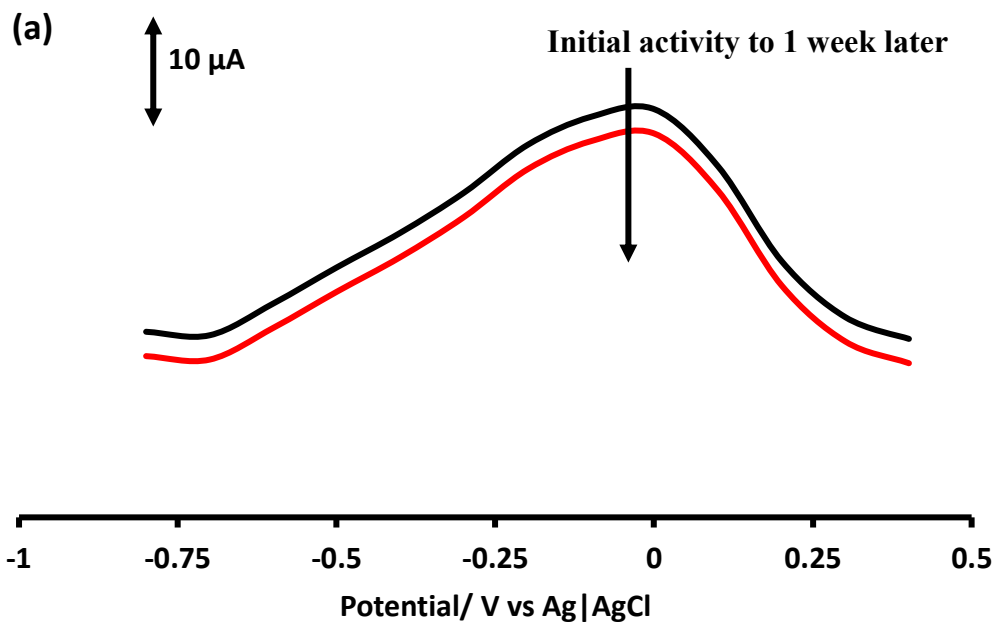
Table 5.13: K_{amp} values determined from the detection of PSA in a complex mixture.

Electrode	K_{AMP} (BSA)	K_{AMP} (Glucose)	K_{AMP} (L-cysteine)
GCE-AuNPs-Aptamer	-4.18×10^{-4}	-1.00×10^{-3}	-4.75×10^{-4}
GCE \emptyset CoPc(2)-Aptamer	3.96×10^{-4}	4.57×10^{-4}	4.37×10^{-4}
GCE-AuNPs \emptyset CoPc(2)-Aptamer	-2.7×10^{-5}	-5.4×10^{-6}	7.61×10^{-5}

The stability, repeatability, and reproducibility of the proposed aptasensors were also investigated by DPV using a 2 pM PSA in PBS solution of pH 7.4 (30 mM). Table 5.14 summarizes the results obtained. To verify the reproducibility of the aptasensors, each electrode was fabricated three times and tested in the PSA solution of same concentration. The relative standard deviation (% RSD) was determined as 4.89 %, 7.1 % and 0.91 % (Table 5.14) for GCE-AuNPs-Aptamer, GCE \emptyset CoPc(2)-Aptamer and GCE-AuNPs \emptyset CoPc(2)-Aptamer respectively. The aptasensor with the CoPc(2) and AuNPs combined proved to be the best performing after being refabricated a few times over.

After incubation the PSA solution, the DPV scans were run for 50 cycles and the change in current response was monitored (Figure not shown). The first and the last scan were compared using the marked peaks. The determined % RSD values were 0.81 %, 2.04 %, 0.83 % for GCE-AuNPs-Aptamer, GCE \emptyset CoPc(2)-Aptamer and GCE-AuNPs \emptyset CoPc(2)-Aptamer, respectively, Table 5.14.

When the electrode was not in use, it was stored in the fridge at 4 °C. After a week of storage, the final run was compared to an initial run done before storage (Fig. 5.21, point of RSD determination marked with arrows). The % RSD determined for the fabricated aptasensors (Table 5.14) were 4.35 %, 6.97 % and 4.23 % for GCE-AuNPs-Aptamer, GCE \emptyset CoPc(2)-Aptamer and GCE-AuNPs \emptyset CoPc(2)-Aptamer respectively. The most stable electrodes appear to be the ones with the AuNPs which implies that these nanostructures provide greater stability for the immobilization of the aptamer when coupled with the CoPc(2).



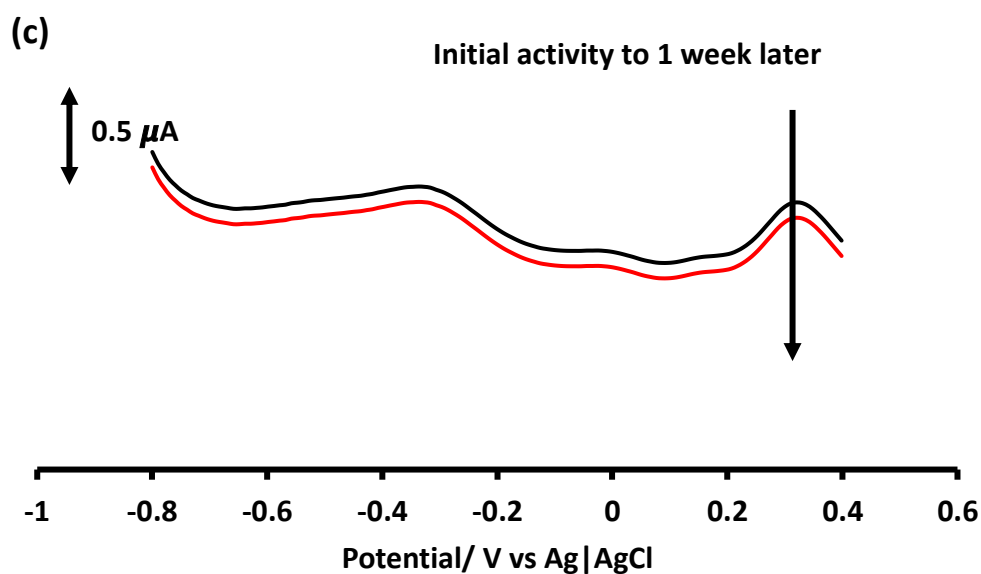


Figure 5.21: Differential pulse voltammograms of (a) GCE-AuNPs-Aptamer, (b) GCE \emptyset CoPc(2)-Aptamer and (c) GCE-AuNPs \emptyset CoPc(2)-Aptamer in a PSA solution of concentration 2.0 pM measured before and after a week.

Table 5.14: % RSD values determined for stability, repeatability and reproducibility of fabricated aptasensors.

Electrode	Linear range/pM	Stability (RSD%)	Repeatability (RSD%)	Reproducibility (RSD%)
GCE-AuNPs-Aptamer	1.2-2.0	4.35	0.81	4.89
GCE \emptyset CoPc(2)-Aptamer	1.2-2.0	6.97	2.04	7.10
GCE-AuNPs \emptyset CoPc(2)-Aptamer	1.2-2.0	4.23	0.83	0.91

5.3 Conclusions

This chapter has discussed the electrochemical sensing ability of various fabricated sensors. Initially, the electrodes modified with QDs and MPc were used to catalyze L-cysteine to verify their synergistic effects for further use as signal amplifiers and aptamer immobilizers for aptasensing. The synergistic effects of these nanocomposites improved signal output and showed good promise in being applied as signal enhancers and aptamer immobilization platforms towards the fabrication of PSA aptasensors. Thereafter, the GQDs-CoPc(1)($\pi\pi$) conjugate was used as an example, together with aptamer for the detection of PSA in buffer solutions. Various combinations of these composites were immobilized via adsorption on glassy carbon electrodes to determine the best combination that would produce low detection limits and prove superior to other combinations used. It was clearly shown that the sequentially modified electrode, GCE-GQDs-CoPc(1)($\pi\pi$)-Aptamer (sequential), showed the best performance, therefore this modification sequence was used for further study involving the comparison of structure and composition of QDs. The comparative study showed that all electrodes produced low detection limits with good stability, reproducibility, and repeatability as well as selectivity for PSA in complex samples. The NGQDs-based aptasensor however, performed the best in terms of detection limits, especially.

CoPc complexes were also compared, and it was found that the nature of the substituent influenced the performance of the aptasensor towards the detection of PSA. Complex 2 performed the best, owing to the resonance effect of the dominant substituents it possesses, as well as the presence of the nitrogen atoms at the periphery that complex 1 does not possess.

The study was shifted from QDs to AuNPs which are commonly used in PSA aptasensors and the influence of combining these AuNPs with CoPc(2) towards PSA detection was studied. It was proven that incorporating a CoPc complex to the sensor improved its performance. Moreover, using covalent immobilization of the nanocomposites increased the stability of the aptasensor. The aptasensors containing AuNPs also showed good stability, reproducibility, and repeatability. Scan rate studies indicated adsorption-controlled processes occurring between electrode and analyte.

6. Real sample analyses

To validate the reliability and feasibility of the fabricated aptasensors discussed in the previous chapter, they were tested in spiked human serum samples. This was also to prove the trends observed when the PSA was analyzed in buffer. In preparation for this analysis, the serum samples were diluted 100-fold with PBS (pH 7.4) to reduce the matrix effects of the real sample. Thereafter, different concentrations of PSA were added to the diluted serum solutions. The analytical methods as well as concentrations used in this study were the same as the methods used for PSA detection in PBS. The real sample tests were run using DPV and EIS for the sake of comparison of both techniques unless stated otherwise. Table 6.1 summarizes the detection limits obtained in buffer solution and serum samples.

Table 6.1: Summary of determined LoD (ng/mL) values in buffer and spiked serum samples of aptasensors using EIS unless stated otherwise.

Electrode	LoD _{BUFFER}	LoD _{SERUM}
GCE-GQDs-CoPc(1)($\pi\pi$)-Aptamer	0.051	0.059 (DPV) 0.058
GCE -NGQDs-CoPc(1)($\pi\pi$)-Aptamer	0.044 (DPV) 0.046	0.043
GCE-gCNQDs-CoPc(1) ($\pi\pi$)-Aptamer	0.053 (DPV) 0.055	0.047 (DPV) 0.046
GCE-gCNQDs@aptamer	0.042	0.054
GCE-gCNQDs@aptamer-CoPc(1) ($\pi\pi$)	0.031	0.032
GCE-gCNQDs@aptamer-CoPc(2) ($\pi\pi$)	0.023	0.027
GCE-AuNPs-Aptamer	0.035 0.031 (DPV)	0.037 0.040 (DPV)
GCE \emptyset CoPc(2)-Aptamer	0.052 0.031 (DPV)	0.056 0.043 (DPV)
GCE-AuNPs \emptyset CoPc(2)-Aptamer	0.026 0.025 (DPV)	0.028 0.027 (DPV)

6.1 $\pi\pi$ -conjugates

The following conjugates were used as examples to verify the feasibility of the fabricated aptasensors to be used in clinical studies towards the electrochemical detection of PSA: GCE-GQDs-CoPc(1)($\pi\pi$)-Aptamer (sequential), GCE-NGQDs-CoPc(1)($\pi\pi$)-Aptamer (sequential) and GCE-gCNQDs-CoPc(1)($\pi\pi$)-Aptamer (sequential).

Different concentrations of PSA were added to the diluted serum solutions for analysis. The analytical methods as well as concentrations used for analysis of these real samples were the same as the methods used for PSA detection in buffer where the concentration ranged from 1.2 to 2 pM. The verification of the reliability and feasibility of the aptasensors was taken further by determining the % recovery in the concentration range of 1.2-2 pM, using EIS. The recovery was calculated as the ratio of the sensor performance in spiked human serum samples to that obtained in buffer for the same concentrations of PSA as reported in literature [141]. The amount of PSA found in spiked serum was determined by calculating the percentage signal based on PSA detection in the chosen buffer. All experiments were run in triplicate and the recorded values are an average of the values recorded for each run.

For GQDs-CoPc(1)($\pi\pi$)-Aptamer both DPV and EIS were employed, DPV is used as an example. The obtained responses in DPV for the GQDs-CoPc(1)($\pi\pi$)-Aptamer electrode are shown in Figure 6.1. The LoD for GQDs-CoPc(1)($\pi\pi$)-Aptamer was determined from the signal at 0 V as it was the most prominent one. The LoD was determined as 0.059 ng/mL using DPV, which is below the cut-off value of 4 ng/mL in patients suspected to have prostate cancer [118, 237, 238]. The LoD determined from EIS was 0.058 ng/mL which is close to the value obtained in DPV for GQDs-

CoPc(1)($\pi\pi$)-Aptamer, Table 6.1. EIS results for the determination of % recoveries are shown in Table 6.2. The percentage recovery calculated was 80.5% at the highest concentration level analyzed and 93.5 % at the lowest concentration level analyzed.

For the NGQDs-based electrode, EIS was used as the analytical tool to detect PSA in the spiked human serum samples for the determination of the LoD and percentage recoveries. DPV was not included as the peaks were too broad for the determination of LoD. The obtained responses in EIS are shown in Figure 6.2. The LoD was determined as 1.52 pM (0.043 ng/mL) which is again below the cut-off value of 4 ng/mL. The recovery results obtained are shown in Table 6.3. The amount of PSA found in spiked serum was also determined. The percentage recovery calculated was 85.9 % at the lowest concentration level of 1.2 pM and 93.7 % at the highest concentration level of 2 pM.

The obtained responses in DPV for the gCNQDs-based electrode are shown in Figure 6.3. The LoD was determined from the signal at 0 V as it was the most prominent one. The LoD was determined as 0.936 pM (0.027 ng/mL) in DPV and 0.929 pM (0.026 ng/mL), (Table 6.1), in EIS which is also below the cut-off value of 4 ng/mL. The verification of the reliability and feasibility were performed as explained above. The results obtained are shown in Table 6.4. The percentage recovery calculated was 86 % at the lowest concentration level analyzed and 94.9 % at the highest concentration level analyzed.

In summary, it has been shown that the results obtained from detecting PSA in buffer are feasible as they are comparable to the values determined in serum samples, Table 6.1. The R_{ct} values were lower in serum compared to PBS. The decrease could indicate some protein-protein interaction which results in a decrease in sensitivity

hence the reduced R_{ct} values obtained in serum analyses compared to those done in PBS. The interferences, however, are not strong enough to affect the ability of the aptasensor to detect PSA in real samples. Some literature reports have shown detection limits determined from electrochemically detecting PSA in spiked serum samples [226, 230, 231, 239-241] for PSA electrochemical detection. When compared to the data obtained herein, the fabricated sensors in this work showed better performance.

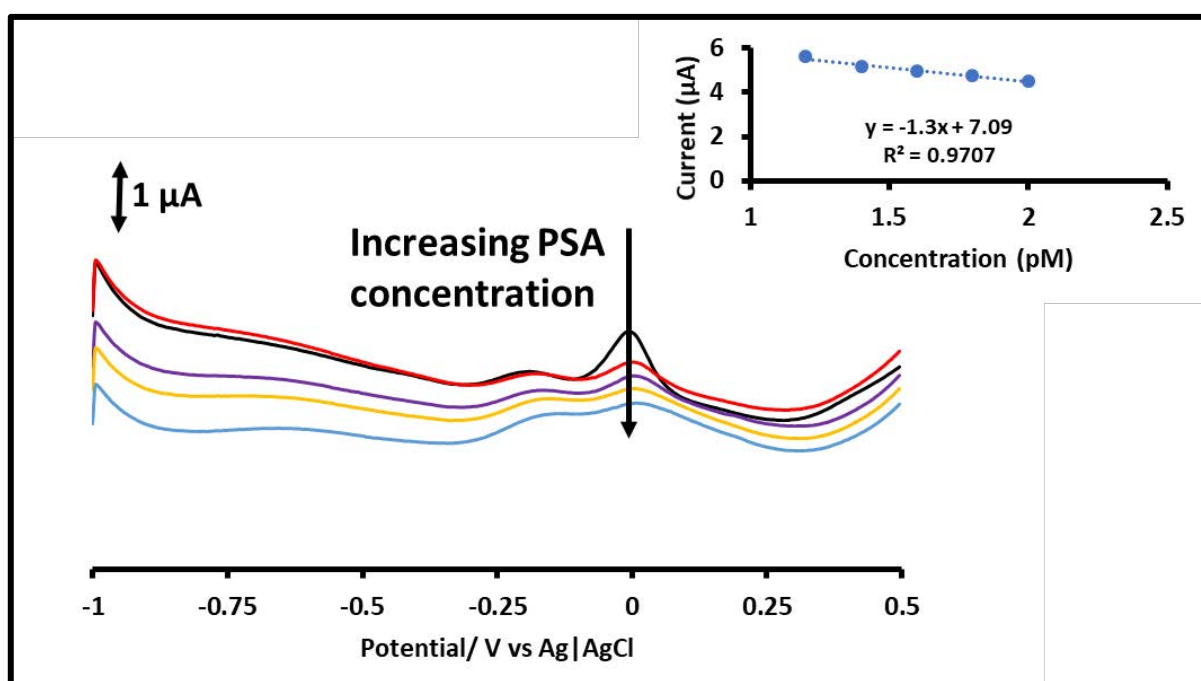


Figure 6.1: Differential pulse voltammograms of GCE-GQDs-CoPc(1)($\pi\pi$)-Aptamer in spiked human serum with PSA concentrations ranging from 1.2-2.0 pM. Insert: Linear responses of currents to changing concentration.

Table 6.2: Summary of recovery measurements of PSA in spiked human serum samples for the GCE-GODs-CoPc(1)($\pi\pi$)-Aptamer aptasensor. % RSD = relative standard deviation (standard deviation/mean \times 100; n = 3).

[PSA] added/ pM In buffer	R_{ct} (k Ω) In buffer	[PSA] found/ pM In serum	R_{ct} (k Ω) In serum	% RSD	% Recovery
1.2	3.1	1.12	2.9	4.2	93.5
1.4	4.2	1.30	3.9	6.1	92.8
1.6	5.8	1.46	4.7	5.4	81.0
1.8	7.9	1.20	6.8	4.5	86.1
2.0	10.3	0.97	8.3	7.4	80.5

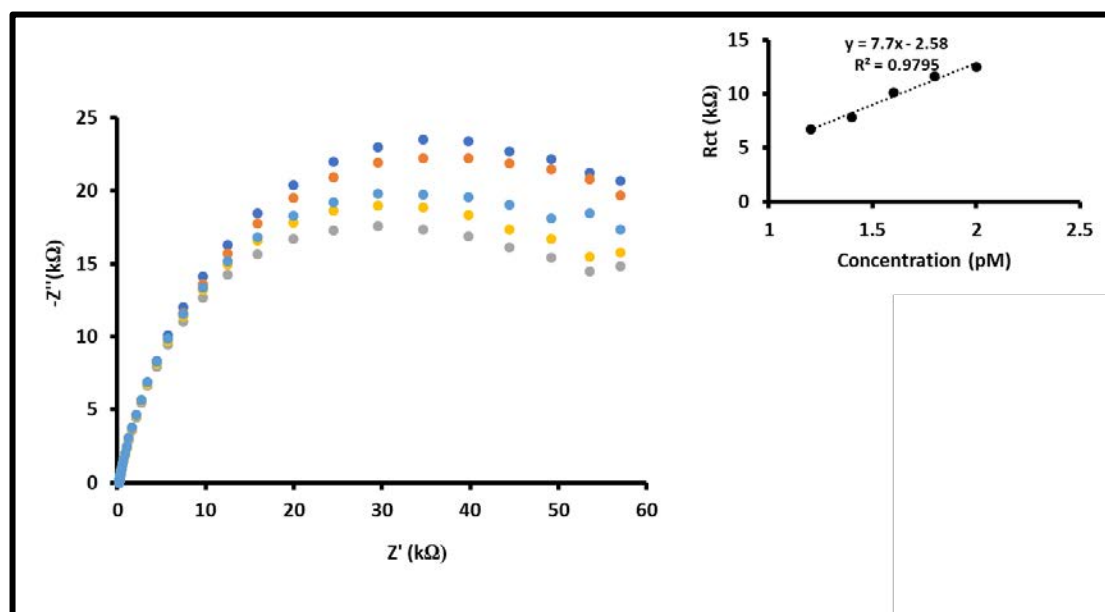


Figure 6.2: Nyquist plots of GCE-NGQDs-CoPc(1)($\pi\pi$)-Aptamer in spiked human serum with PSA concentrations ranging from 1.2-2.0 pM. Insert: Linear responses of currents and resistance to changing concentration.

Table 6.3: Summary of recovery measurements of PSA in spiked human serum samples for the GCE-NGQDs-CoPc(1)($\pi\pi$)-Aptamer aptasensor. % RSD = relative standard deviation (standard deviation/mean \times 100; n = 3).

[PSA] added/ pM In buffer	R_{ct} (k Ω) In buffer	[PSA] found/ pM In serum	R_{ct} (k Ω) In serum	% RSD	% Recovery
1.2	7.80	1.03	6.7	5.9	85.9
1.4	8.59	1.16	7.1	5.4	82.6
1.6	10.9	1.48	10.1	6.2	92.7
1.8	11.8	1.77	11.6	4.9	98.3
2.0	12.8	1.87	12.0	8.6	93.7

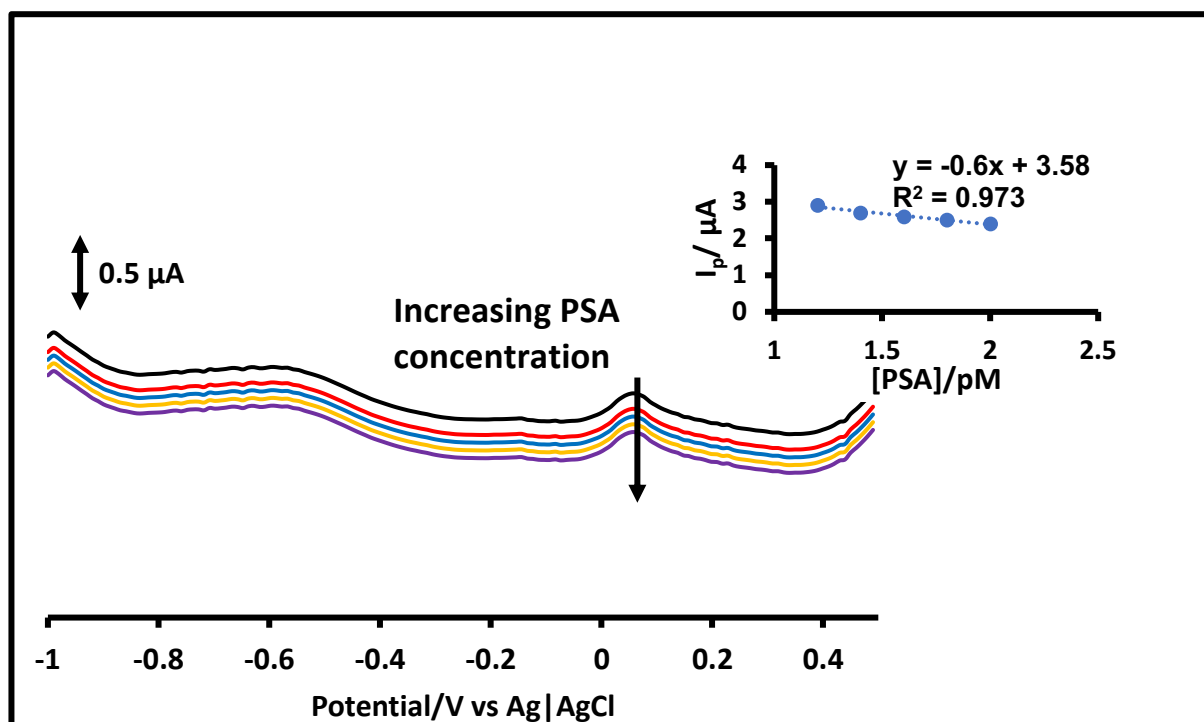


Figure 6.3: Differential pulse voltammograms of GCE-gCNQDs-CoPc(1)($\pi\pi$)-Aptamer in spiked human serum with PSA concentrations ranging from 1.2-2.0 pM. Insert: Linear responses of current to changing concentration.

Table 6.4: Summary of recovery measurements of PSA in spiked human serum samples for the GCE-gCNQDs-CoPc(1)($\pi\pi$)-Aptamer aptasensor. % RSD = relative standard deviation (standard deviation/mean \times 100; n = 3).

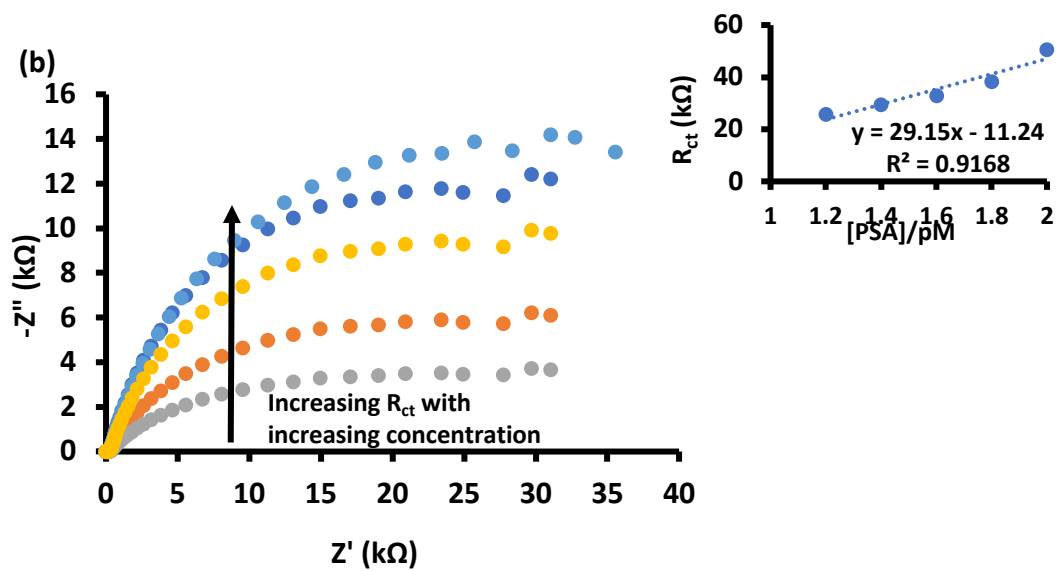
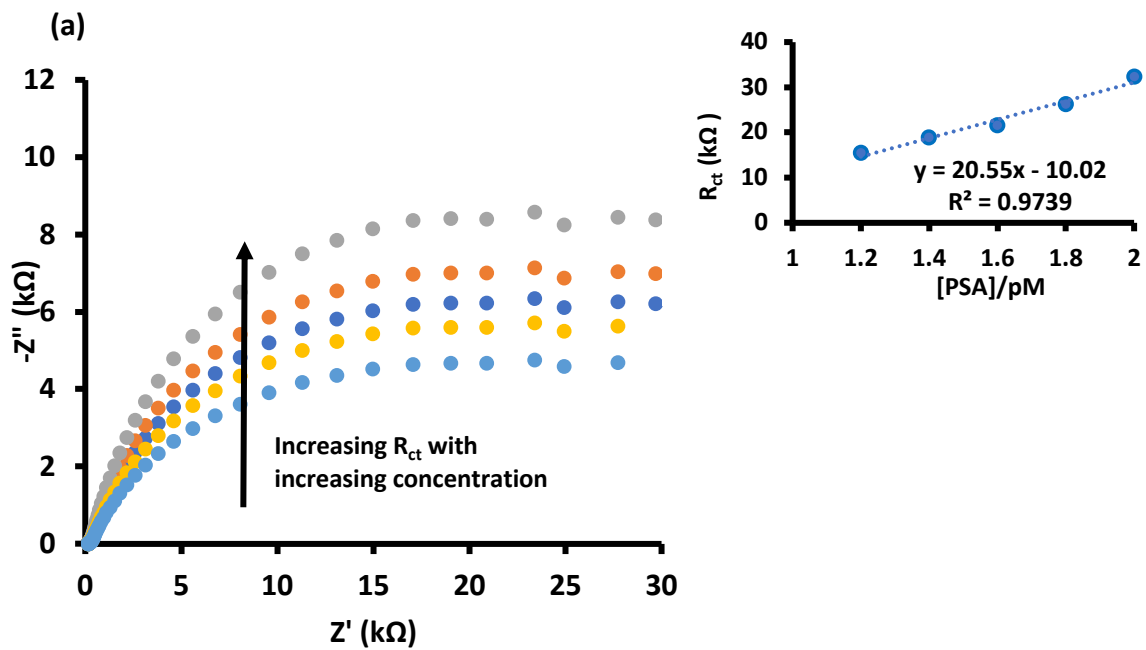
[PSA] added/ pM In buffer	R _{ct} (k Ω) In buffer	[PSA] found/ pM In serum	R _{ct} (k Ω) In serum	% RSD	% Recovery
1.2	4.66	1.03	4.01	6.2	86.0
1.4	6.47	1.38	6.39	5.9	98.7
1.6	7.46	1.56	7.28	2.3	97.6
1.8	8.46	1.77	8.33	8.1	98.5
2.0	11.7	1.89	11.1	8.3	94.9

6.2 Covalently linked conjugates followed by $\pi\pi$ conjugation

The following conjugates were used as examples to verify the feasibility of the fabricated aptasensors to be used in clinical studies towards the electrochemical detection of PSA: GCE-gCNQDs@Aptamer, GCE-gCNQDs@Aptamer-CoPc(1) ($\pi\pi$) and GCE-gCNQDs@Aptamer-CoPc(2) ($\pi\pi$).

The obtained responses of the gCNQDs@Aptamer based sensors are shown in Fig. 6.4. The detection limits were determined as 0.054, 0.032 and 0.023 ng/mL, which are as those obtained for PSA in buffer and are still below the cut-off value of 4 ng/mL of patients suspected to have prostate cancer. When CoPc complexes were immobilized on the electrode surface and tested in a ferricyanide solution, complex 2 compared to complex 1 showed better electrocatalytic ability. In addition, a higher surface coverage was calculated for complex 2 (Table 4.1) which would indicate a larger surface area for aptamer immobilization. With a higher aptamer concentration at the surface as well as better current output due to the substituents complex 2 possesses, the aptasensor with complex 2 is expected to perform better. The verification of the reliability and feasibility of these aptasensor was also done by calculating the % recovery in the concentration range of 1.2-2 pM, using EIS. The recovery was calculated as was done for previously discussed aptasensors. The results obtained are shown in Table 6.5 corresponding to the aptamer-based electrodes. The percentage recoveries calculated ranged within an 85 and 98 % window in general for all sensors fabricated. Although the results obtained from EIS indicate some interference due to the complexity of the serum which resulted in a decrease in sensitivity (i.e., reduced R_{ct} values obtained in serum analyses compared to those done in the buffer solution), the differences in recorded values are minimal,

making these aptasensors feasible for further use in clinical studies. Moreover, the good recoveries also prove their reliability.



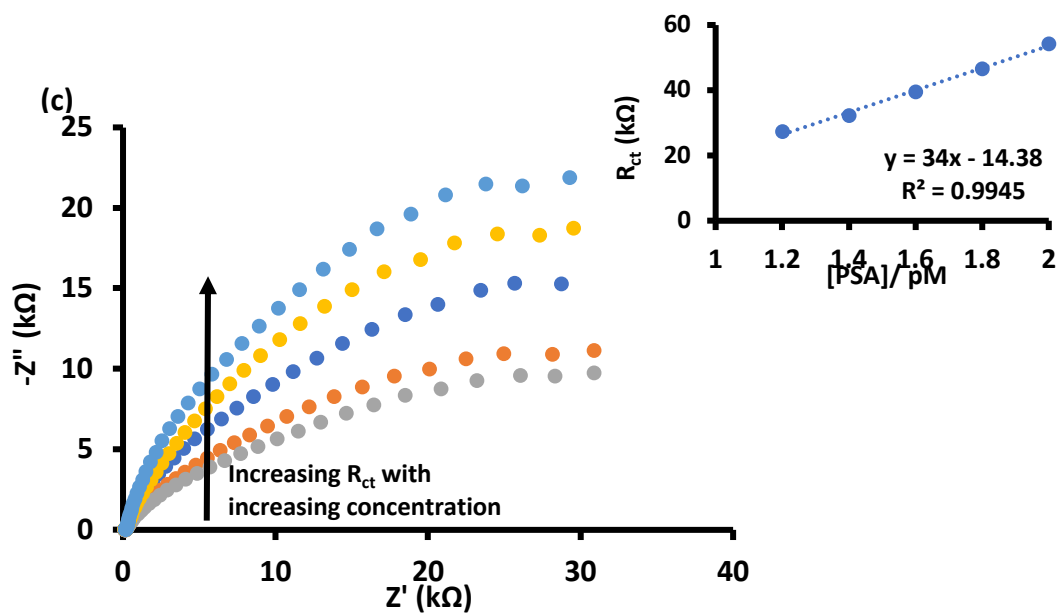


Figure 6.4: Electrochemical impedance (EIS) Nyquist plots of (a) GCE-gCNQDs@Aptamer, (b) GCE-gCNQDs@Aptamer-CoPc(1)($\pi\pi$) and (c) GCE-gCNQDs@Aptamer-CoPc(2)($\pi\pi$) in spiked human serum with PSA concentrations ranging from 1.2-2.0 pM. Insert: Linear responses of currents and resistance to changing concentration.

Table 6.5: Summary of recovery measurements of PSA in spiked human serum samples for the aptasensors. % RSD. (relative standard deviation) = standard deviation/mean \times 100; n = 3.

[PSA] added/ pM in buffer	R _{ct} (k Ω) in buffer	[PSA] found/ pM In serum	R _{ct} (k Ω) In serum	% RSD	% Recovery
GCE-gCNQDs@Aptamer					
1.2	16.4	1.13	15.4	1.8	93.9
1.4	19.3	1.37	18.9	2.1	97.9
1.6	24.7	1.39	21.5	1.2	87.0
1.8	28.8	1.64	26.2	3.3	90.9
2.0	33.2	1.94	32.3	7.2	97.3
GCE-gCNQDs@AptamerCoPc(1)($\pi\pi$)					
1.2	26.7	1.16	25.8	1.4	96.6
1.4	30.5	1.35	29.5	2.6	96.7
1.6	37.9	1.38	32.8	1.8	86.5
1.8	44.9	1.54	38.4	3.8	85.5
2.0	51.6	1.96	50.5	6.2	97.9
GCE-gCNQDs@Aptamer-CoPc(2)($\pi\pi$)					
1.2	29.2	1.13	27.4	5.4	93.8
1.4	36.2	1.25	32.3	3.1	89.2
1.6	41.6	1.52	39.6	2.8	95.2
1.8	49.2	1.70	46.5	1.2	94.5
2.0	58.9	1.84	54.3	1.7	92.2

6.3 Self-assembly, electrografting and click chemistry

The following electrodes were used after modification by self-assembly and covalent linking, to show the synergistic effects of AuNPs combined with complex 2: GCE-AuNPs-Aptamer, GCE \emptyset CoPc(2)-Aptamer and GCE-AuNPs \emptyset CoPc(2)-Aptamer.

The aptasensors based on AuNPs and complex 2 were also verified in spiked serum samples. The real sample tests were run using DPV and EIS. The obtained responses are shown in Fig. 6.5(a) (DPV) and Fig. 6.5(b) (EIS) as examples of the plots used to extract the validating data from. The best performing aptasensor was the one where the AuNPs and CoPc(2) were coupled, as expected with detection limits determined as 0.028 ng/mL (EIS) and 0.027 ng/mL (DPV), Table 6.1. These values are similar to those determined from analyses done in PBS and are still well below the cut-off value of 4 ng/mL (13.3 nM) of patients suspected to have prostate cancer. The % recovery in the concentration range of 1.2-2 pM, using EIS was also determined. The results obtained are shown in Table 6.6, 6.7 and 6.8 for GCE-AuNPs-Aptamer, GCE \emptyset CoPc(2)-Aptamer and GCE-AuNPs \emptyset CoPc(2)-Aptamer, respectively. All experiments were run in triplicate and the recorded values are an average of the values recorded for each run. The percentage recoveries were higher and more reliable for the aptasensor in which the AuNPs and CoPc(2) are coupled. This shows that the results obtained from detecting PSA in buffer are feasible. Moreover, these results obtained from EIS also indicate some protein-protein interactions which results in a decrease in sensitivity hence the reduced R_{ct} values obtained in serum analyses compared to those done in PBS.

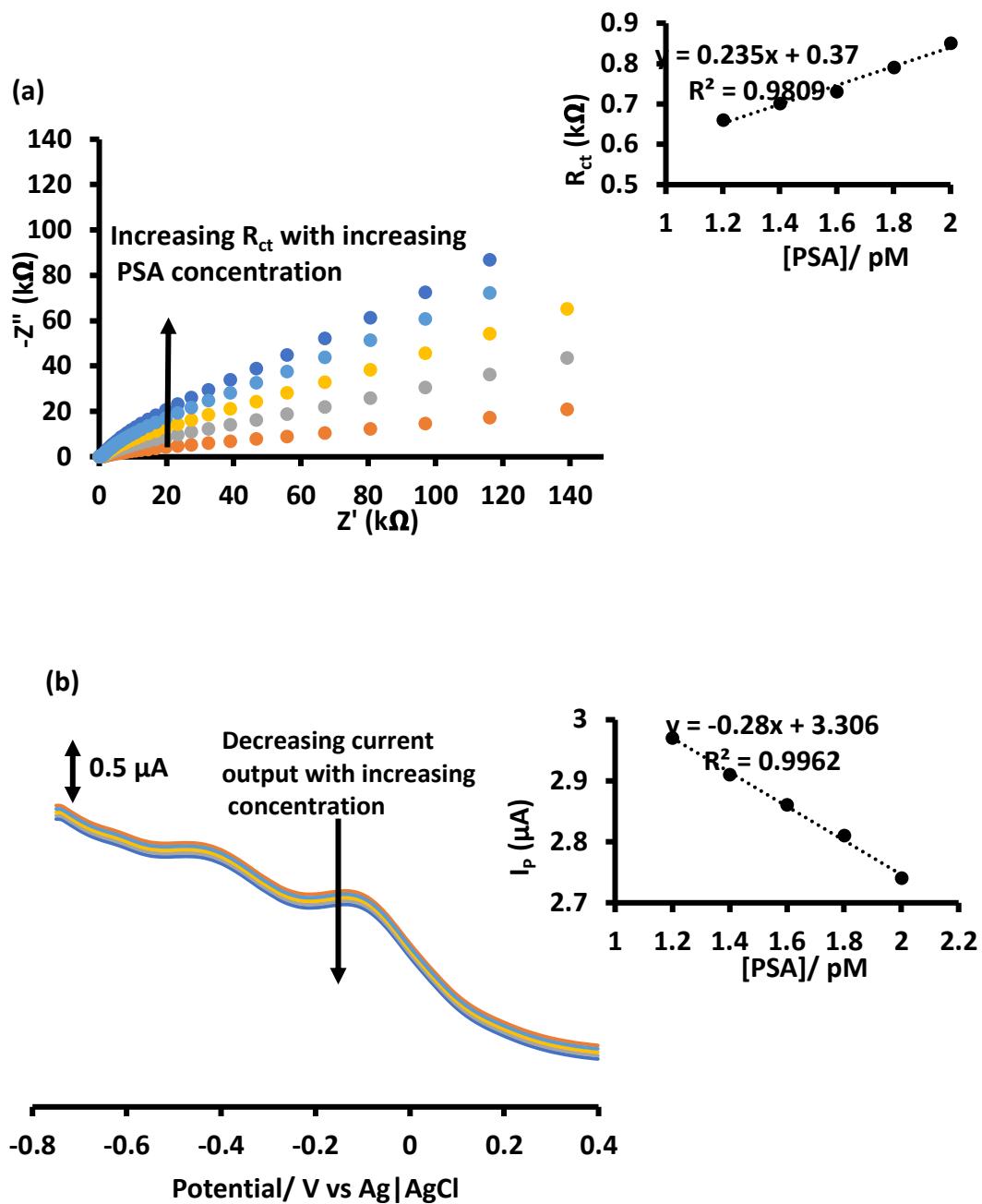


Figure 6.5: (a) EIS Nyquist plots and (b) differential pulse voltammograms (DPV) of GCE/CoPc(2)-Aptamer in a 30 mM PBS solution of pH 7.4 containing PSA concentrations ranging from 1.2-2.0 pM. **Inserts:** Linear responses of resistance to changing concentrations.

Table 6.6: Summary of recovery measurements of PSA in spiked human serum samples for the GCE-AuNPs-Aptamer aptasensor. % RSD (relative standard deviation) = standard deviation/mean × 100; n = 3.

[PSA] added/ pM In buffer	R_{ct} (kΩ) In buffer	[PSA] found/ pM In serum	R_{ct} (kΩ) In serum	% RSD	% Recovery
1.2	0.586	0.26	0.127	2.79	21.7
1.4	0.602	0.30	0.131	1.53	21.8
1.6	0.776	0.31	0.145	3.62	18.7
1.8	0.877	0.31	0.153	1.43	17.4
2.0	1.25	0.25	0.155	2.67	12.4

Table 6.7: Summary of recovery measurements of PSA in spiked human serum samples for the GCE/CoPc(2)-Aptamer aptasensor. % RSD (relative standard deviation) = standard deviation/mean × 100; n = 3.

[PSA] added/ pM In buffer	R_{ct} (kΩ) In buffer	[PSA] found/ pM In serum	R_{ct} (kΩ) In serum	% RSD	% Recovery
1.2	0.854	0.82	0.587	2.73	68.7
1.4	0.861	0.95	0.600	1.63	67.7
1.6	0.868	1.12	0.617	2.36	71.1
1.8	0.877	1.31	0.637	3.35	72.6
2.0	0.892	1.45	0.647	2.35	72.5

Table 6.8: Summary of recovery measurements of PSA In spiked human serum samples for the GCE-AuNPs@CoPc(2)-Aptamer aptasensor. % RSD. (relative standard deviation) = standard deviation/mean × 100; n = 3.

[PSA] added/ pM	R_{ct} (kΩ) In buffer	[PSA] found/ pM In serum	R_{ct} (kΩ) In serum	% RSD	% Recovery
1.2	24.9	1.18	24.6	5.46	98.7
1.4	27.2	1.39	27.0	6.80	99.3
1.6	29.4	1.57	28.9	6.68	98.3
1.8	31.7	1.73	30.5	2.94	96.2
2.0	33.5	1.98	33.2	1.62	99.1

6.4 Conclusions

The aptasensors fabricated in this work showed good performance in spiked serum samples with low detection limits. Moreover, they showed good recoveries and the results verified their feasibility to be used in clinical studies. Comparing the performances of these fabricated aptasensors, the GCE-NGQDs-CoPc(1)($\pi\pi$)-Aptamer showed the lowest detection limits in serum and buffer where the QDs were concerned using where EIS was used. The GCE-AuNPs \emptyset CoPc(2)-Aptamer fabricated sensor showed improved performance when AuNPs and CoPc(2) were combined and the best performance when compared to all the sensors fabricated in this work. This proves the combination of MPc with other nanostructures is ideal for the fabrication and development of stable, efficient, low cost aptasensor.

7. Summary, conclusions, and prospects

This chapter summarizes all the work discussed in this thesis and highlights again the novelty of the work and the new perspective it has brought to the fabrication and the development of PCa early diagnostic tools.

7.1 Overview of the thesis.

This thesis reported for the first time, the combination of graphene-based quantum dots, AuNPs, MPCs and an aptamer for the fabrication of electrochemical aptasensors, towards the detection of PSA. The nanostructures were synthesized and fully characterized prior to being used as electrode modifiers. Capillary electrophoresis coupled to mass spectrometry was used for the first time in this work so as to help elucidating these nano-structures, as the synthesis theoretical allows for various sizes and functionalization rates, and the structuration can lead to multi-layers. Then the synergistic effects of the quantum dots, AuNPs and CoPcs were proven using electrochemical methods. Glassy carbon electrodes or plates were modified and characterized at each modification step. Where covalent linkage was employed, XPS analyses verified the success of the formation of new bonds. Using adsorption and click chemistry as surface modification techniques yielded stable electrochemical sensors. The aptasensors were used to detect PSA in buffer solution and proved to be efficient, selective, and specific and showed low detection limits which were compared to reported literature values. The best performing aptasensors that were fabricated herein were then used to detect PSA in spiked serum samples to verify their feasibility and potential use in clinical studies. The results agreed with those obtained in buffer analyses and some performed slightly better in serum analyses. In addition, the sensors were stable, reproducible, and proved to be reusable for several experiments before having to refabricate them. It is important to note that the combination of MPCs with other nanomaterials contributed greatly to the enhancement of the signal output of the fabricated aptasensors, thus obtaining low detection limits. Moreover, the characteristics of

these nanostructures, also contributed to the increased sensitivity, stability, and reproducibility of the sensors.

7.2 Future prospects and final remarks.

If more work and optimization is invested in advancing this study, where MPCs are conjugated to graphene-based quantum dots and AuNPs for the development of aptasensors, this work has the potential to contribute greatly to the accessibility of medical care, especially early cancer diagnostics of various diseases. The materials used have a high shelf life, are stable and cost less than current systems in place; therefore, further exploration in this area of study would be greatly beneficial.

References

- [1] C.G. Claessens, U.W.E. Hahn, T. Torres, Phthalocyanines: From outstanding electronic properties to emerging applications, *Chem. Rec.* 8 (2008) 75-97.
- [2] D. Klyamer, A. Sukhikh, S. Gromilov, P. Krasnov, T. Basova, Fluorinated metal phthalocyanines: interplay between fluorination degree, films orientation, and ammonia sensing properties, *Sensors* 18 (2018) 2141-2154.
- [3] Y. Wang, X. Zheng, X. Liu, Y. Feng, H. Shan, L. Dong, G. Fang, Z.-X. Xu, A study of different central metals in octamethyl-substituted phthalocyanines as dopant-free hole-transport layers for planar perovskite solar cells, *Org. Electron.* 56 (2018) 276-283.
- [4] V.N. Nemykin, E.A. Lukyanets, Synthesis of substituted phthalocyanines, *Arkivoc.* (2010) 136-208.
- [5] G. Dilber, H. Altunparmak, A. Nas, H. Kantekin, M. Durmuş, The peripheral and non-peripheral 2H-benzotriazole substituted phthalocyanines: Synthesis, characterization, photophysical and photochemical studies of zinc derivatives, *Spectrochim. Acta Part A Mol. Biomol. Spectrosc.* 217 (2019) 128-140.
- [6] E.N. Kaya, S. Tuncel, T. V Basova, H. Banimuslem, A. Hassan, A.G. Gürek, V. Ahsen, M. Durmuş, Effect of pyrene substitution on the formation and sensor properties of phthalocyanine-single walled carbon nanotube hybrids, *Sens. Actuators B Chem.* 199 (2014) 277-283.
- [7] B.N. Şen, H. Mert, H. Dinçer, A. Koca, Synthesis and characterization of terminalalkynyl-substituted unsymmetrical zinc phthalocyanine conjugated with well-defined polymers, *Dye. Pigment.* 100 (2014) 1-10.

- [8] G. de la Torre, C.G. Claessens, T. Torres, Phthalocyanines: The need for selective synthetic approaches, *European J. Org. Chem.* 2000 (2000) 2821-2830.
- [9] J. Rak, P. Pouckova, J. Benes, D. Vetvicka, Drug delivery systems for phthalocyanines for photodynamic therapy, *Anticancer Res.* 39 (2019) 3323-3339.
- [10] Y. Baygu, Y. Gök, A highly water-soluble zinc (II) phthalocyanines as potential for PDT studies: Synthesis and characterization, *Inorg. Chem. Commun.* 96 (2018) 133-138.
- [11] F. Yurt, M. Ince, S.G. Colak, K. Ocakoglu, O. Er, H.M. Soylu, C. Gunduz, C.B. Avci, C.C. Kurt, Investigation of in vitro PDT activities of zinc phthalocyanine immobilised TiO₂ nanoparticles, *Int. J. Pharm.* 524 (2017) 467-474.
- [12] A.Y. Tolbin, M.S. Savelyev, A.Y. Gerasimenko, L.G. Tomilova, N.S. Zefirov, Thermally stable J-type phthalocyanine dimers as new non-linear absorbers for low-threshold optical limiters, *Phys. Chem. Chem. Phys.* 18 (2016) 15964-15971.
- [13] O.M. Bankole, J. Britton, T. Nyokong, Photophysical and non-linear optical behavior of novel tetra alkynyl terminated indium phthalocyanines: Effects of the carbon chain length, *Polyhedron* 88 (2015) 73-80.
- [14] A.C.S. Lobo, A.D. Silva, V.A. Tomé, S.M.A. Pinto, E.F.F. Silva, M.J.F. Calvete, C.M.F. Gomes, M.M. Pereira, L.G. Arnaut, Phthalocyanine labels for near-infrared fluorescence imaging of solid tumors, *J. Med. Chem.* 59 (2016) 4688-4696.

- [15] F. Lv, X. He, L. Wu, T. Liu, Lactose substituted zinc phthalocyanine: A near infrared fluorescence imaging probe for liver cancer targeting, *Bioorg. Med. Chem. Lett.* 23 (2013) 1878-1882.
- [16] G. Avşar, F.A. Sari, A.C. Yuzer, H.M. Soylu, O. Er, M. Ince, F.Y. Lambrecht, Intracellular uptake and fluorescence imaging potential in tumor cell of zinc phthalocyanine, *Int. J. Pharm.* 505 (2016) 369-375.
- [17] W. Vallejo, C. Diaz-Urbe, A. Cantillo, Methylene blue photocatalytic degradation under visible irradiation on TiO₂ thin films sensitized with Cu and Zn tetracarboxy-phthalocyanines, *J. Photochem. Photobiol. A Chem.* 299 (2015) 80-86.
- [18] Q. Liang, M. Zhang, C. Liu, S. Xu, Z. Li, Sulfur-doped graphitic carbon nitride decorated with zinc phthalocyanines towards highly stable and efficient photocatalysis, *Appl. Catal. A Gen.* 519 (2016) 107-115.
- [19] W.-L. He, C.-D. Wu, Incorporation of Fe-phthalocyanines into a porous organic framework for highly efficient photocatalytic oxidation of arylalkanes, *Appl. Catal. B Environ.* 234 (2018) 290-295.
- [20] Z. Jiang, Y. Wang, X. Zhang, H. Zheng, X. Wang, Y. Liang, Revealing the hidden performance of metal phthalocyanines for CO₂ reduction electrocatalysis by hybridization with carbon nanotubes, *Nano Res.* 12 (2019) 2330-2334.
- [21] T.T. Tasso, T. Furuyama, N. Kobayashi, Absorption and electrochemical properties of cobalt and iron phthalocyanines and their quaternized derivatives:

- aggregation equilibrium and oxygen reduction electrocatalysis, *Inorg. Chem.* 52 (2013) 9206–9215.
- [22] A. Pizarro, G. Abarca, C. Gutiérrez-Cerón, D. Cortés-Arriagada, F. Bernardi, C. Berrios, J.F. Silva, M.C. Rezende, J.H. Zagal, R. Oñate, Building pyridinium molecular wires as axial ligands for tuning the electrocatalytic activity of iron phthalocyanines for the oxygen reduction reaction, *ACS Catal.* 8 (2018) 8406–8419.
- [23] D.-D. Ma, S.-G. Han, C. Cao, X. Li, X.-T. Wu, Q.-L. Zhu, Remarkable electrocatalytic CO₂ reduction with ultrahigh CO/H₂ ratio over single-molecularly immobilized pyrrolidinonyl nickel phthalocyanine, *Appl. Catal. B Environ.* 264 (2020) 118530.
- [24] K.I. Ozoemena, T. Nyokong, Comparative electrochemistry and electrocatalytic activities of cobalt, iron and manganese phthalocyanine complexes axially coordinated to mercaptopyridine self-assembled monolayer at gold electrodes, *Electrochim. Acta* 51 (2006) 2669–2677.
- [25] J.H. Zagal, M.A. Gulppi, G. Cárdenas-Jirón, Metal-centered redox chemistry of substituted cobalt phthalocyanines adsorbed on graphite and correlations with MO calculations and Hammett parameters. Electrocatalytic reduction of a disulfide, *Polyhedron* 19 (2000) 2255–2260.
- [26] L.S. Mpeti, P. Sen, T. Nyokong, The effects of asymmetry in combination with reduced graphene oxide nanosheets on hydrazine electrocatalytic detection on cobalt phthalocyanines, *Electroanalysis* 32 (2020) 2723–2732.

- [27] E. Güzel, M.N. Yarasir, A.R. Özkaya, Low symmetry solitaire- and trans-functional porphyrazine/phthalocyanine hybrid complexes: Synthesis, isolation, characterization, and electrochemical and in-situ spectroelectrochemical properties, *Synth. Met.* 262 (2020) 116331.
- [28] C. Zúñiga, F. Tasca, S. Calderon, D. Farías, F.J. Recio, J.H. Zagal, Reactivity indexes for the electrocatalytic oxidation of hydrogen peroxide promoted by several ligand-substituted and unsubstituted Co phthalocyanines adsorbed on graphite, *J. Electroanal. Chem.* 765 (2016) 22-29.
- [29] E.T. Acar, T.A. Tabakoglu, D. Atilla, F. Yuksel, G. Atun, Synthesis, electrochemistry and electrocatalytic activity of cobalt phthalocyanine complexes - Effects of substituents for oxygen reduction reaction, *Polyhedron* 152 (2018) 114-124.
- [30] R. Nkhahle, T. Nyokong, Creating the ideal push-pull system for electrocatalysis: A comparative study on symmetrical and asymmetrical cardanol-based cobalt phthalocyanines, *Electroanalysis* 33 (2021) 11-22.
- [31] J. Mack, N. Kobayashi, Low symmetry phthalocyanines and their analogues, *Chem. Rev.* 111 (2011) 281-321.
- [32] S.S. Erdem, I. V Nesterova, S.A. Soper, R.P. Hammer, Solid-phase synthesis of asymmetrically substituted "AB₃-Type" phthalocyanines, *J. Org. Chem.* 73 (2008) 5003-5007.

- [33] D.R. Cooper, B. D'Anjou, N. Ghattamaneni, B. Harack, M. Hilke, A. Horth, N. Majlis, M. Massicotte, L. Vandsburger, E. Whiteway, Experimental review of graphene, *Int. Sch. Res. Not.* 2012 (2012) 1-56.
- [34] H. Nakano, H. Tetsuka, M.J.S. Spencer, T. Morishita, Chemical modification of group IV graphene analogues, *Sci. Technol. Adv. Mater.* 19 (2018) 76-100.
- [35] M.H. Kang, L.O. Prieto López, B. Chen, K. Teo, J.A. Williams, W.I. Milne, M.T. Cole, Mechanical robustness of graphene on flexible transparent substrates, *ACS Appl. Mater. Interf.* 8 (2016) 22506-22515.
- [36] S. Saxena, T.A. Tyson, S. Shukla, E. Negusse, H. Chen, J. Bai, Investigation of structural and electronic properties of graphene oxide, *Appl. Phys. Lett.* 99 (2011) 13104.
- [37] Y. Chong, Y. Ma, H. Shen, X. Tu, X. Zhou, J. Xu, J. Dai, S. Fan, Z. Zhang, The in vitro and in vivo toxicity of graphene quantum dots, *Biomater.* 35 (2014) 5041-5048.
- [38] M. Bacon, S.J. Bradley, T. Nann, Graphene quantum dots, *Part. Part. Syst. Charact.* 31 (2014) 415-428.
- [39] Y. Zhan, Z. Liu, Q. Liu, D. Huang, Y. Wei, Y. Hu, X. Lian, C. Hu, A facile and one-pot synthesis of fluorescent graphitic carbon nitride quantum dots for bio-imaging applications, *New J. Chem.* 41 (2017) 3930-3938.
- [40] A. Kalluri, D. Debnath, B. Dharmadhikari, P. Patra, Graphene quantum dots: Synthesis and applications, *Methods Enzymol.* 609 (2018) 335-354.

- [41] S. Gu, C.-T. Hsieh, Y.-M. Chiang, D.-Y. Tzou, Y.-F. Chen, Y.A. Gandomi, Optimization of graphene quantum dots by chemical exfoliation from graphite powders and carbon nanotubes, *Mater. Chem. Phys.* 215 (2018) 104-111.
- [42] H. Sun, H. Ji, E. Ju, Y. Guan, J. Ren, X. Qu, Synthesis of fluorinated and nonfluorinated graphene quantum dots through a new top-down strategy for long-time cellular imaging, *Chem. Eur. J.* 21 (2015) 3791-3797.
- [43] R. Tian, S. Zhong, J. Wu, W. Jiang, Y. Shen, T. Wang, Solvothermal method to prepare graphene quantum dots by hydrogen peroxide, *Opt. Mater.* 60 (2016) 204-208.
- [44] G. Wang, Q. Guo, D. Chen, Z. Liu, X. Zheng, A. Xu, S. Yang, G. Ding, Facile and highly effective synthesis of controllable lattice sulfur-doped graphene quantum dots via hydrothermal treatment of durian, *ACS Appl. Mater. Interf.* 10 (2018) 5750-5759.
- [45] C. Zhang, Y. Cui, L. Song, X. Liu, Z. Hu, Microwave assisted one-pot synthesis of graphene quantum dots as highly sensitive fluorescent probes for detection of iron ions and pH value, *Talanta* 150 (2016) 54-60.
- [46] P. Atienzar, A. Primo, C. Lavorato, R. Molinari, H. García, Preparation of graphene quantum dots from pyrolyzed alginate, *Langmuir* 29 (2013) 6141-6146.
- [47] K. Habiba, V. Makarov, B. Weiner, G. Morell, Fabrication of Nanomaterials by Pulsed Laser Synthesis. In: A. Waqar, N. Ali (editors). *Manufacturing Nanostructures*. Altrincham: One Central Press (OCN); 2014. 263-292.

- [48] B.P. Kafle, Chapter 6 - Introduction to nanomaterials and application of UV-Visible spectroscopy for their characterization, in: B.P. Kafle (editors), *Chemical analysis and material characterization by spectrophotometry*, Amsterdam. Elsevier, 2020: pp. 147-198.
- [49] H.-H. Cho, H. Yang, D.J. Kang, B.J. Kim, Surface engineering of graphene quantum dots and their applications as efficient surfactants, *ACS Appl. Mater. Interf.* 7 (2015) 8615-8621.
- [50] S. Wang, Z.-G. Chen, I. Cole, Q. Li, Structural evolution of graphene quantum dots during thermal decomposition of citric acid and the corresponding photoluminescence, *Carbon* 82 (2015) 304-313.
- [51] R. Adel, S. Ebrahim, A. Shokry, M. Soliman, M. Khalil, Nanocomposite of CuInS/ZnS and nitrogen-doped graphene quantum dots for cholesterol sensing, *ACS Omega* 6 (2021) 2167-2175.
- [52] M. Mokaddem, P. Gareil, J. Belgaied, A. Varenne, A new insight into suction and dilution effects in capillary electrophoresis coupled to mass spectrometry via an electrospray ionization interface. Part I-Suction effect, *Electrophoresis* 29 (2008) 1957-1964.
- [53] J.S. Toraño, R. Ramautar, G. de Jong, Advances in capillary electrophoresis for the life sciences, *J. Chromatogr. B.* 1118 (2019) 116-136.
- [54] L. Trapiella-Alfonso, F. d'Orlyé, A. Varenne, Recent advances in the development of capillary electrophoresis methodologies for optimizing, controlling, and characterizing the synthesis, functionalization, and

- physicochemical, properties of nanoparticles, *Anal. Bioanal. Chem.* 408 (2016) 2669-2675.
- [55] S. Fermas, F. Gonnet, A. Varenne, P. Gareil, R. Daniel, Frontal analysis capillary electrophoresis hyphenated to electrospray ionization mass spectrometry for the characterization of the antithrombin/heparin pentasaccharide complex, *Anal. Chem.* 79 (2007) 4987-4993.
- [56] N.B. Cech, C.G. Enke, Practical implications of some recent studies in electrospray ionization fundamentals, *Mass Spectrom. Rev.* 20 (2001) 362-387.
- [57] G. Bonvin, J. Schappler, S. Rudaz, Capillary electrophoresis-electrospray ionization-mass spectrometry interfaces: Fundamental concepts and technical developments, *J. Chromatogr. A.* 1267 (2012) 17-31.
- [58] Z. Qian, J. Ma, X. Shan, L. Shao, J. Zhou, J. Chen, H. Feng, Surface functionalization of graphene quantum dots with small organic molecules from photoluminescence modulation to bioimaging applications: an experimental and theoretical investigation, *RSC Adv.* 3 (2013) 14571-14579.
- [59] J.-P. Zou, L.-C. Wang, J. Luo, Y.-C. Nie, Q.-J. Xing, X.-B. Luo, H.-M. Du, S.-L. Luo, S.L. Suib, Synthesis and efficient visible light photocatalytic H₂ evolution of a metal-free g-C₃N₄/graphene quantum dots hybrid photocatalyst, *Appl. Catal. B Environ.* 193 (2016) 103-109.
- [60] D.A. Nguyen, H.M. Oh, N.T. Duong, S. Bang, S.J. Yoon, M.S. Jeong, Highly enhanced photoresponsivity of a monolayer WSe₂ photodetector with nitrogen-doped graphene quantum dots, *ACS Appl. Mater. Interf.* 10 (2018) 10322-10329.

- [61] J. Lu, M. Yan, L. Ge, S. Ge, S. Wang, J. Yan, J. Yu, Electrochemiluminescence of blue-luminescent graphene quantum dots and its application in ultrasensitive aptasensor for adenosine triphosphate detection, *Biosens. Bioelectron.* 47 (2013) 271-277.
- [62] E. Sharma, D. Vashisht, A. Vashisht, V.K. Vats, S.K. Mehta, K. Singh, Facile synthesis of sulfur and nitrogen co-doped graphene quantum dots for optical sensing of Hg and Ag ions, *Chem. Phys. Lett.* 730 (2019) 436-444.
- [63] Y. Zhou, S. Yang, X. Yin, J. Han, M. Tai, X. Zhao, H. Chen, Y. Gu, N. Wang, H. Lin, Enhancing electron transport via graphene quantum dot/SnO₂ composites for efficient and durable flexible perovskite photovoltaics, *J. Mater. Chem. A.* 7 (2019) 1878-1888.
- [64] S. Campuzano, P. Yáñez-Sedeño, J.M. Pingarrón, Carbon dots and graphene quantum dots in electrochemical biosensing, *Nanomater.* 9 (2019) 634-651.
- [65] H. Zhao, Y. Chang, M. Liu, S. Gao, H. Yu, X. Quan, A universal immunosensing strategy based on regulation of the interaction between graphene and graphene quantum dots, *Chem. Commun.* 49 (2013) 234-236.
- [66] S. Chaiyo, E. Mehmeti, W. Siangproh, T.L. Hoang, H.P. Nguyen, O. Chailapakul, K. Kalcher, Non-enzymatic electrochemical detection of glucose with a disposable paper-based sensor using a cobalt phthalocyanine-ionic liquid-graphene composite, *Biosens. Bioelectron.* 102 (2018) 113-120.
- [67] X. Chen, T. Wang, B. Li, M. Zeng, J. Yang, N. Hu, Y. Su, Z. Zhou, Z. Yang, Enhancing room-temperature NO₂ gas sensing performance based on a metal

- phthalocyanine/graphene quantum dot hybrid material, *RSC Adv.* 11 (2021) 5618-5628.
- [68] O.J. Achadu, T. Nyokong, Application of graphene quantum dots decorated with TEMPO-derivatized zinc phthalocyanine as novel nanoprobe: probing the sensitive detection of ascorbic acid, *New J. Chem.* 40 (2016) 8727-8736.
- [69] O.J. Achadu, T. Nyokong, Fluorescence "turn-ON" nanosensor for cyanide ion using supramolecular hybrid of graphene quantum dots and cobalt pyrene-derivatized phthalocyanine, *Dye. Pigment.* 160 (2019) 328-335.
- [70] O.J. Achadu, T. Nyokong, Graphene quantum dots decorated with maleimide and zinc tetramaleimido-phthalocyanine: Application in the design of "OFF-ON" fluorescence sensors for biothiols, *Talanta* 166 (2017) 15-26.
- [71] S. Guo, E. Wang, Synthesis and electrochemical applications of gold nanoparticles, *Anal. Chim. Acta* 598 (2007) 181-192.
- [72] Y. Hu, Y. Song, Y. Wang, J. Di, Electrochemical synthesis of gold nanoparticles onto indium tin oxide glass and application in biosensors, *Thin Solid Films* 519 (2011) 6605-6609.
- [73] C. Zou, B. Yang, D. Bin, J. Wang, S. Li, P. Yang, C. Wang, Y. Shiraishi, Y. Du, Electrochemical synthesis of gold nanoparticles decorated flower-like graphene for high sensitivity detection of nitrite, *J. Colloid Interface Sci.* 488 (2017) 135-141.

- [74] S. Singh, D.V.S. Jain, M.L. Singla, One step electrochemical synthesis of gold-nanoparticles-polypyrrole composite for application in catechin electrochemical biosensor, *Anal. Methods* 5 (2013) 1024-1032.
- [75] H. Ma, B. Yin, S. Wang, Y. Jiao, W. Pan, S. Huang, S. Chen, F. Meng, Synthesis of silver and gold nanoparticles by a novel electrochemical method, *Chem. Phys. Chem.* 5 (2004) 68-75.
- [76] E.C. Dreaden, A.M. Alkilany, X. Huang, C.J. Murphy, M.A. El-Sayed, The golden age: gold nanoparticles for biomedicine, *Chem. Soc. Rev.* 41 (2012) 2740-2779.
- [77] K. Saha, S.S. Agasti, C. Kim, X. Li, V.M. Rotello, Gold nanoparticles in chemical and biological sensing, *Chem. Rev.* 112 (2012) 2739-2779.
- [78] A.S. Matias, F.F. Carlos, P. Pedrosa, A.R. Fernandes, P. V Baptista., Gold nanoparticles in molecular diagnostics and molecular therapeutics, In: Rai, Ph.D M., Shegokar, Ph.D R. (editors) *Metal Nanoparticles in Pharma*, Springer Heidelberg. (2017) 365-387.
- [79] T.T-T. Ho, C.-H. Dang, T.K-C.Huynh, T.K-D.Hoang, T-D. Nguyen, In situ synthesis of gold nanoparticles on novel nanocomposite lactose/alginate: Recyclable catalysis and colorimetric detection of Fe (III), *Carbohydr. Polym.* 251 (2021) 116998.
- [80] G. Han, P. Ghosh, V.M. Rotello, Functionalized gold nanoparticles for drug delivery, *Nanomed.* 2 (2007) 113-123.

- [81] A. Ananthi, K.L. Phani, Self-assembly of gold nanoparticles on sulphide functionalized polydopamine in application to electrocatalytic oxidation of nitric oxide, *J. Electroanal. Chem.* 764 (2016) 7-14.
- [82] D.J. Siegwart, A. Srinivasan, S.A. Bencherif, A. Karunanidhi, J.K. Oh, S. Vaidya, R. Jin, J.O. Hollinger, K. Matyjaszewski, Cellular uptake of functional nanogels prepared by inverse mini-emulsion ATRP with encapsulated proteins, carbohydrates, and gold nanoparticles, *Biomacromolecules* 10 (2009) 2300-2309.
- [83] X. Chen, X. Zhao, G. Wang, Review on marine carbohydrate-based gold nanoparticles represented by alginate and chitosan for biomedical application, *Carbohydr. Polym.*(2020) 116311.
- [84] D. Shahdeo, V. Kesarwani, D. Suhag, J. Ahmed, S.M. Alshehri, S. Gandhi, Self-assembled chitosan polymer intercalating peptide functionalized gold nanoparticles as nanoprobe for efficient imaging of urokinase plasminogen activator receptor in cancer diagnostics, *Carbohydr. Polym.*(2021) 118138.
- [85] A.A. Saeed, B. Singh, M.N. Abbas, Y.M. Issa, E. Dempsey, Electrocatalytic nitrite determination using iron phthalocyanine modified gold nanoparticles. *Electroanalysis* 27 (2015) 1086-1096.
- [86] V.P. Chauke, E. Antunes, T. Nyokong, Comparative behavior of conjugates of tantalum phthalocyanines with gold nanoparticles or single walled carbon nanotubes towards bisphenol A electrocatalysis, *J. Electroanal. Chem.* 661 (2011) 1-7.

- [87] A.J. Jeevagan, S.A. John, Synthesis of non-peripheral amine substituted nickel(ii) phthalocyanine capped gold nanoparticles and their immobilization on electrode for the electrocatalytic oxidation of hydrazine, *RSC Adv.* 3 (2013) 2256-2264.
- [88] Q. Xu, H. Yuan, X. Dong, Y. Zhang, M. Asif, Z. Dong, W. He, J. Ren, Y. Sun, F. Xiao, Dual nanoenzyme modified microelectrode based on carbon fiber coated with AuPd alloy nanoparticles decorated graphene quantum dots assembly for electrochemical detection in clinic cancer samples, *Biosens. Bioelectron.* 107 (2018) 153-162.
- [89] M. Lakshmanakumar, N. Nesakumar, S. SethuRaman, K.S. Rajan, U.M. Krishnan, J.B.B. Rayappan, Functionalized graphene quantum dot interfaced electrochemical detection of cardiac Troponin I: An antibody free approach, *Sci. Rep.* 9 (2019) 17348.
- [90] B.D. Mansuriya, Z. Altintas, Enzyme-Free Electrochemical nano-immunosensor based on graphene quantum dots and gold nanoparticles for cardiac biomarker determination, *Nanomaterials* 11 (2021) 578-595.
- [91] Z. Shekari, H.R. Zare, A. Falahati, Electrochemical sandwich aptasensor for the carcinoembryonic antigen using graphene quantum dots, gold nanoparticles and nitrogen doped graphene modified electrode and exploiting the peroxidase-mimicking activity of a G-quadruplex DNAzyme, *Microchim. Acta* 186 (2019) 530.
- [92] Z. Fredj, M. Ben Ali, M.N. Abbas, E. Dempsey, Determination of prostate cancer biomarker acid phosphatase at a copper phthalocyanine-modified screen printed gold transducer, *Anal. Chim. Acta* 1057 (2019) 98-105.

- [93] F. Duan, C. Guo, M. Hu, Y. Song, M. Wang, L. He, Z. Zhang, R. Pettinari, L. Zhou, Construction of the 0D/2D heterojunction of Ti₃C₂T_x MXene nanosheets and iron phthalocyanine quantum dots for the impedimetric aptasensing of microRNA-155, *Sensors Actuators B Chem.* 310 (2020) 127844.
- [94] E.B. Aydın, M. Aydın, A. Yuzer, M. Ince, K. Ocakoğlu, M.K. Sezgintürk, Detection of kallikrein-related peptidase 4 with a label-free electrochemical impedance biosensor based on a Zinc(II) phthalocyanine tetracarboxylic acid-functionalized disposable Indium Tin Oxide electrode, *ACS Biomater. Sci. Eng.* 7 (2021) 1192-1201.
- [95] H. Xu, C. Liao, Y. Liu, B.-C. Ye, B. Liu, Iron phthalocyanine decorated nitrogen-doped graphene biosensing platform for real-time detection of nitric oxide released from living cells, *Anal. Chem.* 90 (2018) 4438-4444.
- [96] F. Duan, M. Hu, C. Guo, Y. Song, M. Wang, L. He, Z. Zhang, R. Pettinari, L. Zhou, Chromium-based metal-organic framework embedded with cobalt phthalocyanine for the sensitively impedimetric cytosensing of colorectal cancer (CT26) cells and cell imaging, *Chem. Eng. J.* 398 (2020) 125452.
- [97] J. Kang, Z. Li, G. Wang, A novel signal amplification strategy electrochemical immunosensor for ultra-sensitive determination of p53 protein, *Bioelectrochem.* 137 (2021) 107647.
- [98] M. Hu, K. Zhang. The application of aptamers in cancer research: an up-to-date review. *Future Oncol.* 9 (2013) 369-376.

- [99] J. Zhou, J. Rossi, Aptamers as targeted therapeutics: current potential and challenges. *Nat. Rev Drug Discov.* 16 (2017) 181-202.
- [100] A.D. Keefe, S.T. Cload. SELEX with modified nucleotides. *Current Opinion in Chem. Bio.* 12 (2008) 448-456.
- [101] R. Stoltenburg, C. Reinemann, B. Strehlitz. SELEX—A (r)evolutionary method to generate high-affinity nucleic acid ligands. *Biomol. Eng.* 24 (2007) 381-403.
- [102] K-N.Kang, Y-S. Lee. RNA aptamers: A review of recent trends and applications. *Future Trends in Biotech.* 131 (2012) 153-169.
- [103] K-T. Guo, A. Paul, C. Schichor, G. Ziemer, H.P. Wendel. CELL-SELEX: Novel perspectives of aptamer-based therapeutics. *Int. J. Mol. Sci.* 9 (2008) 668-678.
- [104] J.K. Herr, J.E. Smith, C.D. Medley, D. Shangguan, W. Tan. Aptamer-conjugated nanoparticles for selective collection and detection of cancer cells. *Anal. Chem.* 78 (2006) 2918-2924.
- [105] Y-F.Huang, K. Sefah, S. Bamrungsap, H-T. Chang, W. Tan. Selective photothermal therapy for mixed cancer cells using aptamer-conjugated nanorods. *Langmuir* 24 (2008) 11860-11865.
- [106] X. Chen, M.-C.Estévez, Z. Zhu, Y-F. Huang, Y. Chen, L. Wang, W. Tan. Using aptamer-conjugated fluorescence resonance energy transfer nanoparticles for multiplexed cancer cell monitoring. *Anal. Chem.* 81 (2009) 7009-7014.

- [107] R. Savla, O. Taratula, O. Garbuzenko, T. Minko. Tumor targeted quantum dot-mucin 1 aptamer-doxorubicin conjugate for imaging and treatment of cancer. *J. Controlled Release* 153 (2011) 16-22.
- [108] J.A. Hanson, J. Wang, A-N. Kawde, Y. Xiang, K.V. Gothelf, G. Collins. Quantum-dot/aptamer-based ultrasensitive multi-analyte electrochemical biosensor. *J. Am. Chem. Soc.* 128 (2006) 2228-2229.
- [109] F-B.Wang, Y. Rong, M. Fang, J-P.Yuan, C-W.Peng, S-P. Liu, Y. Li. Recognition and capture of metastatic hepatocellular carcinoma cells using aptamer-conjugated quantum dots and magnetic particles. *Biomater.* 34 (2013) 3816-3827.
- [110] Y. Cao, H. Dong, Z. Yang, X. Zhong, Y. Chen, W. Dai, X. Zhang. Aptamer-conjugated graphene quantum dots/porphyrin derivative theranostic agent for intracellular cancer-related microRNA detection and fluorescence-guided photothermal/photodynamic synergetic therapy. *Appl. Mater. Interf.* 9 (2017) 159-166.
- [111] Z. S. Qian, X.Y. Shan, L.J. Chai, J.R. Chen, H. Feng. A fluorescent nanosensor based on graphene quantum dots-aptamer Probe and graphene oxide platform for detection of lead(II)ion. *Biosens.Bioelectron.* 68 (2015) 225-231.
- [112] Y. Liu, K. Yan, J. Zhang. Graphitic carbon nitride sensitized with CdS quantum dots for visible-light-driven photoelectrochemical aptasensing of tetracycline. *Appl. Mater. Interf.* 8 (2016) 28255-28264.
- [113] C-Y. Zhang, La.W. Johnson. Single quantum-dot-based aptameric nanosensor for cocaine. *Anal. Chem.* 81 (2009) 3051-3055.

- [114] V. Bagalkot, L. Zhang, E. Levy-Nissenbaum, S. Jon, P.W. Kantoff, R. Langer, O.C. Farokhzad. Quantum dot–aptamer conjugates for synchronous cancer imaging, therapy, and sensing of drug delivery based on bi-fluorescence resonance energy transfer. *Nano Lett.* 7 (2007) 3065-3070.
- [115] Y. Shibui, R. Sakai, Y. Manabe, T. Masuyama. Comparisons of L-cysteine and D-cysteine toxicity in 4-week repeated dose toxicity studies of rats receiving daily oral administration, *J. Toxicol. Pathol.* 3 (2017) 217-229.
- [116] H. Lilja, D. Ulmert, A.J. Vickers, -Prostate-specific antigen and prostate cancer: prediction, detection and monitoring, *Nat. Rev. Cancer* 8 (2008) 268-278.
- [117] U-H. Stenman, J. Leinonen, W-M. Zhang, P. Finne, Prostate-specific antigen, *Seminars in Cancer Biol.* 9 (1999) 83-93.
- [118] D. Ilic, M. Djulbegovic, J. H. Jung, E. C. Hwang, Q. Zhou, A. Cleves, T. Agoritsas, P. Dahm, Prostate cancer screening with prostate-specific antigen (PSA) test: a systematic review and meta-analysis, *British Med. J.* 362 (2018) k3519-k3531.
- [119] K. Matsumoto, N. Konishi, Y. Hiasa, E. Kimura, Y. Takahashi, K. Shinohara, T. Samori, A highly sensitive enzyme-linked immunoassay for serum free prostate specific antigen (f-PSA), *Clin. Chim. Acta* 281 (1999) 57-69.
- [120] H.H. Lee, M.A. Dineva, Y.L. Chua, A. Ritchie, I. Ushiro-Lumb, C.A. Wisniewski, Simple amplification-based assay: A nucleic acid-based point-of-care platform for HIV-1 testing, *J. Infect. Dis.* 201 (2010) S65-S71.

- [121] T. Yang, P. Hou, L.L. Zheng, L. Zhan, P.F. Gao, Y.F. Li, C.Z. Huang, Surface-engineered quantum dots/electrospun nanofibers as a networked fluorescence aptasensing platform toward biomarkers, *Nanoscale* 9 (2017) 17020–17028.
- [122] R.-M.Kong, X. Zhang, L. Ding, D. Yang, F. Qu, Label-free fluorescence turn-on aptasensor for prostate-specific antigen sensing based on aggregation-induced emission-silica nanospheres, *Anal.Bioanal. Chem.* 409 (2017) 5757–5765.
- [123] Y.-B.Choi, N.-H.Kim, S.-H.Kim, G.-S.Tae, H.-H. Kim, Heterogeneous Electrochemical Immunoassay of Hippuric Acid on the Electrodeposited Organic Films, *Sensors* 14 (2014) 18886–18897.
- [124] S.B. Nimse, M.D. Sonawane, K.-S.Song, T. Kim, Biomarker detection technologies and future directions, *Analyst* 141 (2016) 740–755.
- [125] S. Gutkin, O. Green, G. Raviv, D. Shabat, O. Portnoy, Powerful Chemiluminescence Probe for Rapid Detection of Prostate Specific Antigen Proteolytic Activity: Forensic Identification of Human Semen, *Bioconj. Chem.* 31 (2020) 2488–2493.
- [126] G. Ertürk, H. Özen, M.A. Tümer, B. Mattiasson, A. Denizli, Microcontact imprinting based surface plasmon resonance (SPR) biosensor for real-time and ultrasensitive detection of prostate specific antigen (PSA) from clinical samples, *Sens. Actuators B Chem.* 224 (2016) 823–832.
- [127] P. Singh, SPR Biosensors: Historical perspectives and current challenges, *Sens. Actuators B Chem.* 229 (2016) 110–130.

- [128] Y.Z. Grasso, M.K. Gupta, H.S. Levin, C.D. Zippe, E.A. Klein, Combined nested RT-PCR Assay for prostate-specific antigen and prostate-specific membrane antigen in prostate cancer patients: correlation with pathological stage, *Cancer Res.* 58 (1998) 1456-1459.
- [129] L. Xie, X. Yang, Y. He, R. Yuan, Y. Chai, Polyacrylamide gel-contained Zinc finger peptide as the "lock" and zinc ions as the "key" for construction of ultrasensitive prostate-specific antigen SERS immunosensor, *ACS Appl. Mater. Interf.* 10 (2018) 15200-15206.
- [130] Y.C. Cao, R. Jin, C.A. Mirkin, Nanoparticles with Raman spectroscopic fingerprints for DNA and RNA detection, *Science* 297 (2002) 1536-1540.
- [131] M. Souada, B. Piro, S. Reisberg, G. Anquetin, V. Noël, M.C. Pham, Label-free electrochemical detection of prostate-specific antigen based on nucleic acid aptamer, *Biosens. Bioelectron.* 68 (2015) 49-54.
- [132] J.S. Wysock, Genetic mutations associated with prostate cancer and normal serum PSA and DRE—implications for prostate cancer screening and management: NYU case of the month November 2020, *Rev. Urol.* 22 (2020) 177-181.
- [133] S. Saini, PSA and beyond: alternative prostate cancer biomarkers, *Cell. Oncol.* 39 (2016) 97-106.
- [134] B. Liu, L. Lu, E. Hua, S. Jiang, G. Xie, Detection of the human prostate-specific antigen using an aptasensor with gold nanoparticles encapsulated by graphitized mesoporous carbon, *Microchim. Acta* 178 (2012) 163-170.

- [135] Q. Hu, S. Gan, Y. Bao, Y. Zhang, D. Han, L. Niu. Electrochemically controlled ATRP for cleavage-based electrochemical detection of the prostate-specific antigen at femtomolar level concentrations. *Anal Chem.* 92 (2020) 15982-15988.
- [136] Y.J. Li, M.J. Ma, G. Yin, Y. Kong, J.J. Zhu, Phthalocyanine-sensitized graphene-CdS nanocomposites: an enhanced photoelectrochemical immunosensing platform, *Chemistry* 19 (2013) 4496-505.
- [137] D. Wu, Y. Liu, Y. Wang, L. Hu, H. Ma, G. Wang, Q. Wei, Label-free electrochemiluminescent immunosensor for detection of prostate specific antigen based on aminated graphene quantum dots and carboxyl graphene quantum dots, *Sci. Rep.* 6 (2016) 20511.
- [138] H. Wang, X. Huang, A. Wang, X. Luo, W. Liu, P. Yuan, J. Feng, Construction of efficient "on-off-on" fluorescence aptasensor for ultrasensitive detection of prostate specific antigen via covalent energy transfer between g-C₃N₄ quantum dots and palladium triangular plates, *Anal. Chim. Acta* 1104 (2020) 53-59.
- [139] Q. Zhou, Y. Lin, K. Zhang, M. Li, D. Tang, Reduced graphene oxide/BiFeO₃ nanohybrids-based signal-on photoelectrochemical sensing system for prostate-specific antigen detection coupling with magnetic microfluidic device, *Biosens. Bioelectron.* 101 (2018) 146-152.
- [140] Y. Wei, X. Li, X. Sun, H. Ma, Y. Zhang, Q. Wei, Dual-responsive electrochemical immunosensor for prostate specific antigen detection based on Au-CoS/graphene and CeO₂/ionic liquids doped with carboxymethyl chitosan complex, *Biosens. Bioelectron.* 94 (2017) 141-147.

- [141] P. Jolly, P. Zhuravski, J.L. Hammond, A. Miodek, S. Liébana, T. Bertok, Jan Tkáč, P. Estrela, Self-assembled gold nanoparticles for impedimetric and amperometric detection of a prostate cancer biomarker, *Sens. Actuators B Chem.* 251 (2017) 637-643.
- [142] A.R. Jalalvand, Fabrication of a novel and ultrasensitive label-free electrochemical aptasensor for detection of biomarker prostate specific antigen, *Int. J. Biol. Macromol.* 126 (2019) 1065-1073.
- [143] F. Duan, S. Zhang, L. Yang, Z. Zhang, L. He, M. Wang, Bifunctional aptasensor based on novel two-dimensional nanocomposite of MoS₂ quantum dots and g-C₃N₄ nanosheets decorated with chitosan-stabilized Au nanoparticles for selectively detecting prostate specific antigen, *Anal. Chim. Acta* 1036 (2018) 121-132.
- [144] A. Rahi, N. Sattarahmady, H. Heli, Label-free electrochemical aptasensing of the human prostate-specific antigen using gold nanospears, *Talanta* 156-157 (2016) 218-224.
- [145] E. Heydari-Bafrooei, N.S. Shamszadeh, Electrochemical bioassay development for ultrasensitive aptasensing of prostate specific antigen, *Biosens. Bioelectron.* 91 (2017) 284-292.
- [146] G. Zhang, Z. Liu, L. Fan, Y. Guo, Electrochemical prostate specific antigen aptasensor based on hemin functionalized graphene-conjugated palladium nanocomposites, *Microchim. Acta* 185 (2018) 1-8.

- [147] G.J. Ashwell, A.T. Williams, S.A. Barnes, S.L. Chappell, L.J. Phillips, B.J. Robinson, B. Urasinska-Wojcik, P. Wierzchowiec, I.R. Gentle, B.J. Wood, Self-Assembly of amino- thiols via gold- nitrogen links and consequence for in situ elongation of molecular wires on surface-modified electrodes, *J. Phys. Chem. C.* 115 (2011) 4200-4208.
- [148] M. Cesbron, E. Levillain, T. Breton, C. Gautier, Click chemistry: A versatile method for tuning the composition of mixed organic layers obtained by reduction of diazonium cations, *ACS Appl. Mater. Interf.* 10 (2018) 37779-37782.
- [149] Y. Liu, D.D. Díaz, A.A. Accurso, K.B. Sharpless, V. V Fokin, M.G. Finn, Click chemistry in materials synthesis. III. Metal-adhesive polymers from Cu (I)-catalyzed azide-alkyne cycloaddition, *J. Polym. Sci. Part A Polym. Chem.* 45 (2007) 5182-5189.
- [150] G. Fomo, N. Nwaji, T. Nyokong, Low symmetric metallophthalocyanine modified electrode via click chemistry for simultaneous detection of heavy metals, *J. Electroanal. Chem.* 813 (2018) 58-66.
- [151] D. Akyüz, A. Koca, An electrochemical sensor for the detection of pesticides based on the hybrid of manganese phthalocyanine and polyaniline, *Sens. Actuators B Chem.* 283 (2019) 848-856.
- [152] B. Öztaş, D. Akyüz, A. Koca, Immobilization of alkynyl functionalized manganese phthalocyanine via click electrochemistry for electrocatalytic oxygen evolution reaction, *Phys. Chem. Chem. Phys.* 19 (2017) 26121-26131.

- [153] Y. İpek, H. Dinçer, A. Koca, Electrode modification based on "click electrochemistry" between terminal-alkynyl substituted cobalt phthalocyanine and 4-azidoaniline, *Sens. Actuators B Chem.* 193 (2014) 830-837.
- [154] C.S.J.N. O'Donoghue, G. Fomo, T. Nyokong, Electrode modification using alkyne manganese phthalocyanine and click chemistry for electrocatalysis, *Electroanal.* 28 (2016) 3019-3027.
- [155] D. Evrard, F. Lambert, C. Policar, V. Balland, B. Limoges, Electrochemical functionalization of carbon surfaces by aromatic azide or alkyne molecules: a versatile platform for click chemistry, *Chem. Eur. J.* 14 (2008) 9286-9291.
- [156] H.R. Phillip, E.A. Taft, Kramers-Kronig Analysis of Reflectance Data for Diamond, *Phys. Rev.* 136 (1964) A1445-A1448.
- [157] G. C. Eastmond, P. C. B. Page, J. Paprotny, R. E. Richards and R. Shaunak, Poly (ether imide)s with hindering substituents in the anhydride moiety: synthesis, properties and gas permeabilities, *Polymer* 35 (1994) 4215-4227.
- [158] X. Zhang, L. Mao, D. Zhang, L. Zhang. Synthesis, characterization and electrochemistry of novel unsymmetrical zinc phthalocyanines sensitizer with extended conjugation. *J. Mol. Struc.* 1022 (2012) 153-158.
- [159] D. Quinton, E. Antunes, S. Griveau, T. Nyokong, F. Bedioui, Cyclic Voltammetry and Spectroelectrochemistry of a Novel Manganese Phthalocyanine Substituted with Hexynyl Groups. *Inorg. Chem. Comm.* 14 (2011) 330-332.

- [160] M.S. Ağirtas, M.S. Izgi, Synthesis and Characterization of New Metallophthalocyanines with Four Phenoxyacetamide Units. *J. Mol. Structure* 927 (2009) 126-128.
- [161] O.J. Achadu, T. Nyokong, In situ one-pot synthesis of graphitic carbon nitride quantum dots and its 2,2,6,6-tetramethyl(piperidin-1-yl)oxyl derivatives as fluorescent nanosensors for ascorbic acid, *Anal. Chim. Acta* 991 (2017) 113-126.
- [162] O.J. Achadu, T. Nyokong, Interaction of Graphene Quantum Dots with 4-Acetamido-2,2,6,6-Tetramethylpiperidine-Oxyl Free Radicals: A Spectroscopic and Fluorimetric Study. *J. Fluoresc.* 26 (2016) 283-295.
- [163] J. Cheng, B.A. Teply, I. Sherifi, J. Sung, G. Luther, F.X. Gu, E. Levy-Nissenbaum, A.F. Radovic-Moreno, R. Langer, O.C. Farokhzad, Formulation of functionalized PLGA-PEG nanoparticles for in vivo targeted drug delivery, *Biomaterials* 28 (2007) 869-876.
- [164] P. Jolly, N. Formisano, J. Tkáč, P. Kasák, C.G. Frost, P. Estrela, Label-free impedimetric aptasensor with antifouling surface chemistry: A prostate specific antigen case study, *Sens. Actuators B Chem.* 209 (2015) 306-312.
- [165] T. Hezard, K. Fajerweg, D. Evrard, V. Colliere, P. Behra, P. Gros, Gold nanoparticles electrodeposited on glassy carbon electrode using cyclic voltammetry: Application to Hg(II) trace analysis. *J. Electroanal. Chem.* 664 (2012) 46-52.
- [166] A.B. Shivanandareddy, M. Kumar, V. Lakshminarayanan, RSC Advances Self-assembly of thiolated graphene oxide onto a gold surface and in the

- supramolecular order of discotic liquid crystals y, *RSC Adv.* 5 (2015) 47692-47700.
- [167] S. Griveau, D. Mercier, C. Vautrin-UI, A. Chaussé, Electrochemical grafting by reduction of 4-aminoethylbenzenediazonium salt: Application to the immobilization of (bio)molecules, *Electrochem. Commun.* 9 (2007) 2768-2773.
- [168] D. Bélanger, J. Pinson. Electrografting: a powerful method for surface modification. *Chem. Soc. Rev.* 40 (2011) 3995-4048.
- [169] J. C. Lacroix, G. Trippe-Allard, J. Ghilane, P. Martin, Optical nanoparticles: synthesis and biomedical application. *Adv. Nat. Sci.: Nanosci. Nanotech.* 5 (2014) 015001.
- [170] L.S. Mpeti, G. Fomo, T. Nyokong, Click chemistry electrode modification using 4-ethynylbenzyl substituted cobalt phthalocyanine for applications in electrocatalysis, *J. Coord. Chem.* 71 (2018) 1623-1638.
- [171] F. Zhang, F. Liu, C. Wang, X. Xin, J. Liu, S. Guo, J. Zhang, Effect of Lateral Size of Graphene Quantum Dots on Their Properties and Application. *ACS Appl. Mater. Interf.* 8 (2016) 2104-2110.
- [172] L. Trapiella-Alfonso, G. Ramírez-García, F. d'Orlyé, A. Varenne, Electromigration separation methodologies for the characterization of nanoparticles and the evaluation of their behavior in biological systems, *Trends Anal. Chem.* 84 (2016) 121-130.

- [173] E. Dervishi, Z. Ji, H. Htoon, M. Sykora, S.K. Doorn, Raman spectroscopy of bottom-up synthesized graphene quantum dots: Size and structure dependence, *Nanoscale* 11 (2019) 16571-16581.
- [174] T. Fan, W. Zeng, W. Tang, C. Yuan, S. Tong, K. Cai, Y. Liu, W. Huang, Y. Min, A.J. Epstein, Controllable size-selective method to prepare graphene quantum dots from graphene oxide, *Nanoscale Res. Lett.* 10 (2015) 1-8.
- [175] S. Bansal, J. Singh, U.Kumari, I.P. Kaur, R.P. Barnwal, R. Kumar, S. Singh, G. Singh, M. Chatterjee, Development of biosurfactant-based graphene quantum dot conjugate as a novel and fluorescent theranostic tool for cancer, *Int. J. Nanomedicine* 14 (2019) 809-818.
- [176] H. Shah, W. Xie, Y. Wang, X. Jia, A. Nawaz, Q. Xin, M. Song, J.R. Gong, Preparation of blue- and green-emissive nitrogen-doped graphene quantum dots from graphite and their application in bioimaging, *Mater. Sci. Eng. C.* 119 (2021) 111642.
- [177] S. Barman, M. Sadhukhan, Facile bulk production of highly blue fluorescent graphitic carbon nitride quantum dots and their application as highly selective and sensitive sensors for the detection of mercuric and iodide ions in aqueous media, *J. Mater. Chem.* 22 (2012) 21832-21837.
- [178] S. Thaweesak, S. Wang, M. Lyu, M. Xiao, P. Peerakiatkhajohna, L. Wang. Boron-doped graphitic carbon nitride nanosheets for enhanced visible light photocatalytic water splitting, *Dalton Trans.* 46 (2017) 10714-10720.

- [179] C.J. Chirayil, J. Abraham, R. Kumar Mishra, S.C. George, S. Thomas, Chapter 1- Instrumental Techniques for the Characterization of Nanoparticles, in: S. Thomas, R. Thomas, A.K. Zachariah, R.K. Mishra (editors), Thermal and Rheological Measurement Techniques for Nanomaterials Characterization., Elsevier, Boston (2017) 1-36.
- [180] K. Syamantak, C.V. Navneet, G. Prashant, J. Sanjhal, G. Souvik G, K.N. Chayan, Mechanistic Insight into the Carbon Dots: Protonation induced Photoluminescence, J. Mat. Sci. Eng. 7 (2018) 1-6.
- [181] D. Bhattacharya, M.K. Mishra, G. De, Carbon Dots from a Single Source Exhibiting Tuneable Luminescent Colors through the Modification of Surface Functional Groups in ORMOSIL Films, J. Phys. Chem. C. 121 (2017) 28106–28116.
- [182] M. Öhman, H. Wan, M. Hamberg, L.G. Blomberg, Separation of conjugated linoleic acid isomers and parinaric fatty acid isomers by capillary electrophoresis, J. Sep. Sci. 25 (2002) 499-506.
- [183] G. Ramirez-Garcia, L. Trapiella-Alfonso, F. d’Orlyé, A. Varenne. Electrophoretic methods for characterizing nanoparticles and evaluating their bio-interactions for their further use as diagnostic, imaging and therapeutic tools. In : Capillary Electromigration Separation Methods, Handbooks in Separation Science, Elsevier (2018), 397-421.
- [184] M.J. Stillman, T. Nyokong In: Eds. Phthalocyanines: Properties and applications, edited by Leznoff CC, Lever ABP VCH, New York, Vol.1, (1989) Chapt 3.

- [185] S. Roy, E. Reisner, Visible-Light-Driven CO₂ Reduction by Mesoporous Carbon Nitride Modified with Polymeric Cobalt Phthalocyanine, *Angew. Chemie - Int. Ed.* 58 (2019) 12180-12184.
- [186] A. Aravind, P. Jeyamohan, R. Nair, S. Veerananarayanan, Y. Nagaoka, Y. Yoshida, T. Maekawa, D.S. Kumar, AS1411 aptamer tagged PLGA-lecithin-PEG nanoparticles for tumor cell targeting and drug delivery, *Biotechnol. Bioeng.* 109 (2012) 2920-2931.
- [187] Z. Zhang, S. Liu, Y. Shi, Y. Zhang, D. Peacock, F. Yan, P. Wang, L. He, X. Feng, S. Fang, Label-free aptamer biosensor for thrombin detection on a nanocomposite of graphene and plasma polymerized allylamine, *J. Mat. Chem. B.* 2 (2014) 1530-1538.
- [188] S. Ni, Z. Shen, P. Zhang, G. Liu, Enhanced performance of an electrochemical aptasensor for real-time detection of vascular endothelial growth factor (VEGF) by nanofabrication and ratiometric measurement, *Anal. Chim. Acta* 1121 (2020) 74-82.
- [189] S. Chung, J.M. Moon, J. Choi, H. Hwang, Y.B. Shim, Magnetic force assisted electrochemical sensor for the detection of thrombin with aptamer-antibody sandwich formation, *Biosens. Bioelectron.* 117 (2018) 480-486.
- [190] W.T. Johnson, Imaging DNA in Solution with the AFM, *Agil. Technol. Oct.* (2008).

- [191] G.G. Matlou, N. Kobayashi, M. Kimura, T. Nyokong, Physicochemical properties of water soluble unsymmetrical phthalocyanine-folic acid conjugates, *Dye.Pigment.* 149 (2018) 393-398.
- [192] S. Pang, T.P. Labuza, L. He, Development of a single aptamer-based surface enhanced Raman scattering method for rapid detection of multiple pesticides. *Analyst* 139 (2014)1895-1901.
- [193] S. Liu, Y. Huo, J. Bai, B. Ning, Y. Peng, S. Li, D. Han, W. Kang, Z. Gao, Rapid and sensitive detection of prostate-specific antigen via label-free frequency shift Raman of sensing graphene, *Biosens. Bioelectron.*158 (2020) 112184.
- [194] A. Zasedatelev, T. Dubinina, D. Krichevsky, V. Krasovskii, V. Gak, V. Pushkarev, L. Tomilova, A. Chistyakov, Plasmon-induced light absorption of phthalocyanine layer in hybrid nanoparticles: Enhancement factor and effective spectra. *J. Phys. Chem.* 120 (2016) 1816-1823.
- [195] S. Nyoni, T. Mugadza, and T. Nyokong, Improved l-cysteine electrocatalysis through a sequential drop dry technique using multi-walled carbon nanotubes and cobalt tetraaminophthalocyanine conjugates. *Electrochim. Acta* 128 (2014) 32-40.
- [196] N. Hashemzadeh, M. Hasanzadeh, N. Shadjou, J. Eivazi-Ziaei, M. Khoubnasabjafari, A. Jouyban, Graphene quantum dot modified glassy carbon electrode for the determination of doxorubicin hydrochloride in human plasma, *J. Pharma. Anal.* 6 (2016) 235-241.

- [197] C.A. Caro, F. Bedioui, J.H. Zagal. Electrocatalytic oxidation of nitrite on a vitreous carbon electrode modified with cobalt phthalocyanine, *Electrochim. Acta* 47 (2002) 1489-1494.
- [198] L. Trnková, Electrochemical behavior of DNA at a silver electrode studied by cyclic and elimination voltammetry, *Talanta* 56 (2002) 887-894.
- [199] J. Jankowska-Śliwińska, M. Dawgul, J. Kruk, D. G. Pijanowska, Comparison of electrochemical determination of purines and pyrimidines by means of carbon, graphite and gold paste electrodes, *Int. J. Electrochem. Sci.* 12 (2017) 2329 - 2343.
- [200] J. Gooding, V. Praig, E. Hall. Platinum-Catalyzed Enzyme Electrodes Immobilized on Gold Using Self-Assembled Layers, *Anal. Chem.* 70 (1998) 2396-2402.
- [201] Z. Li, M. Lieberman, W. Hill. XPS and SERS Study of Silicon Phthalocyanine Monolayers: Umbrella vs Octopus Design Strategies for Formation of Oriented SAMs, *Langmuir* 17 (2001) 4887-4894.
- [202] M.B. Jensen, D.E. Tallman, A LabVIEW-based virtual instrument for simulation and analysis of SECM approach curves, *J. Solid State Electrochem.* 17 (2013) 2999-3003.
- [203] G. Cai, Z. Yu, R. Ren, D. Tang, Exciton-Plasmon Interaction between AuNPs/Graphene Nanohybrids and CdS Quantum Dots/TiO₂ for Photoelectrochemical aptasensing of prostate-specific antigen, *ACS Sens.* 3 (2018) 632-639.

- [204] A. Maringa, E. Antunes, T. Nyokong, Electrochemical behavior of gold nanoparticles and Co tetraaminophthalocyanine on glassy carbon electrode, *Electrochim. Acta* 121 (2014) 93-101.
- [205] M. Delamar, R. Hitmi, J. Pinson, J.M. Saveant. Covalent Modification of Carbon Surfaces by Grafting of Functionalized Aryl Radicals Produced from Electrochemical Reduction of Diazonium Salts. *J. Am. Chem. Soc.* 114 (1992) 5883-5884.
- [206] L. Gonzalez-Macia, S. Griveau, F. d'Orlyé, A. Varenne, C. Sella, L. Thouin, F. Bedioui, Electrografting of aryl diazonium on thin layer platinum microbands: Towards customized surface functionalization within microsystems, *Electrochem. Commun.* 70 (2016) 78-81.
- [207] D. Mwanza, S. Mvango, S. Khene, T. Nyokong, P. Mashazi, Exploiting Click Chemistry for the Covalent Immobilization of Tetra (4-Propargyloxyphenoxy) Metallophthalocyanines onto phenylazide-grafted gold surfaces, *Electrochim. Acta* 254 (2017) 89-100.
- [208] A. Devia, H. Castillo, V. Benavides, Y. Arango, J. Quintero, Growth and characterization of AuN films through the pulsed arc technique, *Mater. Mater. Charact. - Material Characterization* 59 (2008) 105-107.
- [209] S. Prakash, T.M. Long, J.C. Selby, J.S. Moore, M.A. Shannon, "Click" modification of silica surfaces and glass microfluidic channels, *Anal. Chem.* 79 (2007) 1661-1667.

- [210] X. Yan, T. Xu, G. Chen, S. Yang, H. Liu, Q. Xue, Preparation and characterization of electrochemically deposited carbon nitride films on silicon substrate, *J. Phys. D: Appl. Phys.* 37 (2004) 1-7.
- [211] S. Krishnan, Y. Chipatecua, Deep Eutectic Solvent-Assisted Synthesis of Au Nanostars Supported on Graphene Oxide as an Efficient Substrate for SERS-Based Molecular Sensing, *ACS Omega.* 5 (2020) 1384-1393.
- [212] I.G. Casella, M. Contursi, Electrocatalytic oxidation of some hydrazine compounds at glassy carbon electrode modified with co-gluconate complex, *Electroanalysis* 24 (2012) 752-758.
- [213] S. Maree, T. Nyokong. Electrocatalytic behavior of substituted cobalt phthalocyanines towards the oxidation of cysteine, *J. Electroanal. Chem.* 492 (2000) 120-127.
- [214] C.E. Banks, R.G. Compton. New electrodes for old: from carbon nanotubes to edge plane pyrolytic graphite, *Analyst* 131 (2006) 15-21.
- [215] Z. Galus, *Fundamentals of Electrochemical Analysis*, Ellis Horwood Press, New York, 1976, p. 313, Ch. 10.
- [216] R. Devasenathipathy, V. Mani, S-M. Chen, K. Kohilarani, S. Ramaraj. Determination of L-cysteine at Iron Tetrasulfonated Phthalocyanine Decorated Multiwalled Carbon Nanotubes Film Modified Electrode, *Int. J. Electrochem. Sci.* 10 (2015) 682 - 690.
- [217] A.P Gutierrez, M.R. Argote, S.E Griveau, J.H. Zagal, S.G. Granados, A.A. Ordas, F. Bedioui. Catalytic activity of electrode materials based on polypyrrole, multi-

- walled carbon nanotubes and cobalt phthalocyanine for the electrooxidation of glutathione and L-cysteine, *J. Chil. Chem. Soc.* 57 (2012) 1244-1247.
- [218] N. Hernández-Ibáñez, I. Sanjuán, M.Á. Montiel, C.W. Foster, C.E. Banks, J. Iniesta, L-cysteine determination in embryo cell culture media using Co (II)-phthalocyanine modified disposable screen-printed electrodes, *J. Electroanal.Chem.* 780 (2016) 303-310.
- [219] J. Bisquert, A. Compte, Theory of the electrochemical impedance of anomalous diffusion, *J. Electroanal. Chem.* 499 (2001) 112-120.
- [220] P. Salazar, M. Martín, J.L. González-Mora In situ electrodeposition of cholesterol oxidase-modified polydopamine thin film on nanostructured screen printed electrodes for free cholesterol determination, *J. Electroanal. Chem.* 837 (2019) 191-199
- [221] E. Sabatani, I. Rubinstein, Organized self-assembling monolayers on electrodes. 2. Monolayer-based ultramicroelectrodes for the study of very rapid electrode kinetics, *J. Phys. Chem.* 91 (1987) 6663-6669.
- [222] R.I. Stefan, J.F. van Staden, H.Y. Aboul-Enein, *Electrochemical Sensors in Bioanalysis*, Marcel Dekker, New York, 2001.
- [223] R. Jannatifar, K. Parivar, Na. HayatiRoodbari, M.H. Nasr-Esfahani, Effects of N-acetyl-cysteine supplementation on sperm quality, chromatin integrity and level of oxidative stress in infertile men, *Reprod. Biol. Endocrinol.* 17 (2019) 24-32.
- [224] M. Mazloum-Ardakani, P. Pourhakkak, M. Salavati-Niasari, M. A. Karimid, M. H. Mashhadizadehe, Highly Selective and Sensitive Membrane Salicylate Electrode

Based on Complex of (1,8-Diamino-3,6-dioxaoctane) Nickel(II), *J. Braz. Chem. Soc.* 22 (2011) 30-37.

[225] K. Mao, D. Wu, Y. Li, H. Ma, Z. Ni, H. Yu, C. Luo, Q. Wei, B. Du, Label-free electrochemical immunosensor based on graphene/methylene blue nanocomposite, *Anal. Biochem.* 422 (2012) 22-27.

[226] C. Ibaú, M.K. Md Arshad, S.C.B. Gopinath, M. Nuzaihan, M.F.M. Fathil, P. Estrela. Gold interdigitated triple-microelectrodes for label-free prognosticative aptasensing of prostate cancer biomarker in serum, *Biosens. Bioelectron.* 136 (2019) 118-127.

[227] F.-M. Wang, J. Rick, Synergy of Nyquist and Bode electrochemical impedance spectroscopy studies to commercial type lithium ion batteries, *Solid State Ion.* 268 (2014) 31-34.

[228] A.A. Shah, N. Yasmeen, G. Rahman, S. Bilal, High Electrocatalytic Behaviour of Ni Impregnated Conducting Polymer Coated Platinum and Graphite Electrodes for Electrooxidation of Methanol, *Electrochim. Acta* 224 (2017) 468-474.

[229] G. Bouvet, D.D. Nguyen, S. Mallarino, S. Touzain, Analysis of the non-ideal capacitive behaviour for high impedance organic coatings, *Prog. Org. Coat.* 77 (2014) 2045-2053.

[230] W. Argoubi, A. Sánchez, C. Parrado, N. Raouafi, R. Villalonga, Label-free electrochemical aptasensing platform based on mesoporous silica thin film for the detection of prostate specific antigen, *Sens. Actuators B Chem.* 255 (2018) 309-315.

- [231] C. Thunkhamrak, P. Chuntib, K. Ounnunkad, P. Banet, P.-H.Aubert, G. Saianand, A.-I. Gopalan, J. Jakmune, Highly sensitive voltametric immunosensor for the detection of prostate specific antigen based on silver nanoprobe assisted graphene oxide modified screen printed carbon electrode, *Talanta* 208 (2020) 120389.
- [232] F. Tahmasebi, A. Noorbakhsh, Sensitive electrochemical prostate specific antigen aptasensor: Effect of carboxylic acid functionalized carbon nanotube and glutaraldehyde linker, *Electroanalysis* 28 (2016) 1134-1145.
- [233] W. Kong, F. Qu, L. Lu, A photoelectrochemical aptasensor based on p-n heterojunction CdS-Cu₂O nanorod arrays with enhanced photocurrent for the detection of prostate-specific antigen, *Anal. Bioanal. Chem.* 412 (2020) 841-848.
- [234] Y.-K.Yen, C.-H.Chao, Y.-S. Yeh, A Graphene-PEDOT:PSS Modified Paper-Based Aptasensor for Electrochemical Impedance Spectroscopy Detection of TumorMarker, *Sensors* 20 (2020) 1372-1382.
- [235] V. Bernal, A. Erto, L. Giraldo, J.C. Moreno-Piraján, Effect of Solution pH on the Adsorption of Paracetamol on Chemically Modified Activated Carbons, *Molecules* 22 (2017) 1032-1045.
- [236] J.H. Zagal, M.A. Gulppi, C. Depretz, D. Lelièvre, Synthesis and electrocatalytic properties of octaalkoxycobalt phthalocyanine for the oxidation of 2-mercaptoethanol, *J. Porphyr. Phthalocyanines.* 3 (1999) 355-363.

- [237] W.J. Catalona, D.S. Smith, T.L. Ratliff, K.M. Dodds, D.E. Coplen, J.J. Yuan, J.A. Petros, G.L. Andriole, Measurements of Prostate-Specific Antigen in Serum as Screening Test for Prostate Cancer. *New Engl. J. Med.* 324 (1991) 1156-1161.
- [238] H. Liu, Z. Tian, Z. Lu, Z. Zhang, M. Zhang, D. Pang, Direct electrochemistry and electrocatalysis of heme-proteins entrapped in agarose hydrogel films, *Biosens. Bioelectron.* 20 (2004) 294-304.
- [239] M. Srivastava, N.R. Nirala, S.K. Srivastava, R. Prakash, A comparative Study of Aptasensor Vs Immunosensor for Label-Free PSA Cancer Detection on GODs-AuNRs Modified Screen-Printed Electrodes, *Sci. Rep.* 8 (2018) 1923-1933.
- [240] A. Díaz-Fernández, R. Miranda-Castro, P. Estrela, N. de-los-Santos-Álvarez, M.J. Lobo-Castañón, Catching the Sugars: Electrochemical Aptasensors for the Detection of Cancer-Related Glycosylation Changes in Prostate-Specific Antigen, *Proceedings* 60 (2020) 47-51.
- [241] B.P. Crulhas, A.E. Karpik, F.K. Delella, G.R. Castro, V.A. Pedrosa, Electrochemical aptamer-based biosensor developed to monitor PSA and VEGF released by prostate cancer cells, *Anal. Bioanal.Chem.* 409 (2017) 6771-678.

RÉSUMÉ

Dans ce travail de doctorat, des capteurs électrochimiques à base d'aptamères, appelés aptacapteurs, ont été conçus et optimisés pour le diagnostic de l'antigène spécifique de la prostate (PSA). Pour cela, des nanocomposites (des points quantiques à base de graphène non dopés ou dopés, des nanoparticules d'or) et des métallophthalocyanines (MPcs) asymétriques innovants ont été synthétisés et caractérisés physico-chimiquement par diverses méthodes analytiques classiques et un couplage innovant de séparation électrocinétique avec la spectrométrie de masse. Cette caractérisation a permis d'améliorer les protocoles de synthèse des points quantiques de graphène, afin d'atteindre les propriétés attendues de ces objets, en termes de taille, densité de charge, stabilité colloïdale, fonctionnalisation ultérieure ou interaction avec les surfaces d'électrodes. Ces nanocomposites ont ensuite été fonctionnalisés par des aptamères et/ou MPcs, et les combinaisons ont été caractérisées par les méthodes précédentes. Les nanocomposites fonctionnalisés ont été déposés sur la surface d'électrodes en carbone vitreux par adsorption, auto-assemblage, greffage électrochimique et chimie click, afin de générer des aptacapteurs électrochimiques pour la PSA. La quantification a été effectuée par spectroscopie d'impédance électrochimique et voltampérométrie différentielle à impulsions. Ces aptacapteurs ont montré de bonnes sensibilité, sélectivité et répétabilité, avec des limites de détection de l'ordre de 1,2- à 2,0 pM dans des

MOTS CLÉS

Aptasenseurs électrochimiques, phthalocyanines, points quantiques de graphène, nanoparticules d'or, aptamères, antigène spécifique de la prostate, synthèse, caractérisation physico-chimique.

ABSTRACT

In this PhD work, electrochemical sensors based on aptamers, called aptasensors, were designed and optimised for prostate specific antigen (PSA) diagnosis. For this purpose, first innovative nanocomposites that were either undoped or doped graphene-based quantum dots, and gold nanoparticles; as well as asymmetric metallophthalocyanines (MPcs) were synthesised and characterised physico-chemically by various classical analytical methods (in solid state or in solution) and an innovative coupling of electrokinetic separation with mass spectrometry. This characterisation has allowed to improve the synthesis protocols of various graphene quantum dots, in order to achieve the expected properties of these nano-objects, in terms of size, charge density, colloidal stability, and to help for their subsequent functionalisation or the generation of specific interaction with electrode surfaces. These nanocomposites were then functionalized with aptamers and/or MPcs, and the combinations were characterized by the previous methods. The functionalized nanocomposites were deposited on the surface of glassy carbon electrodes by either adsorption, self-assembly, electrochemical grafting or click chemistry to generate electrochemical aptamers for PSA. Quantification was performed by electrochemical impedance spectroscopy and differential pulse voltammetry. These sensors showed good sensitivity, selectivity and repeatability, with detection limits in the range of 1.2- to 2.0 pM in model buffers and spiked serum samples, compatible with early diagnosis of prostate cancer. In addition, the synergistic effects of AuNPs and CoPcs-based quantum dots were demonstrated using electrochemical methods.

KEYWORDS

Electrochemical aptasensors, phthalocyanines, graphen quantum dots, gold nanoparticles, aptamers, prostate specific antigen, synthesis, physico-chemical characterization